DOCTOR OF SCIENCES

Modelling optical and plasmonic responses of 2D materials

Majerus, Bruno

Award date:
2022

Awarding institution:
University of Namur

Université de Namur
Namur Institute of Structured Matter (NISM)
Laboratoire de Physique du Solide (LPS)

Modelling optical and plasmonic responses of 2D materials

Presented by Majérus Bruno

For the degree of doctor in sciences

October 2022

Prof. Henrard Luc (Supervisor)	Université de Namur
Prof. Deparis Olivier (Co-Supervisor)	Université de Namur
Prof. Hackens Benoît	Université Catholique de Louvain
Prof. Charlier Jean-Christophe	Université Catholique de Louvain
Prof. Kockaert Pascal	Université Libre de Bruxelles
Prof. Sporken Robert (Chairman)	Université de Namur

Remerciements

Après plus de 6 ans de doctorat et l'écriture d'une thèse, on prend plaisir à regarder, non sans fierté, le chemin parcouru et l'ampleur de la tâche que l'on vient d'accomplir. Pourtant, la qualité de cette thèse serait bien moindre sans un grand nombre de personnes qui, par leur collaboration, leur aide et/ou leur soutien, ont contribué à ce manuscrit. Je tiens à les remercier en ces quelques lignes.

Je remercie évidemment mon promoteur, le professeur Luc Henrard, pour m'avoir donné l'opportunité de réaliser un mémoire puis une thèse sous sa supervision. Toujours disponible, ses nombreux conseils avisés m'ont grandement aidé à finaliser ce projet. Qui plus est, grâce à lui, plusieurs collaborations ont abouti à des publications dans des journaux prestigieux.

Je peux également remercier le professeur Olivier Deparis, co-promoteur, qui, notamment par sa relecture attentive de la première version de cette thèse, m'a permis d'améliorer considérablement la qualité du manuscrit.

Durant ces quelques années, j'ai eu la chance d'avoir des intéractions enrichissantes, voire des collaborations avec les autres membres du jury. Merci à eux pour cela, mais également pour leurs commentaires constructifs lors de la défense privée.

Durant ces 6 ans, j'ai pu travailler avec d'autres chercheurs d'un peu partout dans le monde. A Namur d'abord, je pense à Mika, qui, bien que nos chemins scientifiques se soient un peu écartés depuis quelques années, reste une des personnes qui m'a le plus accompagné dans ma carrière, mais aussi à mes anciens mémorants, Emerick et Lisa ; à Nicolas Reckinger, Mirko ou encore Philippe Lambin. Merci à chacun d'eux. A l'étranger, je me dois de remercier Evdokia Dremetsika ; Raul Arenal et Mario Palaez Fernandez de l'université de Saragosse ; Péter Vancsó, Levente Tapasztó et toute son équipe du Centre for Energy research de Budapest ; Paulina Kuzhir et les chercheurs du Research Institute for Nuclear Problems à Minsk pour m'avoir accueilli et, finalement Olivier Martin et son équipe à l'EPFL.

Bien évidemment, je ne peux oublier mes collègues du LPS grâce à qui l'environnement de travail a été agréable et motivant. Ces dernières années ont été des plus chouettes avec vous tous (malgré le covid)! Je me dois de remercier quelques personnes en particulier. En premier, Jeff, pour la cuisson des barbecues et surtout le commérage pendant les 5 ans passés dans le bureau avec toi! Merci à la nouvelle équipe du bureau 150b (Nicolas, Tanguy et Emerick), c'était agréable de retrouver un bureau plein de vie (sauf pour les plantes…) après ces longs mois de télétravail. Mais surtout merci à Pauline pour l'énergie qu'elle a su donner pour le labo, l'organisation des week-ends LPS et de tout le reste.

Je remercie également l'équipe des assistants, les collaborateurs didactiques ainsi que Fernande Frising et Laurent Zanotto, pour leur aide et la solidarité dont ils ont fait preuve, notamment durant les années covid. J'ai une pensée également pour les assistants organisateurs de "la journée des assistants" qui fût une chouette expérience.

Merci à Héloïse, Mathilde, Stéphanie, Coraline, Valentin, Thomas, Adrien et compagnie, pour ces super années d'études passées ensemble.

Je n'aurai jamais pu aller au bout de ma thèse s'il n'y avait pas eu tous ces moments de décompression et de détente passés avec les collègues et amis du département de physique (je ne les cite pas tous au risque d'en oublier, ils se reconnaitront). A la coloc', en rando, aux wallos, et j'en passe, c'est des centaines de super souvenirs que je garderais de ces années de thèse. Un gros merci à eux.

Le confinement aurait été bien plus difficile à vivre sans les super colocs que sont Romain, Florian, Dik et Florent (sans oublier Sebastien avant ça). Merci à eux de m'avoir supporté tout ce temps (les pauvres ont découvert mon côté obscur...)!

Merci à tous les autres amis que je n'ai pas encore cités, mais qui n'ont pas manqué de m'apporter leur soutien ces dernières années.

Merci bien évidemment à ma famille pour leurs encouragements durant toutes ces années. Ils ont été une de mes principales sources de motivation.

Enfin, un énorme merci à Marie qui a réussi à me supporter durant ces derniers longs mois de thèse, malgré ses propres épreuves pour devenir docteure. Merci pour ton écoute et l'aide que tu m'a apportée qui m'ont permis à tenir le coup jusqu'à la fin.

Résumé

Les matériaux 2D, composés d'un ou quelques atomes d'épaisseur, sont étudiés depuis leur découverte en 2004 pour leur propriétés électroniques et optiques uniques, permettant d'entrevoir des applications dans divers domaines. Par exemple le graphène en tant que matériau transparent conducteur pourrait être intégré dans des panneaux solaires ou dans des smartphones. D'un autre côté, certains dichalcogénures de métal de transition tel que le diséléniure de molybdène sont des semi-conducteurs qui pourraient se substituer aux semi-conducteurs conventionnels dans les puces électroniques. Dans ces matériaux 2D, des plasmons peuvent également être observés. Ces phénomènes de résonance entre la lumière et les électrons libres, sont à l'origine d'un confinement intense de l'énergie électromagnétique autour de nanoparticules et autres structures de taille nanométrique. Cela rend possible le design de guide d'ondes optique bien plus petit que ceux actuellement utiliser ou encore la création de biosenseurs de grande sensibilité.

Pour étudier les propriétés optiques des matériaux 2D et en particulier les plasmons, de nombreuses méthodes d'électrodynamique classique adaptées aux matériaux « volumiques » sont utilisées. Cependant, des questions se posent sur la façon de modéliser ces matériaux d'épaisseur atomique de manière adéquate. Faut-il considérer une épaisseur finie pour la couche 2D ou peut-on les modéliser comme une couche infiniment fine ? Est-ce que l'anisotropie des matériaux 2D joue un rôle déterminant dans leur réponse optique ? Dans cette thèse, des éléments de réponses sont apportés en comparant analytiquement et numériquement les différents modèles utilisés. Notamment, il est montré que les modèles isotropes sont peu adaptés et que les modèles anisotropes d'épaisseur respectivement finie et infiniment fine sont relativement similaires tant que le déphasage de l'onde dû au feuillet 2D n'est pas trop importante.

D'un autre côté, des nanostructures de matériaux 2D peuvent être étudiés de manière quantique, en considérant la structure atomique du matériau et en résolvant de manière approximée l'équation de Schrödinger. La fonction diélectrique microscopique obtenue à partir de ces calculs permet d'étudier les plasmons dans ces nanostructures. Dans cette thèse, il est montré que du graphène corrugué peut contenir des plasmons localisés dans les corrugations. Ce type de surface permet d'exalter la réponse optique de certaines molécules de façon à ce qu'on puisse les détecter même en quantité infime. Il est également prouvé théoriquement dans la thèse que des plasmons peuvent se propager dans des joints de grains de diséléniure de molybdène. La caractérisation de ces matériaux et la détermination du nombre de défauts linéaires serait donc possible par l'observation de résonances plasmoniques.

Abstract

2D materials, composed of one or a few atoms thick, have been studied since their discovery in 2004 for their unique electronic and optical properties, allowing to foresee applications in various fields. For example, graphene as a transparent conductive material could be integrated in solar panels or smartphones. On the other hand, some transition metal dichalcogenides such as molybdenum diselenide are semiconductors that could replace conventional semiconductors in electronic chips. In these 2D materials, plasmons can also be observed. These phenomena of resonance between light and free electrons, are at the origin of an intense confinement of the electromagnetic energy around nanoparticles and other structures of nanometric size. This makes it possible to design optical waveguides much smaller than those currently used or to create highly sensitive biosensors.

To study the optical properties of 2D materials and in particular plasmons, many classical electrodynamic methods adapted to "bulk" materials are used. However, questions arise on how to model these atomically thin materials adequately. Should we consider a finite thickness for the 2D layer or can we model is as an infinitely thin layer? Does the anisotropy of 2D materials play a determining role in their optical response? In this thesis, some answers are brought by comparing analytically and numerically the different models used. In particular, it is shown that isotropic models are not very well adapted and that anisotropic models of respectively finite and infinitely thin thickness are relatively similar as long as the phase shift of the wave due to the 2D film is not too important.

On the other hand, nanostructures of 2D materials can be studied in a quantum way, considering the atomic structure of the material and solving the Schrödinger equation in an approximate way. The microscopic dielectric function obtained from these calculations allows to study plasmons in these nanostructures. In this thesis, it is shown that corrugated graphene can sustain plasmons localized in the corrugations. This type of surface allows to exalt the optical response of some molecules such that they can be detected even in extremely small quantities. It is also theoretically proven in the thesis that plasmons can propagate in molybdenum diselenide grain boundaries. The characterization of these materials and the determination of the number of linear defects would thus be possible by the observation of plasmonic resonances.

Contents

List of publications

[A] B. Majérus, J. Butet, G. D. Bernasconi, R. T. Valapu, M. Lobet, L. Henrard, and O. J. F. Martin, *Optical Second Harmonic Generation from Nanostructured Graphene: A Full Wave Approach*, Opt. Express **25**, 27015 (2017).
DOI: 10.1364/OE.25.027015

[B] B. Majérus, M. Cormann, N. Reckinger, M. Paillet, L. Henrard, P. Lambin, and M. Lobet, *Modified Brewster Angle on Conducting 2D Materials*, 2D Mater. **5**, 025007 (2018).
DOI: 10.1088/2053-1583/aaa574

[C] B. Majérus, E. Dremetsika, M. Lobet, L. Henrard, and P. Kockaert, *Electrodynamics of Two-Dimensional Materials: Role of Anisotropy*, Phys. Rev. B **98**, 125419 (2018).
DOI: 10.1103/PhysRevB.98.125419

[D] G. Dobrik, P. Nemes-Incze, B. Majérus, P. Süle, P. Vancsó, G. Piszter, M. Menyhárd, B. Kalas, P. Petrik, L. Henrard and L. Tapasztó, *Large-Area Nanoengineering of Graphene Corrugations for Visible-Frequency Graphene Plasmons*, Nat. Nanotechnol. **17**, 61 (2022).
DOI: 10.1038/s41565-021-01007-x

[E] M. Pelaez-Fernandez, B. Majérus, D. Funes-Hernando, R. Dufour, J.-L. Duvail, L. Henrard, and L. Arenal, *Toward Laser-Induced Tuning of Plasmonic Response in High Aspect Ratio Gold Nanostructures*, Nanophotonics, vol. 11, no. 16, 2022, pp. 3719-3728 (2022).
DOI: 10.1515/nanoph-2022-0193

[F] B. Majérus, L. Henrard, and P. Kockaert, *Optical modelling of 2D materials and multilayer systems: a complete picture*, submitted (2022).

[G] B. Majérus, E. Guillaume, and L. Henrard, *Anisotropy and effective medium approach in the optical response of 2D material heterostructures*, manuscript in preparation (2022).

Introduction

At the beginning of the 21st century, materials science has been challenged by the incredible rise of the research on 2D materials, materials with one or a few atoms of thickness [1]. Since the first experimental isolation of graphene, a layer of carbon atoms arranged in a honeycomb lattice, by Geim and Novoselov [2, 3], hundred thousands of papers have been published, exploring the electronic, optical, and mechanical properties of a large variety of 2D materials.

As a flexible transparent conductor with an extremely small thickness, graphene has gained much attention in the early 2000s. It was quickly expected that graphene could be integrated into electronic devices. While this idea has been discarded since then, principally because graphene is a gapless semi-metal [4], nanostructured graphene has been investigated in order to modify its electronic properties. Other 2D materials have also grasped growing interest in the scientific community [1]. Some like MoS_2 are semi-conductors, which could lead to the design of field effect transistors of atomic thickness [5]. Another famous 2D material is hexagonal boron nitride (hBN), often associated with other 2D materials in order to improve their stability and electronic properties [6].

These 2D materials have also been investigated for their optical properties. As an electronic conductor, graphene absorbs a small part of the light incident on it [7]. In the range of micro-waves, it can even absorb a high proportion of the incoming energy in some conditions [8]. Other peculiar optical effects such as the Goos-Hänchen shift [9–11] and the Brewster angle [12–18] are modified by the presence of a 2D materials at the surface of a dielectric. In this thesis, the shift of the Brewster angle induced by a conducting 2D material has been investigated. It is shown that for 2D materials with small conductivity, the shift is proportional to the conductivity. Using this result, experimental determination of the conductivity of graphene from the measurement of the Brewster angle shift has been performed. It is also shown that a significant modification of the angle can be controlled actively by applying a gate voltage to the graphene samples.

In order to study optical phenomena in 2D materials in a classical electrodynamics framework, accurate and efficient models should be used. Indeed, bulk materials are generally considered in state-of-the-art methods, and including 2D materials is not straightforward. A first question on the modelling is how different are models which consider the 2D layer as infinitely thin (2D models) to models with a small but finite thickness (3D model)s. These two kinds of models have been adopted indifferently in the literature but few studies have been performed to justify their use. Another challenge in the modelling of 2D material is their intrinsic anisotropy. This optical anisotropy is sometimes disregarded in numerical simulations. Few articles has yet investigate these questions [19–23]. For example in [19] and [24], they compared the 2D and the 3D models but only at normal incidence, which does not permit to study the effect of the anisotropy. In the most complete study to date [21], the models (2D, 3D, isotropic and anisotropic) are compared based on ellipsometric and reflectivity measurements. However, a more general theoretical study has not been proposed before.

A large part of this thesis is focused on these anisotropy and thickness considerations. The goal is to propose a coherent overview of the modelling of 2D materials and determine

the limits of the common models. The appropriate response functions are rigorously derived for in-plane and out-of-planes excitations from a microscopic point of view. Based on these responses function, the models are compared numerically and analytically. It is shown that 2D and 3D anisotropic models are equivalent for small phase shifts in the 2D materials but that the isotropic 3D model can be inaccurate due to fake plasmon resonances. Furthermore, effective models are proposed to describe heterostructures of 2D materials.

Another optical phenomena observed in nanostructured 2D materials are surface plasmon resonances [25]. Plasmons results from strong light-matter interactions, in which the free electrons of a metal are in resonance with the electromagnetic field [26]. At a plasmonic resonance, the electromagnetic energy is confined in a small region near the particle. Plasmons have been studied for several decades, in particular in noble metal nanoparticles, and are especially of great interest for applications in biosensing and photonics. For example, nanowires and nanorods have been proposed as plasmonic waveguides [27–29]. With a largely reduced sized compared to conventional glass waveguides, these metallic nanostructures are of fundamental interest in order to manipulate and propagate light at a sub-wavelength scale. Recent studies on nanowires have shown that Fabry-Pérot plasmonic modes follow the dispersion relation of polaritons in infinite nanowires [30–32]. In particular, high aspect-ratio nanowires exhibit plasmonic resonances at relatively low energy and long wavelength [33]. One of the chapters of this thesis is dedicated to our research article on the plasmonic resonances in high aspect-ratio gold nanowires. In particular, the robustness of the plasmons when modifying the morphology of the edges of the nanowires is investigated. It is shown that at low energy, the plasmons remain unaffected by the presence of spherical nanoparticles at the extremities of the nanowires. On the other hand, at high energy, when the size of the nanoparticles is of the order of the plasmon wavelength, the plasmon energy is shifted. As the morphology of the nanowires may be changed after the synthesis of the nanowire by means of laser irradiation, this may be proposed as a way to tune the plasmonic responses.

In graphene and other 2D materials, plasmons exhibit larger confinement and can even be actively tuned [25]. For graphene nanoparticles, the plasmonic resonances occur in the terahertz or infrared ranges [34]. Researches are currently performed to attempt to shift the resonance in the visible range. As the resonance energy increase when the size of the nanoparticle decrease, graphene nanoparticles of the size of a few nanometers have been suggested. However, as the size decrease, quantum effects become significant, and charge scattering on the edges tends to damp critically the plasmons [35]. Nonetheless, the plasmon resonances in graphene nanoparticles, and the resulting field enhancement, could be used for different purposes such as biosensing and optical characterization. Surprisingly, plasmonic resonances may also occur in nanostructured 2D insulators and semi-conductors, owing to atomic defects in their structures. Indeed, some linear defects or edges in semiconductors 2D materials have been shown to be metallic channels [36, 37].

The last part of the thesis is focused on the study of plasmonic resonance in nanostructured 2D materials. First, it is shown how plasmons in a dimer of graphene disk

enhance the electric field [38]. This high electric field can be used to enhance the non-linear response, and it is shown how the geometry influences this response. Two other nanostructures have been investigated. These are systems of size around the nanometer, where quantum effects are prevailing. Therefore the optical properties of the system must be calculated in a quantum framework. The plasmons are analyzed using the microscopic dielectric function derived from time-dependent density functional theory. The first system is corrugated graphene. It is shown that localized plasmons with a resonance frequency in the visible range occur in the corrugation. Graphene plasmons in the visible range were long-awaited because extremely small nanoparticles, in which plasmon damping is high due to the charge carriers scattering on the edges, are needed [39]. Such corrugated graphene can serve as an efficient substrate to enhance the Raman response of specific molecules [40]. The second system is a linear grain boundary in transition metal dechalcogenides which contains metallic states [41]. In consequence, these linear defects may sustain propagating plasmons. Therefore, optical characterization of the number of defects could be performed by analyzing the plasmonic response of the considered samples.

The manuscript is organized in the following manner:

- The first chapter is a short introduction to optics and plasmonics, in general, and in the context of 2D materials.

- In the second chapter, an overview of the calculation of the dielectric function from a microscopic point of view is presented. This will be useful to describe the method of analysis of plasmons in nanostructure. Then the method to obtain the macroscopic permittivity from the microscopic dielectric function is detailed.

- State-of-the-art methods for studying optics and plasmonics in classical systems are described in the third chapter. Three complementary methods are detailed: the rigorous coupled wave analysis (RCWA), the discrete dipole approximation (DDA), and the surface integral equation (SIE).

- In chapter four, the numerical analysis of localized plasmons in gold nanowires is compared with experimental results.

- In the fifth chapter, the different ways to model 2D materials are described and compared, accounting for the anisotropy. In particular, the different surface susceptibilities that should be used for the in-plane polarization and the out-of-plane polarization are derived. The effective models for vertical and horizontal heterostructures are presented. In the sixth chapter, the shift of the Brewster angle due to conducting 2D materials is demonstrated, and it is shown how to retrieve experimentally the surface susceptibility with a non-contact method.

- The last chapter describes some cases of plasmonic resonances in nanostructured 2D materials. First, nanodisks of graphene are investigated in a classical framework. The last two sections are centered on quantum systems with atomic structures responsible for extremely confined plasmons. First, it is shown that corrugated

graphene sustains localized plasmons in its corrugations. Then, propagating plasmons in metallic grain boundaries and edges of transition metal dechalcogenides are investigated.

Chapter 1

Plasmonics in 2D materials

With their large variety of electronic and mechanical properties and their extremely small thickness, 2D materials are good candidates to replace bulk materials in lots of devices. Their optical properties have interested researchers in nanophotonics and plasmonics, with possible applications in biosensing, waveguides, and photovoltaics. This first chapter is a short overview of optics for 2D materials. In the first section, a theoretical introduction to plasmonics is proposed. Then, common 2D materials are presented. Finally, in the last section, the optical response of graphene in particular and the plasmonic properties of 2D materials and nanostructured 2D materials are described.

1.1 Optics and plasmonics

The vast majority of optical phenomena observed in everyday life are explained using classical electrodynamics. This theory, governed by Maxwell's equations established in the mid-19th century, is still one of the most successful and employed in applied physics and engineering. Among all the peculiar phenomena discovered and explained more recently using classical electrodynamics stands those in the field of plasmonics. Plasmons are collective oscillations of free electrons strongly coupled to the electric field in metals. In particular, surface plasmons occur at the metal-dielectric interface of metallic structures or nanoparticles. As visible light or other electromagnetic waves can couple to such plasmons, the electromagnetic energy is confined at a scale much smaller than the wavelength, allowing to manipulate light at the nanoscale, or to enhance the field intensity up to extreme value. These properties of plasmons permit a broad range of applications in various domains such as plasmonic waveguides, better photovoltaic efficiency or ultrasensitive biosensing.

Classical electrodynamics

The Maxwell's equations are at the core of classical electrodynamics. Their macroscopic forms are written [42]:

$$\nabla \cdot \mathbf{D} = \rho_f, \tag{1.1}$$

$$\nabla \cdot \mathbf{B} = 0, \tag{1.2}$$

$$\nabla \times \mathbf{E} = -\frac{\partial \mathbf{B}}{\partial t}, \tag{1.3}$$

$$\nabla \times \mathbf{H} = \mu_0 \mathbf{J}_f + \frac{\partial \mathbf{D}}{\partial t}, \tag{1.4}$$

where ρ_f and $\mathbf{J}_f$ are the charge and current densities of the free charges. The constitutive equations are

$$\mathbf{D} = \varepsilon_0 \varepsilon \mathbf{E}, \tag{1.5}$$

and

$$\mathbf{H} = \frac{1}{\mu_0 \mu} \mathbf{B}, \tag{1.6}$$

where ε and μ are the relative permittivity and permeability of the medium. If these quantities are known, the system of equations can be solved to determine the fields. Other relevant quantities such as the Poynting vector, the scattering cross section or the reflected/transmitted intensity may be calculated from the total fields. Note that, in this thesis, only non-magnetic materials are considered ($\mu = 1$). In a homogeneous medium, the solution of the Maxwell equations is the solution to the following wave equation:

$$\nabla \times \nabla \times \mathbf{E} = -\varepsilon \frac{1}{c^2} \frac{\partial^2 \mathbf{E}}{\partial t^2}, \tag{1.7}$$

which is a plane wave:

$$\mathbf{E} = \mathbf{E}_0 e^{i(\mathbf{k} \cdot r - \omega t)}, \tag{1.8}$$

In inhomogeneous media, the electromagnetic wave undergoes discontinuities at the interfaces between materials. The boundary conditions at the interfaces between two media 1 and 2 of different permittivities are found from Maxwell's equations:

$$\mathbf{n} \cdot [\mathbf{D}_2 - \mathbf{D}_1] = \sigma, \tag{1.9}$$

$$\mathbf{n} \cdot [\mathbf{B}_2 - \mathbf{B}_1] = 0, \tag{1.10}$$

$$\mathbf{n} \times [\mathbf{E}_2 - \mathbf{E}_1] = 0, \tag{1.11}$$

$$\mathbf{n} \times [\mathbf{H}_2 - \mathbf{H}_1] = \mathbf{J}_s, \tag{1.12}$$

with σ and $\mathbf{J}_s$ the surface charge and surface current densities and $\mathbf{n}$ the unit vector normal to the interface. These equations are used to calculate the charges at the interface from which the induced coulomb potential can be obtained. It will be shown in a later chapter that these equations must be generalized in the case of 2D materials lying at the interface.

The Drude model

As plasmons occur in metals, different models has been established to describe the frequency dependency of the permittivity. In the Drude model, the motion of the free electrons is described by a damped oscillator [43]. The dielectric function is given by

$$\varepsilon(\omega) = 1 - \frac{\omega_p^2}{\omega^2 + i\gamma\omega}, \tag{1.13}$$

where γ is the damping frequency, and ω_p, the plasma frequency, depends only on the charge density. The real part of the dielectric function ε_1 is then

$$\varepsilon_1(\omega) = 1 - \frac{\omega_p^2}{\omega^2 + \gamma^2}. \tag{1.14}$$

At high frequencies, $\omega \gg \gamma$, the real part of the permittivity vanishes at the plasma frequency ω_p. According to eq. (1.5), it means that an electric field is sustained in the absence of a displacement field. Reminding that the displacement field corresponds to the field generated by the external source (without the metallic media), the electric field is thus self-sustained. In reality, the imaginary part of the permittivity is small but not negligible. Then the total field is very large compared to the displacement field and in phase quadrature with it. Inverting the Drude formula, one obtain

$$\frac{1}{\varepsilon(\omega)} = 1 - \frac{\omega_p^2}{\omega_p^2 - \omega^2 - i\gamma\omega}, \tag{1.15}$$

which, at the plasma frequency, becomes

$$\frac{1}{\varepsilon(\omega_p)} = 1 - \frac{i\omega_p}{\gamma}. \tag{1.16}$$

The imaginary part of this function becomes large at the plasma frequency for low damping. Therefore, the function $L(\omega)$ defined by

$$L(\omega) = -Im\left(\frac{1}{\varepsilon(\omega)}\right) \tag{1.17}$$

has a peak at the plasma frequency. However this resonant phenomenon is not excitable by light. Indeed, from eq. (1.7) for a plane wave, it can be written

$$\mathbf{k}(\mathbf{k}\cdot\mathbf{E}) - k^2\mathbf{E} = -\varepsilon\frac{\omega}{c^2}\mathbf{E} \tag{1.18}$$

which, for $\varepsilon \to 0$, is only possible for $\mathbf{k} /\!\!/ \mathbf{E}$. This corresponds to a longitudinal wave which cannot be excited by transverse waves such as light waves. These longitudinal resonant waves are the volume plasmons of metals. They can be observed using characterisation techniques involving electrons. For example, in electron energy loss spectroscopy (EELS), a beam of high energy electrons is focused on the sample and, based on the loss of energy of the electrons received on the detector, the energy of the plasmon can be determined. Longitudinal waves can be detected since the electrons can transfer their momentum to the plasmon. Theoretically, it can be shown that the EELS intensity is proportional to the function $L(\omega)$ defined above. As the energy loss of the electrons is maximal when this function is maximal, it is called the loss function [43].

Surface plasmons

As the volume plasmons described above cannot be excited by light, its interest in optics is limited. However, plasmons taking place at the surface of metal and metallic particles may be excited by light and have been intensively investigated for various domains of application in optics.

Surface plasmon polaritons (SPPs) stand at the interface between a dielectric and an extended metallic material. Transverse magnetic (TM) waves can propagate along the surface in both media with wave vector β, while only evanescent waves are possible in the perpendicular direction. As an example, figure 1.1 (from [43]) displays the real (solid lines) and imaginary (dashed lines) parts of the dispersion relation of a silver/air (gray curve) and silver/silica (black curve) interface calculated using the Drude dielectric function.

At the surface plasmon frequency, given by

$$\omega_{sp} = \frac{\omega_p}{\sqrt{1+\varepsilon_m}} \tag{1.19}$$

with ω_p the plasma frequency and ε_m the permittivity of the dielectric, the wave vector is maximum (or infinite if there is no loss) and the plasmon wavelength is greatly decreased compared to the free-space wavelength. However, as the dispersion curve lies below the corresponding light line, a direct coupling between light and the SPP is not possible. Various phase-matching techniques have been developed to excite SPPs with light as, for example, prism coupling, grating coupling or near-field illumination [43].

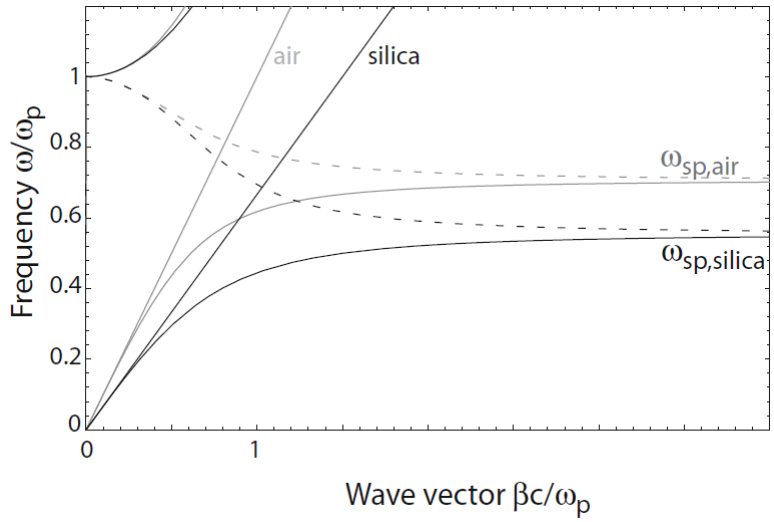

Figure 1.1: Dispersion relation of SPPs at the interface between a Drude metal with negligible collision frequency ($\gamma = 0$) and air (gray curves) and silica (black curves). Reproduced from [43].

The second type of surface plasmons are localized surface plasmons (LSP) at the surface of nanoparticles. These plasmons are electromagnetic standing waves on closed metallic surfaces. For dipolar modes, such as represented in figure 1.2 reproduced from [44], the particle's polarizability is maximum at the plasmon frequency. For spheres much smaller than the wavelength, the condition to have a localized surface plasmon resonance (LSPR) is

$$Re\left(\varepsilon\left(\omega\right)\right) = -2\varepsilon_m. \tag{1.20}$$

For larger spheres, the Mie theory predicts that the resonance energy is redshifted compared to this value [43]. For different sizes, shapes and compositions of the particles, the resonance frequency is also modified. In consequence, a large variety of particles has been investigated to characterize their properties.

Plasmons may also be studied by considering the microscopic dielectric function of an inhomogeneous medium. This microscopic function contains all the information about the optical response of the considered system. Therefore, when surface plasmons are excited inside the nanostructure, the total field is large compared to the applied field and the real part of the dielectric function vanishes [45]. In order to model this dielectric function in nanostructures, a single-pole model has been proposed, based on the Lorentz dielectric function for bound charges [45, 46]:

$$\varepsilon\left(\omega\right) = 1 + \frac{\omega_p^2}{\omega_0^2 - \left(\omega + i\gamma\right)^2} \tag{1.21}$$

This function is represented in figure 1.3. The real part of the dielectric function crosses zero at two frequencies. Near the frequency ω_0, the dielectric function goes from positive to negative values. As the imaginary part of the dielectric function is large at ω_0, the loss function is not high. At the frequency $\omega_{pl} = \sqrt{\omega_p^2 + \omega_0^2}$, the real part of dielectric

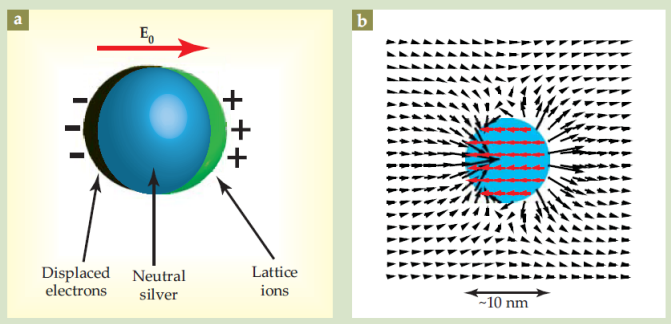

Figure 1.2: An instantaneous snapshot of the localization of an optical field in a nanosystem. (a) When an external light wave is incident on a silver sphere, its electric field E_0 periodically displaces the sphere's electrons with respect to the lattice. The result is an oscillating electron density, a localized surface plasmon. (b) The electric field (black arrows) from displaced electrons is greatly amplified on opposite sides just outside a silver 10-nanometer-diameter sphere, as calculated here for a resonant photon energy of 3.5 eV. Inside the sphere, the electric field is uniform (red arrows) and is on the same order of magnitude as the local field outside the sphere. Reproduced from [44].

function goes from negative to positive value, the imaginary part of the dielectric function is small and the loss function is maximum. This frequency ω_{pl} corresponds to the plasmon resonance frequency.

Quantum effects

The surface plasmons on nanoparticles and on planar surfaces are explained quite comprehensively by the classical electrodynamics theory. However, when the size of the structure or the nanoparticle is shrunk to a few nanometers, quantum effects become significant [35]. The quantum effects are many. Most importantly, there is a quantisation of the energy level. But other effects should be accounted: the electronic states of the edges must be considered when the number of edge atoms becomes significant; the size of the particles becomes smaller than the mean free path of electrons and tunneling effects are possible. A full quantum electrodynamics theory is not always necessary but the electronic properties of the nanostructures must be determined using the quantum theory.

Applications

Interestingly, the plasmonic properties of nanoparticles have been used for centuries without an understanding of the underlying phenomena. Stained glass and other decorative items such as the Lycurgus cup have been manufactured using colloidal metallic nanoparticles to obtained peculiar coloration [44]. But recently, plasmonic effects have been mostly used for biosensing. Due to the dramatic effect of the environment on the plasmonic resonance, in particular in presence of molecules, specific molecules can be

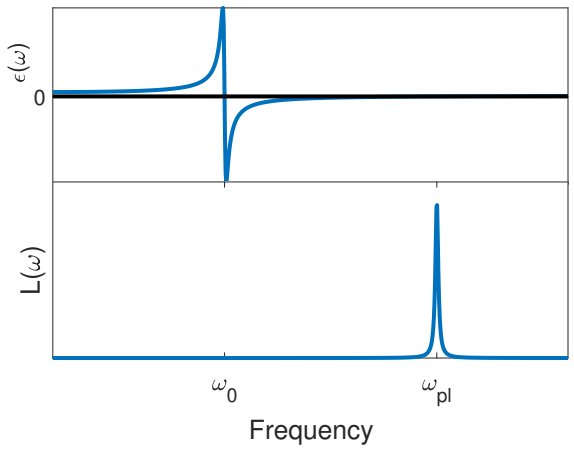

Figure 1.3: Real part of the dielectric function (top) and loss function (bottom) for the Lorentz model of eq. (1.21).

detected. It is used, for example, in antigenic test [44, 47]. Another effect useful for biosensing is the enhancement of the electric field near plasmonic particles. In Raman spectroscopy, the inelastic optical response of molecules is strongly dependent on the local electric field. The principle of surface enhanced Raman spectroscopy is to use a plasmonic surface to benefits from the intense field. This method enables to detect a single molecule due to plasmonic resonance on plasmonic surfaces [40]. Other applications are, for example, plasmonic waveguides that can transmit information using light through nanostructure [48], or increasing the light capture in photovoltaic panels [49].

1.2 2D materials

Since the beginning of the century, the interest for 2D materials has been growing intensively. During the last 2 decades, more than 200 000 research works on graphene or 2D materials were published in peer-reviewed journals, mobilizing thousands of researchers[1]. In this context, the diversity of the materials and their properties is extremely large. I present here a few of these materials and their general properties before focusing on their optical properties in the next section.

More than 1500 2D materials have been identified, though most of them only theoretically [50]. Among them is, of course, graphene, which has been focusing attention as much in the academic realm than in the mainstream media. Its relatively easy isolation, the abundance of its source component and its peculiar mechanical and electrical properties are certainly the reasons of this success [51].

However, for more than 15 years now, other 2D materials have grasped a growing interest owing to their various properties. Like graphene, some 2D materials are the fundamental component of layered materials, like transition metal dichalcogenide or

[1]According to the research portal Scopus, on July 2022.

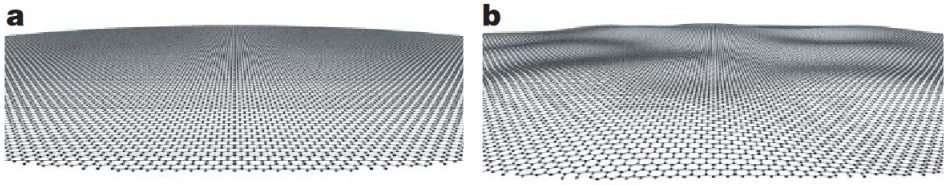

Figure 1.4: a) Flat graphene crystal in real space (perspective view). b) The same for corrugated graphene. The roughness shown imitates quantitatively the roughness found experimentally. Reproduced from [53].

hexagonal boron nitride (hBN). On the other hand, some 2D materials do not have bulk counterparts. It is the case of graphene-like group IV honeycomb materials: silicene, germanene and stanene [1].

At first, due to thermodynamic considerations, 2D materials were thought to be unstable [1]. In reality, acoustic phonons do not prevent the isolation of 2D materials but are responsible of the presence of ripples in 2D materials [52, 53] see figure 1.4. Therefore, although extremely flat graphene has been realized using mica substrate [54], a 2D materials cannot be perfectly flat. Conversely, ultra-corrugated 2D materials may be obtained by amplifying these natural ripples, which can dramatically change the properties of the materials, as it will be shown in chapter 4.

These materials have various electronic properties, ranging from insulator to semiconductor, semi-metal, conductor and superconductor. In consequence, they have been suggested as candidates for various applications in electronics, optronics, photovoltaics, sensing, photonics and much others [1, 55].

Few applications with low quality graphene are already commercialized. Batteries, conducting inks, lubricants and even padel rackets benefit from the peculiar properties of graphene [55]. However, several challenges are still to be overcome to achieve industrialisation, especially in the production of high quality 2D materials at large scale.

Synthesis of 2D materials

Graphene was first isolated by mechanical exfoliation using adhesive tape [2]. Though this method produces graphene flakes of high quality, the size of the flakes is often limited to less than a micrometer squared [56], and it has a poor reproducibility. Note that for industrial use, chemical exfoliation, which produces 2D materials in solvent is also possible, with a lower quality [57].

Exfoliation is not possible for 2D materials without 3D counterparts but other methods have been developed. One of the most efficient way to synthesized 2D materials in large quantities is the chemical vapor deposition (CVD) [58]. In production of graphene using CVD, a carbon source is heated until the carbon is deposited on a metallic substrate. The use of CVD enables the control of the shape and the size of the graphene flakes: single crystal graphene flakes can now reach the millimeter scale [58]. Other growth

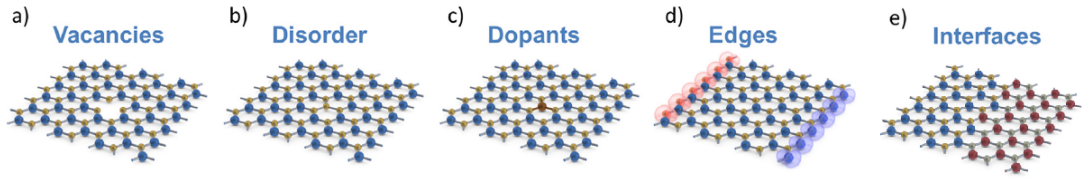

Figure 1.5: In 2D materials, (a–c) vacancies, disorder and dopants create point defects. Edges, and interfaces (d,e) create line defects. Adapted from [61].

techniques are also used, like e-beam evaporation or molecular beam epitaxy, depending on the substrate and the wanted 2D materials or heterostructures [59, 60].

Defects are a major obstacle to produce 2D materials with high quality (mainly high electron mobility). Those defects can be point defects such as vacancies, disorder or substitution (dopants) and line defects such as edge reconstructions or grain boundaries and interfaces, as depicted on figure 1.5 [61]. Controlling the size of single-crystal 2D materials is thus a critical point to master before industrialisation of 2D materials whose quality must be high. However, those defects can be desired features, for example in the chemical doping of a material. Grain boundaries can also be a platform for plasmonics. Such optical effets in grain boundaries are discussed in chapter 4.

Graphene

Graphene has been first isolated in 2004 by Nobel prize Andre Geim and Konstantin Novoselov. In their paper [2], they provided experimental proofs to the ambipolar behaviour of the few layers graphene. Graphene is a material consisting of carbon atoms disposed in honeycomb lattice, with 3 valence electrons forming σ bonds (sp^2 hybridisation). The last valence electron, which is in a π-state, is responsible for the semi-metallic character of graphene. In the band structure of graphene, the π-states form a conical band, with the valence and conduction bands touching at the point K and K', see fig 1.6. Therefore graphene is considered as a semi-metal with a zero band gap because the conductivity does not vanish at $0\,K$. The most interesting electronic property of graphene is its linear dispersion near the K points. This means that electrons behave like massless Dirac fermions, with an effective velocity of $c/300$ [4]. The mobility of charge carriers in graphene is also particularly high: experimentally, it can reach more than $120\,000$ $cm^2V^{-1}s^{-1}$ [62, 63]. As explained above, this mobility can be highly limited depending on the quality of the fabrication method, the number of defects and the substrate.

Transition metal dechalcogenides

Transition metal dechalcogenides (TMDs) are layered materials of chemical formula MX_2, with a unit cell composed of 1 transition metal atom (M) for 2 chalcogen atoms (X), disposed on three atomic plane, see figure 1.7 [64]. Each layer of the materials has

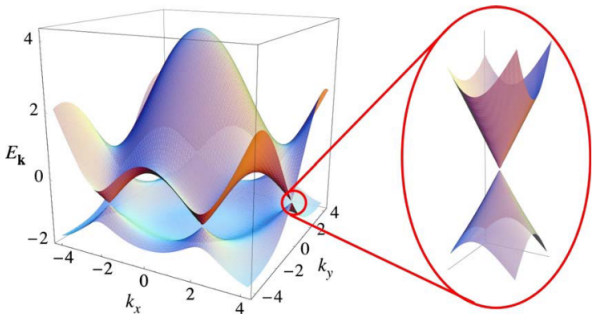

Figure 1.6: Electronic dispersion of graphene. Left: energy spectrum. Right: zoom in of the energy bands close to one of the Dirac points. Reproduced from [4].

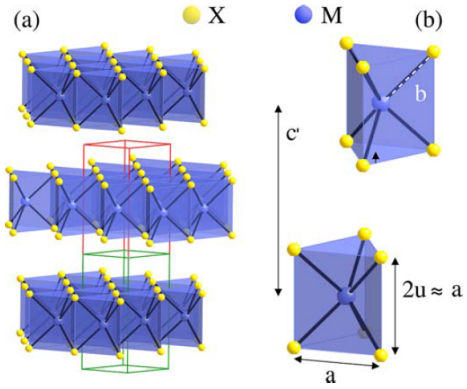

Figure 1.7: (a) Schematic representation of the atomic structure of MX_2. The bulk compound has a $2H - MX_2$ structure with two MX_2 layers per unit cell, each layer being built up from a trigonal prism coordination unit. The small green rectangle represents the unit cell of a monolayer of MX_2, which is doubled (red extension) in the bulk crystal. (b) Detail of the trigonal prisms for the two layers in the bulk compound, showing the lattice constants and the definition of the structural angles used in the text. Reproduced from [64].

a thickness of around $0.6 - 0.7$ nm and as graphene in graphite, can be exfoliated to form a 2D material. Most of them are semi-conductors but some are metals or can even display super-conductivity. The nature of the 2D materials may be different than the 3D counterparts. For example, the band gap of monolayer MoS_2 compared to its bulk counterpart increases from 0.8 eV to 1.7 eV [64] but changes from indirect to direct band gap. These semi-conductor 2D materials have been intensively investigated for applications in electronics, in particular for field-effect transistors [65–67].

Heterostructures

2D materials can be seen as building blocks of artificial layered materials. By assembling vertically or horizontally 2D materials while taking advantages of the weak van der Walls

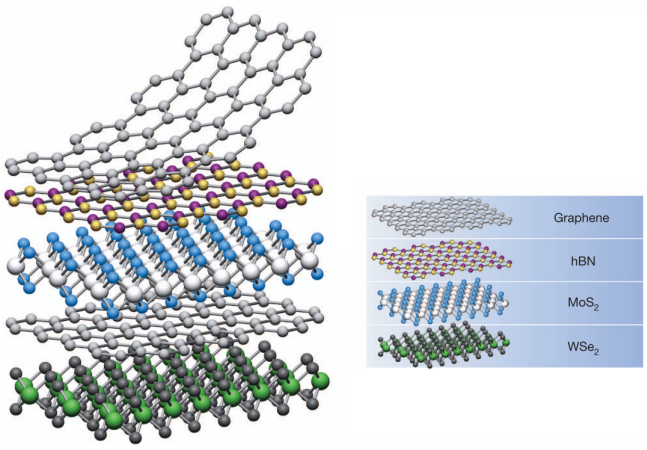

Figure 1.8: The construction of a huge variety of vertical heterostructures becomes possible using single layers of van der Waals materials as elementary bricks. Adapted from [68].

interaction between the parallel planes, a large number of new materials can be obtained, see figure 1.8 [68]. In particular, the hexagonal form of boron nitride, whose structure is similar to that of graphene, with a lattice mismatch of 1.7 %, is often used in combination with other 2D materials. It is used as an insulating and protecting layer for the considered material. Graphene and TMDs encapsulated in hBN have shown extremely high carrier mobilities even after long exposure to ambient air [68–70]. Another impressive example of heterostructure are graphene twisted bilayers where a rotation by a "magic" angle of $1.1°$ create a flat-band in graphene which is responsible for superconducting behaviours [71].

1.3 2D materials optics and plasmonics

Due to their extremely small thickness and their electronic properties, some 2D materials are of first interest for applications in optics. The metallic ones can be used as transparent conductors or as platforms for plasmonics with dramatic confinement of the field. Semiconductor 2D materials can be used in photovoltaics or LED.

Graphene optics

The most striking optical characteristic of graphene is that the optical absorption in the visible spectrum is constant and determined by its so-called universal conductivity $\sigma_0 = \frac{e^2}{4\hbar}$. This phenomenon is explained by the direct interband transitions between the valence and conduction bands in the linear dispersion regime [72, 73]. However, graphene is always intrinsically doped and the Fermi level E_F is, in general, not located at the intersection between the conduction and the valence bands, with value ranging from 0.1 to 1.0 eV. Due to Pauli blocking, interband transition are forbidden below the incident energy $\hbar\omega = 2E_F$ (see figure 1.9a) [73].

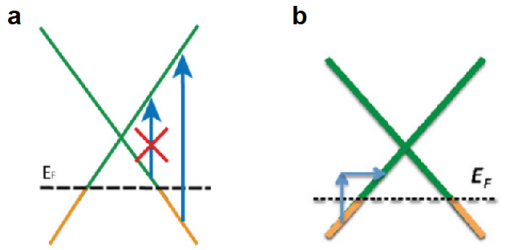

Figure 1.9: Transition in the Dirac cone of graphene. a) direct interband transitions are only possible when the energy of the transition is larger than $2E_F$; b) intraband transitions need a momentum transfer. Reproduced from [73].

At incident energies larger than 1 eV, the dispersion is not linear (figure 1.6), and the conductivity varies. In particular, the π-plasmon of graphene is responsible for a high conductivity around 5 eV. Using the Kubo formalism and a tight binding approach, the authors of [74] propose the following formula for the interband conductivity:

$$\Re\sigma_{inter}(\omega) = \sigma_0 \frac{\pi t^2}{12\sqrt{3}\hbar\omega}\rho(\hbar\omega/2)\left[18 - (\hbar\omega)^2/t^2\right]\left[\tanh\frac{\hbar\omega + 2E_F}{4k_BT} + \tanh\frac{\hbar\omega - 2E_F}{4k_BT}\right], \tag{1.22}$$

where $\sigma_0 = \frac{e^2}{4\hbar}$ is the universal conductivity, t the hoping parameters, and a the carbon-carbon distance. The density of states $\rho(E)$ is

$$\rho(E) = \frac{2E}{t^2\pi^2}\begin{cases} \frac{1}{\sqrt{F(E/t)}}K\left(\frac{4E/t}{F(E/t)}\right), & 0 < E < t, \\ \frac{1}{\sqrt{4E/t}}K\left(\frac{F(E/t)}{4E/t}\right), & t < E, \end{cases} \tag{1.23}$$

and the functions $F(x)$ and $K(m)$ are:

$$F(x) = (1+x)^2 - \frac{(x^2-1)^2}{4}, \tag{1.24}$$

$$K(m) = \int_0^1 \left[\left(1-x^2\right)\left(1-mx^2\right)\right]^{-1/2} dx. \tag{1.25}$$

This conductivity is obtained in an independent particle framework and does not include electron-hole interactions. For a total description of the UV conductivity, excitonic effects must be considered. For this purpose, a Fano model is proposed in [73]:

$$\sigma'_{inter} = \frac{(q+\Omega)^2}{1+\Omega^2}\sigma_{inter}, \tag{1.26}$$

where q^2 is the ratio of the strengths of the excitonic resonance and the band-to-band resonance and

$$\Omega = \frac{(\omega - \omega_{res})}{(\Gamma/2)}, \tag{1.27}$$

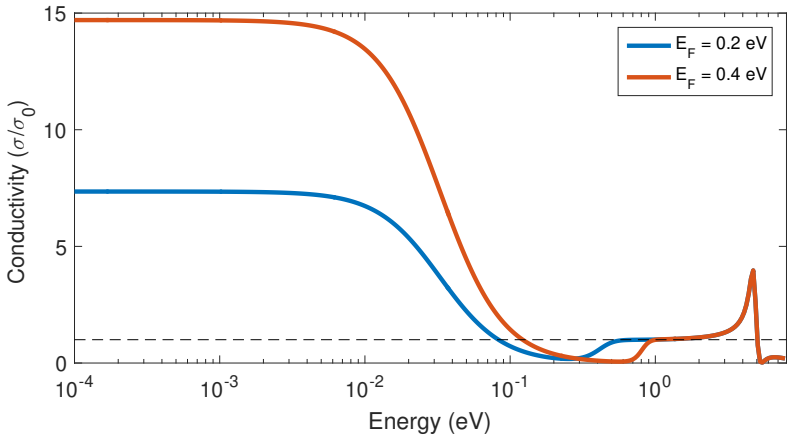

Figure 1.10: Real part of the surface conductivity of graphene calculated from the Kubo formula in the unit of $\sigma_0 = \frac{e^2}{4\hbar}$. The dotted line corresponds to $\sigma = \sigma_0$.

with ω_{res} the resonance energy of the π-plasmon, close to 5 eV and Γ its width. The imaginary part of the interband term may be then calculated using the Kramers-Kronig relations.

At energies lower than $2E_F$, when interband transition are forbidden, intraband transitions play a major role. However, due to momentum mismatch, these transitions involve scattering with phonons or defects (figure 1.9b). This scattering can be taken into account into the damping term of an appropriate Drude model as proposed in [75]. This gives an intraband term for the conductivity :

$$\sigma_{intra} = \frac{ie^2 E_F}{\pi\hbar^2 \left(\omega + i\tau^{-1}\right)}. \tag{1.28}$$

where τ is the relaxation time of the charge carriers. The inter- and intraband transition conductivities both depend on the Fermi level. By tuning the Fermi level by means of gate voltage or chemical doping, the optical properties of graphene can be adjusted, in particular in the infrared range where graphene plasmons take place.

The total surface conductivity of graphene $\sigma_g = \sigma_{intra} + \sigma'_{inter}$ obtained for the parameters $T = 300$ K, $\tau = 20$ fs, $t = 2.6$ eV, $q = -1.7$ eV, $\hbar\omega_{res} = 4.85$ eV, $\Gamma = 780$ meV) and for two values of the Fermi level, $E_F = 0.2$ eV (blue) and $E_F = 0.4$ eV (orange) is plotted on a logarithmic scale in figure 1.10. In the thesis, the chosen values for the relaxation time τ are highly conservative, between 20 and 100 fs, which corresponds to low quality graphene and has been used frequently in plasmonics [25, 38]. Experimental results in different frequency ranges are consistent with these values [76]. The modification of the Fermi level does not only change the amplitude of the conductivity at low energy but also change the energy position of transition between the interband and the intraband regime (between 0.1 and 1 eV). The universal conductivity is then attained at different energies. At 5 eV, the peak corresponds to the π-plasmon.

The absorption of a single layer of graphene on a substrate of refractive index n at

normal incidence is given by [77]:

$$A = \frac{4Re\left(\frac{\sigma_g}{\varepsilon_0 c}\right)}{\left|1 + n + \frac{\sigma_g}{\varepsilon_0 c}\right|^2}. \tag{1.29}$$

For suspended graphene (i.e. $n = 1$), in the visible range, where the conductivity is small ($\frac{\sigma_g}{\varepsilon_0 c} = 0.023$), the absorption is given by

$$A = \frac{\sigma_g}{\varepsilon_0 c} = 0.023 = 2.3\%, \tag{1.30}$$

which is small enough for graphene to be transparent but large enough to be visible by a trained naked eye. At smaller frequencies, for example in the GHz range, the conductivity is larger and the absorption of a single layer of graphene can be as large as 50% [78], which is surprisingly large for an atomically thin layer. It was even demonstrated that perfect absorption could be achieve by using metamaterials as substrate [8]. Indeed, from eq. (1.29) it can be shown that the maximum of absorption of a 2D material on a substrate is

$$A_{max} = \frac{1}{1 + n} \tag{1.31}$$

if the surface conductivity is $\frac{\sigma_g}{\varepsilon_0 c} = 1 + n$. For an epsilon-near-zero metamaterial, the refractive index of the substrate n tends to 0 and the absorption can reach 100%. In practice, the condition that permits a maximum absorption may be achieved with an heterostructure of 3 graphene layers, isolated by PMMA layers, in the micro-wave range (figure 1.11a). However, for a finite substrate, the perfect absorption is not possible but with an adapted thickness of the substrate, near-perfect absorption can be reached (figure 1.11b) [8].

Graphene plasmonic

As a metallic material, graphene is a good platform for plasmonic. However, as for bulk materials or thin films, the momentum mismatch prohibits the observation of plasmons with light in extended graphene. Structuring or nanoparticles must be employed in order to be able to excite surface plasmons. Due to their low dimensionality, surface plasmons in structured 2D materials are confined to a volume of size 10^6 smaller than the wavelength [25]. Moreover, thanks to the tunability of graphene surface conductivity, the resonance frequency of graphene plasmons may be adjusted actively with gate voltage. These advantages have made graphene an important area of research in plasmonics in the last decade [25, 79, 80].

Graphene has been shown to support SPPs, in nanoribbons for example (see figure 1.12) with a plasmon frequency given by [81]:

$$\omega_{pl} = \frac{e}{\hbar}\sqrt{\frac{E_F}{\pi\eta W \varepsilon_m}}, \tag{1.32}$$

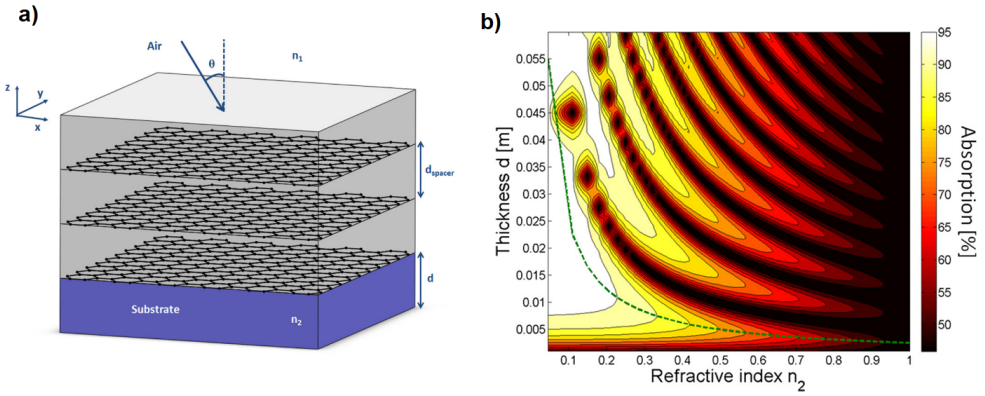

Figure 1.11: a) Electromagnetic radiation impinging on a graphene- PMMA heterostructure composed of three PMMA/graphene units, lying on a substrate of refractive index n, with incident angle θ. b) Absorption of a graphene-PMMA heterostructure consisting of three PMMA/graphene units on a finite slab of thickness d as a function of thickness of the substrate d and its refractive index n. Refractive index n varies from 0.04 to 1. Green dotted line indicates maximal absorption. Reproduced from [8].

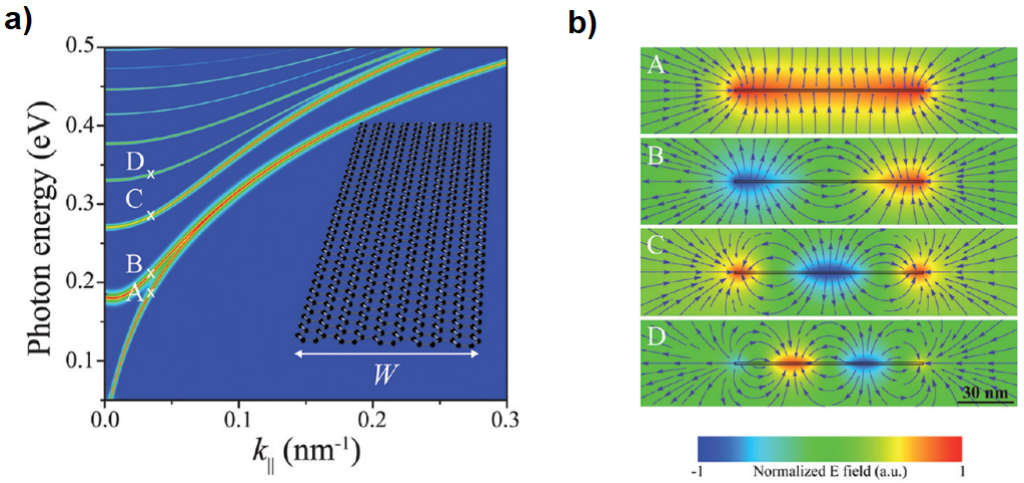

Figure 1.12: Guided plasmons in individual doped graphene ribbons. (a) Dispersion diagram of a self-standing ribbon of width $W = 100$ nm and Fermi energy $E_F = 0.5$ eV. (b) Real part of the electric field amplitude (density plots) along the ribbon direction corresponding to modes labeled $A - D$ in panel (a) for a parallel wave vector $k_{||} = 0.035$ nm^{-1}. Reproduced from [81].

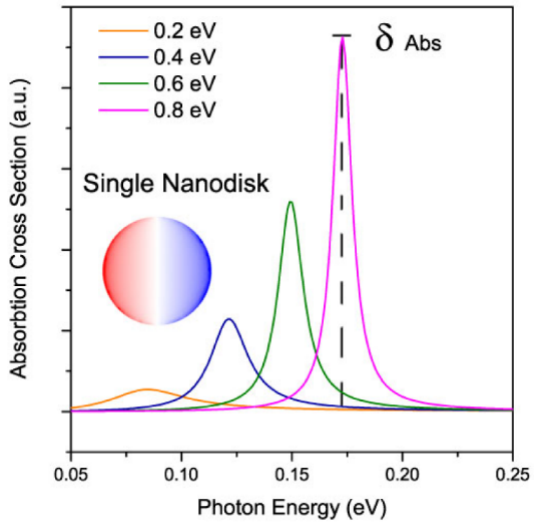

Figure 1.13: Calculated individual graphene nanodisk absorption cross-section for different Fermi energy values. The inset shows the plasmon induced charge density for a single nanodisk. Reproduced from [82].

where W is the width of the ribbon, ε_m the permittivity of the surrounding medium and η a parameter that depends only on the product $k_{\|}W$, with $k_{\|}$ the wavevector.

In graphene nanoparticles, LSP stands at the edges of the nanoparticles (see for example figure 1.13). For nanodisks, the plasmon frequency of the dipolar mode is

$$\omega_{pl} = \frac{e}{2\pi\hbar}\sqrt{\frac{12.5E_F}{\varepsilon_0 d}} \tag{1.33}$$

where d is the diameter of the disk.

In both cases (SPP and LSP), for a characteristic length of about 100 nm, the plasmon frequency lies between 0.1 and 0.5 eV. To approach the visible frequencies (between 1.5 and 3.5 eV, one must decrease the size of the structure down to a few nanometers [35]. However, for lengths of a few nanometers, quantum effects become significant and free charge carriers scatter on the edges, decreasing the plasmon lifetimes. This limitation has tempered the interest for graphene in plasmonics, but graphene plasmons in the visible are achievable as it will be shown in chapter 4.

Plasmonics with other 2D materials

Graphene is not the only metallic 2D material. For example some TMDs like $TaSe_2$ and VS_2, or graphene-like group IV 2D materials as silicene are metallic. Plasmons have already been detected in the two TMDs mentioned above [36] and in silicene [83]. Moreover, plasmons may be sustained in metallic channels existing in non-metallic 2D materials due to restructuration at the edges or at boundaries. These kind of plasmons have been evidenced in MoS_2 [36, 37].

It is worth mentioning here topological insulators which could sustain similar plasmons than 2D materials. Topological insulators are insulators that exhibit topologically protected surface metallic states [84]. These surfaces are in some way analog to metallic 2D materials on a insulating substrate. Plasmons have also been identified on such surfaces [85, 86]. Recently, 2D topological insulators, like Jacuntingaite, have been identified [87]. These 2D materials have topologically protected metallic channel on their edges and are good candidates to obtained 1D SPPs on their edges.

Conclusions

The large number of 2D materials identified up to now, and the infinite ways to assemble them in heterostructures, is a playground for materials scientists. At the beginning, graphene was the center of attention due to its peculiar electronic and mechanical properties. In optics, the fact that it is a transparent conductor in the visible, and that its conductivity is tunable at lower frequency make it one of the best candidates for several applications. However, other 2D materials like TMDs or even van der Waals heterostructures also exhibit optical and plasmonic behaviours that could be interesting for applications such as sensing or optoelectronics.

Chapter 2

The dielectric function

The goal of this chapter is to present how the microscopic dielectric function is calculated from the electronic structure and how it allows to obtain the macroscopic dielectric function. The microscopic dielectric function is a central quantity for determining optical properties and in particular investigate plasmonic resonances of quantum systems. On the other hand the macroscopic dielectric function is used in classical electrodynamic methods to determine the optical properties of larger and more complex systems. The relation between the microscopic and macroscopic dielectric function will also bring insight on the modelling of 2D materials.

2.1 Microscopic description of the dielectric function

The dielectric function or relative permittivity is at the core of electromagnetism as it allows us to describe the electric response of a material to an applied electric field. In classical electrodynamics, one uses the macroscopic permittivity, resulting from the spatial average of the fields. For systems at the scale of the nanometer, quantum effects are non-negligible and a quantum description of the system is necessary. For 2D materials, which are atomically thin, a macroscopic description is still possible but with a particular care in the use of the dielectric function. However, for 2D material nanostructures smaller than 10 nm, a quantum method is necessary. For these reasons, the microscopic version of the dielectric function is convenient. It also gives information about plasmons in nanometer-sized systems. In this section, the theoretical background behind the microscopic permittivity is developed succinctly yet comprehensively as the description in the literature is scattered. Original contributions are proposed with an emphasis on results that are important for 2D materials and plasmon analysis.

Definition of the microscopic dielectric function

In electrodynamics, the goal is to find the total electromagnetic field of a system for given charge and current distributions. Rigorously, all charged particles, free and bound ones, should be considered. For such problem, one must solve the microscopic local Maxwell's equations [42]:

$$\nabla \cdot \mathbf{E}(\mathbf{r},t) = \frac{\rho(\mathbf{r},t)}{\varepsilon_0}; \tag{2.1}$$

$$\nabla \cdot \mathbf{B}(\mathbf{r},t) = 0; \tag{2.2}$$

$$\nabla \times \mathbf{E}(\mathbf{r},t) = -\frac{\partial \mathbf{B}(\mathbf{r},t)}{\partial t}; \tag{2.3}$$

$$\nabla \times \mathbf{B}(\mathbf{r},t) = \mu_0 \mathbf{J}(\mathbf{r},t) + \varepsilon_0 \mu_0 \frac{\partial \mathbf{E}(\mathbf{r},t)}{\partial t}. \tag{2.4}$$

Compared to the macroscopic Maxwell equations (1.9)-(1.12), with the electric displacement defined by (1.5), here the permittivity does not appear because the material is directly described by the charge and current densities. The charge and current densities can therefore be separated into external and internal densities, where the external densities $\rho_{ext}(\mathbf{r},t)$ and $\mathbf{J}_{ext}(\mathbf{r},t)$ are the causes of an electromagnetic excitation and the internal densities $\rho_{int}(\mathbf{r},t)$ and $\mathbf{J}_{int}(\mathbf{r},t)$ compose the materials of the considered system. The sources of the excitation are for example dipoles, electron beams or antennas. In practice, the electric field induced by the external charges is known. The problem consists then to determine how the internal densities respond to this electric field applied to the system $\mathbf{E}_{app}(\mathbf{r},t)$ i.e. to find the induced fields $\mathbf{E}_{ind}$ and densities $\rho_{ind}(\mathbf{r},t)$ and $\mathbf{J}_{ind}(\mathbf{r},t)$.

Here the case of external sources far from the system is considered. The electromagnetic field is then described as a plane wave i.e.:

$$\mathbf{E}_{app}(\mathbf{r},t) = E_0 e^{i(\mathbf{k}\cdot\mathbf{r}-\omega t)}\mathbf{e}, \tag{2.5}$$

with E_0 the amplitude of the field, $\mathbf{k}$ the wave vector, ω the angular frequency and $\mathbf{e}$ the unit vector giving the polarisation. To calculate the total electromagnetic field, one needs to find the tensor $\bar{\zeta}\left(\mathbf{r}, \mathbf{r}', t, t'\right)$ such that:

$$\mathbf{E}_{tot}\left(\mathbf{r}, t\right) = \int\int \bar{\zeta}\left(\mathbf{r}, \mathbf{r}', t, t'\right) \mathbf{E}_{app}\left(\mathbf{r}', t'\right) d\mathbf{r}' dt', \tag{2.6}$$

where the tensorial nature is noted with an overline. The function $\bar{\zeta}\left(\mathbf{r}, \mathbf{r}', t, t'\right)$ is the kernel of an integral operator (or transform) that applies on the applied field to give the total field. Other relevant quantities such as the Poynting vector and the scattering cross sections are deduced from the total electric fields afterwards. The tensor $\bar{\zeta}\left(\mathbf{r}, \mathbf{r}', t, t'\right)$ is in fact the kernel of the inverse of the transform whose kernel is the microscopic dielectric function $\bar{\varepsilon}\left(\mathbf{r}, \mathbf{r}', t, t'\right)$ defined as follow:

$$\mathbf{E}_{app}\left(\mathbf{r}, t\right) = \int\int \bar{\varepsilon}\left(\mathbf{r}, \mathbf{r}', t, t'\right) \mathbf{E}_{tot}\left(\mathbf{r}', t'\right) d\mathbf{r}' dt, \tag{2.7}$$

which is just another way to write the better known constitutive equation of materials:

$$\mathbf{D}\left(\mathbf{r}, t\right) = \varepsilon_0 \int\int \bar{\varepsilon}\left(\mathbf{r}, \mathbf{r}', t, t'\right) \mathbf{E}_{tot}\left(\mathbf{r}', t'\right) d\mathbf{r}' dt, \tag{2.8}$$

where the displacement field $\mathbf{D}\left(\mathbf{r}, t\right)$ in a material is associated to the applied field. The function $\bar{\zeta}$ is now called the inverse dielectric function, is written $\bar{\varepsilon}^{-1}\left(\mathbf{r}, \mathbf{r}', t, t'\right)$ and relates to the dielectric function tensor via:

$$\int\int \bar{\varepsilon}^{-1}\left(\mathbf{r}, \mathbf{r}', t, t'\right) \bar{\varepsilon}\left(\mathbf{r}', \mathbf{r}'', t', t''\right) d\mathbf{r}' dt' = \bar{I}\delta\left(\mathbf{r}, \mathbf{r}''\right) \delta\left(t, t''\right), \tag{2.9}$$

with $\bar{I}$ the 3×3 identity matrix. Because the response only depends on the time difference $t' - t$ and the fields are time harmonic (eq. (2.5)) one can work in the frequency domain by performing a Fourier transform. Eq. (2.6) can be written as

$$\mathbf{E}_{tot}\left(\mathbf{r}, \omega\right) = \int \bar{\varepsilon}^{-1}\left(\mathbf{r}, \mathbf{r}', \omega\right) \mathbf{E}_{app}\left(\mathbf{r}', \omega\right) d\mathbf{r}'. \tag{2.10}$$

Before describing the derivation of the dielectric function, two remarks should be done:

- If the applied field is spatially constant, by integrating the inverse dielectric function over $\mathbf{r}'$, eq. (2.10) becomes:

  $$\mathbf{E}_{tot}\left(\mathbf{r}\right) = \bar{\varepsilon}^{-1}\left(\mathbf{r}\right) \mathbf{E}_{app}. \tag{2.11}$$

  If one chooses an applied field of unit amplitude, the total field is directly given by the tensorial product of $\bar{\varepsilon}^{-1}$ and a unit vector $\mathbf{E}_{app}$.

- Equation like eq. (2.10) become a matrix equation on a discretized spatial grid:

  $$\mathbf{E}_{tot} = \bar{\varepsilon}^{-1}\mathbf{E}_{app}, \tag{2.12}$$

with ε^{-1} a rank-2 tensor of size $3N \times 3N$ with N the number of grid points. Like any other inverse function f^{-1} defined as followed:

$$\int f^{-1}(\mathbf{r}, \mathbf{r}') f(\mathbf{r}', \mathbf{r}'') d\mathbf{r}' = \delta(\mathbf{r}, \mathbf{r}''), \tag{2.13}$$

the inverse dielectric function matrix is the inverse matrix of the dielectric function matrix.

Response functions from the linear response time-dependent density functional theory

For a system of the size of a few Angstroms, optical response functions such as the dielectric function must be obtain in a quantum framework. They are deduced from the solutions of the Schrödinger equation. In practice, a number of approximations are performed in order to decrease the complexity of the problem. The most current one is the Born-Oppenheimer approximation which states that the kinetic energy of the nuclei is negligible. The effect of the nuclei is reduced to a static potential V and the Schrödinger equation becomes

$$\hat{H}\psi = \left[\sum_{i=1}^{N}\left(-\frac{\hbar^2}{2m}\nabla_i^2\right) + \sum_{i=1}^{N} V(\mathbf{r}_i) + \sum_{i,j<i}^{N} U(\mathbf{r}_i, \mathbf{r}_j)\right]\psi = E\psi \tag{2.14}$$

where $\psi = \psi(\mathbf{r}_1, \ldots, \mathbf{r}_N)$ is the multi-electron wave-function. The first term in the bracket is the kinetic energy of electrons, the second the potential due to the nuclei and the third the electron-electron interaction. The complexity of such equations still increases very quickly with the number of electrons N and other approximations are generally done. The density functional theory (DFT), which is particularly adapted to extended materials, has been used in this thesis to calculate the electronic properties of the systems of interest [88]. The DFT is based on the Hohenberg and Kohn theorem that states that the total energy is a unique functional of the electron density $\rho(\mathbf{r}')$. In other words, there is a one-to-one correspondence between the potential and the electron density, which therefore contains all the information on the many-electron system. Kohn and Sham then proved that the many-electron problem can be replaced by an equivalent set of one-electron equations, namely the Kohn-Sham equations [88]:

$$\left(-\frac{\hbar^2}{2m}\nabla^2 + V_{KS}(\mathbf{r})\right)\phi_i(\mathbf{r}) = \epsilon_i(\mathbf{r})\,\phi_i(\mathbf{r}) \tag{2.15}$$

with

$$V_{KS}(\mathbf{r}) = V_{ion}(\mathbf{r}) + V_H(\mathbf{r}) + V_{xc}(\mathbf{r}). \tag{2.16}$$

the Kohn-Sham potential. In this equation V_H is the Hartree potential:

$$V_H = e^2 \int \frac{\rho(\mathbf{r}')}{|\mathbf{r}' - \mathbf{r}|} d\mathbf{r}' \tag{2.17}$$

and V_{ion} is the electron-ion potential. In practice, a pseudo-potential V_{ext} that account for the core electrons is used instead of V_{ion} to reduce the complexity of the problem. The last term of eq. (2.16), V_{xc} is the functional derivative of the exchange-correlation energy functional:

$$V_{xc}(\mathbf{r}) = \frac{\delta E_{xc}[\rho(\mathbf{r})]}{\delta \rho(\mathbf{r})} \tag{2.18}$$

The exchange-correlation energy functional can be expressed from the exchange-correlation energy per electron at point $\mathbf{r}$, $e_{xc}(\mathbf{r})$:

$$E_{xc}[\rho(\mathbf{r})] = \int e_{xc}(\mathbf{r})\,\rho(\mathbf{r})\,d\mathbf{r} \tag{2.19}$$

but cannot be known exactly. The simplest approximation is to consider e_{xc} as the exchange-correlation energy of an electron in an homogeneous electron gas with the same density as the electron gas at point $\mathbf{r}$. This method is called the local density approximation (LDA) and has been widely used due to its simplicity and its accurate results for a large number of systems [88]. Another method, the generalized gradient approximation (GGA) that account for nearby inhomogeneities in the density has been proposed by Perdew, Burke and Ernzerhof (PBE) [89]. Both these methods (LDA and GGA-PBE) have been used in this work.

When V_{xc} has been calculated, a trial density is chosen and the Kohn-Sham equations (eq. (2.15)) are solved self-consistently to obtain the orbitals $\phi_i(\mathbf{r})$ that reproduce the true electronic density $\rho(\mathbf{r})$ of the system.

When an time-dependent potential $V_{ext}(\mathbf{r},t)$ is applied on the system, the time-dependent DFT (TDDFT) must be used to calculate the time dependent wave-functions. Similarly to the Hohenberg and Kohn theorem, the Runge-Gross theorem shows that there is a one-to-one mapping between the time dependent density $\rho(\mathbf{r},t)$ and the time dependent external potential $V_{ext}(\mathbf{r},t)$. Consequently, a time dependent Kohn-Sham system of equations can be written:

$$\left(-\frac{\hbar^2}{2m}\nabla^2 + V_{KS}(\mathbf{r},t)\right)\phi_i(\mathbf{r},\mathbf{t}) = i\frac{\partial}{\partial t}\phi_i(\mathbf{r},t) \tag{2.20}$$

with the Kohn-Sham potential given by:

$$V_{KS}(\mathbf{r},t) = V_{ext}(\mathbf{r},t) + V_H(\mathbf{r},t) + V_{xc}(\mathbf{r},t)\,. \tag{2.21}$$

The exchange correlation potential V_{xc} is, in general, a functional of the density and of the true initial states of the system ψ and must be approximated. An initial set of orbitals $\phi(\mathbf{r},0)$ that reproduces the true density of the ground state must be chosen and the Kohn-Sham equations (eq. (2.20)) are solved to determine the time-dependent wave-functions.

In the linear response regime, we consider a small time-varying potential V_{app} applied to a system in its ground state (with $V_{ext,0}$ the external potential of the ground state):

$$V_{ext}(\mathbf{r},t) = V_{ext,0}(\mathbf{r}) + V_{app}(\mathbf{r},t) \tag{2.22}$$

such that only the first order term of the change in electronic density is retained (with the ground state density ρ_0):

$$\rho(\mathbf{r},t) = \rho_0(\mathbf{r}) + \rho_{ind}(\mathbf{r},t) \tag{2.23}$$

where the relation between the applied potential V_{app} and the induced density ρ_{ind} is linear:

$$\rho_{ind}(\mathbf{r},t) = \int\int \alpha(\mathbf{r},\mathbf{r}',t,t')\, V_{app}(\mathbf{r}',t')\, d\mathbf{r}'dt'. \tag{2.24}$$

To obtain the so-called external polarizability α one must first calculate the irreducible polarizability α^0 defined as follow [1]:

$$\rho_{ind}(\mathbf{r},t) = \int\int \alpha^0(\mathbf{r},\mathbf{r}',t,t')\, \delta V_{KS}(\mathbf{r}',t')\, d\mathbf{r}'dt'. \tag{2.25}$$

Using time-dependent perturbation theory, one can show that the irreducible polarizability α^0 is given, in the frequency domain, by [91]:

$$\alpha^0(\mathbf{r},\mathbf{r}',\omega) = \sum_{i,j}(f_i - f_j)\frac{\phi_i(\mathbf{r})\,\phi_j^*(\mathbf{r})\,\phi_j(\mathbf{r}')\,\phi_i^*(\mathbf{r}')}{\omega - E_j + E_i + i\eta}, \tag{2.26}$$

where E_i is the energy of the electronic ground states i, f_i the Fermi-Dirac distribution and η a smearing parameter. The term δV_{KS} in eq. (2.25) is the change in the Kohn-Sham potential of eq. (2.21) due to the time-varying potential V_{app}:

$$\delta V_{KS}(\mathbf{r},t) = V_{app}(\mathbf{r},t) + \int \frac{\rho_{ind}(\mathbf{r},t)}{|\mathbf{r}-\mathbf{r}'|}d\mathbf{r}' + \int\int f_{xc}[\rho_0]((\mathbf{r},\mathbf{r}',t,t'))\,\rho_{ind}(\mathbf{r}',t')\,d\mathbf{r}'dt'. \tag{2.27}$$

The second term in the above equation is the Hartree potential due to the induced charge. The third term is the variation to the exchange-correlation potential, that depends on the exchange-correlation kernel f_{xc}, which is the functional derivative of the exchange-correlation potential evaluated at the ground state density:

$$f_{xc}[\rho_0](\mathbf{r},\mathbf{r}',t,t') = \left.\frac{\delta v_{xc}[\rho](\mathbf{r},t)}{\delta n(\mathbf{r}',t')}\right|_{\rho_0} \tag{2.28}$$

The external and the irreducible polarizability are related by a Dyson-like equation [91]:

$$\begin{aligned}\alpha(\mathbf{r},\mathbf{r}',t,t') =& \alpha^0(\mathbf{r},\mathbf{r}',t,t') \\ &+ \int\int\int \alpha^0(\mathbf{r},\mathbf{r}_1,t,t_1) \\ &\times \left(\frac{\delta(t_1-t_2)}{|\mathbf{r}_1-\mathbf{r}_2|} + f_{xc}[\rho_0](\mathbf{r}_1,\mathbf{r}_2,t_1,t_2)\right)\alpha(\mathbf{r}_2,\mathbf{r}',t_2,t')\,dt_1dt_2d\mathbf{r}_1d\mathbf{r}_2\end{aligned} \tag{2.29}$$

[1] These two polarizabilities have different names in the literature, I have chosen the one given in [90].

Afterwards, the dielectric function and other response functions can be calculated from the polarizabilities. This will be done in the next section where a more general approach, including vector potentials, is proposed.

In the random-phase approximation (RPA), the exchange-correlation kernel f_{xc} is set to zero, which simplifies greatly eq. (2.29). Although it removes all purely quantum effects in the calculation of the response function of a quantum system, the RPA has been widely used due to the simplicity of its implementation and the numerical gain of neglecting the exchange-correlation kernel functional. The use of the RPA in our case is justified because only qualitative results were expected.

Two main problems remain when performing TDDFT calculations, in particular within the RPA, due to the many-body effects. The first is that, when exciting an electron in the conduction band, we cannot consider the system in its ground state anymore. The second problem is that the difference between the electronic gap (the energy needed to create an electron-hole pair) and the optical gap (the electronic gap energy plus the energy to dissociate the exciton) is not taken into account and the creation of excitons is neglected. These issues are settled by methods accounting for exchange-correlation effects. The first problem is solved using the GW approach [92, 93].The second is overcome using the Bethe-Salpeter equation [92]. However, these two supplemental methods demand intensive calculations. For optical calculations of large structures the ground state approach is already computationally demanding and I have decided neither to use nor to describe these methods here. For more details on DFT, TDDFT and the particular methods used in this thesis, I suggest the following references: [88, 94–96].

The parameters of the calculations performed in this thesis are given in the appendix.

Linear responses functions in the RPA

In the following, the microscopic dielectric function is derived from response functions obtained in TDDFT. Here, the RPA is used such that quantum effects are neglected in the calculations of the optical response function, apart from the calculation of the electronic ground state of the system. In consequence, the linear response theory developed thereafter can be applied also to classical systems as proposed in section 2.3. Moreover, as vector potentials are also considered here, a more general approach is proposed, compared to the one often provided in the literature [91, 96, 97], where only scalar potentials are assumed, as shown in the previous section. In the following, the frequency dependencies are omitted by means of simplicity.

In order to determine the dielectric function, the total field is first expressed as the sum of the applied field and the induced field:

$$\mathbf{E}_{tot}(\mathbf{r}) = \mathbf{E}_{app}(\mathbf{r}) + \mathbf{E}_{ind}(\mathbf{r}). \tag{2.30}$$

By finding a relation between the induced field and the applied field or total field, the dielectric function may be calculated from the equation above. The induced field can be expressed from the induced scalar and vector coulomb potential $V_{ind}(\mathbf{r})$ and $\mathbf{A}_{ind}(\mathbf{r})$

[42]:

$$\mathbf{E}_{ind}(\mathbf{r}) = -\nabla V_{ind}(\mathbf{r}) - \frac{\partial \mathbf{A}_{ind}(\mathbf{r})}{\partial t}, \tag{2.31}$$

with

$$V_{ind}(\mathbf{r}) = \frac{1}{4\pi\varepsilon_0}\int \frac{\rho_{ind}(\mathbf{r}')}{|\mathbf{r}-\mathbf{r}'|}d\mathbf{r}' \tag{2.32}$$

and

$$\mathbf{A}_{ind}(\mathbf{r}) = \frac{\mu_0}{4\pi}\int \frac{\mathbf{J}_{ind}(\mathbf{r}')}{|\mathbf{r}-\mathbf{r}'|}d\mathbf{r}'. \tag{2.33}$$

The induced field is then:

$$\mathbf{E}_{ind}(\mathbf{r}) = -\frac{1}{4\pi\varepsilon_0}\nabla\int \frac{\rho_{ind}(\mathbf{r}')}{|\mathbf{r}-\mathbf{r}'|}d\mathbf{r}' - \frac{\mu_0}{4\pi}\frac{\partial}{\partial t}\int \frac{\mathbf{J}_{ind}(\mathbf{r}')}{|\mathbf{r}-\mathbf{r}'|}d\mathbf{r}'. \tag{2.34}$$

The induced densities are related to the total potential by the irreducible polarizability α^0 and conductivity $\bar{\sigma}^0$ [90] :

$$\rho_{ind}(\mathbf{r}') = \int \alpha^0(\mathbf{r}',\mathbf{r}'')\, V_{tot}(\mathbf{r}'')\, d\mathbf{r}''; \tag{2.35}$$

$$\mathbf{J}_{ind}(\mathbf{r}') = i\omega\int \bar{\sigma}^0(\mathbf{r}',\mathbf{r}'')\, \mathbf{A}_{tot}(\mathbf{r}'')\, d\mathbf{r}''. \tag{2.36}$$

The irreducible polarizability and conductivity are the response functions of non-interacting charges to an external potential, or equivalently the response of the charge to the total potential. They are therefore not the appropriate response functions to describe the response of the material to an applied field. The irreducible polarizability has already been discussed in the previous section (eq. (2.25)), where the total potential V_{tot} is equivalent to the change in the Kohn-Sham potential δV_{KS}. The irreducible conductivity is defined from the constitutive equation of the current density in materials:

$$\mathbf{J}_{ind}(\mathbf{r}') = \int \bar{\sigma}^0(\mathbf{r}',\mathbf{r}'')\, \mathbf{E}_{tot}(\mathbf{r}'')\, d\mathbf{r}''. \tag{2.37}$$

Here, plane waves are considered. The vector potential of a plane wave is written in the form

$$\mathbf{A}_{app}(\mathbf{r}) = A_0 e^{i(\mathbf{k}\cdot\mathbf{r}-\omega t)}\mathbf{e} \tag{2.38}$$

in a gauge where the scalar potential is zero, $V_{app} = 0$. However a longitudinal wave ($\mathbf{k} \,/\!/\, \mathbf{e}$) can also be described in a gauge where the vector potential is zero:

$$\mathbf{A}_{app}(\mathbf{r}) = 0 \; ; \; V_{app}(\mathbf{r}) = V_0 e^{i(\mathbf{k}\cdot\mathbf{r}-\omega t)}. \tag{2.39}$$

In both gauges, for longitudinal waves, the electric field writes:

$$\mathbf{E}_{app}(\mathbf{r}) = E_0 e^{i(\mathbf{k}\cdot\mathbf{r}-\omega t)}\frac{\mathbf{k}}{k} \tag{2.40}$$

with $E_0 = -ikV_0$ or $E_0 = -i\omega A_0$ and the magnetic field is zero. Therefore, in order to describe a longitudinal excitation, one only needs the irreducible polarizability to

calculate a longitudinal dielectric function. In the most general case including transverse waves, the irreducible conductivity is needed to obtain the dielectric function.

The expressions of the irreducible polarizability and conductivity have both been derived theoretically from TDDFT [98], as previously shown for the polarizability. However, due to complexity of the general case, only the longitudinal dielectric function has been calculated in quantum simulations. Indeed, researchers developing quantum methods only refer to articles describing the longitudinal case [91, 97, 99–101] and therefore they use the formalism described in the previous section. The longitudinal dielectric function is useful for studying volume plasmons which are longitudinal waves. For light illumination, the wave number k is often considered to be small compared to characteristic sizes of the materials i.e. the size of the unit cell. It is equivalent to the electrostatic case. Transverse and longitudinal waves are thus indistinguishable and the longitudinal dielectric function corresponds to the transverse dielectric function. However, for high energy electromagnetic waves, for example in case of UV illumination, the wavelength can be of the same order of magnitude as the length of large unit cells (for example for nanostructured systems like 2D materials nanoribbons) and the $k \to 0$ limit cannot be taken. In this context, it is of great interest to obtain the transverse microscopic dielectric function.

In the following, the dielectric function is derived in the most general case from the irreducible conductivity, with a vector potential of the form (2.38) before particularizing to the longitudinal case.

Tensorial dielectric function from the conductivity

In the gauge with $V_{app} = 0$ corresponding to eq. (2.38), one can write from eq. (2.34) and (2.37)

$$\mathbf{E}_{ind}(\mathbf{r}) = i\frac{\omega\mu_0}{4\pi}\int\int \frac{\bar{\sigma}^0(\mathbf{r}', \mathbf{r}'')}{|\mathbf{r} - \mathbf{r}'|}\mathbf{E}_{tot}(\mathbf{r}'')\, d\mathbf{r}'' d\mathbf{r}'. \tag{2.41}$$

The expression of the irreducible conductivity is given in [98], but as it is quite complex and it has not been used for calculation of optical spectra, I do not write it explicitly here. The microscopic irreducible susceptibility $\bar{\chi}$ is defined as:

$$\bar{\chi}(\mathbf{r}, \mathbf{r}') = -i\frac{\omega\mu_0}{4\pi}\int \frac{\bar{\sigma}^0(\mathbf{r}'', \mathbf{r}')}{|\mathbf{r} - \mathbf{r}''|} d\mathbf{r}'', \tag{2.42}$$

therefore one obtains:

$$\mathbf{E}_{ind}(\mathbf{r}) = -\int \bar{\chi}(\mathbf{r}, \mathbf{r}')\, \mathbf{E}_{tot}(\mathbf{r}')\, d\mathbf{r}'. \tag{2.43}$$

which is the microscopic equivalent of the relation between the polarization density and the electric field:

$$\mathbf{P} = \varepsilon_0 \chi_M \mathbf{E}_{tot} \tag{2.44}$$

where χ_M is the macroscopic susceptibility, and $\mathbf{P} = -\mathbf{E}_{ind}$. Because the total field is the sum of the applied field and the induced field, eq. (2.30), from eq. (2.43) one deduces:

$$\mathbf{E}_{app} = \int \left(\bar{I}\delta(\mathbf{r}, \mathbf{r}') + \bar{\chi}(\mathbf{r}, \mathbf{r}')\right) \mathbf{E}_{tot}(\mathbf{r}')\, d\mathbf{r}' \tag{2.45}$$

The term inside the parenthesis is the microscopic dielectric function introduced previously, eq. (2.7):

$$\bar{\varepsilon}\left(\mathbf{r},\mathbf{r}'\right)=\bar{I}\delta\left(\mathbf{r},\mathbf{r}'\right)+\bar{\chi}\left(\mathbf{r},\mathbf{r}'\right)=\bar{I}\delta\left(\mathbf{r},\mathbf{r}'\right)-i\frac{\omega\mu_0}{4\pi}\int\frac{\bar{\sigma}^0\left(\mathbf{r}'',\mathbf{r}'\right)}{\left|\mathbf{r}-\mathbf{r}''\right|}d\mathbf{r}''. \tag{2.46}$$

Now, having the microscopic dielectric function, one can invert it to obtain the inverse dielectric function and the total field can be calculated from the applied field. However, another conductivity is usually introduced, the external conductivity $\bar{\sigma}$, which is defined explicitly by [90, 98]:

$$\mathbf{J}_{ind}\left(\mathbf{r}\right)=i\omega\int\bar{\sigma}\left(\mathbf{r},\mathbf{r}'\right)\mathbf{A}_{app}\left(\mathbf{r}'\right)d\mathbf{r}'', \tag{2.47}$$

which gives the response of the interacting charges to an applied field. From this quantity the microscopic external susceptibility $\bar{\xi}$ is defined:

$$\bar{\xi}\left(\mathbf{r},\mathbf{r}'\right)=-i\frac{\omega\mu_0}{4\pi}\int\frac{\bar{\sigma}\left(\mathbf{r}'',\mathbf{r}'\right)}{\left|\mathbf{r}-\mathbf{r}''\right|}d\mathbf{r}'', \tag{2.48}$$

and then

$$\mathbf{E}_{ind}\left(\mathbf{r}\right)=-\int\bar{\xi}\left(\mathbf{r},\mathbf{r}'\right)\mathbf{E}_{app}\left(\mathbf{r}'\right)d\mathbf{r}'. \tag{2.49}$$

The macroscopic equivalent of the external susceptibility $\bar{\xi}$ would be ξ_M such that

$$\mathbf{P}=\xi_M\mathbf{D}. \tag{2.50}$$

To the best of my knowledge, ξ_M is not used in the literature. However, it will later appeared to be a key quantity in our analysis of the anisotropic optical response of 2D materials. Now, the inverse dielectric function can be determined using eq. (2.30):

$$\mathbf{E}_{tot}\left(\mathbf{r}\right)=\int\left(\bar{I}\delta\left(\mathbf{r},\mathbf{r}'\right)-\bar{\xi}\left(\mathbf{r},\mathbf{r}'\right)\right)\mathbf{E}_{app}\left(\mathbf{r}'\right)d\mathbf{r}', \tag{2.51}$$

where the term in the parenthesis is nothing else but the inverse dielectric function introduced previously:

$$\bar{\varepsilon}^{-1}\left(\mathbf{r},\mathbf{r}'\right)=\bar{I}\delta\left(\mathbf{r},\mathbf{r}'\right)-\bar{\xi}\left(\mathbf{r},\mathbf{r}'\right)=\bar{I}\delta\left(\mathbf{r},\mathbf{r}'\right)+i\frac{\omega\mu_0}{4\pi}\int\frac{\bar{\sigma}\left(\mathbf{r}'',\mathbf{r}'\right)}{\left|\mathbf{r}-\mathbf{r}''\right|}d\mathbf{r}''. \tag{2.52}$$

Relation (2.51) is now written

$$\mathbf{E}_{tot}\left(\mathbf{r}\right)=\int\bar{\varepsilon}^{-1}\left(\mathbf{r},\mathbf{r}'\right)\mathbf{E}_{app}\left(\mathbf{r}'\right)d\mathbf{r}'. \tag{2.53}$$

By inserting eq. (2.53) in eq. (2.41) and identifying with eq. (2.48)-(2.49), the external conductivity is found directly from the irreducible conductivity:

$$\bar{\sigma}\left(\mathbf{r},\mathbf{r}'\right)=\int\bar{\sigma}^0\left(\mathbf{r},\mathbf{r}''\right)\bar{\varepsilon}^{-1}\left(\mathbf{r}'',\mathbf{r}'\right)d\mathbf{r}'' \tag{2.54}$$

$$=\int\bar{\sigma}^0\left(\mathbf{r},\mathbf{r}''\right)\left(\bar{I}\delta\left(\mathbf{r}',\mathbf{r}''\right)-i\frac{\omega\mu_0}{4\pi}\int\frac{\bar{\sigma}^0\left(\mathbf{r}''',\mathbf{r}''\right)}{\left|\mathbf{r}'-\mathbf{r}'''\right|}d\mathbf{r}'''\right)^{-1}d\mathbf{r}''. \tag{2.55}$$

Longitudinal dielectric function from the polarizability

The longitudinal dielectric function ε_L, i.e. the dielectric function for an applied field and a total field polarized along $\mathbf{u} = \frac{\mathbf{k}}{k}$, is found by projecting the dielectric tensor $\bar{\varepsilon}$ on this vector:

$$\varepsilon_L = \mathbf{u}^T \cdot \bar{\varepsilon} \mathbf{u}. \tag{2.56}$$

However, as explained before, in the longitudinal case, one can work in the gauge where $\mathbf{A}$ is zero (eq. (2.39)). It's common to define a microscopic dielectric function as the scalar function relating the scalar potentials [97, 101]:

$$V_{app}(\mathbf{r}) = \int \epsilon(\mathbf{r}, \mathbf{r}') V_{tot}(\mathbf{r}') d\mathbf{r}'. \tag{2.57}$$

The function $\epsilon(\mathbf{r}, \mathbf{r}')$ is called here the pseudo-dielectric function. Indeed, it differs from the true microscopic dielectric function $\bar{\varepsilon}(\mathbf{r}, \mathbf{r}')$. It is usually called the dielectric function because the macroscopic average of this dielectric function is the same as the macroscopic average of the longitudinal dielectric function as it will be shown in the next section. The difference between $\epsilon(\mathbf{r}, \mathbf{r}')$ and $\bar{\varepsilon}(\mathbf{r}, \mathbf{r}')$ appears by calculating the applied electric field from the previous equation, projected along $\mathbf{u}$:

$$\mathbf{u}^T \cdot \mathbf{E}_{app}(\mathbf{r}) = -\frac{\partial}{\partial \mathbf{u}} V_{app}(\mathbf{r}) = \int -\frac{\partial}{\partial \mathbf{u}} \epsilon(\mathbf{r}, \mathbf{r}') V_{tot}(\mathbf{r}') d\mathbf{r}', \tag{2.58}$$

with $\frac{\partial}{\partial \mathbf{u}}$ the directional derivative and comparing with

$$\mathbf{u}^T \cdot \mathbf{E}_{app}(\mathbf{r}) = \int \mathbf{u}^T \varepsilon(\mathbf{r}, \mathbf{r}') \mathbf{u}\, \mathbf{u}^T \cdot \mathbf{E}_{tot}(\mathbf{r}') d\mathbf{r}' \tag{2.59}$$

obtained from eq. (2.7) projected on $\mathbf{u}$. Before establishing a relation between the pseudo-dielectric function ϵ and the longitudinal dielectric function ε_L, the relation between the polarizability and the pseudo-dielectric function is derived as it is done in most textbooks and papers [96, 97]. In the frame of RPA, the irreducible polarizability, define implicitly in eq. (2.35):

$$\rho_{ind}(\mathbf{r}) = \int \alpha^0(\mathbf{r}, \mathbf{r}') V_{tot}(\mathbf{r}') d\mathbf{r}' \tag{2.60}$$

is given by eq. (2.26). The external polarizability α is:

$$\rho_{ind}(\mathbf{r}) = \int \alpha(\mathbf{r}, \mathbf{r}') V_{app}(\mathbf{r}') d\mathbf{r}' \tag{2.61}$$

i.e. it is the response function of interacting charges to an applied potential. The induced potential is obtained by applying the coulomb operator v_c on the charge density:

$$V_{ind}(\mathbf{r}) = \frac{1}{4\pi\varepsilon_0} \int \int \frac{\alpha^0(\mathbf{r}', \mathbf{r}'')}{|\mathbf{r} - \mathbf{r}'|} V_{tot}(\mathbf{r}') d\mathbf{r}'' d\mathbf{r}' \tag{2.62}$$

or

$$V_{ind}(\mathbf{r}) = \frac{1}{4\pi\varepsilon_0} \int \int \frac{\alpha(\mathbf{r}', \mathbf{r}'')}{|\mathbf{r} - \mathbf{r}'|} V_{app}(\mathbf{r}') d\mathbf{r}'' d\mathbf{r}', \tag{2.63}$$

depending on the choice of polarizability. Two pseudo-susceptibilities, χ and ξ, are defined as the response functions of an induced field to respectively a total and an applied field:

$$V_{ind}(\mathbf{r}) = -\int \chi(\mathbf{r},\mathbf{r}')\, V_{tot}(\mathbf{r}')\, d\mathbf{r}', \tag{2.64}$$

$$V_{ind}(\mathbf{r}) = -\int \xi(\mathbf{r},\mathbf{r}')\, V_{app}(\mathbf{r}')\, d\mathbf{r}', \tag{2.65}$$

with

$$\chi(\mathbf{r},\mathbf{r}') = -\frac{1}{4\pi\varepsilon_0}\int \frac{\alpha^0(\mathbf{r}'',\mathbf{r}')}{|\mathbf{r}-\mathbf{r}''|} d\mathbf{r}'', \tag{2.66}$$

$$\xi(\mathbf{r},\mathbf{r}') = -\frac{1}{4\pi\varepsilon_0}\int \frac{\alpha(\mathbf{r}'',\mathbf{r}')}{|\mathbf{r}-\mathbf{r}''|} d\mathbf{r}''. \tag{2.67}$$

These pseudo-susceptibilities are different from the longitudinal components of the tensorial susceptibilities (the proof is similar than for the pseudo-dielectric function). The pseudo-dielectric function is, in analogy with the previous development:

$$\epsilon(\mathbf{r},\mathbf{r}') = \delta(\mathbf{r},\mathbf{r}') + \chi(\mathbf{r},\mathbf{r}') = \delta(\mathbf{r},\mathbf{r}') - \frac{1}{4\pi\varepsilon_0}\int\int \frac{\alpha^0(\mathbf{r}'',\mathbf{r}')}{|\mathbf{r}-\mathbf{r}''|} d\mathbf{r}'', \tag{2.68}$$

or

$$\epsilon^{-1}(\mathbf{r},\mathbf{r}') = \delta(\mathbf{r},\mathbf{r}') - \xi(\mathbf{r},\mathbf{r}') = \delta(\mathbf{r},\mathbf{r}') + \frac{1}{4\pi\varepsilon_0}\int\int \frac{\alpha(\mathbf{r}'',\mathbf{r}')}{|\mathbf{r}-\mathbf{r}''|} d\mathbf{r}''. \tag{2.69}$$

The relations between the polarizabilities is, in analogy with eq. (2.55):

$$\alpha(\mathbf{r},\mathbf{r}') = \alpha^0(\mathbf{r},\mathbf{r}'')\left(\delta(\mathbf{r}',\mathbf{r}'') - \frac{1}{4\pi\varepsilon_0}\int\int \frac{\alpha^0(\mathbf{r}''',\mathbf{r}'')}{|\mathbf{r}'-\mathbf{r}'''|} d\mathbf{r}'''\right)^{-1}. \tag{2.70}$$

which is equivalent to the relation (2.29). Now the relation between the tensorial susceptibility and the pseudo-susceptibility for longitudinal waves can be derived. The induced field along $\mathbf{u}$ is deduced from both gauges ($\mathbf{A}_{app} = 0$ or $V_{app} = 0$) such that

$$-\mathbf{u}^T \cdot \mathbf{E}_{ind}(\mathbf{r}) = -\frac{\partial}{\partial \mathbf{u}} V_{ind}(\mathbf{r}). \tag{2.71}$$

Replacing the induced field and potential given by eq. (2.49) and (2.65) and noting from eq. (2.39) that the applied potential is related to the applied field by $V_{app}(\mathbf{r}) = \frac{i}{k}\mathbf{u}^T \cdot \mathbf{E}_{app}(\mathbf{r})$, eq. (2.71) becomes:

$$\int \mathbf{u}^T \bar{\xi}(\mathbf{r},\mathbf{r}')\, \mathbf{u}\, \mathbf{u}^T \cdot \mathbf{E}_{app}(\mathbf{r}')\, d\mathbf{r}' = \int \frac{\partial}{\partial \mathbf{u}} \xi(\mathbf{r},\mathbf{r}')\, \frac{i}{k}\mathbf{u}^T \cdot \mathbf{E}_{app}(\mathbf{r}')\, d\mathbf{r}', \tag{2.72}$$

$$\mathbf{u}^T \bar{\xi}(\mathbf{r},\mathbf{r}')\, \mathbf{u} \equiv \xi_L = \frac{i}{k}\frac{\partial}{\partial \mathbf{u}} \xi(\mathbf{r},\mathbf{r}'), \tag{2.73}$$

i.e. the longitudinal susceptibility depends of the directional derivative of the pseudo-susceptibility. Using the relation between the external susceptibilities and the dielectric functions ((2.52) and (2.69)), it can be proven that the same relation holds between the pseudo-dielectric function and the tensorial dielectric function:

$$\mathbf{u}^T \varepsilon(\mathbf{r}, \mathbf{r}')\mathbf{u} = \frac{i}{k}\frac{\partial}{\partial \mathbf{u}}\epsilon(\mathbf{r}, \mathbf{r}')\,. \tag{2.74}$$

In conclusion, in the case of longitudinal waves, the tensorial dielectric function and the pseudo-dielectric function contain the same information and both can be used equally. Most of the time, only the pseudo-dielectric function is exploited, due to the simplicity to derive the polarizability from the wave functions (eq. (2.26)), and the ease to use scalar quantities. For these reasons, in the following sections, only the pseudo-dielectric function is used.

Fourier transform of the dielectric function

In solid state physics, the dielectric function is used to study the optical properties of crystalline materials. Due to the structure of these materials, the fields and potentials are periodic and the calculation of the microscopic dielectric function in the crystal's unit cell is sufficient. For plane wave excitations, one can write the potential as a Bloch wave:

$$V(\mathbf{r}) = \tilde{V}(\mathbf{r})\, e^{i\mathbf{k}\cdot\mathbf{r}}, \tag{2.75}$$

where $\tilde{V}(\mathbf{r})$ is a lattice periodic function. From now, the tilde over a field will signify it is a lattice periodic function. The relation between the applied field and the total field (equation (2.57)) writes now

$$\tilde{V}_{app} e^{i\mathbf{k}\cdot r} = \int \epsilon(\mathbf{r}, \mathbf{r}')\, \tilde{V}_{tot}(\mathbf{r}')\, e^{i\mathbf{k}\cdot r'} d\mathbf{r}'. \tag{2.76}$$

The phase factors can be grouped into the integral:

$$\tilde{V}_{app} = \int \epsilon(\mathbf{r}, \mathbf{r}')\, e^{i\mathbf{k}\cdot(\mathbf{r}'-\mathbf{r})} \tilde{V}_{tot}(\mathbf{r}')\, d\mathbf{r}' \tag{2.77}$$

or equivalently

$$\tilde{V}_{tot}(\mathbf{r}) = \int \epsilon^{-1}(\mathbf{r}, \mathbf{r}')\, e^{i\mathbf{k}\cdot(\mathbf{r}'-\mathbf{r})} \tilde{V}_{app}\, d\mathbf{r}'. \tag{2.78}$$

It is worth reminding here that the integral is performed over the whole space while a variable position $\mathbf{r}$ in the unit cell is enough to describe the whole system. In DFT codes, the calculation of the pseudo-dielectric function is in fact the calculation of $\epsilon(\mathbf{k}, \mathbf{r}, \mathbf{r}') \equiv \epsilon(\mathbf{r}, \mathbf{r}')\, e^{i\mathbf{k}\cdot(\mathbf{r}'-\mathbf{r})}$. The total potential in the unit cell is

$$\tilde{V}_{tot}(\mathbf{r}) = \int \epsilon^{-1}(\mathbf{k}, \mathbf{r}, \mathbf{r}')\, d\mathbf{r}' \tilde{V}_{app} \equiv \epsilon^{-1}(\mathbf{k}, \mathbf{r})\, \tilde{V}_{app}. \tag{2.79}$$

Here $\epsilon^{-1}(\mathbf{k}, \mathbf{r})$ is the local inverse dielectric function: it is the ratio between the applied potential and the total potential at a point $\mathbf{r}$ in the unit cell.

Furthermore, as the system is periodic, the dielectric function can be written in the reciprocal space. In fact, as ground state calculation of the quantum electronic states of

periodic materials is already performed in the reciprocal space, it is the simplest way to calculate it. For example, the Fourier transform of the polarizability is

$$\alpha\left(\mathbf{k},\mathbf{G},\mathbf{G}'\right)=\frac{1}{\Omega}\int\int e^{-i\mathbf{G}\cdot\mathbf{r}}\alpha\left(\mathbf{k},\mathbf{r},\mathbf{r}'\right)e^{i\mathbf{G}'\cdot\mathbf{r}'}d\mathbf{r}\,d\mathbf{r}', \tag{2.80}$$

with $\alpha\left(\mathbf{k},\mathbf{r},\mathbf{r}'\right)\equiv\alpha\left(\mathbf{r},\mathbf{r}'\right)e^{i\mathbf{k}\cdot\left(r'-\mathbf{r}\right)}$ and $\mathbf{G}$, $\mathbf{G}'$ are reciprocal vectors in the first Brillouin zone. Taking this into account, eq. 2.80 rewrites as

$$\alpha\left(\mathbf{k},\mathbf{G},\mathbf{G}'\right)=\frac{1}{\Omega}\int\int e^{-i(\mathbf{k}+\mathbf{G})\cdot\mathbf{r}}\alpha\left(\mathbf{r},\mathbf{r}'\right)e^{i(\mathbf{k}+\mathbf{G}')\cdot\mathbf{r}'}d\mathbf{r}\,d\mathbf{r}'. \tag{2.81}$$

From eq. (2.26), the well known irreducible polarizability in reciprocal space is obtained :

$$\alpha^{0}\left(\mathbf{k},\mathbf{G},\mathbf{G}'\right)=\frac{1}{\Omega}\sum_{\mathbf{q}}\sum_{i,j'}\left(f_{i\mathbf{q}}-f_{j\mathbf{q}+\mathbf{k}}\right)\frac{\rho_{i\mathbf{q},j\mathbf{q}+\mathbf{k}}\left(\mathbf{G}\right)\rho^{*}_{i\mathbf{q},j\mathbf{q}+\mathbf{k}}\left(\mathbf{G}'\right)}{\omega-E_{i\mathbf{q}}-E_{j\mathbf{q}+\mathbf{k}}+i\eta}, \tag{2.82}$$

with

$$\rho_{i\mathbf{q},j\mathbf{q}+\mathbf{k}}\left(\mathbf{G}\right)=\left\langle\psi_{i\mathbf{q}}\left(\mathbf{r}\right)\left|e^{i(\mathbf{k}+\mathbf{G})\cdot\mathbf{r}}\right|\psi_{j\mathbf{q}+\mathbf{k}}\left(\mathbf{r}\right)\right\rangle. \tag{2.83}$$

The dielectric function in the reciprocal space is

$$\epsilon\left(\mathbf{k},\mathbf{G},\mathbf{G}'\right)=\frac{1}{\Omega}\int\int e^{-i(\mathbf{k}+\mathbf{G})\cdot\mathbf{r}}\epsilon\left(\mathbf{r},\mathbf{r}'\right)e^{i(\mathbf{k}+\mathbf{G}')\cdot\mathbf{r}'}d\mathbf{r}\,d\mathbf{r}'. \tag{2.84}$$

Because the Fourier transform of the coulomb potential v_c is of the form $\frac{1}{|\mathbf{q}|^2}$, it can also be written as follows [97]:

$$\epsilon\left(\mathbf{k},\mathbf{G},\mathbf{G}'\right)=\delta\left(\mathbf{G}-\mathbf{G}'\right)-\frac{1}{\varepsilon_0\left|\mathbf{k}+\mathbf{G}\right|^2}\alpha^{0}\left(\mathbf{k},\mathbf{G},\mathbf{G}'\right) \tag{2.85}$$

or

$$\epsilon^{-1}\left(\mathbf{k},\mathbf{G},\mathbf{G}'\right)=\delta\left(\mathbf{G}-\mathbf{G}'\right)+\frac{1}{\varepsilon_0\left|\mathbf{k}+\mathbf{G}\right|^2}\alpha\left(\mathbf{k},\mathbf{G},\mathbf{G}'\right). \tag{2.86}$$

The same procedure can be applied to the tensorial dielectric function and its inverse.

Eigenmode decomposition of the dielectric functions

The dielectric functions and susceptibilities (tensorial or scalar), their inverses and their counterparts in reciprocal space, when calculated on a spatial grid, are matrix operators that can be diagonalized. From the eigenvalues and eigenvectors, precious information about the optical properties can be retrieved, in particular the spatial distributions of the charges and fields or potentials. This method has been developed first by K. Andersen from the DTU in [45] and is described in detail here. For simplicity, the $\mathbf{k}$ vector is fixed and is omitted in the following.

The dielectric function matrices are applied to the electric field or potential. Therefore the right eigenvectors represent the field or potential of the eigenmodes. On a discretized basis, the eigenvalue equation for the pseudo-dielectric function writes

$$\sum_{\mathbf{r}'}\epsilon_{\mathbf{r},\mathbf{r}'}V_{i,\mathbf{r}'}=\epsilon_i V_{i,\mathbf{r}}, \tag{2.87}$$

where $V_{i,\mathbf{r}}$, an eigenvector, is the total potential of the mode i and ϵ_i is a constant, i.e. it differs only by a scalar factor. This means that, for an eigenmode, the applied potential

$$V_{i,app,\mathbf{r}} = \epsilon_i V_{i,\mathbf{r}} \tag{2.88}$$

is spatially similar to the total potential. The eigenvalues ϵ_i can thus be considered as the dielectric function of the mode i.

From the general properties of the eigenvalues and eigenvectors the following facts are deduced. They will allow us to manipulate the eigenvalues easily afterwards:

- The eigenvalues of $\epsilon^{-1}_{\mathbf{r},\mathbf{r}'}$ are the inverse of the eigenvalues ϵ_i of $\epsilon_{\mathbf{r},\mathbf{r}'}$, $\epsilon_i^{-1} = \frac{1}{\epsilon_i}$;
- The eigenvalues of $\epsilon_{\mathbf{r},\mathbf{r}'}$ are related to the eigenvalues of $\chi_{\mathbf{r},\mathbf{r}'}$ by $\epsilon_i = 1 + \chi_i$;
- The eigenvalues of $\epsilon^{-1}_{\mathbf{r},\mathbf{r}'}$ are related to the eigenvalues of $\xi_{\mathbf{r},\mathbf{r}'}$ by $\frac{1}{\epsilon_i} = 1 - \xi_i$.

K. Andersen has shown that the left eigenvectors corresponds to the charge density noted $\rho_{i,\mathbf{r}'}$ [45]. Therefore, in the basis of the eigenvectors, the dielectric function is written

$$\epsilon_{\mathbf{r},\mathbf{r}'} = \sum_i \epsilon_i V_{i,\mathbf{r}} \rho^*_{i,\mathbf{r}'}, \tag{2.89}$$

which in reciprocal space is

$$\epsilon_{\mathbf{G},\mathbf{G}'} = \sum_i \epsilon_i V_{i,\mathbf{G}} \rho^*_{i,\mathbf{G}'}. \tag{2.90}$$

This representation is useful to calculate the macroscopic dielectric function as it will be shown in the next section.

The same procedure can be performed for the tensorial dielectric function, which will result in eigenvectors corresponding to vector potential and current densities, with similar conclusions.

Plasmons identification from the eigenmode decomposition

It was shown in chapter 1 that a bulk plasmon in a homogeneous material is a collective excitation of electrons that occurs at a frequency where the macroscopic permittivity is zero. However, these plasmons cannot be excited by transverse waves as their excitation needs $\mathbf{k} \cdot \mathbf{E} \neq 0$. Here, this notion of plasmon is generalized using the eigenmodes of the system. By means of the properties of the eigenvalues and eq. (2.88), it can be written:

$$V_{i,\mathbf{r}} = \epsilon_i^{-1} V_{app,i,\mathbf{r}} \tag{2.91}$$

where $V_{app,i,\mathbf{r}}$ is an eigenvector of ϵ_i^{-1} corresponding to the applied potential. Then if $\epsilon_i = 0$ at a given frequency ω, a potential $V_{i,\mathbf{r}}$ can be sustained without applied potential. Actually, at that resonance frequency we always have $\Re e(\epsilon_i) = 0$ and $\Im m(\epsilon_i) \gtrsim 0$ such

that at that frequency, a small applied potential results in a large, out-of-phase, total potential. The loss function for an eigenmode is:

$$L_i = -\Im m \frac{1}{\epsilon_i}. \tag{2.92}$$

As it was shown in chapter 1, the plasmon can be identified when the loss function is maximum, relatively to the frequency. From the properties of the eigenvalues, the loss function can be written using the external susceptibility:

$$L_i = \Im m \left(\xi_i\right), \tag{2.93}$$

with

$$V_{ind,i,\mathbf{r}} = \xi_i V_{app,i,\mathbf{r}}. \tag{2.94}$$

When the loss function is high, the imaginary part of the induced field (in phase quadrature with the applied field) is dominant compared to the real part, and large compared to the applied field.

To summarize, using the eigenmode method, one can identify plasmons, which have been characterized here as modes for which the intensity of the induced or total field is large compared to the applied field. The strength of this method is that it cannot only identify bulk plasmons but also surface plasmons. If there is a structure in the unit cell, the surface plasmons around this structure enhance the fields and potentials: a mode has to be associated to this plasmon. These structures can be confined in either 1 , 2 or 3 dimensions. In the last case, which corresponds to a quantum well, the plasmons are equivalent to LSPs, while for the first two cases, they are SPPs. However, all these plasmonic modes are not necessarily detectable. As it will be shown in the next section, not all modes contribute to the macroscopic dielectric function and only plasmons whose symmetry permits it are measurable in the far field.

Conclusions

The microscopic dielectric function is a fundamental quantity that contains a lot of information about the optical properties of the quantum system. In particular, for structured systems, the eigenvalue decomposition of the tensor allows us to find plasmonic resonances. However, DFT codes only calculate the longitudinal dielectric function, which is sufficient for plasmons but could be limiting for studying interaction of transverse wave with large systems. Moreover, the microscopic dielectric function calculated in these codes does not corresponds to the usual definition because it relates the scalar potentials and not the electric fields. As it was shown, this is not a problem because the two quantities are related but particular care must be taken when manipulating this microscopic dielectric function, to not misinterpret the results.

2.2 Macroscopic description of the dielectric function

In the same way that the microscopic dielectric function relates the microscopic fields, the macroscopic dielectric function relates the macroscopic fields i.e. fields that have

been averaged over the unit cell. The macroscopic fields are plane waves with constant amplitude because the material is considered homogeneous and infinite. As the material is homogeneous, the dielectric function is defined using the amplitude of the field :

$$\left\langle \tilde{\mathbf{E}}_{app}\left(\mathbf{r}\right)\right\rangle_{\mathbf{r}} = \varepsilon^{M}\left\langle \tilde{\mathbf{E}}_{\mathbf{tot}}\left(\mathbf{r}\right)\right\rangle_{\mathbf{r}}, \tag{2.95}$$

where $\langle\rangle_{\mathbf{r}}$ represents the spatial average over the unit cell. Here, ε^{M} is a tensor. However, as the material is homogeneous, we can find a basis in which the tensor is diagonal. Then, the matrix equation above reduces to three independent equations. Without loss of generality, the polarization can be fixed along one of the principal axis, such that a single scalar equation remains:

$$\left\langle \tilde{E}_{app,j}\left(\mathbf{r}\right)\right\rangle_{\mathbf{r}} = \varepsilon_{jj}^{M}\left\langle \tilde{E}_{tot,j}\left(\mathbf{r}\right)\right\rangle_{\mathbf{r}}, \tag{2.96}$$

where $\left\langle \tilde{E}_{j}\left(\mathbf{r}\right)\right\rangle_{\mathbf{r}}$ means $\left\langle \tilde{\mathbf{E}}\left(\mathbf{r}\right)\right\rangle_{\mathbf{r}} \cdot \mathbf{e}_{j}$ and $\varepsilon_{jj}^{M} = \mathbf{e}_{j} \cdot \varepsilon_{jj}\mathbf{e}_{j}$ with $\mathbf{e}_{j}$ a unit vector along a principal axis. By means of simplicity, the index j is dropped in the following. Now we consider that $\tilde{E}_{app}$ is constant in space, which is the case for a plane wave, the dielectric function can be written using eq. (2.10):

$$\varepsilon^{M}\left(\mathbf{k}\right) = \frac{\left\langle \tilde{E}_{app}\left(\mathbf{r}\right)\right\rangle_{\mathbf{r}}}{\left\langle \tilde{E}_{tot}\left(\mathbf{r}\right)\right\rangle_{\mathbf{r}}}, \tag{2.97}$$

$$\varepsilon^{M}\left(\mathbf{k}\right) = \frac{\tilde{E}_{app}}{\frac{1}{\Omega}\int\int\varepsilon^{-1}\left(\mathbf{k},\mathbf{r},\mathbf{r}'\right)\tilde{E}_{app}d\mathbf{r}'d\mathbf{r}}, \tag{2.98}$$

with Ω the volume of the unit cell. The macroscopic dielectric function is thus the inverse of the spatial average of the inverse dielectric function:

$$\varepsilon^{M}\left(\mathbf{k}\right) = \frac{1}{\frac{1}{\Omega}\int\int\varepsilon^{-1}\left(\mathbf{k},\mathbf{r},\mathbf{r}'\right)d\mathbf{r}'d\mathbf{r}}. \tag{2.99}$$

From eq. (2.52), it comes

$$\varepsilon^{M}\left(\mathbf{k}\right) = \frac{1}{1-\frac{1}{\Omega}\int\int\bar{\xi}\left(\mathbf{k},\mathbf{r},\mathbf{r}'\right)d\mathbf{r}'d\mathbf{r}} \equiv \frac{1}{1-\xi^{M}\left(\mathbf{k}\right)}, \tag{2.100}$$

where ξ^{M} is the macroscopic external susceptibility. As suggested before, eq. (2.50), this susceptibility relates the macroscopic displacement field $\mathbf{D}$ to the polarization field $\mathbf{P}$:

$$\mathbf{P} = \xi^{M}\mathbf{D}. \tag{2.101}$$

The usual susceptibility χ defined from $\mathbf{P} = \varepsilon_{0}\chi\left(\mathbf{k}\right)\mathbf{E}$ can be expressed using ξ^{M} :

$$\chi\left(\mathbf{k}\right) = \varepsilon^{M}\left(\mathbf{k}\right) - 1 = \frac{\xi^{M}\left(\mathbf{k}\right)}{1-\xi^{M}\left(\mathbf{k}\right)}. \tag{2.102}$$

In chapter 4, it will be shown that the external susceptibility ξ is the proper quantity to describe the out-of-plane response of 2D materials, while the susceptibility χ is not convenient.

In the literature, a distinction is done between the dielectric function including or not the local field effects. These effects arise from high variations of the electric field over the unit cell. The dielectric function defined by eq. (2.100) account for the local field effects. If one neglects the local field effects, the amplitude of the total field or potential is assumed constant in the unit cell i.e. $E_{tot}(\mathbf{r}) = \tilde{E}_{tot} e^{i\mathbf{k}\cdot\mathbf{r}}$, similarly to the applied field. In brief this means that the material does not induces spatial variation of the field. With this approximation, eq. (2.97) can be rewritten

$$\varepsilon^{M,NLF}(\mathbf{k}) = \frac{\left\langle \tilde{E}_{app}(\mathbf{r}) \right\rangle_{\mathbf{r}}}{\left\langle \tilde{E}_{tot}(\mathbf{r}) \right\rangle_{\mathbf{r}}} \tag{2.103}$$

$$\varepsilon^{M,NLF}(\mathbf{k}) = \frac{\frac{1}{\Omega}\int\int \varepsilon(\mathbf{k},\mathbf{r},\mathbf{r}')\,\tilde{E}_{tot} d\mathbf{r}' d\mathbf{r}}{\tilde{E}_{tot}} = \frac{1}{\Omega}\int\int \varepsilon(\mathbf{k},\mathbf{r},\mathbf{r}')\,d\mathbf{r}' d\mathbf{r}. \tag{2.104}$$

using the subscript NLF for no-local-field. The principal observation here is that the spatial average of the microscopic dielectric function is equivalent to the macroscopic dielectric function only if local field effects are negligible. Moreover, from eq. (2.46) relating the microscopic dielectric function to the microscopic irreducible susceptibility the previous equation becomes:

$$\varepsilon^{M,NLF}(\mathbf{k}) = 1 + \frac{1}{\Omega}\int\int \bar{\chi}(\mathbf{k},\mathbf{r},\mathbf{r}')\,d\mathbf{r}' d\mathbf{r} \equiv 1 + \chi^{M}, \tag{2.105}$$

where χ^M is the spatial average of the microscopic irreducible susceptibility. Only if the local fields are negligible is χ^M equivalent to χ, the usual susceptibility. Otherwise, the relation (2.102) should be used.

Longitudinal macroscopic dielectric function

It was shown in section 2.1 that in the case of longitudinal excitation and response, the pseudo-dielectric function defined from the potential can be used. For a polarization in the direction of $\mathbf{k}$, eq. (2.97) can be rewritten

$$\varepsilon^{M}(\mathbf{k}) = \frac{\left\langle \nabla\left(V_{app}(\mathbf{r})\right) e^{-i\mathbf{k}\cdot\mathbf{r}} \right\rangle_{\mathbf{r}}}{\left\langle \nabla\left(V(\mathbf{r})\right) e^{-i\mathbf{k}\cdot\mathbf{r}} \right\rangle_{\mathbf{r}}} \tag{2.106}$$

because $\mathbf{E}(\mathbf{r}) = \tilde{\mathbf{E}}(\mathbf{r}) e^{i\mathbf{k}\cdot\mathbf{r}} = -\nabla V(\mathbf{r})$ thus $\tilde{\mathbf{E}}(\mathbf{r}) = -\nabla V(\mathbf{r}) e^{-i\mathbf{k}\cdot\mathbf{r}}$. Applying the gradient, it comes, for a uniform applied potential:

$$\varepsilon^{M}(\mathbf{k}) = \frac{\left\langle i\mathbf{k}\tilde{V}_{app} \right\rangle_{\mathbf{r}}}{\left\langle \nabla\tilde{V}(\mathbf{r}) + i\mathbf{k}\tilde{V}(\mathbf{r}) \right\rangle_{\mathbf{r}}} \tag{2.107}$$

$$\varepsilon^{M}(\mathbf{k}) = \frac{i\mathbf{k}\tilde{V}_{app}}{\left\langle \nabla\tilde{V}(\mathbf{r}) \right\rangle_{\mathbf{r}} + \left\langle i\mathbf{k}\tilde{V}(\mathbf{r}) \right\rangle_{\mathbf{r}}} \tag{2.108}$$

and, because the spatial average of the gradient of a periodic function is zero, we have, using eq. (2.79):

$$\varepsilon^M(\mathbf{k}) = \frac{\tilde{V}_{app}}{\left\langle \tilde{V}(\mathbf{r}) \right\rangle_{\mathbf{r}}} = \frac{\tilde{V}_{app}}{\frac{1}{\Omega}\int\int \epsilon^{-1}(\mathbf{k},\mathbf{r},\mathbf{r}')\,\tilde{V}_{app} d\mathbf{r}' d\mathbf{r}} \tag{2.109}$$

$$\varepsilon^M(\mathbf{k}) = \frac{1}{\frac{1}{\Omega}\int\int \epsilon^{-1}(\mathbf{k},\mathbf{r},\mathbf{r}')\,d\mathbf{r}' d\mathbf{r}} \tag{2.110}$$

and the macroscopic dielectric function can be also obtained from the pseudo-dielectric function. Again, if local fields are neglected, one obtains:

$$\varepsilon^{M,NLF}(\mathbf{k}) = \frac{1}{\Omega}\int\int \epsilon(\mathbf{k},\mathbf{r},\mathbf{r}')\,d\mathbf{r}' d\mathbf{r}. \tag{2.111}$$

In brief, from a macroscopic point of view, for longitudinal waves (and a forteriori for $\mathbf{k} \to 0$), the use of the microscopic pseudo-dielectric function is equivalent to the case of the tensorial dielectric function.

Macroscopic dielectric function in reciprocal space

In reciprocal space, taking the spatial average over the unit cell is equivalent to take $\mathbf{G} = 0$. In consequence, the macroscopic dielectric functions are calculated as

$$\varepsilon^M(\mathbf{k}) = \frac{1}{\varepsilon^{-1}(\mathbf{k}, \mathbf{G}=0, \mathbf{G}'=0)}, \tag{2.112}$$

or, when neglecting local field effects:

$$\varepsilon^{M,NLF}(\mathbf{k}) = \varepsilon(\mathbf{k}, \mathbf{G}=0, \mathbf{G}'=0). \tag{2.113}$$

These two equations are generally presented in most articles using TDDFT to calculate the macroscopic dielectric function [96, 97, 99–101].

Long wavelength limit

When $\mathbf{k} \to 0$, i.e. the long wavelength limit, the Coulomb kernel $\frac{1}{\varepsilon_0|\mathbf{k}+\mathbf{G}|^2}$ diverges if $\mathbf{G} = 0$ and particular care must be taken when calculating the irreducible polarizability. According to [97], the transition matrix can be approximate by

$$\left\langle \psi_{i\mathbf{q}}(\mathbf{r}) \left| e^{i(\mathbf{k}+\mathbf{G})\cdot\mathbf{r}} \right| \psi_{j\mathbf{q}+\mathbf{k}}(\mathbf{r}) \right\rangle_{\mathbf{k}\to 0, \mathbf{G}=0} = -i\mathbf{k}\left\langle \psi_{i\mathbf{q}}(\mathbf{r}) \left| \nabla \right| \psi_{j\mathbf{q}}(\mathbf{r}) \right\rangle. \tag{2.114}$$

This equation is in general directly implemented in the DFT codes calculating the dielectric function.

Macroscopic dielectric function from the eigenvalue decomposition

The macroscopic dielectric function can be evaluated using the eigenvalue decomposition proposed in section (3.1). This approach was not developed by the authors of [45] and it is therefore an original contribution. The pseudo-dielectric function is decomposed in reciprocal space. From eq. (2.90), (2.112) and (2.113) one obtains:

$$\varepsilon^M = \frac{1}{\sum_i \epsilon_i \, V_{i,\mathbf{G}=\mathbf{0}} \, \rho^*_{i,\mathbf{G}'=\mathbf{0}}}, \tag{2.115}$$

$$\varepsilon^{M,NLF} = \sum_i \epsilon_i \, V_{i,\mathbf{G}=\mathbf{0}} \, \rho^*_{i,\mathbf{G}'=\mathbf{0}}. \tag{2.116}$$

The quantity $V_{i,\mathbf{G}=\mathbf{0}} \, \rho^*_{i,\mathbf{G}=\mathbf{0}}$ is the product of the spatial and time averaged values of the potential and charge density. Here, this quantity can be considered as the weight w_i of the mode i :

$$w_i = V_{i,\mathbf{G}=\mathbf{0}} \, \rho^*_{i,\mathbf{G}=\mathbf{0}}, \tag{2.117}$$

such that

$$\varepsilon^{M,NLF} = \sum_i w_i \epsilon_i, \tag{2.118}$$

$$\varepsilon^M = \frac{1}{\sum_i w_i \frac{1}{\epsilon_i}}. \tag{2.119}$$

If the local fields effect are negligible, then one must have:

$$\sum_i w_i \epsilon_i = \frac{1}{\sum_i w_i \frac{1}{\epsilon_i}}. \tag{2.120}$$

Mathematically, this can be verified if either there is only one mode j with non-vanishing weight, with $w_j = 1$ at a given frequency or if all the eigenvalues are equal since the sum of the weights is equal to one. The second possibility must be ruled out because the number of mode is equal to the number of $\mathbf{G}$ vectors, which is arbitrary and depends on the discretization. Therefore if local field effects are negligible, only one mode is present. The potential associated to this mode corresponds to a constant field over the unit cell, which is coherent with the local fields being negligible in homogeneous materials.

For surface plasmon resonances, which are only possible with nanostructures in the unit cell, $\epsilon_i = 0$ or more realistically $\Re(\epsilon_i) = 0$ at a given frequency, because the total field becomes very large compared to the applied field. The permittivity $\varepsilon^{M,NLF}$ does not account for this fundamental feature because the contribution of one particular mode with $\epsilon_i = 0$ is negligible in eq. (2.118) compared to other modes. On the other hand, ε^M can account for the corresponding behavior in the dielectric function: indeed if $\epsilon_i = 0$, then $\varepsilon^M = 0$ in eq. (2.119).

From the definition of the loss function and from eq. (2.119), it can be seen that the macroscopic loss function L_M is the weighted sum of the individual loss functions for

each mode L_i:

$$L_M \equiv -\Im m \frac{1}{\varepsilon^M}, \tag{2.121}$$

$$L_M = -\Im m \sum_i w_i \frac{1}{\epsilon_i}, \tag{2.122}$$

$$L_M = \sum_i w_i L_i. \tag{2.123}$$

In fact, this is related to the fact that the macroscopic external susceptibility ξ^M is directly the weighted sum of the eigenvalues ξ_i, as it can be deduced from the relations between the eigenvalues ϵ_i and ξ_i:

$$\xi^M = \sum_i w_i \xi_i. \tag{2.124}$$

The same relation is also valid for the macroscopic internal susceptibility when there are no local field effect :

$$\chi^{M,NLF} = \sum_i w_i \chi_i. \tag{2.125}$$

It was noticed that, when a plasmonic mode has a large weight, it contributes greatly to the macroscopic loss function. Moreover, the macroscopic loss function is a linear combination of the loss function of each mode (see eq. (2.123)). In some sense, the eigenvalue ϵ_i can be considered as the macroscopic dielectric function of the particular substructure responsible for the plasmon in the unit cell. Indeed, if only this plasmonic mode has a large weight, the macroscopic dielectric function is only dependent on the corresponding eigenvalue. As the weight is proportional to the average values of the charge density and potential that are concentrated around the structure responsible for the plasmon, it will be proportional to the spatial occupation of this structure in the cell.

This method is a powerful tool to obtain a clear spatial description of a complex quantum system. The main limitation of this method is that the size of system that can be studied is small due to the high computational resources needed for large systems in TDDFT.

Example of the eigenvalue decomposition method: graphite

Here, I propose to illustrate the principle of the eigenmode decomposition of the dielectric function described above on a relatively simple and known system. Graphite as been chosen because it is related to graphene and its two main volume plasmons, the π and $\pi + \sigma$ plasmons are well described [102, 103]. The loss spectrum is analysed for two polarizations: perpendicular to the optical axis (parallel to the graphite planes) and parallel to the optical axis (perpendicular to the graphite planes).

Polarization perpendicular to the optical axis

The dielectric function of graphite is obtained from TDDFT calculations. As an example, the input files and the script for the eigenmode method are provided in the appendix.

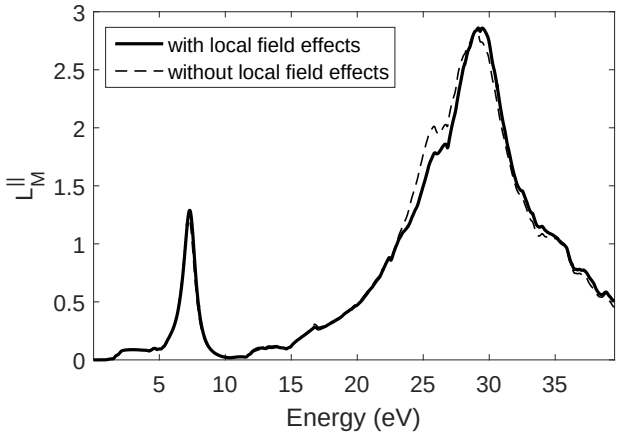

Figure 2.1: Loss function of graphite with and without local field effects in the direction parallel to the layers with $k = 0.30$ Å^{-1}.

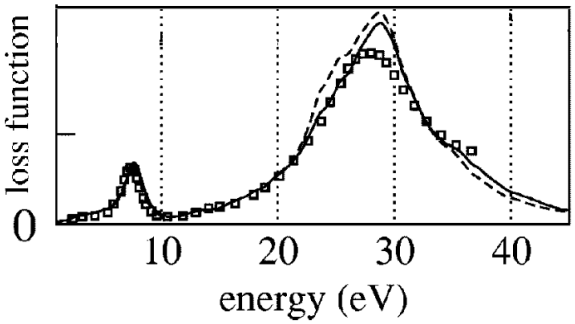

Figure 2.2: Loss function of graphite obtained theoretically using DFT with (full line) and without (dotted line) local field effects and experimentally (square) for an in-plane momentum $k = 0.44$ Å^{-1}. Reproduced from [103].

The loss spectrum for an in-plane momentum $k = 0.30$ Å^{-1} is represented on figure 2.1. Two main peaks corresponding to the π-plasmon and the $\pi + \sigma$ plasmon are observed, respectively around 7 eV and 29 eV. Neglecting local field effects is a valid approximation in this case because the material is homogeneous along the atomic plane. This graph is consistent with other DFT theoretical and experimental results. For example in [103], they compared experimental loss spectra with DFT calculation with and without local field effects (see fig. 2.2) for an in-plane momentum $k = 0.44$ Å^{-1}. The same feature appears around 25 eV, in particular without the local field effects.

The eigenmode decomposition of the dielectric function is performed to obtain the modes individual dielectric functions $\varepsilon_i^{\parallel}$, loss functions $L_i^{\parallel}$ and weight $w_i^{\parallel}$ (figure 2.3). Only two modes have a non vanishing weight. Moreover, at a given frequency, there is only one dominant mode whose weight is close to 1 as expected when there is no local field effects. The first mode is dominant below 7 eV and the second mode is dominant beyond 7 eV. From the individual loss function, compared to the total loss function of figure 2.1, it can be seen that these modes correspond respectively to the π and $\pi + \sigma$

plasmons. As suggested by eq. (2.123), the total loss function is directly the sum of the individual loss functions of the two modes. The real part of the modes dielectric functions crosses zero close to the resonance energy, describing a curve as predicted by the Drude-Lorentz formula given in chapter 1.

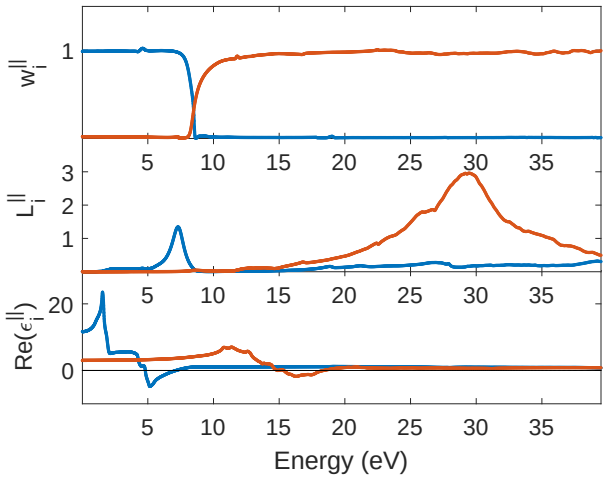

Figure 2.3: Weight, loss function and real part of the dielectric function for the two main modes of graphite in the direction parallel to the layers.

Polarization parallel to the optical axis

The loss spectrum is quite different in this direction due to the strong anisotropy of graphite (figure 2.4). A large peak stands around 18 eV. The local fields effects are significant here because of the layered structure of graphite. In particular the local field effects tend to decrease the loss response at this peak.

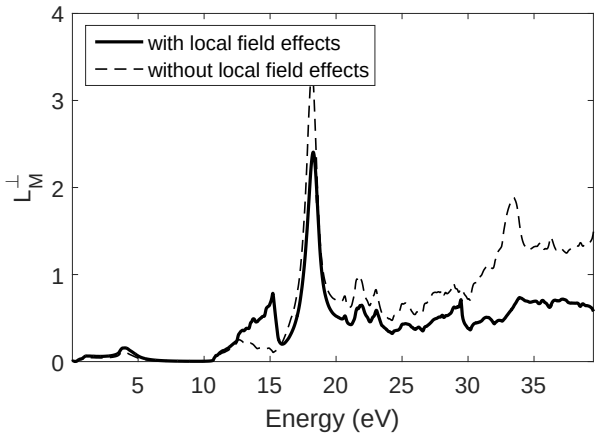

Figure 2.4: Loss function of graphite with and without local field effects in the direction perpendicular to the layers.

The eigenmode decomposition confirms that, at a given wavelength, few modes

contribute to the macroscopic loss function over a total of about 1500 modes. Some of these modes exhibit a peak in the loss spectrum but only a few of them have the real part of the dielectric function crossing zero. A mode which have a peak in the loss spectrum without having the real part of the dielectric function crossing zero will now be referred as a quasi-plasmon mode. Here, 6 modes have a non negligible weight in the relevant range, however only 3 modes which contribute to the peak at 18 eV are plotted for clarity (figure 2.5). The mode shown as dotted blackened on figure 2.5 exhibits a high loss function but, as its weight is negligible, this mode does not contribute to the macroscopical optical spectra. In consequence, the peak around 18 eV in the total loss spectra is due to the other modes (in orange and yellow on figure 2.5).

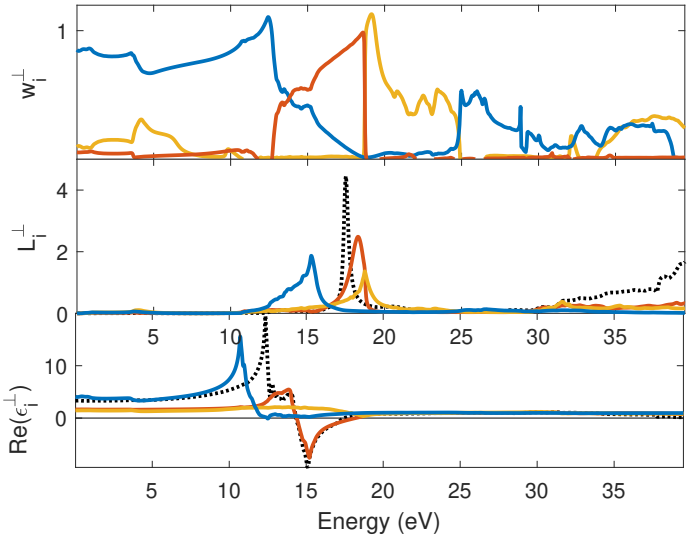

Figure 2.5: Weight, loss function and real part of the dielectric function for the two main modes of graphite in the direction perpendicular to the layers.

In conclusion this example confirms that this method is efficient to discriminate plasmons in materials and nanostructures.

Separation of bound and free charges

In textbooks of eletrodynamics, the macroscopic Maxwell equations separate the contribution of bound charges and free charges in a material. In particular, Gauss's law and Ampère's law can be written in terms of the density of free charges ρ_f and the current density of free charges $\mathbf{J}_f$:

$$\nabla \cdot \mathbf{D} = \rho_f, \tag{2.126}$$

$$\nabla \times \mathbf{H} = \mathbf{J}_f + \frac{\partial \mathbf{D}}{\partial t}, \tag{2.127}$$

while the polarization density $\mathbf{P}_b$ relates only to the bound charges ρ_b:

$$\nabla \cdot \mathbf{P}_b = -\rho_b, \tag{2.128}$$

with the constitutive equation

$$\mathbf{D} = \varepsilon_0 \mathbf{E} + \mathbf{P}_b. \tag{2.129}$$

With these equations, the relative permittivity is

$$\varepsilon = 1 + \chi_b, \tag{2.130}$$

where the susceptibility χ_b is related to the behavior of the bound charges via the polarization density

$$\mathbf{P}_b = \varepsilon_0 \chi_b \mathbf{E}. \tag{2.131}$$

In brief, with the relation (2.130), the permittivity defined as such only accounts for the bound electrons. In order to include the contributions of the free electrons to the permittivity, the constitutive equation (2.129) is rewritten [98]:

$$\mathbf{D} = \varepsilon_0 \mathbf{E} + \mathbf{P}_b + \int \mathbf{J}_f dt, \tag{2.132}$$

with $\mathbf{J}_f = \sigma_f \mathbf{E}$ such that

$$\varepsilon = 1 + \chi_b + i\frac{\sigma_f}{\varepsilon_0 \omega}. \tag{2.133}$$

This approach, which consists in accounting for bound electrons in the susceptibility χ_b and for the free electrons in the conductivity σ_f , has drawbacks. First, in the beginning of this section, it was shown that the permittivity can be calculated from the microscopic dielectric function that does not discriminates bound and free electrons. The response of all electrons is included in the susceptibility. In some physical system, this separation is even ambiguous, if not arbitrary. In covalent materials, the electrons are delocalized and the bound charges cannot simply be described as dipoles. In another extreme case, the π electrons of graphene behave like free electrons in the plane but are necessarily bound in the plane when the electric field is perpendicular to the sheet. For metamaterials, the free electrons of metallic components and particles embedded in a dielectric medium can also be considered as bound to their particles.

Another approach is to consider that the polarization density and the current density are equivalent quantities that can represent all charges. The first one relates to the position of the charges while the second relates to the velocity of the charges. To have a better insight on this, we can look at the average of the polarization density and the current density over the unit cell Ω :

$$\mathbf{P}_b = \frac{1}{V} \int_\Omega \rho_b (\mathbf{r})\, \mathbf{r}\, d\mathbf{r}, \tag{2.134}$$

$$\mathbf{J}_f = \frac{1}{V} \int_\Omega \rho_f (\mathbf{r})\, \mathbf{v} (\mathbf{r})\, d\mathbf{r}. \tag{2.135}$$

To the polarizability of bound charges is associated a current density of bound charge $\mathbf{J}_b$:

$$\mathbf{J}_b = \frac{\partial \mathbf{P}_b}{\partial t} = \frac{-i}{V} \int_\Omega \rho_b (\mathbf{r})\, \mathbf{r}\omega\, dV, \tag{2.136}$$

$$\mathbf{J}_b = \frac{-i}{V} \int_\Omega \rho_b (\mathbf{r})\, \mathbf{v}_b (\mathbf{r})\, dV, \tag{2.137}$$

with $\mathbf{v}_b = \mathbf{r}\omega$ is a velocity associated to bound charges for harmonic fields oscillating at ω. The bound electron current is similar to a free electron current, but is out of phase with the excitation field. Similarly, to the current density of free charge one associates a polarization density $\mathbf{P}_f$:

$$\mathbf{P}_f = \int \mathbf{J}_f dt = \frac{i}{V}\int_\Omega \rho_f(\mathbf{r})\frac{\mathbf{v}}{\omega}dV, \tag{2.138}$$

$$\mathbf{P}_f = \frac{i}{V}\int_\Omega \rho_f(\mathbf{r})\,\mathbf{d}_f dV, \tag{2.139}$$

with $\mathbf{d}_f = \frac{\mathbf{v}}{\omega}$ the distance travelled by the free electrons during a time period of the oscillating fields. The free electron polarization is similar to a bound electron polarizability but is out of phase with the excitation field. Note that the notion of bound electron current and free electron polarization still make sense. As bound charges are moving, a current can really be associated to them. On the other hand, a dipole is defined using the relative distance between charges such that even free electrons can be assigned a polarization density. With $\mathbf{P} = \mathbf{P}_f + \mathbf{P}_b$ and $\mathbf{J} = \mathbf{J}_f + \mathbf{J}_b$, one can either choose to write eq. (2.132) as

$$\mathbf{D} = \varepsilon_0\mathbf{E} + \mathbf{P}, \tag{2.140}$$

or

$$\mathbf{D} = \varepsilon_0\mathbf{E} + \int \mathbf{J}dt, \tag{2.141}$$

which corresponds respectively to these permittivities:

$$\varepsilon = 1 + \chi^{all}, \tag{2.142}$$

$$\varepsilon = 1 + i\frac{\sigma^{all}}{\varepsilon_0\omega}, \tag{2.143}$$

where χ^{all} and σ^{all} are the susceptibility and conductivity due to all the electrons. To describe a material, one can then choose between conductivity or susceptibility as far as they are defined in this way. For a metal, the conductivity should be obviously the convenient choice. However, it would not be a convenient choice for the study of 2D materials, even for conducting materials such as graphene, see fig 2.6. For 2D materials, a surface conductivity is sometimes defined such that it does not depend on the arbitrary choice of the thickness d: $\sigma_s = \sigma/d$. Thus a surface current density $\mathbf{J}_s$ (of unit $\mathrm{Am^{-1}}$) is defined:

$$\mathbf{J}_s = \mathbf{J}d = \sigma_s\mathbf{E}, \tag{2.144}$$

with an easy interpretation: it is the current $\mathbf{I}$ going through a unit length perpendicular to the flow of charges in the 2D sheet (see figure 2.6a):

$$\mathbf{J}_s = \mathbf{J}d = \frac{\mathbf{I}}{hd}d = \frac{\mathbf{I}}{h}. \tag{2.145}$$

But this new concept breaks apart when considering fields perpendicular to the sheet. Indeed, we have (see figure 2.6b):

$$\mathbf{J}_s = \mathbf{J}d = \frac{\mathbf{I}}{S}d, \tag{2.146}$$

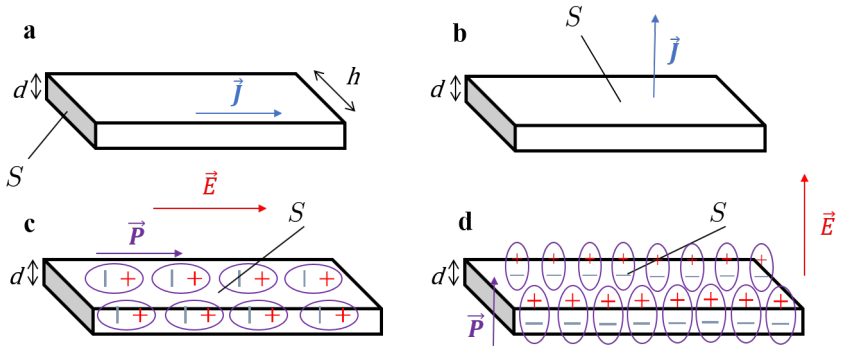

Figure 2.6: Representation of a,b) the 2D density current and c,d) the 2D polarization density for applied electric fields a,c) parallel and b,d) perpendicular to the 2D material.

which is hardly intuitive. The polarization density however has a 2D counterpart which is just the number of dipole moment by unit area, and this definition holds for all direction of the fields (see figure 2.6c and d): $\mathbf{P}_s = \mathbf{P}d = \varepsilon_0 \chi_S \mathbf{E}$ with $\chi_S = \chi d$.

For these reasons, at least in section involving the anisotropy of graphene, the choice of the susceptibility (eq. (2.142)) rather than the conductivity, is preferably used in the thesis.

2.3 The local response approximation

For systems that are larger than a few nanometers in size, quantum calculations are impossible. Most optical calculations of classical systems are performed using the framework of the local response approximation. In this approximation, one assumes that the electric field varies slowly in the near vicinity of $\mathbf{r}$. Using a Taylor expansion of $\mathbf{E}_{tot}$ around $\mathbf{r}$, eq. (2.7) writes, for $\mathbf{r}'$ close to $\mathbf{r}$:

$$\mathbf{E}_{app}(\mathbf{r}) = \int \varepsilon(\mathbf{r}, \mathbf{r}')\, d\mathbf{r}'\, \mathbf{E}_{tot}(\mathbf{r}), \tag{2.147}$$

or, equivalently

$$\mathbf{E}_{app}(\mathbf{r}) = \varepsilon^M(\mathbf{r})\, \mathbf{E}_{tot}(\mathbf{r}), \tag{2.148}$$

with ε^M the macroscopic permittivity of the material at $\mathbf{r}$. This approximation is valid as long as there are no interfaces between different materials. Indeed, such interfaces are responsible for high gradients of electric field due to the change of permittivity and the Taylor expansion is not valid anymore. To study complex systems with different materials, a second approximation is implicitly taken: the interfaces between different materials are infinitely thin and the local response approximation can be applied on both sides infinitely close to the interfaces. In the equations, it can be translated to the definition of a local dielectric function $\tilde{\varepsilon}(\mathbf{r})$ which, at a particular point $\mathbf{r}$, is equal to the macroscopic dielectric function of the (homogeneous) material at this point. The local dielectric function is thus defined in a piecewise manner :

$$\tilde{\varepsilon}(\mathbf{r}) = \sum \varepsilon_i \Omega_i(\mathbf{r}) \tag{2.149}$$

where $\Omega_i(\mathbf{r})$ is the Boolean function equal to 1 in the regions of the system where $\tilde{\varepsilon}(\mathbf{r}) = \varepsilon_i$ and 0 elsewhere. However, this local dielectric function is fundamentally different from the microscopic dielectric function of the system which relates the applied field to the total field at every point in space (equation (2.11)). Instead, it relates the local displacement field to the local total field ($\mathbf{D} = \varepsilon\mathbf{E}$) but the displacement field does not correspond to the external applied field anymore as it accounts for the fields induced by the charges at the interfaces between different materials. In practice, the local dielectric function is used to treat the boundary conditions, which allows us to calculate the surface charge and surface current densities. Once the densities are known, the total potentials or fields are calculated from Coulomb's law.

Here, a new classical method is presented, using a similar development than the derivation of the microscopic dielectric function, in order to illustrate how the local dielectric function is used to calculate total fields of macroscopic system. Here the media are assumed isotropic such that the local dielectric function is a scalar. First, let us note that, with the updated constitutive equation (2.132), we have:

$$\nabla \cdot \mathbf{D} = \rho - \rho_b - \rho_f = 0, \tag{2.150}$$

by virtue of the continuity equation $\nabla \cdot \mathbf{J_f} = -\frac{\partial \rho_f}{\partial t}$, of eq. (2.128), and of the microscopic Gauss's law, $\nabla \cdot \mathbf{E} = \frac{\rho_b + \rho_f}{\varepsilon_0} = \frac{\rho}{\varepsilon_0}$. Therefore, eq. (2.126) does not stand anymore. Developing the displacement field, one can isolate the charge density:

$$\nabla \cdot (\varepsilon_0 \varepsilon \mathbf{E}) = 0, \tag{2.151}$$

$$\varepsilon_0 \nabla\varepsilon \cdot \mathbf{E} + \varepsilon\rho = 0, \tag{2.152}$$

$$\rho(\mathbf{r}) = -\varepsilon_0 \frac{\nabla\varepsilon}{\varepsilon} \cdot \mathbf{E}. \tag{2.153}$$

For sharp boundaries, the dielectric function can be described by some kind of Heaviside function, whose gradient is the Dirac function: it confirms that charges are located at the boundaries. It is possible to have a smoother transition by replacing the Heaviside function with a sigmoïde function. For example, the transition along the direction x, between two media with respective permittivity ε_a and ε_b can be expressed by the dielectric function:

$$\varepsilon(x) = \frac{\varepsilon_b - \varepsilon_a}{1 + e^{-\eta x}} + \varepsilon_a, \tag{2.154}$$

with η the smoothing parameters: the larger η the sharper the boundary.

For a sphere of radius r_s and of permittivity ε_b in a medium of permittivity ε_a, a radial form of the function may be used

$$\varepsilon(r) = \frac{\varepsilon_b - \varepsilon_a \left(\frac{r_s}{r}\right)^\eta}{1 + \left(\frac{r_s}{r}\right)^\eta}, \tag{2.155}$$

and the term $\frac{\nabla\varepsilon}{\varepsilon}$ becomes:

$$\frac{\nabla\varepsilon}{\varepsilon} = \frac{(\varepsilon_b - \varepsilon_a)\,\eta r^{-1}}{(r^\eta + r_s^\eta)(\varepsilon_b + \varepsilon_a r_s^\eta r^{-\eta})}\mathbf{e}_r, \tag{2.156}$$

with $\mathbf{e}_r$ the radial unit vector.

Replacing (2.153) in the Coulomb potential, it comes for the induced potential:

$$V_{ind}(\mathbf{r}) = -\frac{1}{4\pi\varepsilon_0}\int \frac{1}{|\mathbf{r}-\mathbf{r}'|}\varepsilon_0\frac{\nabla\varepsilon(\mathbf{r}')}{\varepsilon(\mathbf{r}')}\cdot\mathbf{E}_{tot}(\mathbf{r}')\,d\mathbf{r}', \tag{2.157}$$

and for the induced electric fields:

$$\mathbf{E}_{ind}(\mathbf{r}) = \frac{1}{4\pi\varepsilon_0}\int \nabla_{\mathbf{r}}\frac{1}{|\mathbf{r}-\mathbf{r}'|}\varepsilon_0\frac{\nabla\varepsilon(\mathbf{r}')}{\varepsilon(\mathbf{r}')}\cdot\mathbf{E}_{tot}(\mathbf{r}')\,d\mathbf{r}', \tag{2.158}$$

$$\mathbf{E}_{ind}(\mathbf{r}) = \frac{1}{4\pi\varepsilon_0}\int \frac{(\mathbf{r}-\mathbf{r}')}{|\mathbf{r}-\mathbf{r}'|^3}\varepsilon_0\frac{\nabla\varepsilon(\mathbf{r}')}{\varepsilon(\mathbf{r}')}\cdot\mathbf{E}_{tot}(\mathbf{r}')\,d\mathbf{r}'. \tag{2.159}$$

By identification with the definition of the microscopic irreducible susceptibility (2.43) one have:

$$\bar{\chi}(\mathbf{r},\mathbf{r}') = -\frac{1}{4\pi|\mathbf{r}-\mathbf{r}'|^3\varepsilon(\mathbf{r}')}(\mathbf{r}-\mathbf{r}')\nabla\varepsilon(\mathbf{r}'), \tag{2.160}$$

with $(\mathbf{r}-\mathbf{r}')\nabla\varepsilon(\mathbf{r}')$ a dyadic product such that the tensor components can be written:

$$\chi_{i,j}(\mathbf{r},\mathbf{r}') = -\frac{1}{4\pi|\mathbf{r}-\mathbf{r}'|^3\varepsilon(\mathbf{r}')}((\mathbf{r}-\mathbf{r}')\cdot e_i)(\nabla\varepsilon(\mathbf{r}')\cdot e_j). \tag{2.161}$$

From the irreducible susceptibility, the tensor elements of the effective dielectric function of the system may be calculated:

$$\varepsilon_{i,j}(\mathbf{r},\mathbf{r}') = 1 + \chi_{i,j}(\mathbf{r},\mathbf{r}'). \tag{2.162}$$

This dielectric function can be inverted to find the microscopic inverse dielectric function. Then, from eq. (2.11) ,

$$\mathbf{E}_{tot}(\mathbf{r}) = \bar{\varepsilon}^{-1}(\mathbf{r})\,\mathbf{E}_{app} \tag{2.163}$$

the total electric field can be calculated. In brief, the method describing the derivation of the microscopic dielectric function is general and can also be applied to larger systems to calculate the effective dielectric function of a complex system. In practice, this method is inefficient because it requires to discretize all the space. State-of-the-art methods available are far more efficient as they benefit from large optimization. Moreover, they often rely on a discretization of either only the volume of the particle or the surface of the particle.

Effective medium theory for multilayers

When the size of periodic structure in a material is small enough compared to the wavelength in the medium, generally around 10 times smaller, one can consider that the applied electric field is constant over the structure. In the same way that a macroscopic permittivity can be found for homogeneous materials, an effective permittivity can be calculated for such materials. This is the principle of optical metamaterials whose refractive index can be designed at wish using structured materials. When the dielectric

function $\varepsilon_{i,j}(\mathbf{r},\mathbf{r}')$ is known, as exemplified in the last paragraph, one uses eq. (2.99) to calculate the effective permittivity. For example, in periodically layered system, it has been shown rigorously that the effective permittivities of the system is [104]:

$$\varepsilon_{eff}^{\parallel} = \sum_i \frac{d_i}{L}\varepsilon_i, \tag{2.164}$$

$$\frac{1}{\varepsilon_{eff}^{\perp}} = \sum_i \frac{d_i}{L}\frac{1}{\varepsilon_i}, \tag{2.165}$$

where the superscripts $\perp$ and $\parallel$ respectively means that the electric field is perpendicular or parallel to the layer, d_i is the thickness of each layer of the unit cell and L its total thickness. Interestingly, using the irreducible and the external susceptibilities $\chi_{eff}^{\parallel} = \varepsilon_{eff}^{\parallel} - 1$ and $\xi_{eff}^{\perp} = 1 - \frac{1}{\varepsilon_{eff}^{\perp}}$, one can write the previous two equations as

$$\chi_{eff}^{\parallel} = \sum_i \frac{d_i}{L}\chi_i^{\parallel}, \tag{2.166}$$

$$\xi_{eff}^{\perp} = \sum_i \frac{d_i}{L}\xi_i^{\perp}. \tag{2.167}$$

The external susceptibility is revealed to be an adequate tool to study the out-of-plane component of the fields in layered materials. In particular, it will play an important role in the description of 2D materials.

These relations can be determined by considering the boundary conditions at interfaces. For a polarization that is tangential to the interfaces, the electric fields must by conserved at the interfaces. As the field can thus be considered constant everywhere, the effective irreducible susceptibility is:

$$\chi_{eff}^{\parallel} = \frac{\langle P^{\parallel}\rangle}{\varepsilon_0\langle E^{\parallel}\rangle} = \frac{\sum_i f_i P_i^{\parallel}}{\varepsilon_0 E^{\parallel}} = \sum_i \frac{d_i}{L}\frac{P_i^{\parallel}}{\varepsilon_0 E_i^{\parallel}} = \sum_i \frac{d_i}{L}\chi_i^{\parallel}, \tag{2.168}$$

where f_i is the filling fraction of the layer i in the unit cell and $E^{\parallel} = E_i^{\parallel}$ for each layer i due to the conservation of the tangential field. Similarly, for a polarization perpendicular to the layers, the displacement field is conserved at the interfaces and is thus constant in the unit cell. The external susceptibility is then, from eq. (2.101),

$$\xi_{eff}^{\perp} = \frac{\langle P^{\perp}\rangle}{\langle D^{\perp}\rangle} = \frac{\sum_i f_i P_i^{\perp}}{D^{\perp}} = \sum_i \frac{d_i}{L}\frac{P_i^{\perp}}{D_i^{\perp}} = \sum_i \frac{d_i}{L}\xi_i^{\perp}, \tag{2.169}$$

with $D^{\perp} = D_i^{\perp}$ for each layer i. Equations (2.164) and (2.165) can be retrieved by the same reasoning.

These effective models may be generalized in the case of continuous variations of the dielectric function. Indeed with $d_i \to 0$, eq. (2.164) and (2.165) becomes

$$\varepsilon_{eff}^{\parallel} = \frac{1}{L}\int \varepsilon(x)\,dx, \tag{2.170}$$

and

$$\frac{1}{\varepsilon_{eff}^{\perp}} = \frac{1}{L}\int \frac{1}{\varepsilon\left(x\right)}dx, \tag{2.171}$$

if the dielectric function varies along x.

These effective models are useful to study complex systems whose characteristic sizes are much smaller than the wavelength. However, plasmonic resonances cannot be captured by such approximations. Due to this limitations this method is restricted to few interesting systems. In general, one needs a complete method to calculate the fields. Some of these methods are presented in the next chapter.

Chapter 3

Numerical methods for optics

The theoretical study of nanomaterials and nanoparticles requires adapted tools, that depends on the geometry and the size of the considered system. In particular, 2D materials are anisotropic and their low dimensionality makes their modelling more complex. Particular care is therefore needed in the choice of the methods. The aim of this chapter is to present the various, state-of-the-art, methods used throughout this thesis. The rigorous coupled wave analysis allows to study stratified media containing periodic structures. In the discrete dipole approximation, nanoparticles are discretized into dipoles. The surface integral equation method consists to discretize the surface of a nanoparticle which is generally much faster than a volume discretization.

3.1 Rigorous coupled wave analysis for anisotropic media

The rigorous coupled wave analysis is a method developed first in 1981 by M. Moharam and T. Gaylord [105, 106] to study inhomogeneous layered structures. Each layer is homogeneous in its normal direction but periodically structured in the in-plane direction. A MATLAB implementation of this method has been developed by Pr. O. Deparis [107]. Although this method is able to characterize the structural anisotropy of layered materials, the original description does not account for the intrinsic anisotropy of the components themselves. Recent papers proposed an anisotropic version of the RCWA [108, 109]. In parallel, master student E. Guillaume developed its own version of the anisotropic RCWA under supervision of Pr. L. Henrard and myself [110]. This anisotropic version is particularly interesting when studying structured 2D materials for which the anisotropy in the out-of-plane direction cannot be ignored. In the following, I briefly describe the basic principles of the RCWA method with a highlight on the modification of the method for anisotropic media. This section is highly inspired from E. Guillaume master thesis [110] and from O. Deparis course on photonics [111].

If the layered system is stratified along the z axis (figure 3.1), only anisotropic materials whose dielectric tensor can be written as follows are considered [1]:

$$\bar{\varepsilon} = \begin{pmatrix} \varepsilon_{xx} & \varepsilon_{xy} & 0 \\ \varepsilon_{yx} & \varepsilon_{yy} & 0 \\ 0 & 0 & \varepsilon_{zz} \end{pmatrix}$$

The periodicity of the dielectric function in a layer implies

$$\varepsilon^{(i,j)}\left(\vec{r}_{\parallel}\right) = \varepsilon^{(i,j)}\left(\vec{r}_{\parallel} + \vec{R}_{\parallel}\right) \tag{3.1}$$

with $\varepsilon^{(i,j)}$ the element i, j of the tensor, $\vec{r}_{\parallel} = (x, y)$ and $\vec{R}_{\parallel}$ is a translation vector of the periodic lattice. Inside the unit cell, the dielectric function consists of a host medium within which islands of different shapes and permittivities are included:

$$\varepsilon^{(i,j)}\left(\vec{r}_{\parallel}\right) = \varepsilon_h^{(i,j)} + \sum_l \left(\varepsilon_l^{(i,j)} - \varepsilon_h^{(i,j)}\right) \Omega^{(l)}\left(\vec{r}_{\parallel}\right) \tag{3.2}$$

[1] This makes sense as the optical axis is often either parallel or perpendicular to the plane.

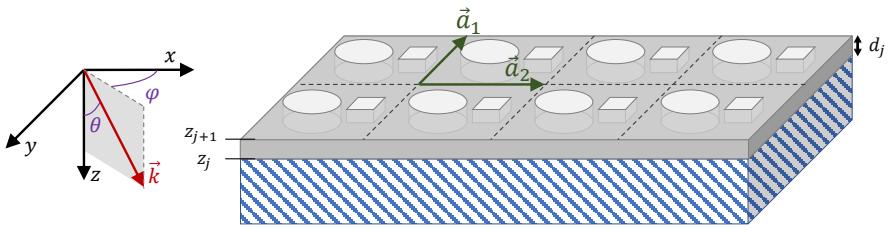

Figure 3.1: Schematic view of a laterally structured layered material. Reproduced from E. Guillaume master thesis [110].

where $\Omega^{(l)}$ is a Boolean function describing the geometry of the island, $\varepsilon_h^{(i,j)}$ the permittivity of the host medium and $\varepsilon_l^{(i,j)}$ the permittivity of the island. The bidimensionnal Fourier series of $\Omega^{(l)}$ is

$$\Omega^{(l)}\left(\vec{r}\right) = \sum_{\vec{g}}^{n_g} \Omega_{\vec{g}}^{(l)} e^{i\vec{g}\cdot\vec{r}} \tag{3.3}$$

where $\vec{g}$ is a vector of the reciprocal lattice and n_g gives the number of $\vec{g}$ vectors in the sum. The Fourier series of the dielectric function of a layer is then written

$$\varepsilon_g^{(i,j)} = \varepsilon_h^{(i,j)}\delta_{g,g_0} + \sum_l \left(\varepsilon_l^{(i,j)} - \varepsilon_h^{(i,j)}\right)\Omega_g^{(l)} \tag{3.4}$$

where g_0 is the 0th order term of the Fourier series.

From Maxwell's equations, one finds the following system of coupled equations:

$$\begin{aligned}
\frac{dE_{x,g}}{dz} &= \frac{i}{\omega\varepsilon_0}\left(k_x + g_x\right)\left[\sum_{g''}\left.\frac{1}{\varepsilon^{(zz)}}\right|_{g-g''}\left[H_{x,g''}\left(k_y + g_y''\right) - H_{y,g''}\left(k_x + g_x''\right)\right]\right] + i\omega\mu_0 H_{y,g} \\
\frac{dE_{y,g}}{dz} &= \frac{i}{\omega\varepsilon_0}\left(k_y + g_y\right)\left[\sum_{g''}\left.\frac{1}{\varepsilon^{(zz)}}\right|_{g-g''}\left[H_{x,g''}\left(k_y + g_y''\right) - H_{y,g''}\left(k_x + g_x''\right)\right]\right] - i\omega\mu_0 H_{x,g} \\
\frac{dH_{x,g}}{dz} &= \frac{i}{\omega\mu_0}\left(k_x + g_x\right)\left[E_{y,g}\left(k_x + g_x\right) - E_{x,g}\left(k_y + g_y\right)\right] - i\omega\varepsilon_0\sum_{g''}\left(\left.\varepsilon^{(yx)}\right|_{g-g''} E_{x,g''} + \left.\varepsilon^{(yy)}\right|_{g-g''} E_{y,g''}\right) \\
\frac{dH_{y,g}}{dz} &= \frac{i}{\omega\mu_0}\left(k_y + g_y\right)\left[E_{y,g}\left(k_x + g_x\right) - E_{x,g}\left(k_y + g_y\right)\right] + i\omega\varepsilon_0\sum_{g''}\left(\left.\varepsilon^{(xx)}\right|_{g-g''} E_{x,g''} + \left.\varepsilon^{(xy)}\right|_{g-g''} E_{y,g''}\right).
\end{aligned} \tag{3.5}$$

Compared to the isotropic case, the diagonal components of the permittivity tensor replace the scalar permittivity appropriately, while the out-of-diagonal components are responsible for another coupling between the fields. There is thus coupling of the fields due to the intrinsic anisotropy of the materials and coupling due to the structural anisotropy.

The system of equations (3.5) must be solved simultaneously for all components. This system can be written in the form:

$$\frac{d\bar{\mathbf{F}}}{dz} = A\bar{\mathbf{F}}, \text{with } \bar{\mathbf{F}} = \begin{pmatrix} \bar{\mathbf{E}}_x \\ \bar{\mathbf{E}}_y \\ \bar{\mathbf{H}}_x \\ \bar{\mathbf{H}}_y \end{pmatrix} \tag{3.6}$$

where $\bar{\mathbf{E}}_x$, $\bar{\mathbf{E}}_y$, $\bar{\mathbf{H}}_x$, $\bar{\mathbf{H}}_y$ are supervectors containing all the Fourier components of the fields. The solution relates the fields in the layer j to the fields in the layer $j-1$:

$$\bar{\mathbf{F}}(z_{j-1}) = e^{A(z_{j-1}-z_j)}\bar{\mathbf{F}}\left(z_j\right) \tag{3.7}$$

or also:

$$\bar{\mathbf{F}}(z_{j-1}) = \mathbf{T}_j\bar{\mathbf{F}}\left(z_j\right) \tag{3.8}$$

where $\mathbf{T}_j$ is the transfer matrix of the layer j [2]. The transfer matrix of the N layers embedded between an incident medium and a substrate is found by multiplying the transfer matrix altogether:

$$\bar{\mathbf{F}}^{inc} = \mathbf{T}_1\mathbf{T}_2...\mathbf{T}_N\bar{\mathbf{F}}^{sub} = \mathbf{T}\bar{\mathbf{F}}^{sub}. \tag{3.9}$$

This global transfer matrix $\mathbf{T}$ relates the fields in the incident medium (incident $\mathbf{i}^+$ and reflected $\mathbf{r}^-$) to the field in the substrate (incident $\mathbf{i}^-$ and refracted $\mathbf{t}^+$) in the polarisation basis:

$$\begin{bmatrix} \mathbf{i}^+ \\ \mathbf{r}^- \end{bmatrix} = \begin{bmatrix} \mathbf{T}^{++} & \mathbf{T}^{+-} \\ \mathbf{T}^{-+} & \mathbf{T}^{--} \end{bmatrix} \begin{bmatrix} \mathbf{t}^+ \\ \mathbf{i}^- \end{bmatrix}. \tag{3.10}$$

It is however more intuitive, and more stable numerically, to use the scattering matrix $\mathbf{S}_j$ of each layer:

$$\begin{bmatrix} \mathbf{t}^+ \\ \mathbf{r}^- \end{bmatrix} = \begin{bmatrix} \mathbf{S}_j^{++} & \mathbf{S}_j^{+-} \\ \mathbf{S}_j^{-+} & \mathbf{S}_j^{--} \end{bmatrix} \begin{bmatrix} \mathbf{i}^+ \\ \mathbf{i}^- \end{bmatrix} \tag{3.11}$$

where the elements of $\mathbf{S}_j$ depend on the elements of $\mathbf{T}_j$. The scattering matrices are then assembled together to form the diffusion matrix of the complete multilayer system using the Pendry "multiplication". Once the fields are known in the incident medium and in the substrate, one can calculate the electromagnetic flux of the incident, reflected and transmitted waves, respectively $\mathbf{J}^+_{inc}$, $\mathbf{J}^-_{inc}$, $\mathbf{J}^+_{sub}$. The total reflectance and transmittance coefficient are then given by:

$$R_{tot} = \left| \frac{\mathbf{J}^-_{inc}}{\mathbf{J}^+_{inc}} \right| \tag{3.12}$$

$$T_{tot} = \left| \frac{\mathbf{J}^+_{sub}}{\mathbf{J}^+_{inc}} \right| \tag{3.13}$$

and the absorptance is then given by

$$A_{tot} = 1 - R_{tot} - T_{tot}. \tag{3.14}$$

Other quantities, like the specular reflectance and transmittance, the local fields and the Stokes vectors can also be calculated. In this thesis, only the total intensity coefficients R, T and A are used.

3.2 The discrete dipole approximation

The discrete dipole approximation (DDA) is a method developped first by Purcell and Pennypacker in 1973 [112] and then by Draine and Flatau in 1994 [113], who developed the program *ddscat* that calculates the field scattered by a group of dipoles of given polarizability. In 2010, Nicolas Geuquet developed the program *ddeels* under the supervision of L. Henrard in order to obtain the EELS spectra of nanoparticles [114]. Both programs have been used in this thesis.

[2] In practice, the fields are expressed in a basis of polarisation of the incident field, and an orthogonal transformation must be applied to $\mathbf{T}$ and $\bar{\mathbf{F}}$.

In the DDA, a nanoparticle is discretized in a large number (N) of dipoles such that the distance between two dipoles d is much smaller than the wavelength. The criteria often retain is :

$$|n|\, kd < 0.5 \tag{3.15}$$

with $|n|$ the modulus of refractive index of the material of the particle and k the wavenumber. The dipolar moment $\mathbf{P}_i$ of a dipole is proportional to the local field at its position : $\mathbf{E}_i^{loc} = \mathbf{E}^{loc}(\mathbf{r}_i)$:

$$\mathbf{P}_i = \alpha_i \mathbf{E}_i^{loc} \tag{3.16}$$

with α_i the polarizability of the dipole. This polarizability can be described by a Clausius-Mossotti-like formula for a dipole of cubic volume d^3 and permittivity $\varepsilon = n^2$. The field induced by a dipole j on the dipole i, $\mathbf{E}_{i,j}^{ind}$ is

$$\mathbf{E}_i^{ind} = -\frac{e^{ikr_{ij}}}{r_{ij}^3}\left(k^2 \mathbf{r}_{ij} \times (\mathbf{r}_{ij} \times \mathbf{P}_i) + \frac{(1 - ikr_{ij})}{r_{ij}^2}\left(r_{ij}^2 \mathbf{P}_i - 3\mathbf{r}_{ij}\,(\mathbf{r}_{ij} \cdot \mathbf{P}_i)\right)\right) \tag{3.17}$$

with $\mathbf{r}_{ij} = \mathbf{r}_j - \mathbf{r}_i$. The previous equation can be expressed as a matrix product:

$$\mathbf{E}_i^{ind} = \sum_{j \neq i} \mathbf{A}_{ij} \mathbf{P}_j. \tag{3.18}$$

The local field is the sum of the applied field $\mathbf{E}_i^{app}$ and the fields induced by the $N-1$ other dipoles such that the dipolar moment becomes

$$\mathbf{P}_i = \alpha_i \left(\mathbf{E}_i^{app} + \sum_{j \neq i} \mathbf{A}_{ij} \mathbf{P}_j\right). \tag{3.19}$$

By defining $\mathbf{A}_{ii} = \alpha_i$, one have an set of N inhomogeneous linear equations:

$$\sum_{j}^{N} \mathbf{A}_{ij} \mathbf{P}_j = \mathbf{E}_i^{app}. \tag{3.20}$$

For optical calculation, as in *ddscat*, the applied field is in the form of a plane wave:

$$\mathbf{E}_i^{app} = \mathbf{E}_0 e^{(i\mathbf{k}\cdot\mathbf{r}_i - i\omega t)} \tag{3.21}$$

and the optical extinction cross section is

$$C_{ext} = \frac{4\pi k}{|\mathbf{E}^{app}|^2} \sum_{j}^{N} Im\left(\mathbf{E}_j^{app,*} \cdot \mathbf{P}_j\right). \tag{3.22}$$

For electron energy loss spectroscopy simulation as in *ddeels*, with an electron trajectory along the z-axis, the applied field is in the form:

$$E_{i,x}^{app} = \frac{e\omega}{2\pi\varepsilon_0 v^2} e^{\left(i\omega \frac{z_i}{v}\right)} \frac{d_{i,x}}{d_i} K_1\left(\frac{\omega d_j}{v}\right); \tag{3.23}$$

$$E_{i,y}^{app} = \frac{e\omega}{2\pi\varepsilon_0 v^2} e^{\left(i\omega \frac{z_i}{v}\right)} \frac{d_{i,y}}{d_i} K_1\left(\frac{\omega d_j}{v}\right); \tag{3.24}$$

$$E_{i,z}^{app} = \frac{e\omega}{2\pi\varepsilon_0 v^2} e^{\left(i\omega\frac{z_i}{v}\right)} iK_0\left(\frac{\omega d_j}{v}\right). \tag{3.25}$$

with K_m is the modified Bessel function of order m and v the electron velocity. The energy loss probability of the electron is

$$\Gamma(\omega) = \frac{1}{\pi\hbar^2}\sum_j^N Im\left(\mathbf{E}_j^{app,*}\cdot\mathbf{P}_j\right). \tag{3.26}$$

Remarkably, this loss probability is somehow similar to the loss spectra $L(\omega)$ obtained from eq. (2.93). To observe this, an appropriate external polarizability α_j^e can be written for each dipoles as follows

$$\mathbf{P}_j = \alpha_j^e \mathbf{E}_j^{app} \tag{3.27}$$

and the previous equation becomes

$$\Gamma(\omega) = \frac{1}{\pi\hbar^2} Im\left(\sum_j^N \alpha_j^e\right)\left|\mathbf{E}_i^{app}\right|^2. \tag{3.28}$$

The loss spectra is indeed proportional to the imaginary part of the external polarizability of the whole system, in a way analogous to what has been shown for the external susceptibility in eq (2.93).

3.3 The surface integral equation method

The surface integral equation (SIE) method is based on the computation of the surface charges and surface currents at the boundary of nanoparticles from which one obtains the induced fields. The principles are similar to the boundary element method (BEM) except that, in the BEM, the equations for the potential are solved while in the FEM, the fields equations are considered.

Supposing a region 1 of volume V_1 inside which one delimits a region 2 of volume V_2 by a surface S. The applied field $\mathbf{E}^{\text{inc}}(\mathbf{r})$ which exists in region 1, induces charges on the surface S. The equation governing the electric and magnetic charge currents is

$$\left(\frac{\omega\mu_i}{i}\int_S \mathrm{d}S'\bar{\mathbf{G}}_i(\mathbf{r},\mathbf{r}')\cdot\mathbf{J}(\mathbf{r}') - \int_S \mathrm{d}S'\left[\nabla'\bar{\mathbf{G}}_i(\mathbf{r},\mathbf{r}')\right]\cdot\mathbf{M}(\mathbf{r}')\right)_{\tan} = \begin{cases}\left(\mathbf{E}_1^{\text{inc}}(\mathbf{r})\right)_{\tan}: & i=1\\ 0: & i=2\end{cases} \tag{3.29}$$

where the index tan indicates that the component tangential to the surfaces is taken and $\bar{\mathbf{G}}_i$ is the dyadic Green's function define for each region $i = 1, 2$ by

$$\nabla\times\nabla\times\bar{\mathbf{G}}_i(\mathbf{r},\mathbf{r}') - k_i^2\bar{\mathbf{G}}_i(\mathbf{r},\mathbf{r}') = \bar{\mathbf{1}}\delta(\mathbf{r},\mathbf{r}'). \tag{3.30}$$

The integral of eq. (3.29) is solved using the so called Method of Moments (MoM) where the surface S is approximated using a discrete mesh and the surface currents are developed in a basis

$$\mathbf{J}(\mathbf{r}) = \sum_{n=1}^N \alpha_n \mathbf{f}_n(\mathbf{r}), \tag{3.31}$$

$$\mathbf{M}(\mathbf{r}) = \sum_{n=1}^{N} \beta_n \mathbf{f}_n(\mathbf{r}). \tag{3.32}$$

For a triangular mesh, the RWG basis can be used [115]. The problem then reduces then to a $2N \times 2N$ matrix inversion.

$$\begin{aligned}\mathbf{E}_i(\mathbf{r}) =& \{ \begin{smallmatrix} + \\ - \end{smallmatrix} \} \sum_n \left[-\alpha_n \frac{\omega \mu_i}{i} \int_{S_n} \mathrm{d}S' \bar{\mathbf{G}}_i(\mathbf{r}, \mathbf{r}') \cdot \mathbf{f}_n(\mathbf{r}') + \beta_n \int_{S_n} \mathrm{d}S' \left[\nabla' G_i(\mathbf{r}, \mathbf{r}') \right] \times \mathbf{f}_n(\mathbf{r}') \right] \\ &+ \begin{cases} \mathbf{E}_1^{\text{inc}}(\mathbf{r}): & i = 1 \text{ and } \mathbf{r} \in V_1 \\ 0: & i = 2 \text{ and } \mathbf{r} \in V_2 \end{cases}\end{aligned} \tag{3.33}$$

The scattering cross-section is

$$\sigma_{\text{sca}}^{\varphi}(\theta) = 4\pi R^2 \frac{\left| \mathbf{E}_{\text{sca}}(\mathbf{r}_{\varphi}(\theta)) \right|^2}{\left| \mathbf{E}_{\text{inc}} \right|^2}, \quad \varphi = \parallel, \perp,$$

with $\mathbf{E}_{\text{sca}} = \mathbf{E}_1 - \mathbf{E}_1^{inc}$.

This method is also used to determined the second harmonic generation (SHG) by nanoparticles [116]. Once the electric field (at the fundamental frequency) inside the material is known, the nonlinear polarization, the source of the SHG, is calculated at the surface of the nanoparticle:

$$\mathbf{P}\left(\mathbf{r}^+\right) = \chi^{(2)} \mathbf{E}\left(\mathbf{r}^-\right) \mathbf{E}\left(\mathbf{r}^-\right) \tag{3.34}$$

where the $+$ superscripts indicates that the fields is taken just above the surface and the $-$ superscript, just below. The non-linear susceptibility $\chi^{(2)}$ is a rank 3 tensor for which only the contribution coming from the surface is considered, because it is the dominant one [116]. The boundary conditions may therefore be written for the fields at the second harmonic. The method of moments is used again to solve the problem, with the surface currents at the second harmonic developed in the RWG basis to calculate the second harmonic electric field. The scattering cross-section at the second harmonic can then be calculated.

Chapter 4

Plasmons in gold nanowires

One of the applications of plasmons is the guiding of light by squeezing it into subwavelength nanostructures. Such waveguides can be nanowires which absorb light at an extremity and emit it at the other side. The robustness of the plasmon with respect to the morphology is important as defects are always possible. In this chapter, plasmons in high aspect-ratio gold nanowires are investigated. These nanowires sustain standing wave-like plasmons at energies ranging from 0.1 eV to 1.2 eV. The modification of the morphology of their extremities is also studied. Experimental results are compared to numerical ones performed using the DDA method.

This article is a summary of our article [E] with an emphasis on the simulation results. This article is the result of a project unrelated to 2D materials leaded by Dr Mario Palaez-Fernandez (MPF) and Pr. Raul Arenal from the Institute of Nanoscience of Aragon, of the University of Zaragoza. MPF performed EELS characterization of high aspect ratio gold nanowires and nanodumbbells. With master student Romain Dufour, and Pr. Luc Henrard, we have numerically investigated the EELS response of the corresponding nanoparticles. The results have been published in the journal *Nanophotonics*. These results will serve as a nice example of the use of a numerical method to study plasmons in metallic nanostructures. In this case, the DDA was more convenient due to the high aspect ratio of the particles. Indeed, for large particles in general, it is preferable to use a method in which the surface is discretized (eg. FEM or BEM) instead of the volume (DDA, FDTD), because the volume grows faster with the characteristic lengths than the surface. However, for large aspect ratio particles (nanowires, thin disks), the surface grows as fast as the volume and the DDA is even more efficient than the BEM.

Metallic nanowires have attracted special interest [27, 29, 117] given their potential use as nanophotonic waveguides, allowing for a much smaller circuitry than their glass counterparts[28, 30]. The high aspect ratio in nanowires also enables to tune the plasmonic resonance to lower energies [31] or to lower the excitation damping [32]. The Fabry-Pérot (FP) resonances for finite size NW have been shown to follow the dispersion relations close to that of an infinite NW, following the basic ideas of FP interference or standing waves [30–32, 118].

Recent studies have shown that it is possible to change the morphology of these nanowires by means of laser irradiation, allowing to tune the response of high aspect-ratio nanostructures [119, 120]. However, the study of very high aspect-ratio Au nanostructures is quite experimentally challenging because they sustain many long wavelength FP modes taking place at low energies (down to 0.1 eV) and most examples found in the literature present a much lower aspect-ratio besides very recent exceptions for Cu nanowires [33].

This EELS study on diverse high aspect-ratio plasmonic nanostructures (namely, plain nanowires, half-dumbbells and dumbbells) shows that, whereas some of the FP modes are extremely robust against such changes of morphology, higher energy (shorter wavelength) modes are affected and can be tuned by a modification of the shape of their extremities.

4.1 Particles

The particles that have been synthesized and characterized are gold nanowires (NW) of length around $3 - 4\,\mu m$, with spherical nanoparticles (NP) potentially attached to their extremities to form half-dumbbells (hDB) and full dumbbells (DB). The dumbells and half-dumbells are obtained by laser irradiation that induces the gold melting at the ends of the NW and the formation of gold nanoparticles attached to the NW. The images of these nanoparticles obtained from scanning transmission electron micoscopy (STEM) are shown on figure 4.1 along with a sketch specifying the actual dimensions of the

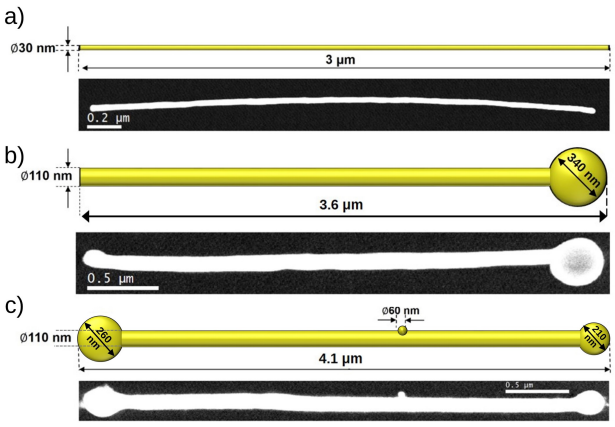

Figure 4.1: STEM pictures and sketch of a) the nanowire, b) the half dumbbell and c) the dumbbell. Reproduced from paper [E].

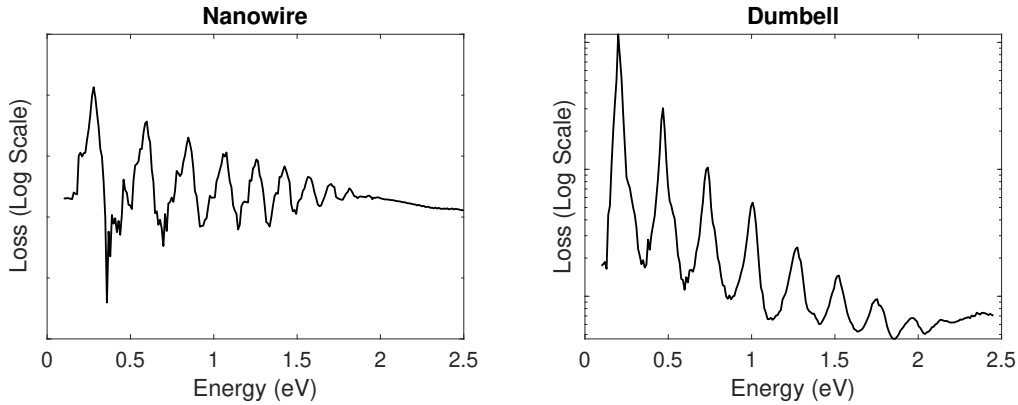

Figure 4.2: Simulated EELS spectra of the nanowire (left) and the dumbbell (right).

particles.

Each particle has been modeled in *ddeels* as cylinders, with spheres at its extremities for DB and hDB. In the present study, the number of dipoles is taken between 38,000 for the smaller nanowire and 110,000 for the longer dumbbell, with a discretization ranging from 4 to 8 nm. The refractive index of gold is taken from [121].

4.2 Spectra and maps for the selected particles

For the sake of brevity, only the EELS spectra and EELS maps of the NW and the DB are shown here. For the full analysis, the reader may refer to the main article [E]. The spectra are obtained by choosing the impact parameter (the position of the electron beam in the plane perpendicular to it) just next to the particle, at mid-distance along the main axis. The maps are obtained at a fixed energy by scanning the surrounding of the particle while changing the impact parameter.

The spectra of the NW and DB (figure 4.2) exhibit a high number of peaks that

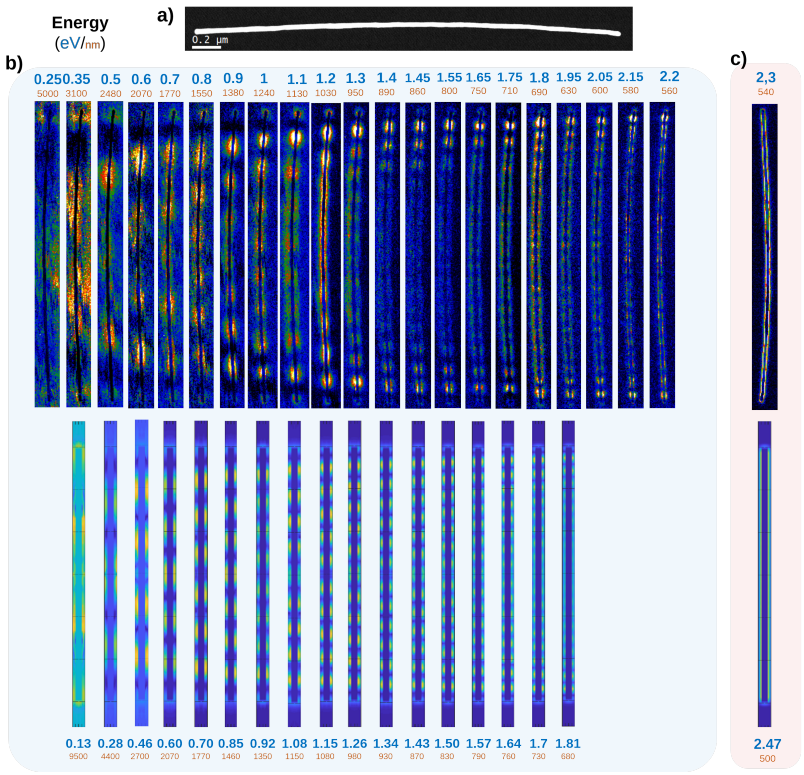

Figure 4.3: a) STEM image of the nanowire. b) Experimental (top) and simulated (bottom) EELS maps of the FP modes. c) Experimental (top) and simulated (bottom) EELS maps of the surface mode. Reproduced from paper [E].

have been assigned in the literature to the nanostructure behaving like a quantified Fabry-Pérot resonator [31, 32, 118]. However, modes with minima at the center of the particles are not visible on these spectra because of the position of the impact parameter. The spectra also present one small feature at high energy (2.4 eV) related to surface plasmon modes of the NW and the NPs.

The maps of each mode have been calculated and compared to the maps obtained by the non-negative matrix factorization (NMF) decomposition of the EELS spectrum-image (SPIM) [122, 123] for the nanowire (figure 4.3) and for the dumbbell (figure 4.4). The simulations reproduce quite well the FP modes visible in the experimental map despite the energy shift, particularly important at low energy for the nanowire. The FP modes are not dramatically modified by the change of morphology at the end of the nanowire.

4.3 Dispersion relations

A wavelength and thus a wavevector k can be associated with each FP peak excitation:

$$k = (n-1) \cdot \pi / L_{AN} \tag{4.1}$$

were n is the number of anti-nodes (excluding the tips) of the EELS map and L_{AN} is the distance between the two furthest antinodes being measured.

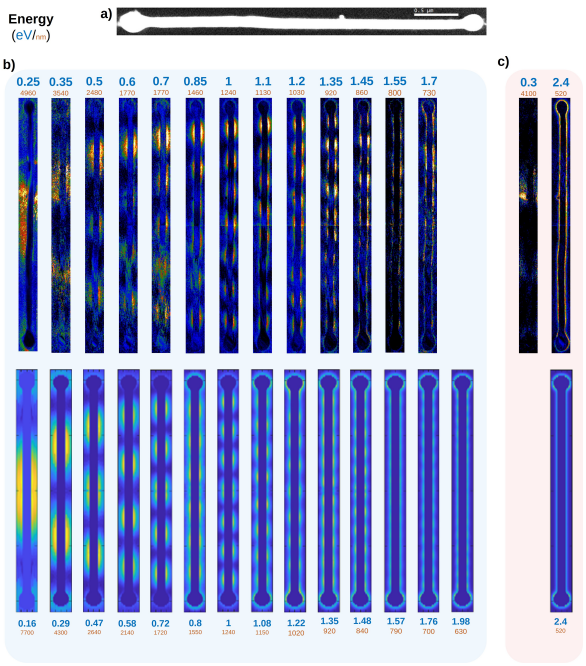

Figure 4.4: a) STEM image of the dumbbell. b) Experimental (top) and simulated (bottom) EELS maps of the FP modes. c) Experimental (top) and simulated (bottom) EELS maps of the surface mode. Reproduced from paper [E].

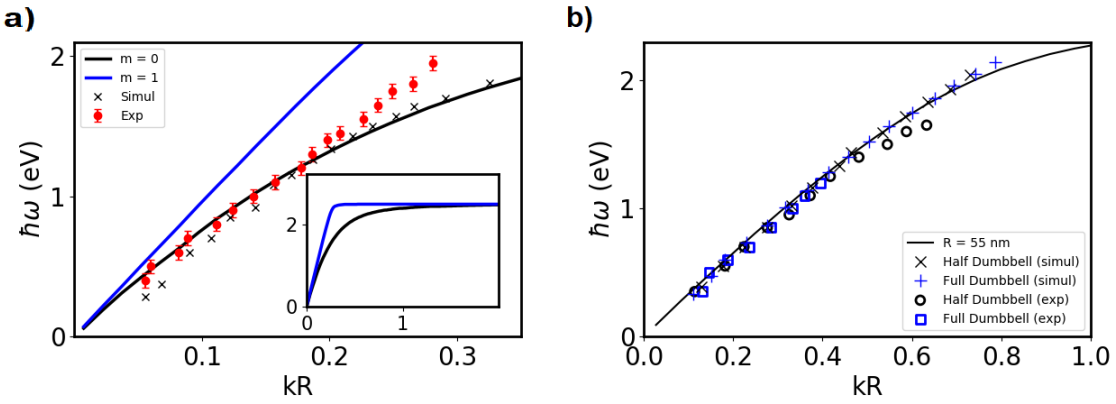

Figure 4.5: a) Dispersion relation of an infinite gold NW (R=15 nm) for m=0 (black curve) and m=1 (blue curve) compared with the data obtained from EELS spectra for finite NW (L=3 μm). $\times$ are for simulated EELS and $\bullet$ are for experimental EELS. The error bars indicate the 0.05 eV experimental spectral resolution. b) Dispersion of the m=0 branch of infinite gold NW of $R = 55$ nm compared with the data extracted from the experimental (open squares and circles) and simulated (crosses) EELS spectra of finite size gold dumbbell and half-dumbbell. The error bars indicate the 0.05 eV experimental spectral resolution. Reproduced from paper [E]. For the simulations, the dielectric function is taken from Ref. [121].

On figure 4.5a, the experimental and simulated dispersion relations associated with the FP modes of the 3 µm long NW (symbols) is compared with the dispersion relation of an infinite NW of the same radius (solid line), calculated using the retarded theory of the SPP on a cylinder [124] adapted for complex dielectric functions. These simulations confirm that a finite size NW behaves like a FP cavity with no modification of the wavelength of the SPP. The good agreement between FP mode resonance energies and the SPP of the same wavenumber confirms that EELS experiments excite the totally symmetric $m = 0$ mode for an $e^{im\phi}$ angular dependence of the induced field [33]. This totally symmetric mode can also be excited by light polarised along the NW axis and it is even the dominant mode in this case for small radius NWs [125]. The dipolar $m = \pm 1$ plasmons are the modes that are predominantly excited by light with a transverse polarisation.

All the plasmon modes (for all m) rapidly converge to the planar surface plasmon energy at 2.45 eV for large k (see figure 4.5a inset). This gives rise to the small energy peak (2.4 eV) in the simulated EELS spectra. As these high k modes cannot be resolved, a continuous excitation probability is observed along the NW and at its extremity.

The solid black line on figure 4.5b gives the analytical dispersion of the $m = 0$ of a perfect infinite NW of radius of 55 nm. The dispersion relations deduced from the EELS data of finite DB and HDB follow it closely. The SPPs can then be regarded as intrinsic modes of the NW itself, regardless of the shape of the extremities. This brings us to the question of the role of the extremity on the FP modes.

4.4 Effect of the nanoparticles

The comparison between the simulated EELS spectra of NW, DB and hDB of the same total length of 4.3 µm with a radius of 56 nm show very similar resonances for the low energy modes (figure 4.6a). On the contrary, a comparison with a NW whose length is reduced to the distance between the spherical extremities displays different resonances at higher energies.

The influence of the extremities on the FP modes of the DB can be further analysed on figure 4.6b, where the EELS spectra of NW ($R_{NP} = 56$ nm) is compared with the ones of DB for different diameters of the spherical ends ($R_{NP} = 104$ nm and $R_{NP} = 128$ nm). The influence of the modification of the extremity is clearly negligible for the low energy, low k (high wavelength) modes and starts to be noticeable when the wavelength of the FP is similar to the size of the perturbation.

This is also illustrated on the figure 4.7 where the simulated EELS map and the associated loss profile are detailed for two specific FP modes of the NW, the DB and the hDB systems. The FP mode at 0.73 eV ($n = 5, \lambda = 1698$ nm) is present for the three plasmonic systems with very similar EELS maps and loss profiles, including at the extremities of the NW. The change of the shape of the extremities, induced by the laser treatment, does not influence neither the energy of the plasmonic response of the NW, nor the field distribution.

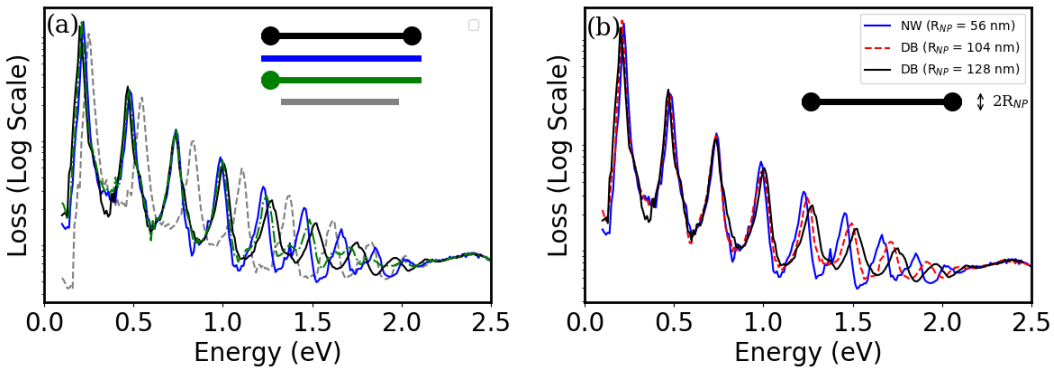

Figure 4.6: a) Comparison of the simulated EELS loss spectra of NWs of total length $L = 4140$ nm for an impact parameter at the mid-length: Dumbbell shape (Black), plain NW (Blue), half-dumbbell shape (dot-dashed green). The radius of the spheres at the extremity is 128 nm. The spectrum for a NW of length $L = 3648$ nm is displayed for comparison (grey dashed). b) Simulated EELS spectra of plain NW and of dumbbell shape structures of total length $L = 4140$ nm with various radii of the spheres at the ends of the NW ($R_{NP} = 104$ nm and $R_{NP} = 128$ nm). Reproduced from paper [E].

For the FP mode $n = 13$, the resonance occurs at $E = 1.66$ eV ($\lambda = 607$ nm) for the perfect NW, at $E = 1.75$ eV ($\lambda = 560$ nm) for the DB and at $E = 1.70$ eV ($\lambda = 591$ nm) for the HDB. A larger damping of the SPP (and shorter propagation length) at this energy explains why the loss probability is lower for all the nanostructures than for the lower energy modes (see the loss profile). It is assumed that, contrary to the FP modes at larger wavelength, the shape of the extremities modifies the reflection of the SPP at these extremities. The change of the reflection coefficient is further evidenced in the profile of the hDB. The position of the maximum loss probabilities follows the pattern of the NW on the perfect extremity whereas it follows the pattern of the DB on the side of the spherical protrusion. This highlights also to role of the shape and of the size of the nanoparticles at the tip of the NW on the exact FP mode energies at small wavelengths. The correct description if this shape and size is then important to predict the exact energy of these modes. This is also illustrated by the dependence of the loss spectra with the size of the spherical NP (figure. 4.6b). This gradual shift of the FP modes energies can be associated with a continuous modification of the reflection coefficient with the size of the extremities. This explains why the match between the simulations and the experimental data are less good for the hDB, which displays a less spherical extremity and a small modification of the other end. (figure 4.5).

Conclusions

Nanowires with high aspect ratio sustain Fabry-Perrot-like plasmonic modes. The modification of the extremities of high aspect ratio metallic NW by laser irradiation enables the control the resonance energy for small wavelength plasmon modes whereas

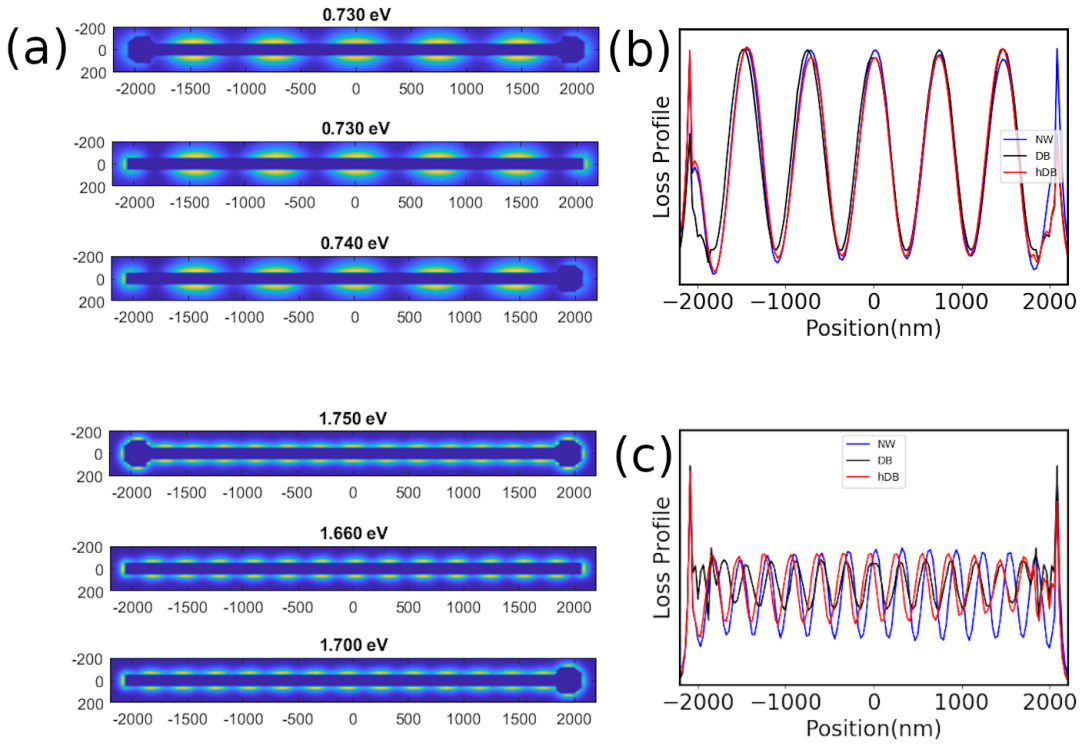

Figure 4.7: a) Simulated EELS maps for the FP modes around 0.73 eV (first and second maps) and 1.7 eV (third and fourth maps), for the dumbbell with $R_{NP} = 128$ nm (first and third maps) and the plain NW (second and fourth maps). b) and c) EELS profiles. Reproduced from paper [E].

longer wavelength modes stay almost unperturbed. The robustness of the dielectric response of the NW against the modification of the extremities reinforces their potential interest as nanophotonic waveguides and low energy resonators. On the other hand, the laser induced tuning of the plasmonic response is of great interest for nanophotonics applications.

Chapter 5

Effective models and optical response of 2D materials as anisotropic materials

2D materials offer a large variety of optical properties. In order to perform numerical simulations to predict these properties, an accurate modeling is necessary. However, the low dimensionality of these materials is an obstacle because the permittivity is most commonly defined for bulk, 3D materials. Different approaches have been proposed to model 2D materials. Here, these methods are presented and compared analytically and numerically. Effective models for vertical and horizontal heterostructures are also proposed. Using these models, the effects of the intrinsic anisotropy of 2D materials and heterostructures on the optical spectra are investigated.

5.1 Effective models for the dielectric function of 2D materials and heterostructures

The description of the EM response of a single 2D material layer has been debated recently [20–23, 126–129]. Two approaches have been widely proposed to describe the optical response of 2D materials: a thin film (3D) model which assigns an effective permittivity to a layer with a given thickness, and a surface polarizability (2D) model which sets a surface response function at the interface between two media [19, 22, 128, 130–133]. These two models have drawbacks because the thickness cannot be defined unambiguously as it will be illustrated below. Moreover, the anisotropy of the 2D materials has been ignored sometimes, due to the simplicity of the isotropic thin film model[13, 134–138]. Nevertheless, recent ellipsometry results on $MoSe_2$ and graphene have proven that the out-of-plane component of the susceptibility and conductivity tensor may play a crucial role in the optical response of 2D materials [21, 22].

The modelling of the EM response of heterostructures of 2D materials is also crucial in view of the increasing importance of these systems. Indeed, the optical properties of these vertical heterostructures ([13, 77, 139–146]) and horizontal heterostructures ([81, 141, 147]) have been investigated extensively in the last decade. The high number of possible heterostructures and their atomic complexity, as well as their intrinsic anisotropy demand a robust but computationally tractable approach.

In this section, the results of work [G] are presented. An original description of the effective permittivity of 2D materials is proposed, based on the microscopic approach discussed in chapter 2. The link between the surface response function of 2D materials and the effective permittivity is rigorously demonstrated. Then, the proposed approach is extended to determine the effective permittivity of vertical and horizontal heterostructures.

Permittivity and surface susceptibilities of 2D materials

2D materials cannot be considered strictly 2D because the wave function extends in the normal direction. Therefore the microscopic dielectric function varies along this direction. The exact description of the permittivity of 2D materials at the atomic level has never been investigated although it should be possible to calculate it from the microscopic dielectric function obtained in TDDFT. Until now, theoretical and experimental studies have only given the average of the permittivity over a thickness L [21, 22, 126, 148]. In the most general case, the layer of thickness L is embedded between two media of different permittivities ε_a and ε_b as represented in figure 5.1, left. However, as depicted on the right of the same figure, this layer can be imagined as the 2D material with thickness d surrounded by two vacuum layers[1]. This representation corresponds to the thin film model (figure 5.2a). It is often used to model 2D materials in numerical simulations, in particular with $d = L$, i.e. with no vacuum layer. In another model, the 2D material

[1]These vacuum layers may for example represent the vacuum layers of the supercell used in TDDFT.

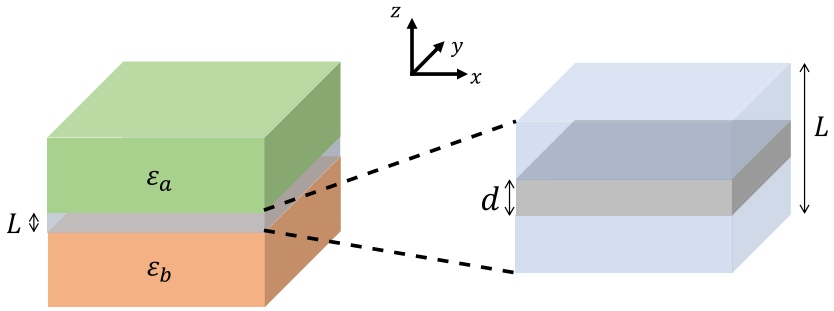

Figure 5.1: Model of a 2D material thick layer in between two media. The layer corresponds to the 2D material sandwiched between two vacuum layers.

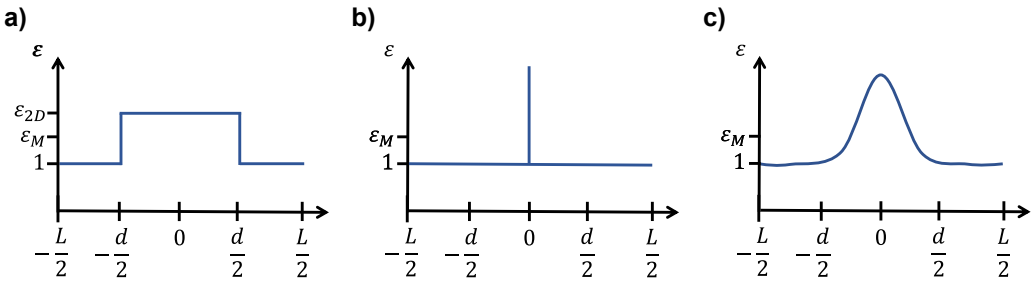

Figure 5.2: Permittivity of the 2D material in the supercell; a) constant permittivity model b) strictly 2D model c) realistic model.

is infinitely thin ($d \to 0$) and the permittivity is represented using a Dirac distribution (figure 5.2b). It corresponds to a finite surface polarization at the interface between two materials. These two models are described in more details in the next section. In a more realistic model, the permittivity is maximum at the center of the atomic layer and decreases rapidly to the permittivity of vacuum after a few Angrstöm, as represented on figure 5.2c.

The average permittivity of the layer of thickness L depends on L (more precisely on the quantity of vacuum in the layer) and is thus an extensive quantity. In TDDFT for instance, the macroscopic dielectric function of 2D materials depends on the size of the chosen supercell size. To accurately describe the optical response of a material, an intensive quantity is more appropriate. In the following, it is shown that the surface susceptibility is an intensive quantity for 2D materials. To describe the relation between the permittivity and the surface susceptibility, the effective model for multilayers described at eq. (2.164) and (2.165) is applied to the three layers system shown in figure 5.1, right.

In-plane polarization

Eq. (2.164) for fields polarized along x or y gives

$$\varepsilon^{\parallel}_{eff} = \sum_i \frac{d_i}{L}\varepsilon_i, \tag{5.1}$$

$$\varepsilon^{\parallel}_{eff} = \frac{L-d}{L}\varepsilon_{vac} + \frac{d}{L}\varepsilon^{\parallel}_{2D}, \tag{5.2}$$

with $\varepsilon^{\parallel}_{eff}$ the effective (or average) permittivity of the three layer system and $\varepsilon^{\parallel}_{2D}$ the permittivity of the 2D material of thickness d for in-plane polarization. It has been shown that the effects of the local fields on the optical properties of stratified media and 2D materials for this polarization are negligible due to their homogeneity [102, 126]. For this reason, the equation (2.105), (the relation between the macroscopic permittivity and the microscopic irreducible susceptibility when local field effects can be neglected) is used, and $\varepsilon^{\parallel}_{eff}$ becomes

$$\varepsilon^{\parallel}_{eff} = 1 + \frac{1}{L}\frac{1}{S}\int\int \chi^{\parallel}(\mathbf{r},\mathbf{r}')\, d^3\mathbf{r}' d^3\mathbf{r} \tag{5.3}$$

with $S = V/d$ the surface of the unit cell, V its volume and $\chi^{\parallel}(\mathbf{r},\mathbf{r}')$ is a scalar function as only one polarization is considered. The surface irreducible susceptibility $\chi^{\parallel}_S$ for in-plane polarization of a 2D material may now be defined as

$$\chi^{\parallel}_S = \frac{1}{S}\int\int \chi^{\parallel}(\mathbf{r},\mathbf{r}')\, d^3\mathbf{r}' d^3\mathbf{r} \tag{5.4}$$

such that

$$\varepsilon^{\parallel}_{eff} = 1 + \frac{\chi^{\parallel}_S}{L}. \tag{5.5}$$

This relation between the effective permittivity of 2D materials and their surface irreducible susceptibility has been intensively used in the last 15 years to model 2D materials, most of the time combined with no response for out-of plane excitations. [130–133]. The surface susceptibility is independent of the chosen thickness L because the integral on $\mathbf{r}$ is performed over L but only the part of the integration over d does not vanish. The equation (5.5) confirms that $\varepsilon^{\parallel}_{eff}$ is dependent of the chosen thickness L. In particular, the effective permittivity tends to infinity when the thickness of the layer vanishes.

Out-of-plane polarization

Eq. (2.165) for fields polarized along z gives

$$\frac{1}{\varepsilon^{\perp}_{eff}} = \sum_i \frac{d_i}{L}\frac{1}{\varepsilon_i}, \tag{5.6}$$

$$\frac{1}{\varepsilon^{\perp}_{eff}} = \frac{L-d}{L}\frac{1}{\varepsilon_{vac}} + \frac{d}{L}\frac{1}{\varepsilon^{\perp}_{2D}}, \tag{5.7}$$

where $\varepsilon_{2D}^{\perp}$ is the permittivity of the layer of thickness d for this polarization. Here, because the LF are not negligible, one must use eq. (2.100) to obtain the effective permittivity of the layer:

$$\frac{1}{\varepsilon_{eff}^{\perp}} = 1 - \frac{1}{L}\frac{1}{S}\int\int \xi^{\perp}\left(\mathbf{r},\mathbf{r}'\right) d^3\mathbf{r}' d^3\mathbf{r} \tag{5.8}$$

The surface external susceptibility is then defined as

$$\xi_S^{\perp} = \frac{1}{S}\int\int \xi^{\perp}\left(\mathbf{r},\mathbf{r}'\right) d^3\mathbf{r}' d^3\mathbf{r} \tag{5.9}$$

and the effective permittivity of the layer is

$$\varepsilon_{eff}^{\perp} = \frac{1}{1-\frac{\xi_S^{\perp}}{L}}. \tag{5.10}$$

For the same reason as before, the surface external susceptibility is independent of the thickness wherever the permittivity depends on the thickness. Surprisingly here, when $L \to 0$, $\varepsilon_{eff}^{\perp} \to 0$. This feature will be investigated later. The previous relation can be inverted if one wants to obtain the surface external susceptibility from the dielectric function:

$$\xi_S^{\perp} = L\left(\frac{\varepsilon_{eff}^{\perp}-1}{\varepsilon_{eff}^{\perp}}\right). \tag{5.11}$$

In some theoretical studies [20, 22], an equivalent equation was employed:

$$\chi_S^{\perp} = L\left(\frac{\varepsilon_{eff}^{\perp}-1}{\varepsilon_{eff}^{\perp}}\right). \tag{5.12}$$

Although the result is the same, it must be noted that the quantity $\chi_S^{\perp}$ as defined above cannot verify

$$\mathbf{P} = \varepsilon_0 \frac{\chi_S^{\perp}}{L}\mathbf{E} \tag{5.13}$$

as it should be expected from a surface irreducible susceptibility. Actually from eq. (2.102) relating the external susceptibility to the irreducible susceptibility, it can be shown that $\chi_S^{\perp}$ is not independent of the thickness and is therefore an inadequate quantity to describe 2D materials out-of-plane response:

$$\chi_S^{\perp} = L\chi^{\perp} = L\frac{\xi^{\perp}}{1-\xi^{\perp}} = \frac{\xi_S^{\perp}}{1-\frac{\xi_S^{\perp}}{L}}. \tag{5.14}$$

If $\xi_S^{\perp}$ does not depends of L, then $\chi_S^{\perp}$ does.

The effective permittivity $\varepsilon_{eff}^{\parallel}$ and $\varepsilon_{eff}^{\perp}$ are bulk quantities that are inherently linked to methods describing 2D materials as thin films while the surface susceptibilities can be used to define a surface polarization field that is purely 2D. These models are the subject of the section 5.2.

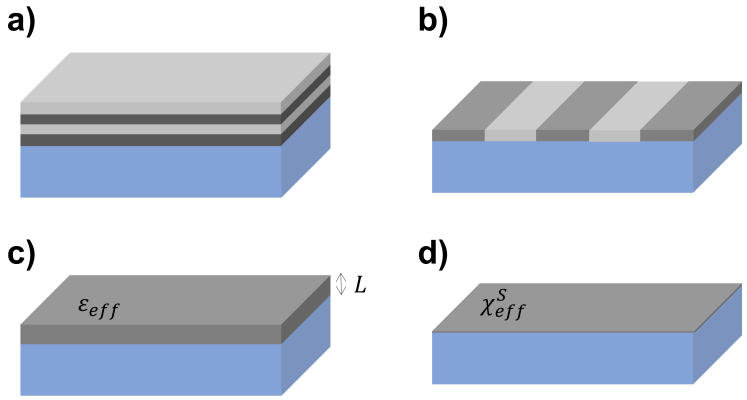

Figure 5.3: Vertical (a) and horizontal (b) heterostructures may be represented using an effective thin film model (c) or a an effective 2D model (d).

Effective medium theory for heterostructures

Heterostructures are associations of various materials to form composite nanomaterials. For 2D materials, there are vertical heterostructures that are overlays of 2D materials, sometimes called van der Waals heterostructures because the 2D layers interact via van der Waals interactions [68, 140] and also horizontal heterostructures or ribbons of 2D materials. In the following, effective models are proposed for each kind of heterostructures. The in-plane and out-of-plane surface susceptibility of vertical (figure 5.3a) and horizontal (figure 5.3b) heterostructures may be related to the bulk effective permittivity of a thin film of finite thickness (figure 5.3c) or to a surface susceptibility (figure 5.3d). By means of simplicity, the case $L = d$ of the model represented in figure 5.2b is chosen, such that there is no vacuum inside a layer. This can be done because the surface susceptibility of a thin layer of vacuum is zero.

Vertical heterostructures

For vertical heterostructures, eq. (2.164) and (2.165) of the effective model for multilayers are applied to a stack of 2D materials of susceptibilities $\chi^{\parallel}_{S,i}$ and $\xi^{\perp}_{S,i}$. For in-plane polarization, it gives

$$\varepsilon^{\parallel}_{eff} = 1 + \frac{\sum \chi^{\parallel}_{S,i}}{L} \tag{5.15}$$

with the sum over all layers surface susceptibility indexed i and L the total thickness of the multilayer. This model is of course valid only if the total thickness is smaller than the wavelength ($L \ll \lambda$). The effective surface susceptibility of the multilayer may be defined as $\chi^{\parallel}_{S,eff} = L\,(\varepsilon_{eff} - 1)$, such that

$$\chi^{\parallel}_{S,eff} = \sum \chi^{\parallel}_{S,i}. \tag{5.16}$$

Similarly, for the out-of-plane polarization we have:

$$\frac{1}{\varepsilon^{\perp}_{eff}} = 1 - \frac{\sum \xi^{\perp}_{S,i}}{L} \tag{5.17}$$

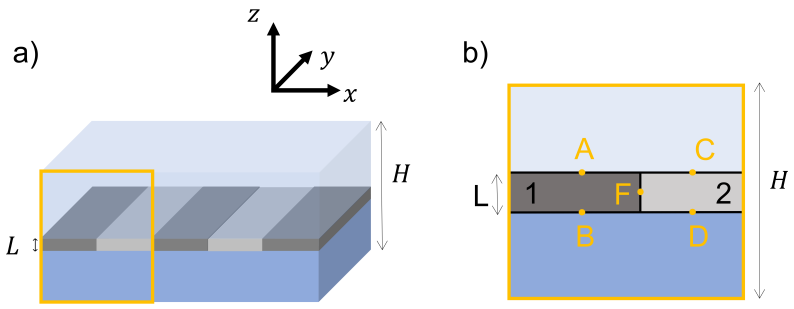

Figure 5.4: a) Schematic view of the unit cell (in yellow) including the ribbon of 2D materials of thickness L and a part of the substrate and of the incident medium in the unit cell for a total thickness H. b) View of the unit cell with the different interfaces labeled from A to F.

and

$$\xi^{\perp}_{S,eff} = \sum \xi^{\perp}_{S,i}. \tag{5.18}$$

In particular, eq. (5.16) and (5.18) applied to N layers of graphene give an effective surface susceptibility that is N times the surface susceptibility of a single layer, as previously shown for the in-plane case [77].

These two equations (5.16) and (5.18) will be called the additivity rules of the susceptibilities for vertical heterostructures

Horizontal heterostructures

The case of horizontal heterostructures or ribbons is more complicated. The effective permittivity of thick ribbons or nanowires is generally given by the same equations used for multilayers, where the equations for parallel polarization (2.164) and perpendicular polarization (2.165) are, respectively, used for polarization parallel and perpendicular to the wire [145, 149]. However, in the case of 2D materials, particular care must be taken because of the extremely thin thickness.

To develop the model, one must consider the displacement field $\mathbf{D}$ and the electric field $\mathbf{E}$ in a unit cell (in yellow in figure 5.4a for an heterostructure made of 2 materials) including a part of the substrate and a part of the incident medium of large thicknesses compared to the thickness of the 2D ribbons L. The total thickness of the system, noted H must still verify the condition $H << \lambda$. The fields must be evaluated at several points at the different interfaces of the system (figure 5.4b).

If the electric field is polarized along the y-axis, it is conserved at the interfaces at all points A, B, C, D and F [2]. Therefore the electric field is constant over the whole structure, which is the condition to apply the equation (2.164) and the effective susceptibility of the layer is

$$\chi^{y}_{S,eff} = \sum f_i \chi^{y}_{S,i}. \tag{5.19}$$

[2] Actually these points are lines along the y-axis.

where f_i is the volume filling fraction of each type of ribbon in the layer of thickness L.

If the electric field is polarized along the x-axis, the electric field is conserved at the interface at all points A, B, C and D. However, at all points F, the displacement field is conserved and the electric field is discontinuous. Therefore, neither the electric field nor the displacement field are constant over the whole structure, and a fortiori over the two ribbons. The conditions to apply the effective model for parallel polarization (eq. (2.164)) or perpendicular polarization (eq. (2.165)) are not fulfilled.

Nonetheless, as the thickness L is supposed to be much smaller than the total thickness H and most importantly, if the width of each ribbon is much larger than L, the electric field does not vary rapidly in the layer, except close to point F. Consequently, in a first approximation, the electric field is constant over the two ribbons and eq. (2.164) can again be used to obtain the effective susceptibility of the layer:

$$\chi^x_{S,eff} = \sum f_i \chi^x_{S,i} \tag{5.20}$$

which gives the same value than the effective susceptibility for the y polarization if all components are isotropic. The layer can thus be approximated as isotropic in its plane.

Finally, for electric fields along the z-axis, the displacement field is conserved at the interfaces A, B, C, D but not F, where the electric field is conserved. Because the layer is extremely thin, the displacement field can be approximated as constant over the ribbons and the effective model for perpendicular polarization can be used (eq. (2.165)):

$$\xi^z_{S,eff} = \sum f_i \xi^z_{S,i} \tag{5.21}$$

Notice that this later development is valid even for width of the same order of magnitude than the wavelength.

As a consequence of the in-plane isotropy of the effective model, the optical response of such structured 2D materials at normal incidence does not depend on the polarization except if there are features that cannot be captured by the effective model. For instance, as surface plasmon resonances are phenomena appearing due to structurating of the material, they cannot be detected in the optical spectra of the effective layer. Therefore, comparing the spectra of the effective system to the exact system and inspecting the discrepancies can highlight the plasmonic resonances taking places in the ribbons.

Equations (5.20) and (5.21) differ from the effective model sometimes used for 2D materials ribbons, reproduced here from the effective model for thick ribbons [145, 150, 151]:

$$\xi^x_{S,eff} = \sum f_i \xi^x_{S,i} \tag{5.22}$$

$$\chi^{y,z}_{S,eff} = \sum f_i \chi^{y,z}_{S,i} \tag{5.23}$$

The original model proposed for 2D materials (eq. (5.19)-(5.21)) is now referred as the thin-ribbon model, and the model of eq. (5.22) and (5.23) is referred as the thick-ribbon model. The validity of these models are tested numerically in section 5.3.

Conclusion

In this section, the two permittivity models that are used to represent 2D materials have been described. In particular, the permittivity of the 3D model has been shown to be dependent on the thickness while the surface susceptibility describing an infinitely thin layer is truly intrinsic to the 2D materials. Effective models of heterostructures have also been proposed. All these models are tested numerically in the two next sections.

5.2 Numerical methods describing 2D materials

Using the models presented in the last section, the thin film (3D) model and the surface polarization (2D) model are presented here. Then analytical and numerical comparisons of the 3D and 2D models are performed. Only transverse magnetic (TM) waves are considered here, because transverse electric (TE) waves cannot excite the out-of-plane response of layered materials. A large part of the results of this section has been published in our article [C].

3D thin film model

The thin film refers to the model presented above where the permittivity of the 2D material is taken constant over a thickness d. With such model, it is straightforward to include a 2D layer in a numerical method such as the transfer matrix method. The basic transfer matrix method only accounts for isotropic layers so that in much studies, the 2D layers are assumed to be isotropic [130–133]. Here, the transfer-matrix method developed in [152] for an anisotropic material layer is used. In this frame, for p-polarized light impinging on uniaxial materials, the transfer matrix of a single layer is given by:

$$T = \begin{bmatrix} \cos\delta & -\frac{i}{\eta}\sin\delta \\ -i\eta\sin\delta & \cos\delta \end{bmatrix} \tag{5.24}$$

with

$$\delta = kd\sqrt{\varepsilon^{\parallel} - \frac{\varepsilon^{\parallel}}{\varepsilon^{\perp}} n_a^2 \sin^2\theta_i} \tag{5.25}$$

and

$$\eta = \frac{1}{\sqrt{\frac{1}{\varepsilon^{\parallel}} - \frac{n_a^2}{\varepsilon^{\parallel}\varepsilon^{\perp}}\sin^2\theta_i}} \tag{5.26}$$

where n_a is the refractive index of the incident isotropic medium and θ_i the incident angle. The Fresnel coefficients are [152]:

$$r_p = \frac{\eta_0 B - C}{\eta_0 B + C} \tag{5.27}$$

$$t_p = \frac{2n_a}{\cos\theta_t}\frac{1}{\eta_0 B + C}. \tag{5.28}$$

with

$$B = \cos\delta - i\frac{\eta_b}{\eta}\sin\delta \tag{5.29}$$

and

$$C = -i\eta\sin\delta + \eta_b\cos\delta \tag{5.30}$$

$\eta_a = \frac{n_a}{\cos\theta_i}$, $\eta_b = \frac{n_b}{\cos\theta_t}$, n_b the refractive index of the isotropic substrate and θ_t the refraction angle.

The reflection and transmission coefficient are then calculated using

$$R = |r_p|^2, \tag{5.31}$$

$$T = \frac{\varepsilon_a k_z^b}{\varepsilon_b k_z^a}|t_p|^2. \tag{5.32}$$

2D polarization sheet model

In the 2D polarization sheet model, as described in our article [C], a surface polarization $\mathbf{P}_S$ is defined at the interface (at $z = 0$) between the incident medium and the substrate:

$$\mathbf{P} = \mathbf{P}_S\delta(z). \tag{5.33}$$

Here, $\delta(z)$ is the dirac distribution such that $\mathbf{P}$ diverge at $z = 0$ due to the vanishing thickness, but $\mathbf{P}_S$ is finite. For in-plane polarization, this corresponds to the model suggested in figure 5.2c. Indeed, if one takes $\chi^{\parallel}(z) = \chi_S^{\parallel}\delta(z)$, where $\chi_S^{\parallel}$ is finite ($\chi^{\parallel}(z)$ diverges at $z = 0$), then

$$P^{\parallel} = \varepsilon_0\chi^{\parallel}E^{\parallel} \tag{5.34}$$

$$P^{\parallel} = \varepsilon_0\chi_S^{\parallel}\delta(z)E^{\parallel} \tag{5.35}$$

$$P^{\parallel} = P_S\delta(z) \tag{5.36}$$

with

$$P_S^{\parallel} = \varepsilon_0\chi_S^{\parallel}E^{\parallel}. \tag{5.37}$$

Taking $\chi^{\parallel}(z) = \chi_S^{\parallel}\delta(z)$ corresponds to a permittivity

$$\varepsilon^{\parallel}(z) = 1 + \chi_S^{\parallel}\delta(z) \tag{5.38}$$

with an average value over a thickness L (supposing the 2D sheet is embedded in vacuum) of

$$\varepsilon_{eff}^{\parallel} = \frac{1}{L}\left\langle\varepsilon^{\parallel}(z)\right\rangle = 1 + \frac{\chi_S^{\parallel}}{L} \tag{5.39}$$

as expected, since $\langle\delta(z)\rangle = 1$. Note that $\varepsilon^{\parallel}(z) \to \infty$ at $z = 0$, in order to have a finite response for a vanishing thickness.

For out-of-planes polarization, the 2D model is a little bit different because the surface external susceptibility must be used instead. The polarization field is written

$$P^{\perp} = \xi^{\perp}D^{\perp}. \tag{5.40}$$

Writing the external susceptibility $\xi^{\perp}(z) = \xi_S^{\perp}\delta(z)$ with $\xi_S^{\perp}$ finite as shown in section 5.1, the polarization field becomes

$$P^{\perp} = \xi_S^{\perp}\delta(z)\, D^{\perp} \tag{5.41}$$

$$P^{\perp} = P_S^{\perp}\delta(z) \tag{5.42}$$

with

$$P_S^{\perp} = \xi_S^{\perp} D^{\perp}. \tag{5.43}$$

However the permittivity is now

$$\varepsilon^{\perp}(z) = \frac{1}{1 - \xi_S^{\perp}\delta(z)} \tag{5.44}$$

and $\varepsilon^{\perp}(z) \to 0$ for $z = 0$ with an average value over the thickness L of

$$\varepsilon_{eff}^{\perp} = \frac{1}{1 - \frac{\xi_S^{\perp}}{L}}. \tag{5.45}$$

This is explained intuitively by the fact that $\varepsilon_{eff}^{\perp}$ is not the appropriate volume response function, but its inverse or $\xi_{eff}^{\perp}$ are more appropriate.

Therefore $\varepsilon^{\perp}(z)$ cannot be described by a Dirac function as sketch in figure 5.2b. Let us suppose that, instead of being described by Dirac functions, the irreducible and external susceptibilities vary as Gaussian functions

$$\chi(z) \text{ or } \xi(z) \propto \frac{1}{a\sqrt{\pi}} e^{-\left(\frac{z}{a}\right)^2} \tag{5.46}$$

with a standard deviation $\sigma = \frac{a}{\sqrt{2}}$, such that when $a \to 0$, the delta distribution is recovered. According to eq. (5.38) and (5.44) the in-plane and out-of-plane permittivities vary differently. In figure 5.5, the variations of the permittivity in the z direction for in-plane (a), and out-of-plane polarizations (b) are represented using the Gaussian model, for different values of a in unit of an arbitrary unit distance z_0. For the in-plane polarization, the permittivity truly tends to a Dirac function while for the out-of-plane polarization, the permittivity tends to zero at the center, but is discontinuous close to the edges. In order to verify and explain this trend, the microscopic dielectric function of a 2D material obtained using TDDFT should be analyzed.

Note that taking

$$P_S^{\perp} = \varepsilon_0 \chi_S^{\perp} E^{\perp} \tag{5.47}$$

as it was done in recent papers [22, 128], is not valid because $\chi_S^{\perp}$ is not adapted for this polarization. Indeed, the relation between the irreducible and external susceptibilities (2.102) is

$$\chi^{\perp} = \frac{\xi^{\perp}}{1 - \xi^{\perp}}. \tag{5.48}$$

Therefore

$$\chi_S^{\perp}\delta(z) = \frac{\xi_S^{\perp}\delta(z)}{1 - \xi_S^{\perp}\delta(z)}, \tag{5.49}$$

$$\chi_S^{\perp} = \frac{\xi_S^{\perp}}{1 - \xi_S^{\perp}\delta(z)} \tag{5.50}$$

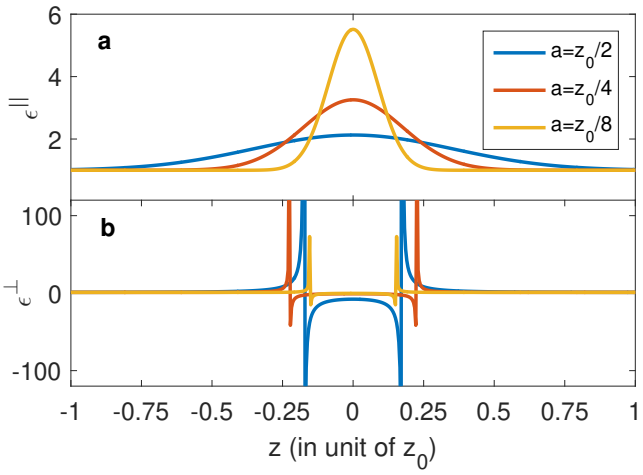

Figure 5.5: In-plane and out-of-plane permittivities of a 2D material if one takes a surface irreducible/external susceptibility that varies as a Gaussian function in the unit cell along z, with different values of the parameter a for an arbitrary distance z_0.

As $\xi_S^\perp$ is finite, $\chi_S^\perp$ vanishes at $z = 0$. Then, if $P_S^\perp$ has to be finite in eq. (5.47), the null value of $\chi_S^\perp$ at the interface requires $E^\perp$ to be infinite in the polarizing sheet, which is not physical. On the contrary the use of equation (5.43) make complete sens as both $\xi_S^\perp$ and $D^\perp$ are finite and well defined at the interface.

Fresnel coefficients

The Fresnel coefficients can be derived from the 2D model. For this purpose, the boundary conditions accounting for these surface polarizations (eq. (5.37) and (5.43)) at the interface between two media of permittivity ε_a and ε_b are considered. The following development has been described in details in article [C], although the irreducible susceptibility was used for the out-of-plane response. This has only a minor impact on the results of the paper, and they have been corrected here. The wavevector $\mathbf{k}$ is chosen into the xOz plane ($k_y = 0$), with

$$k_z = \pm\sqrt{k^2\varepsilon - k_x^2}. \tag{5.51}$$

for transverse magnetic waves. The relation between the components of $\mathbf{D}$ is, from Maxwell equations,

$$D_z = -\frac{k_x}{k_z} D_x \tag{5.52}$$

It has been shown, when a surface polarization stands at the boundary, that the boundary conditions are [153, 154]:

$$\mathbf{e}_z \times [\mathbf{B}_b - \mathbf{B}_a] = \mu_0 \frac{\partial}{\partial t} \mathbf{P}_S, \tag{5.53}$$

$$\mathbf{e}_z \times [\mathbf{E}_b - \mathbf{E}_a] = -\frac{1}{\varepsilon_0} \nabla P_S^\perp. \tag{5.54}$$

The first equation corresponds to the boundary conditions from textbooks [42], while the right-hand side of the second equation is null for interfaces between bulk materials. These equations become, given the expressions of $\mathbf{P}_S$ established above,

$$\frac{k_z^a}{k_z^b} D_x^t = D_x^i - D_x^r + i k_z^a \chi_S^{\parallel} E_x^s, \tag{5.55}$$

$$\frac{\varepsilon_a}{\varepsilon_b} D_x^t = D_x^i + D_x^r + i k_x \xi_S^{\perp} D_z^s \varepsilon_a \tag{5.56}$$

where the superscripts i, r and t refer respectively to the incident, reflected and transmitted waves. The superscript s refers to the field at the interface. It has been suggested to use the average value of the fields in the incident medium and in the substrate in order to estimate these surface fields [155]:

$$E_x^s = \frac{E_x^i + E_x^r + E_x^t}{2}; \tag{5.57}$$

$$D_z^s = \frac{D_z^i + D_z^r + D_z^t}{2}. \tag{5.58}$$

However our article [C], a first order approximation (valid for small phase shifts) is performed by neglecting the effect of the polarization sheet and assuming the continuity of these fields. Then, the surface fields are chosen as $D_z^s = D_z^t$ and $E_x^s = E_x^t$. By setting

$$r = -\frac{D_x^r}{D_x^i} \tag{5.59}$$

and

$$t = \frac{k_z^a}{k_z^b} \frac{D_x^t}{D_x^i} \tag{5.60}$$

the Fresnel coefficients, the system of equations (5.55)-(5.56) becomes

$$t = \frac{\varepsilon_b k_z^a}{\varepsilon_a k_z^b} - \frac{\varepsilon_b k_z^a}{\varepsilon_a k_z^b} r + i \frac{k_x^2}{k_z^b} \xi_S^{\perp} \varepsilon_b t, \tag{5.61}$$

$$t = 1 + r + i \frac{k_z^b}{\varepsilon_b} \chi_S^{\parallel} t. \tag{5.62}$$

The Fresnel coefficients are obtained by solving the above system:

$$r_p = -\frac{n_a \cos\theta_t - n_b \cos\theta_i + i \cos\theta_i \cos\theta_t k \chi_S^{\parallel} - i n_a^3 n_b \sin^2\theta_i k \xi_S^{\perp}}{n_a \cos\theta_t + n_b \cos\theta_i - i \cos\theta_i \cos\theta_t k \chi_S^{\parallel} - i n_a^3 n_b \sin^2\theta_i k \xi_S^{\perp}}, \tag{5.63}$$

$$t_p = \frac{2 n_b \cos\theta_i}{n_a \cos\theta_t + n_b \cos\theta_i - i \cos\theta_i \cos\theta_t k \chi_S^{\parallel} - i n_a^3 n_b \sin^2\theta_i k \xi_S^{\perp}}. \tag{5.64}$$

where the subscript p is added to recall the polarisation However, this solution does not strictly conserve the energy in a sense that $R + T \neq 1$ when χ_x^S and ξ_z^S are real (i.e. there is no absorption) [22]. Fortunately, when the phase shift is small i.e. $k\chi_x^S \ll 1$; $k\xi_z^S \ll 1$, the energy is still approximately conserved. It is consistent with the first order

approximation performed above. I proposed another slightly different version where, instead of taking $E_x^s = E_x^t$, I take $E_x^s = E_x^i$:

$$r_p = -\frac{n_a \cos\theta_t - n_b \cos\theta_i + i \cos\theta_i \cos\theta_t k\chi_S^{\parallel} - i n_a^3 n_b \sin^2\theta_i k\xi_S^{\perp} + n_a^2 n_b \cos\theta_i \sin^2\theta_i k^2 \xi_S^{\perp}\chi_S^{\parallel}}{n_a \cos\theta_t + n_b \cos\theta_i - i \cos\theta_i \cos\theta_t k\chi_S^{\parallel} - i n_a^3 n_b \sin^2\theta_i k\xi_S^{\perp} - n_a^2 n_b \cos\theta_i \sin^2\theta_i k^2 \xi_S^{\perp}\chi_S^{\parallel}}, \tag{5.65}$$

$$t_p = \frac{2n_b \cos\theta_i}{n_a \cos\theta_t + n_b \cos\theta_i - i \cos\theta_i \cos\theta_t k\chi_S^{\parallel} - i n_a^3 n_b \sin^2\theta_i k\xi_S^{\perp} - n_a^2 n_b \cos\theta_i \sin^2\theta_i k^2 \xi_S^{\perp}\chi_S^{\parallel}}. \tag{5.66}$$

This version is consistent with the conservation of energy. However a second order term appears (including $k^2\xi_S^{\perp}\chi_S^{\parallel}$) and it cannot be considered as a first order approximation. Further researches on this problem have been performed recently, principally by P. Kockaert of the ULB, and are the subject of a manuscript submitted to a peer-reviewed journal [F].

Analytical comparison of the models

A first analysis can be done by comparing the Fresnel coefficients obtained using both models, when the thickness of the 3D model tends to zero. From the 3D model, eq. (5.27) and (5.28), using the relation between the permittivities and the susceptibility, and taking the limit $kd \to 0$, except when kd multiplies the susceptibilities, i.e. $kd\chi^{\parallel} = k\chi_S^{\parallel}$ and $kd\xi^{\perp} = k\xi_S^{\perp}$, the Fresnel coefficients become

$$r_p = -\frac{(n_a \cos\theta_t - n_b \cos\theta_i)\cos\delta - i\left(n_a n_b \frac{\delta}{k\chi_S^{\parallel}} - \frac{k\chi_S^{\parallel}}{\delta}\cos\theta_i \cos\theta_t\right)\sin\delta}{(n_a \cos\theta_t + n_b \cos\theta_i)\cos\delta - i\left(n_a n_b \frac{\delta}{k\chi_S^{\parallel}} + \frac{k\chi_S^{\parallel}}{\delta}\cos\theta_i \cos\theta_t\right)\sin\delta} \tag{5.67}$$

$$t_p = \frac{2n_b \cos\theta_i}{(n_a \cos\theta_t + n_b \cos\theta_i)\cos\delta - i\left(n_a n_b \frac{\delta}{k\chi_S^{\parallel}} + \frac{k\chi_S^{\parallel}}{\delta}\cos\theta_i \cos\theta_t\right)\sin\delta} \tag{5.68}$$

with δ defined in eq. (5.25) becoming

$$\delta = k n_a \cos\theta_i \sqrt{\chi_S^{\parallel}\xi_S^{\perp}}. \tag{5.69}$$

Note that, if the out-of-plane response is negligible ($\xi_S^{\perp} \cong 0$), one obtains

$$r_p = -\frac{(n_a \cos\theta_t - n_b \cos\theta_i) + ik\chi_S^{\parallel}\cos\theta_i \cos\theta_t}{(n_a \cos\theta_t + n_b \cos\theta_i) - ik\chi_S^{\parallel}\cos\theta_i \cos\theta_t} \tag{5.70}$$

$$t_p = \frac{2n_b \cos\theta_i}{(n_a \cos\theta_t + n_b \cos\theta_i) - ik\chi_S^{\parallel}\cos\theta_i \cos\theta_t} \tag{5.71}$$

which are equivalent to the Fresnel coefficients obtained from the 2D surface polarization model with no out-of-plane response employed in 2D materials optics for years [8, 77,

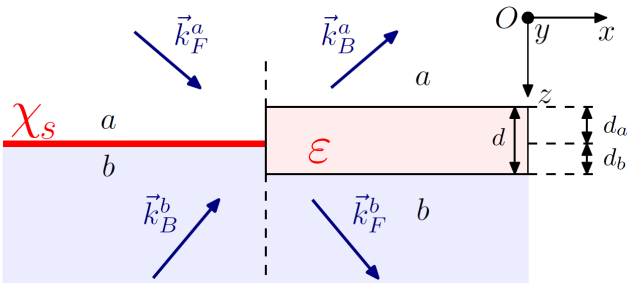

Figure 5.6: Representation of 2D polarization sheet model (left) and 3D thin-film model (right). Adapted from [C].

127]. Moreover, this formula satisfy the energy conservation. Therefore, the two models are strictly equivalent when there is no out-of-plane response for a vanishing thickness.

Taking the first order in $\sin\delta$ and $\cos\delta$ in eq. (5.67) and (5.68), the Fresnel coefficients obtained from the 2D model (eq. (5.63) and (5.64)) are retrieved. However, higher order terms cannot be recover from the 2D model. Rigorously, the two models cannot be equivalent but, for small phase shift, they give nearly equal results. This is verified numerically hereafter.

At the first order, the transfer matrices of the 2D materials in the thin film model and in the 2D model can also be compared as done in our article [C]. Actually, because the 2D model has no thickness, the matrices cannot be compared directly. In figure 5.6, the two models are represented. In the 2D model, the wave travels a distance d_a through medium a and a distance d_b through medium b, on opposite sides of the interfaces, while, in the 3D model, this distance is included in the effective thin film. In consequence, the transfer matrix for the 2D sheet has to be multiplied (before and after) by matrices representing the propagation in media a and b. In the article, it was shown that the two models are equivalent at the first order if the following relations are verified:

$$\varepsilon_{eff}^{\parallel} = \frac{d_a}{d}\varepsilon_a + \frac{d_b}{d}\varepsilon_b + \frac{\chi_S^{\parallel}}{d}, \tag{5.72}$$

$$\frac{1}{\varepsilon_{eff}^{\perp}} = \frac{d_a}{d}\frac{1}{\varepsilon_a} + \frac{d_b}{d}\frac{1}{\varepsilon_b} - \frac{\xi_S^{\perp}}{d}. \tag{5.73}$$

These equations can also be found from the effective model of multilayers applied to the structure of figure 5.6 and therefore are fully consistent.

A practical example is helpful to understand the utility of these equations. Let us imagine a structure composed of 5 identical layers of susceptibilities $\chi_S^{\parallel}$ and $\xi_S^{\perp}$ of total thickness L laying on the substrate of permittivity ε_b (figure 5.7). In the thin film model (right), each layer has an effective permittivity ε_{eff} with a thickness d, which is equivalent to a layer of vacuum including a 2D sheet of susceptibilities $\chi_S^{\parallel}$ and $\xi_S^{\perp}$. The total system has then a thickness of $L = 5 \times d$ and susceptibilities $\chi_{S,tot}^{\parallel} = 5 \times \chi_S^{\parallel}$ and $\xi_{S,tot}^{\perp} = 5 \times \xi_S^{\perp}$ according to the additivity laws of the susceptibilities (equations (5.16) and (5.18)). In order to be equivalent, the structure on the left (2D model) must have

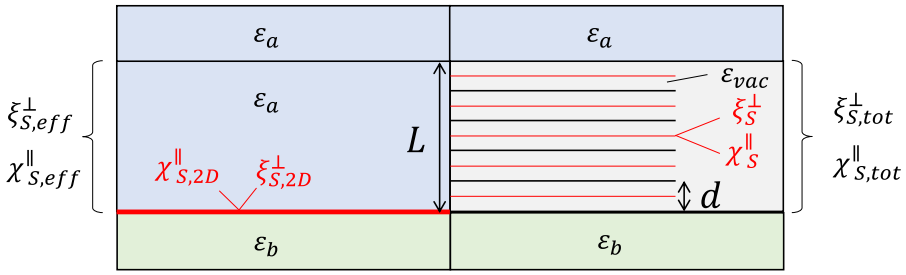

Figure 5.7: Representation of the two model for a system of 5 identical 2D layers.

the same effective surface susceptibilities over the thickness L, such that the effective permittivity of the layer of thickness L is the same in both systems. By choosing to put the 2D layer at the bottom level of the thin film (i.e. $d_b = 0$)[3], the effective surface susceptibilities over the thickness L in the 2D model are (from eq. (5.16) and (5.18)):

$$\chi^{\parallel}_{S,eff} = \chi^{\parallel}_{S,2D} + \chi^{\parallel}_{S,a} \tag{5.74}$$

and

$$\xi^{\perp}_{S,eff} = \xi^{\perp}_{S,2D} + \xi^{\perp}_{S,a} \tag{5.75}$$

where $\chi^{\parallel}_{S,2D}$ and $\xi^{\perp}_{S,2D}$ are the surface susceptibilities of the 2D sheet of vanishing thickness, and $\chi^{\parallel}_{S,a}$ and $\xi^{\perp}_{S,a}$ are the equivalent surface susceptibilities of a layer of thickness L of the incident medium:

$$\chi^{\parallel}_{S,a} = (\varepsilon_a - 1)\, L, \tag{5.76}$$

$$\xi^{\perp}_{S,a} = \left(1 - \frac{1}{\varepsilon_a}\right) L. \tag{5.77}$$

If one imposes $\chi^{\parallel}_{S,eff} = \chi^{\parallel}_{S,tot}$ and $\xi^{\perp}_{S,eff} = \xi^{\perp}_{S,tot}$ (the surface susceptibilities of a layer of thickness L in both models must be equivalent), the surface susceptibility of the 2D sheet must be:

$$\chi^{\parallel}_{S,2D} = \chi^{\parallel}_{S,tot} - \chi^{\parallel}_{S,a} = 5 \times \chi^{\parallel}_{S} - \chi^{\parallel}_{S,a} \tag{5.78}$$

$$\xi^{\perp}_{S,2D} = \xi^{\perp}_{S,tot} - \xi^{\perp}_{S,a} = 5 \times \xi^{\perp}_{S} - \xi^{\perp}_{S,a} \tag{5.79}$$

which is equivalent to the equations (5.72) and (5.73), with $d_a = d = L$ and $d_b = 0$.

This example highlights the fact that the incidence medium and the substrate play a crucial role when comparing the 2 models. If the incidence medium is vacuum, the transition between the two models is quite straightforward using eq. (5.5) and (5.10). In other cases, the propagation of the wave in the incidence medium layer of thickness L must be taken into account in the model.

[3]Although this choice is natural for a 2D material deposited on a substrate, $d_a = 0$ could also have been chosen without modifying the conclusions.

Numerical comparison of the models

In this paragraph, the numerical results reported [C] are summarized. The 2D (surface polarization) and 3D (thin film) models are compared numerically using the methods described in the beginning of this section, respectively the polarization sheet and the transfer matrix methods. The 2D model is used with no out-of-plane response ($\xi_S^\perp = 0$) and the 3D model with either no out-of-plane response ($\varepsilon^\perp = 1$) or an isotropic response ($\varepsilon^\perp = \varepsilon^\parallel$). These models have been commonly used in the literature [13, 19, 130–138], in particular the 2D model and the isotropic thin film model, because they are simpler to implement numerically. However, some researchers have recently investigated the out-of-plane response of 2D materials [18, 20–22]. Nonetheless, as the out-of-plane response is negligible in the visible light and infrared (IR) for most 2D materials and in particular for graphene, the "no out-of-plane response" model is actually pretty accurate. Note that our methods are able to take into account the true value of the out-of-plane susceptibility but at the moment of the publication of the paper, I haven't done the TDDFT calculations of the out-of-plane response of graphene and other 2D materials.

The system studied in the article is a 2D material with a thickness of 0.34 nm, in contact with vacuum, and lying on a substrate of constant refractive index $n = 1.5$. The incidence angle is $75°$ in TM polarization in order to maximize the anisotropic response. The transmittance from the 2D polarization model and the thin film model are calculated as function of the real and imaginary parts of the normalized surface irreducible susceptibility $k\chi_S^\parallel$. The surface susceptibility spans over several orders of magnitude, including the susceptibility of graphene in the visible and IR ranges. Figures 5.8 and 5.9 display the relative error on transmittance defined as:

$$\Delta T = \frac{T_{2D} - T_{\mathrm{tf}}}{T_{\mathrm{2D}}} \tag{5.80}$$

where T_{2D} and T_{tf} are the transmittances calculated using the 2D model and the thin film model, respectively. Two incident wavelengths are compared: in the IR, $\lambda = 1550$ nm, and in the visible, $\lambda = 700$ nm, respectively on the left and on the right of figures 5.8 and 5.9.

In the comparison between the 2D model and the anisotropic ("no out-of-plane response") thin film model (figure 5.8), the transmittance computed in both models are obviously in excellent agreement. The small phase shift condition ($\left|\mathrm{Re}\left(k\chi_S^\parallel\right)\right| \ll 1$) is thus satisfied for a large range of 2D susceptibilities. When the small phase shift condition is relaxed ($\left|\mathrm{Re}\left(k\chi_S^\parallel\right)\right| \gtrapprox 1$), a larger error ΔT is obtained, corresponding to the yellow bands on the left and right sides of figure 5.8 a and b. The difference is of course larger at smaller wavelengths since the phase shift scales with $k = \frac{2\pi}{\lambda}$.

When comparing the 2D model with the isotropic thin film model (figure 5.9), the differences are much more important. Note that the scale of ΔT is different on figure 5.8 and figure 5.9. For a better interpretation of the results of the isotropic case, a range of values of the susceptibility is encircled which displays the susceptibility of graphene at each corresponding wavelength based on the Kubo formula (see chapter I) for a range of Fermi levels from 0.05 eV to 1 eV and a range of relaxation times from 10 fs to 200 fs.

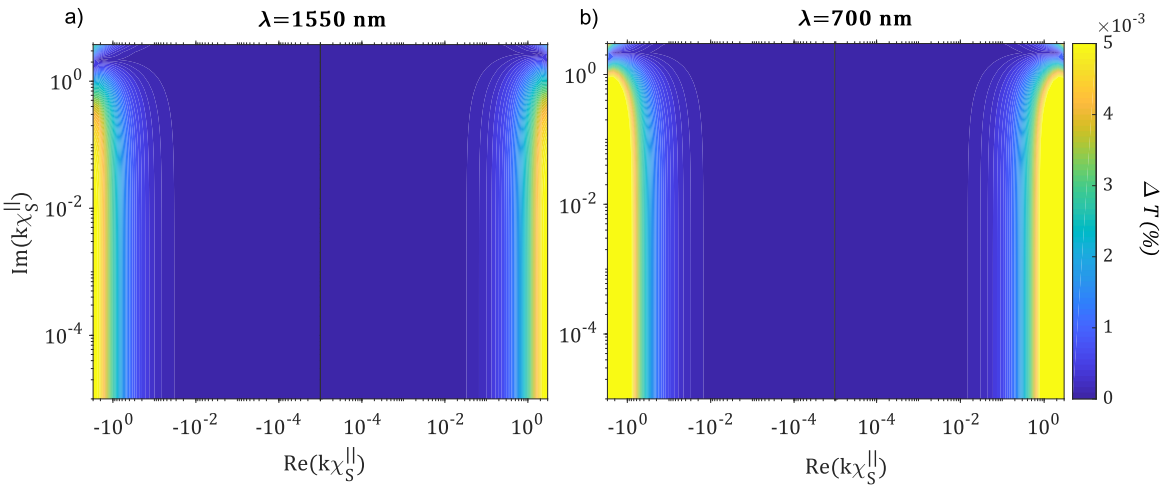

Figure 5.8: Relative difference ΔT between the transmittance computed in the 2D model and in the anisotropic thin film models, with respect to the real and imaginary parts of the 2D material susceptibility. The system considered is vacuum/2D material/glass. The refractive index of glass is taken as 1.5. a) Infrared EM radiation ($\lambda = 1550$ nm); b) Visible light ($\lambda = 700$ nm). Adapted from [C]

Note that for the anisotropic case (figure 5.8), we observe a particularly small ΔT with maximum of $2 \cdot 10^{-3}\%$ in these ranges. Notably, a high value of ΔT is observed on a vertical line in figure 5.9 corresponding to $Re\left(\chi_S^{\parallel}\right) = -d$, for which the real part of the permittivity $\varepsilon = 1 + \chi_S^{\parallel}/d$ vanishes. This shows, similarly to what was reported in [24], that an artificial plasmonic resonance is predicted by an isotropic thin film model, due to the artificial metallic nature of the out-of-plane component of the permittivity tensor. This nonphysical resonance could have dramatic effects on the prediction of the optical properties.

To investigate further the influence of the anisotropy, the difference between the transmittance obtained with the isotropic and anisotropic thin film models for graphene, as a function of the incident wavelength and of the thin film thickness is presented in figure 5.10. The two models give very similar results for a ratio $\lambda/d > 1000$ i.e for very small kd (under the dashed line). This validates the fact that the anisotropy of graphene has been often disregarded without consequences on the validity of the conclusions if the chosen thickness of the thin film is at least three orders of magnitude lower than the wavelength. This relatively good prediction within the isotropic thin-film model is explained in the article [C] by the fact that, when

$$\left|\chi_S^{\parallel}\right|^2 \gg d^2, \tag{5.81}$$

the isotropic thin film model is equivalent to the anisotropic 2D model (with $\xi_s^{\perp} = 0$).

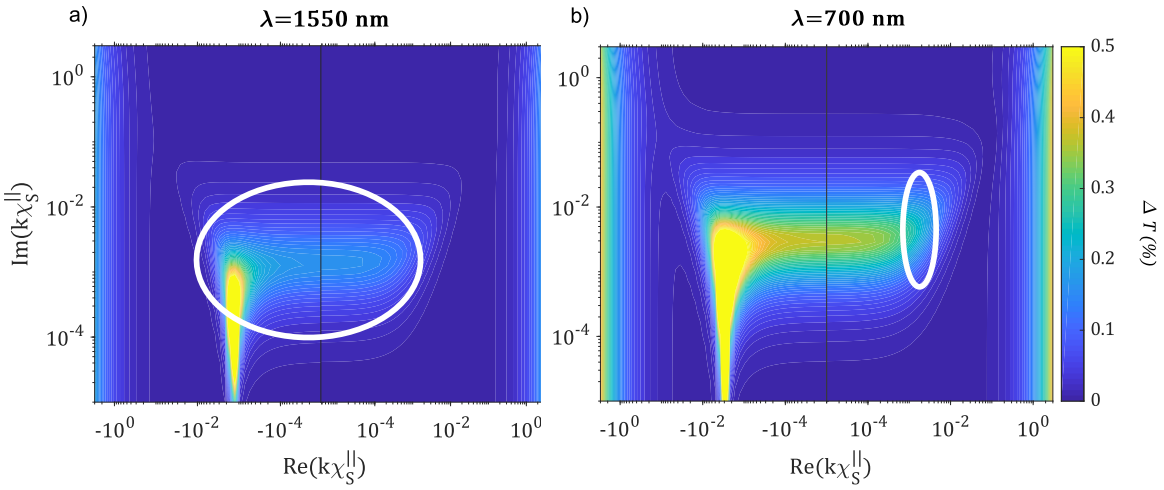

Figure 5.9: Same as figure 5.8 for the isotropic thin film model. The circled areas locate graphene's adimensional parameter $k_0\chi^s$. To determine it, the Kubo formula is used at a fixed wavelength of 700 nm (right) or 1550 nm (left), over a range of Fermi levels from 0.05 eV to 1 eV and a range of relaxation times from 10 fs to 200 fs. Within this range of parameters, an artificial plasmonic resonance appears on the left panel. Adapted from [C].

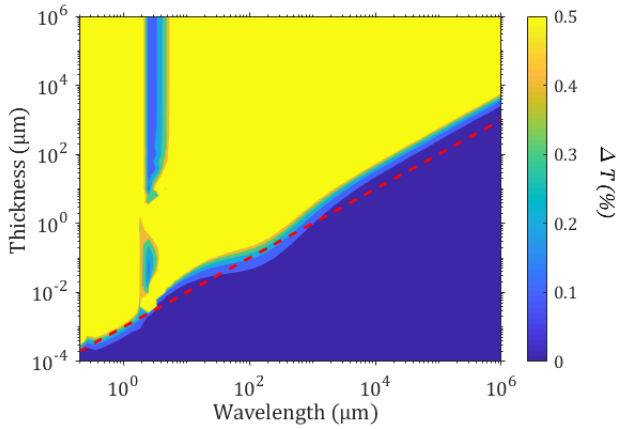

Figure 5.10: Difference of transmittance ΔT between the isotropic and anisotropic thin film models of graphene for a system air/graphene/glass. The refractive index of glass is taken as 1.5. Graphene is modeled using the Kubo formula with $E_F = 0.4$ eV,$\tau = 100$ fs. The red dotted line represents a thickness equal to $1/1000$ of the wavelength. Adapted from [C].

Ellipsometry

Ellipsometry is a powerful spectroscopic technique allowing to obtain information on the optical properties of materials. It gives experimentally access to the complex reflectance ratio

$$\rho = \frac{r_p}{r_s} = \tan\Psi\, e^{i\Delta}. \tag{5.82}$$

Optical constants of graphene and other 2D materials have been obtained by ellipsometry [21, 138]. However, the susceptibilities obtained using different models, the 2D anisotropic (with no out-of-plane response) and the 3D isotropic, in ellipsometry measurements on MoS_2 are different [21]. An explanation and a correction to this error can be brought by an analytical analysis. Using the Fresnel coefficients, isotropic ellipsometric ratios reported in the article [C] are:

$$\frac{\rho}{\rho_0} = 1 + 2\mathrm{i}\frac{\varepsilon_b k_z^a k_x^2}{(\varepsilon_a k_z^b)^2 - (\varepsilon_b k_z^a)^2}\left(\chi_S^{\parallel} - \varepsilon_a\varepsilon_b\xi_S^{\perp}\right). \tag{5.83}$$

where ρ_0 is the ellipsometric ratio without 2D material The factor in the parentheses is defined as the ellipsometric susceptibility

$$\chi_{ell} = \chi_S^{\parallel} - \varepsilon_a\varepsilon_b\xi_S^{\perp}. \tag{5.84}$$

If the thin film is isotropic, one has:

$$\xi_S^{\perp} = \frac{\chi_S^{\parallel}}{1 + \chi_S^{\parallel}/d} \tag{5.85}$$

by means of the equations relating the two susceptibilities (eq. (2.102)). With $\varepsilon_a = 1$, the ellipsometric susceptibility from eq. (5.84) is

$$\chi_{ell} = \left[\chi_S^{\parallel}\right]_i \left(1 - \frac{\varepsilon_b}{1 + \left[\chi_S^{\parallel}\right]_i/d}\right) \tag{5.86}$$

with $\left[\chi_S^{\parallel}\right]_i$ the in-plane susceptibility deduced from the isotropic model. From the anisotropic model with $\xi_S^{\perp} = 0$, χ_{ell} is simply

$$\chi_{ell} = \left[\chi_S^{\parallel}\right]_a \tag{5.87}$$

with $\left[\chi_S^{\parallel}\right]_a$ the in-plane susceptibility deduced from the anisotropic model. Comparing eq. (5.86) and (5.87), the relation between the susceptibilities from the two models (2D anisotropic and 3D isotropic) is expressed as

$$\left[\chi_s^{\parallel}\right]_a = \left[\chi_s^{\parallel}\right]_i - \varepsilon_b d + \frac{\varepsilon_b d}{1 + \left[\chi_S^{\parallel}\right]_i/d}. \tag{5.88}$$

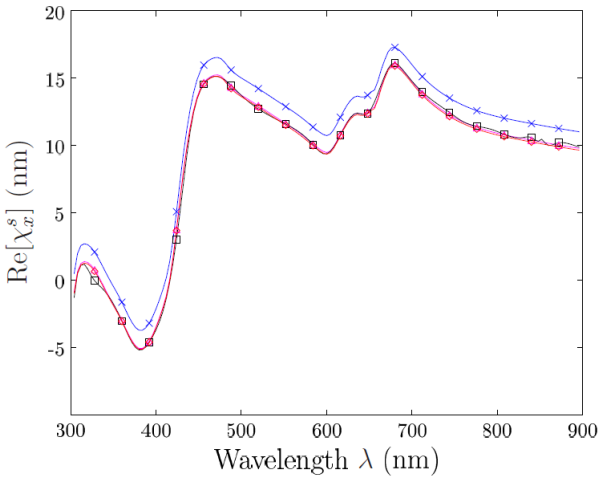

Figure 5.11: Values of $\mathrm{Re}\left(\chi_S^{\parallel}\right)$ for MoS_2 single layer retrieved with the isotropic thin film model ($\left[\chi_s^{\parallel}\right]_i$, blue curve and x symbol) and the anisotropic current sheet model ($\left[\chi_s^{\parallel}\right]_a$, black curve and □ symbol). Data from ref [21]. The red curve (◇ symbol) is calculated from $\left[\chi_s^{\parallel}\right]_i$ shifted by $-\varepsilon_b d$ and is almost superimposed with the black curve. The dielectric function of N-BK7 glass (substrate used in ref [21]) is taken from Sellmeier's equation provided by Schott [156]. Reproduced from [C].

Because, in general, $\left[\chi_S^{\parallel}\right]_i \gg d$, the last term of (5.88) can be ignored. Finally, the correction to the isotropic model is

$$\left[\chi_s^{\parallel}\right]_a = \left[\chi_s^{\parallel}\right]_i - \varepsilon_b d \tag{5.89}$$

In figure 5.11 the susceptibility obtained from the experimental data from [21] are plotted as well as the correction proposed above. In conclusion, the surface susceptibility of 2D materials can be obtained using the isotropic thin-film model if the phase-shift is small enough.

Effective thickness for numerical efficiency

In a thin film model, the thickness may be chosen arbitrarily as long as it is small enough compared to the wavelength, even in an isotropic model (as long as the out-of-plane response is negligible) as shown above. The permittivities are defined using the surface susceptibilities eq. (5.5) and (5.10):

$$\varepsilon_{eff}^{\parallel} = 1 + \frac{\chi_S^{\parallel}}{L}, \tag{5.90}$$

$$\varepsilon_{eff}^{\perp} = \frac{1}{1 - \frac{\xi_S^{\perp}}{L}} \tag{5.91}$$

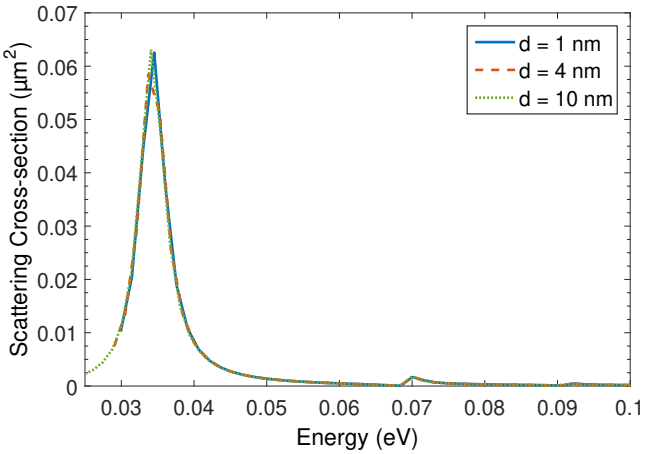

Figure 5.12: Scattering cross section by a ribbon of graphene of width $w = 2\,\mu m$ obtained using the DDA in *ddscat*, for different dipole sizes.

where the value of L must be consistent with the thickness in the methods (for example those presented in section 3). A thickness as small as 3.34 Å for graphene is then not required for example.

One may take advantage of this fact to increase the efficiency of numerical simulations. In methods in which the discretization of the particle must be isotropic (the size of the volume or surface elements must be the same in all directions), choosing a larger thickness permits to decrease drastically the number of elements, hence the computational effect.

In the discrete dipole approximation, if the dipole lattice is cubic and the distance between the dipoles is less than one nanometer, a structure of a few hundred of nm^2 of surface of 2D materials would require millions of dipoles. Using a much larger effective thickness allows us to perform calculations much faster without loss of accuracy as far as the effective permittivity is adapted for each size. I have tested this assumption for the IR response of a system of a graphene ribbons of two micrometers wide using the program *ddscat*. The scattering cross-section has been calculated for three different lattice parameters: $d_1 = 1$ nm , $d_2 = 4$ nm and $d_3 = 10$ nm, resulting in a number of dipoles respectively equal to $N_1 = 40000$, $N_2 = 2500$ and $N_3 = 400$ (figure 5.12). Thus the computation time was greatly reduced with larger dipoles, respectively $t_1 > 3$ days, $t_2 = 5$ h and $t_3 = 2$ h. The dipolar plasmonic resonance at 0.034 eV is nonetheless still well described using a larger grid parameter.

Conclusions

2D materials and heterostructures may be equivalently defined as surface polarization sheets or as thin films to a certain extent. The two methods are shown to be equivalent for small phase-shift, and it can even be numerically efficient to use large thickness in the thin film model. However, for large thickness, particular care must be taken. In particular, in the isotropic case, artificial plasmonic resonances can appears in spectra.

5.3 Optical spectra of anisotropic and structured 2D materials

In this section, the optical spectra of several 2D materials, and structured 2D materials are analyzed. The effective models of the previous section are tested based on ab-initio calculations and using the methods shown in the same section (2D polarization sheet and 3D thin film). A particular attention is put on the influence of the anisotropic and the out-of-plane response of these materials. It is expected that materials with a larger thickness, i.e. with more atoms along the out-of-plane direction, such as TMDs, have a larger out-of-plane response.

The surface susceptibility of different 2D atomic systems have been calculated using the TDDFT implementation in the GPAW code [157, 158], within the random-phase approximation: graphene, hBN, graphene - hBN bilayer, corrugated graphene and $MoSe_2$ (details of the TDDFT calculations are given in the appendix). Because the DFT is performed using a plane-wave extension, a large vacuum layer must be included in each unit cell in order to avoid the interactions between the repeating layers. The thickness of this vacuum must be chosen to converge the results and values between 10 and 15 Å are usually taken. The range of energy is chosen from 0 to 20 eV. It therefore account for UV light excitation, where the out-of-plane response is expected to be relevant. There is no focus on lower energy (in the IR of THz range) because phonons are not described in TDDFT.

Corrugated graphene is modelled using a unit cell containing 50 atoms forming a hill of height 0.25 nm in a cell of height 2.50 nm as described in our article [D] and, later, in section 7.2. The height of the superlattice of graphene and h-BN is 2.70 nm. For the bilayer, the graphene and hBN layers are separated by 0.34 nm, which corresponds to the interlayer distance in graphene and is close to the average interlayer distance of graphene-hBN heterostructures accounting for van der Walls corrections [159]. The total height of the cell is 2.0 nm. The GW and BSE calculations were not performed due to computational limitations, as explained in section 2.1, which could result in inaccurate optical spectra, in particular for semiconductor ($MoSe_2$) and insulator (BN). However, the focus here is on the effect of the anisotropy for optical response of heterostructures, therefore the same level of approximation is considered to be enough when comparing systems. The effective models for the response functions and heterostructures remain valid for all levels of approximation.

Surface susceptibility

The computed surface susceptibilities of the different 2D materials are shown on figure 5.13. For graphene and hBN, the π and the $\pi + \sigma$ plasmons are found around respectively 4.5 eV and 14 eV in the in-plane susceptibility as expected without the GW and BSE correction [103]. The GW correction tends to blueshift the plasmon energy and the BSE has the inverse effect which produces a global blueshift of less than 0.5 eV [129, 160–162].

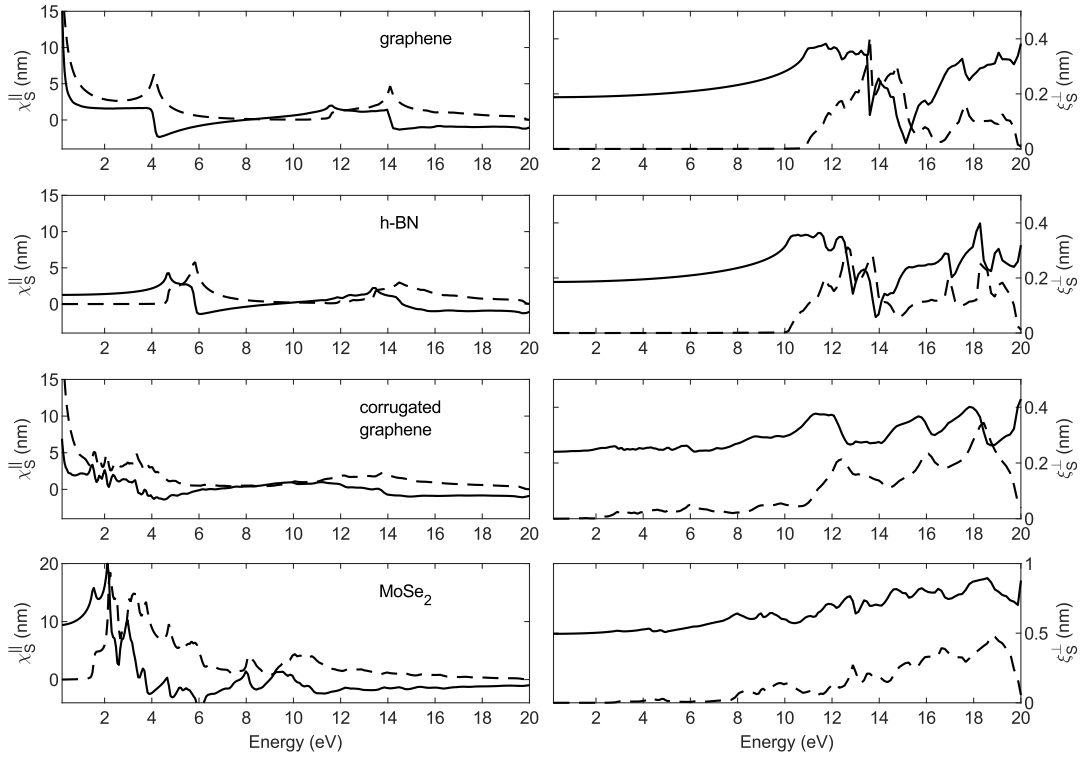

Figure 5.13: In-plane surface irreducible susceptibility (left) and out-of-plane surface external susceptibility (right) of (from top to bottom) graphene, hBN, corrugated graphene and $MoSe_2$. The solid line is the real part, the dashed line is the imaginary part.

The susceptibility of the corrugated graphene has been published in the article [D]. The in-plane susceptibility of $MoSe_2$ is slightly different than previously reported [163], but this can be attributed to the approximation described above.

The imaginary part of the out-of-plane susceptibility, responsible for the absorption is null below 10 eV for graphene and hBN such that the role of the anisotropy will only be relevant at higher energy, in the UV, as mentionned previously. For corrugated graphene and $MoSe_2$ the imaginary part of the out-of-plane susceptibility increases slowly already at energy below 10 eV, due to the atomic structure extending in the normal direction. However, the real part of the out-of-plane susceptibility is also relevant as it can be measured using ellipsometry [22]. It is much higher for materials with a larger thickness such as $MoSe_2$. This is explained by the fact the real part of the susceptibility is related to the density of dipole moment, and the dipole moment is larger when the distance between the charge is longer.

Comparison with the literature

The out-of plane surface susceptibilities or conductivities of some 2D materials have already been calculated from ab initio approaches in recent papers [20, 126, 164]. How-

ever, particular care must be taken considering the out-of-plane susceptibility. In ref [20], the authors obtained the surface conductivities of graphene and silicene from the macroscopic dielectric functions using the following equations:

$$\sigma_S^{\parallel} = -i\varepsilon_0\omega L\left[\varepsilon_{eff}^{\parallel} - 1\right] \tag{5.92}$$

and

$$\sigma_S^{\perp} = -i\varepsilon_0\omega L\left[1 - \frac{1}{\varepsilon_{eff}^{\perp}}\right]. \tag{5.93}$$

These equations are equivalent to eq. (5.5) and (5.10) although the authors remain elusive on the origin of eq. (5.93). Their calculated surface conductivities for graphene are replicated on figure 5.14, on the left. The top panel represents the real part of the conductivity, the bottom one represents the imaginary part, with, in black, the in-plane surface conductivity, and in red the out-of-plane conductivity. The conductivity of graphene (figure 5.14, right panel) obtained using the calculated surface susceptibilities of figure 5.13 (top panel) does not correspond to their results. In particular, my calculations predicts a much smaller out-of-plane response. In their paper, the authors suggest that, for a large vacuum layer in the cell ($L \to \infty$), the following relation holds:

$$L\left[1 - \frac{1}{\varepsilon_{eff}^{\perp}}\right] = L\left[\varepsilon_{eff}^{\perp} - 1\right]. \tag{5.94}$$

According to this, the surface conductivity in the out-of-plane direction is

$$\sigma_S^{\perp} = -i\varepsilon_0\omega L\left[\varepsilon_{eff}^{\perp} - 1\right]. \tag{5.95}$$

Using this equation, the surface conductivities obtained in [20] can be reproduced (figure 5.14, middle panel). However, their approximation is not justified rigorously in [20] and it seems that this approximation is not valid in this particular case as equations (5.93) and (5.95) do not give the same results.

Long range interactions

It has been shown that artificial long range coulomb interactions occur for out-of-plane polarization [126] even for large vacuum layers between the periodically repeated planes of 2D materials in the superlattice of the TDDFT calculations. Ideally these long range interactions must be cut off to study the out-of-plane response of 2D materials. In [126], the authors proposed a mixed-spaced approach to avoid this interaction. By means of simplicity and lack of time, this approach was not implemented here. However, with a large vacuum layer, these interactions can be reduced. To investigate this effect, the surface external susceptibility of graphene for the out-of-plane polarization has been calculated for different sizes of the cell and with different k-grid discretization. In figure 5.15, this susceptibility is plotted for two large values of the vacuum thickness, and for a non trivial k-grid discretization along the z-axis. Below 11 eV, the curves are superimposed. At higher energies, differences appear. First, the fact that increasing

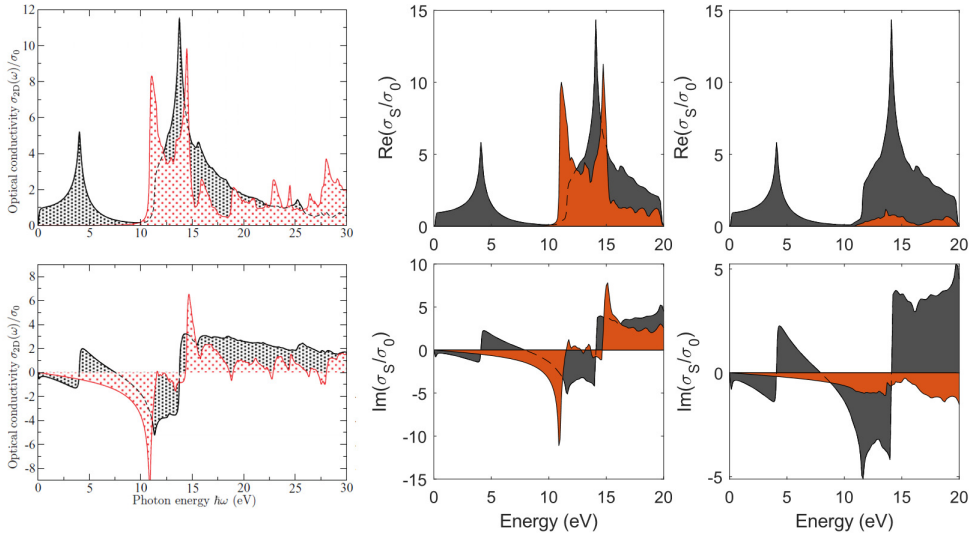

Figure 5.14: Real (top) and imaginary (bottom) parts of the surface conductivity for in-plane (black) and out-of-plane (red) polarization. Left: reproduced from [20]; middle: same as on left, reproduced with eq. (5.92) and (5.95); right: same as on the left, reproduced with eq. (5.92) and (5.93).

the size of the cell changes the susceptibility is an argument in favor of the long range interactions. Then, using a k-grid with more points along the z-axis also changes the average (macroscopic) surface susceptibility which should not be the case if there were no interaction between the repeated layers. However, it seems that using the finer k-grid has a low impact on the spectra for a cell of height 2.68 nm suggesting that, for this quantity of vacuum (a layer of 2.34 nm), a convergence is nearly obtained. However, due to computational limitations, the convergence has not been verified further.

Vertical heterostructures

Two kinds of heterostructures are studied here. First, a multilayer with a large number of identical layers (graphene in this case) in order to estimate the limits of the 2D model compared to the thin film model for heterostructures. The graphene layers must not be interacting such that the system can indeed be considered as a graphene multilayer and not graphite. These structures have been synthesized experimentally up to a few layers using the transfer techniques on CVD graphene [138]. Then, a graphene-hBN bilayer, which has also been synthesized [165, 166] and whose optical properties have already been studied extensively for in-plane polarizations [142, 143, 161]. These systems are used to illustrate the effective model proposed in the first section of this chapter.

In Fig 5.16, the absorption of a single sheet of graphene (black), a multilayer of 10 sheets (blue) and a multilayer of 20 sheets of graphene (red) calculated using the thin film model (solid lines) and the polarization sheet model (dotted lines) are shown. The thickness of a single 2D layer is 3.35 Å in the thin film model. The angle of incidence is $70°$ in TM polarization and the refractive index of the substrate is constant ($n = 1.5$). For

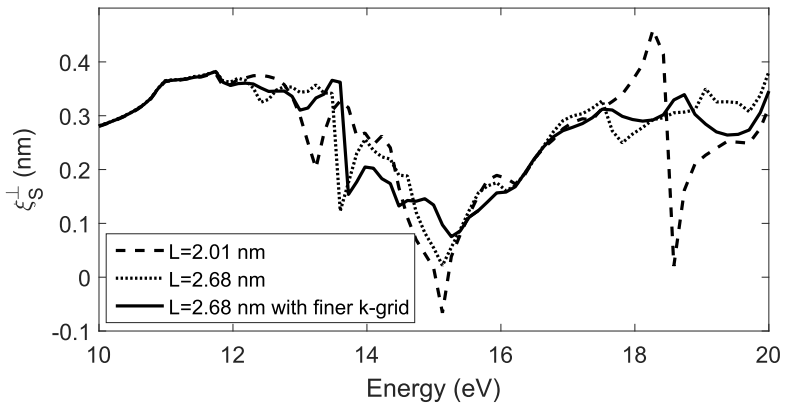

Figure 5.15: Surface external susceptibility for graphene in the out-of-plane polarization. Three case have been considered: a supercell of height 2.01 nm, a supercell of height 2.68 nm and a supercell of height 2.68 nm with a finer k-grid for the representation of the wave-function in the out-of-plane direction.

a single layer and for 10 layers, the two models agree quite perfectly. It shows that the 2D model is quite robust even for large number of layers. For 20 layers, the discrepancies between the models become significant at large energy, in particular around the $\pi + \sigma$ plasmon. In this case, the wavelength in the layer becomes too small compared to thickness L.

Now, the surface susceptibilities of a graphene-hBN vertical heterostructure as obtained by TDDFT are compared to the effective susceptibilities calculated using the susceptibilities of a single layer of graphene or hBN and the additivity rules, equations (5.16) and (5.18) (figure 5.17, dotted lines) with the real part (left) and imaginary part (right) of $\chi_S^{\parallel}$ (top) and $\xi_S^{\perp}$ (bottom) represented. The effective model is accurate for $\chi_S^{\parallel}$ except around the π-plasmon at 4.5 eV. This suggests a coupling between the corresponding π-plasmons of each 2D material because this coupling cannot be captured by the effective model as explained in the first section of the chapter. For $\xi_S^{\perp}$, the effective model fails to reproduce the exact model at high energy, over 10 eV though the global trend is conserved. This is due to long range electronic interactions mentioned above.

In conclusion, the effective model for vertical heterostructures reproduces quite well the exact model though care must be taken for plasmonic resonances and with the long range interaction for out-of-plane polarization.

Horizontal heterostructures

Two horizontal heterostructures are studied here: stacking of graphene nanoribbons to test the validity of the effective models presented in section 5.1 and graphene-hBN nanoribbons that present interesting optical properties [147, 167]. In section 5.1, a model adapted for 2D material ribbons was presented, in contrast to the model usually adopted for bulk material ribbons and sometimes also 2D materials. These models are referred as

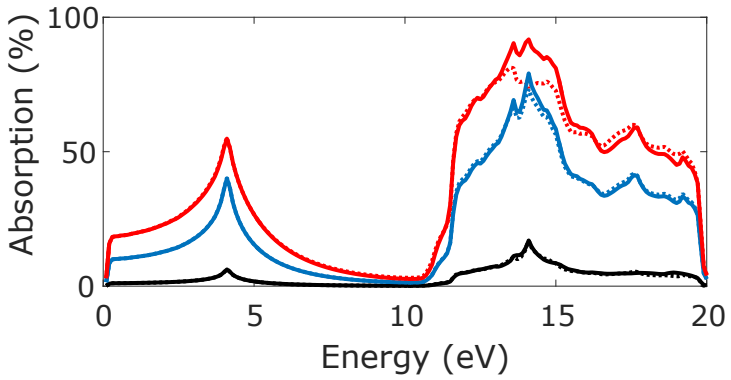

Figure 5.16: Absorption by a single layer (black), 10 layers (blue) of graphene and 20 layers (red) at an incident angle of 70° calculated using the thin film model (solid line) and the 2D model (dotted line).

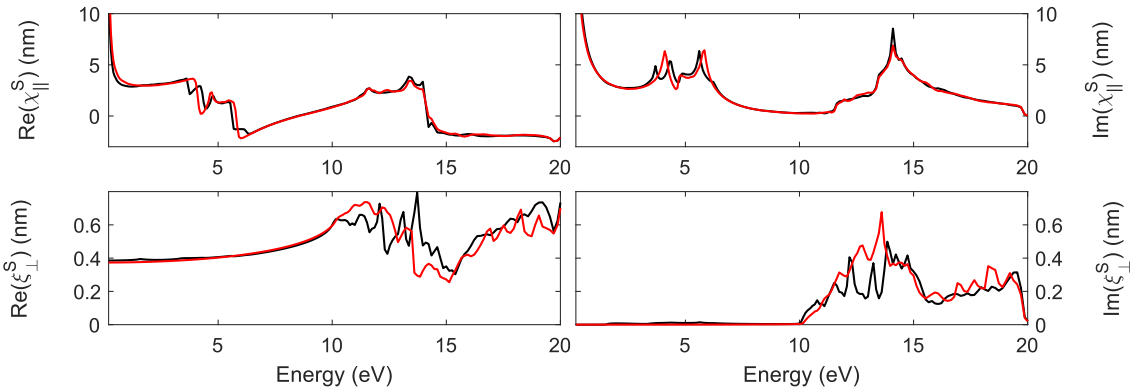

Figure 5.17: Surface susceptibilities of a graphene-hBN heterostructures from the full system (black lines) and the effective model (red lines). The real part is on the left, the imaginary part on the right.

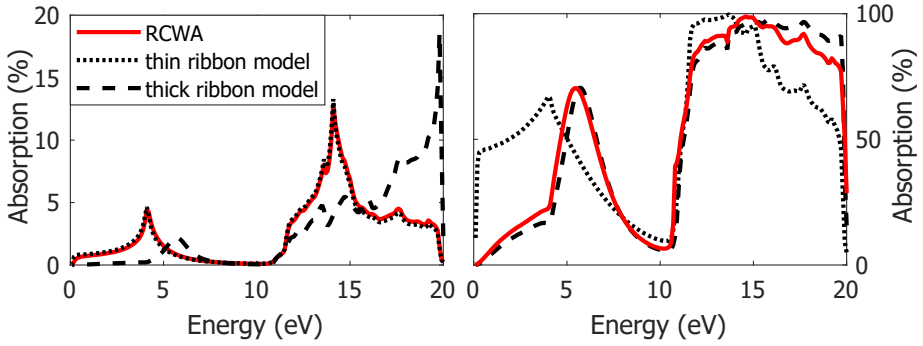

Figure 5.18: Absorption by ribbons of graphene with filling factor of 0.75 at an incident angle of 70°, polarized perpendicularly to the ribbons, for one layer (left), one hundred layer (right).

the thin-ribbon model and the thick-ribbon model respectively. Graphene ribbons of 15 nm, spaced by 5 nm of air, corresponding to a filling factor of $f = 0.75$ are considered. To test the thick-ribbon model, an unrealistic stacking of 100 ribbons with a total thickness of 35 nm is used. The RCWA offers the exact solutions as long as the results are converged in respect to the number of plane waves in the Fourier series[4]. However due to the impossibility to use the RCWA for non-planar or finite systems, the effective models remain interesting. In figure 5.18, the RCWA simulations that account for the lateral heterostructure is compared to the thin-ribbon and the thick-ribbon models, for a single layer of graphene (left) and for a multilayer of 100 sheets of graphene. The thin ribbon model is accurate for ribbons of a single sheet of graphene while the thick ribbon model is better for the multilayer but it appears that no model fits well for both.

To better understand the transition between the two models, the relative error between each effective model and the RCWA solution, obtained as the area between the curves, is displayed on figure 5.19. It confirms that, as shown before for very few layers, the thin ribbon model is accurate whereas, for several tens of layers, the thick ribbon model works better. In between, for a number of layers from 3 to 30, the error is over 15 % for both models and a full description of the system is necessary.

A system of alternating ribbons of single layer graphene and h-BN, with a width of respectively 15 nm and 5 nm is now investigated. This kind of system could sustain plasmons [167], which could be spotted by comparison between the effective and exact models, as explain in section 5.1. In figure 5.20, the three models are compared: the RCWA method, the effective thin film model and the effective surface current model. The three models are in almost perfect agreement, except at two particular energy values. Around 5 eV, the two effective models agreed but fail to reproduce the exact results. This can be explained by a plasmonic resonance that cannot be captured by effective models. This discrepancy was not visible in the graphene-air system which suggests that the plasmon originated from a coupling between the π-plasmon of graphene and that of h-BN similarly to the case of vertical heterostructures. At high energy, above 15

[4]For this particular system, the results converged with a small number of plane waves.

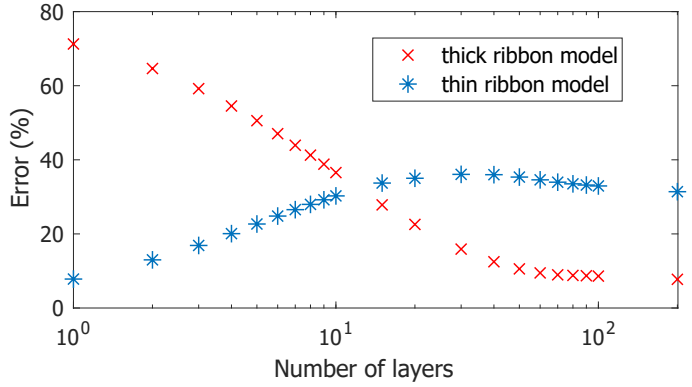

Figure 5.19: Relative error of the effective models (thin ribbon and thick ribbon) compared to the exact RCWA solution.

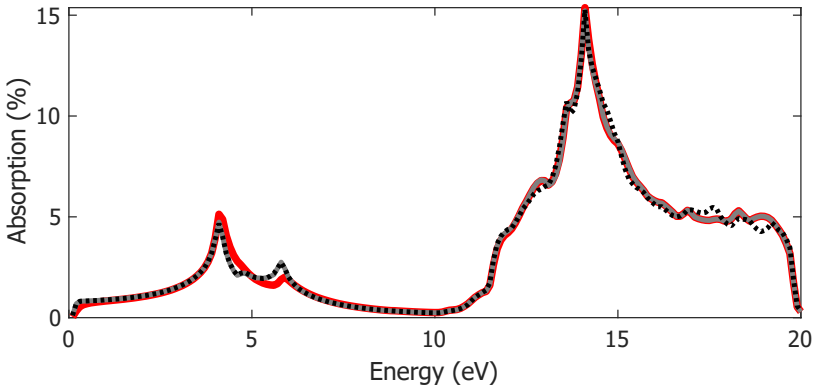

Figure 5.20: Absorption by alternating ribbons of graphene and hBN, with filling factor respectively of 0.75 and 0.25, at an incident angle of $70°$, polarized perpendicularly to the ribbon, for three different models: exact model with RCWA (solid red line), effective thin film model (solid grey line), effective surface current model (dotted black line).

eV, the exact and the effective thin film models are in agreement but the surface current model differs. At high energy, it is expected that the wavelength is small enough that the small phase shift approximation is not valid anymore, as already explained in the previous subsection. The strong result here is that a system composed of two structured anisotropic thin materials can be accurately described by an analytical 2D polarization sheet model.

Role of the out-of-plane component

In this short section the influence of the calculated out-of-plane component of the dielectric tensor on the optical spectra is analysed for five systems composed with 2D materials. In particular, the domain of validity of the isotropic or no out-of-plane response models for describing the permittivity are investigated. The five systems are:

pristine graphene, graphene-hBN vertical heterostructure, ribbons of graphene and hBN, corrugated graphene and $MoSe_2$. The results are plotted on figure 5.21. For each system, the absorption is calculated, at an incident angle of $70°$ in TM polarization, with three different cases for the out-of-plane component: the DFT-calculated z-component (red solid line), no out-of-plane response ($\varepsilon_\perp = 1$) (black dashed line) and an isotropic response ($\varepsilon_\perp = \varepsilon_\parallel$) (black dotted line). As expected for all systems, because the imaginary part of the surface susceptibility $\xi_S^\perp$ becomes large as energy increases, the out-of-plane response is non-negligible at high energy, starting at 10 eV. In particular, the model without out-of-plane response gives the worst approximation in this range. For $MoSe_2$ and corrugated graphene, these differences are even larger because of the large thickness of these materials. At lower energy, the isotropic model is inaccurate around $6 - 8$ eV for all systems containing graphene. The additional peak appearing between 6 and 8 eV is due to artificial plasmonic resonances due to the metallic behaviour of graphene in the normal direction as seen in the previous section and highlighted in our article [C]. In conclusion, the isotropic model for 2D materials should be avoided because of artificial peaks at low energy while the no out-of-plane response model is still accurate below 10 eV. At higher energy, where the out-of-plane response is significant, the complete model should be used.

Conclusions

The original effective models developed in section 5.1 for vertical and horizontal heterostructures have proven to be robust to predict optical spectra. The models for vertical heterostructure reproduce quite well the susceptibility of a bilayer of graphene-hBN from the susceptibility of each 2D material and the absorption of graphene multilayers from both the 2D and 3D methods. Only plasmonic excitation cannot be predicted by the effective models. For horizontal heterostructures and ribbons, two models have been proposed, depending on the thickness of the ribbon. It is shown that the thin ribbon model is good for single to 3-layer ribbons while the thick-ribbon model is better for materials with thickness larger than 30 nm. In many cases, if possible, the RCWA should be used because it gives the exact solution. However, for non-planar surfaces or highly complex structures, the effective model is obviously much easier to implement.

On the modelling of the isotropy of a single layer, it has been shown that the isotropic model for 2D materials is worse than a model without out-of-plane response for metallic 2D materials because of an artificial plasmonic resonance. For the considered materials, at high energy, the fully anisotropic model should be used to accurately describe the optical response, in particular for materials with larger extension in the normal direction, like $MoSe_2$ or corrugated graphene.

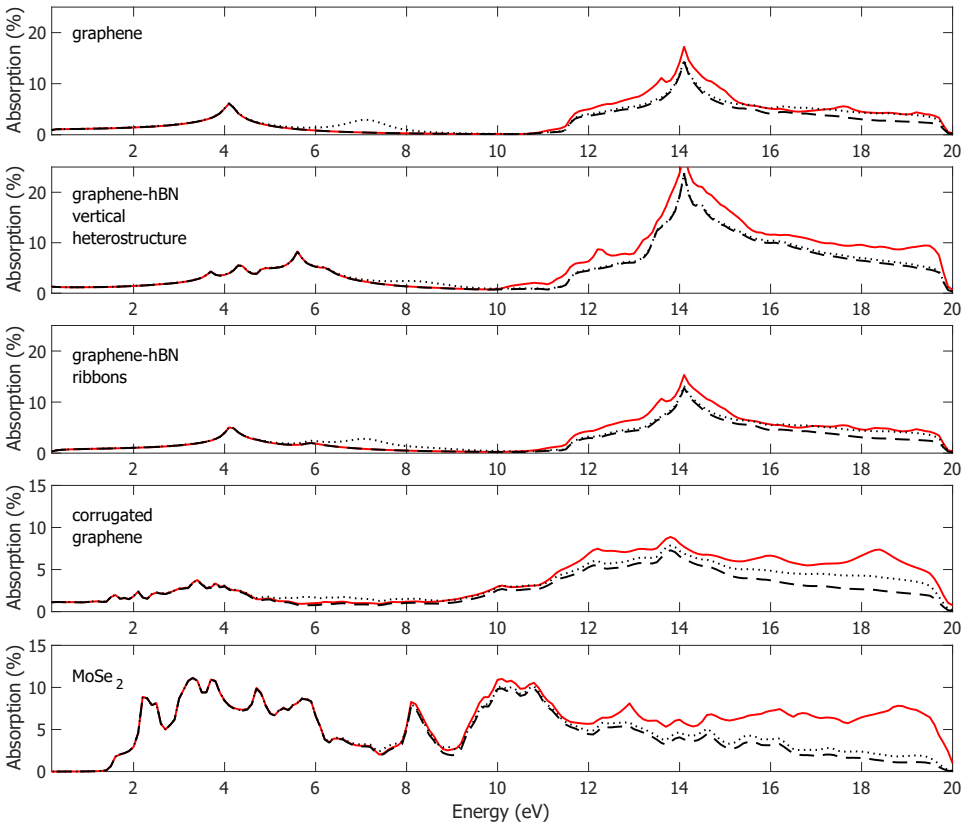

Figure 5.21: Absorption spectra of (from top to bottom) pristine graphene, graphene-hBN vertical heterostructure, ribbons of graphene and h-BN, corrugated graphene and $MoSe_2$. The red solid line corresponds to the DFT-calculated anisotropic model, the dashed black line corresponds to a model without out-of-plane response and the dotted black line corresponds to an isotropic model.

Chapter 6

Brewster angle shift with conducting 2D materials

When a 2D material is deposited on a dielectric surface, it slightly modifies the optical properties of the system, including the reflection and transmission at the interface. An example of that is the shift of the Brewster angle, the angle at which a p-polarized light ray is not reflected. The shift depends on the conductivity of the 2D materials. Graphene, as a semi-metallic 2D material, is therefore a great candidate to experimentally highlight this shift. In this chapter, the origin of the shift is explained, and its relation with the conductivity is explicitly given. The theoretical results are compared with experimental measurements of the shift.

A particular optical phenomenon attributed to a conducting 2D material is the shift it induces on the Brewster angle. A conducting layer at the interface between two media changes the condition at which the reflected wave vanishes in the transverse magnetic polarization. This effect has been reported several times in the last few years [12–18] but our article [B], published in 2018, is one of the first comprehensive study of the phenomenon, with experimental measurements performed on graphene and graphene multilayers. As visible light and IR are considered, the out-of-plane response can be neglected, at least for graphene. It was shown later that this out-of-plane response could have an effect on the shift of the Brewster angle of graphene [18]. To be coherent with our article [B], the surface conductivity is used to describe the electromagnetic response of 2D materials. Here, the article is summarized with a focus on the theoretical results. It is shown that this phenomenon can be used to measure the conductivity of 2D materials. Moreover, due to the optical tunability of graphene in the IR range, an active modification of the shift is possible, paving the way to practical applications in telecommunications.

6.1 Physical origin of the phenomenon

The Brewster effect occurs when light is not reflected in p-polarization [168]. This arises when the polarization density $\mathbf{P}_{tot}$ in the dielectric material is parallel to the wavevector of the reflected wave $\mathbf{k}_r$ (figure 6.1a). In the classical case, i.e. without conducting layer at the interface, the only component of the polarization density is due to the local electric dipoles excited by the refracted wave, i.e. $\mathbf{P}_{tot} = \mathbf{P}_{bulk}$. It follows that $\theta_B + \theta_{B2} = \pi/2$ where θ_B stands for the incident Brewster angle and θ_{B2} for the corresponding refracted angle. The formula giving the Brewster angle is retrieved from Snell law:

$$\tan\theta_B = \frac{n_2}{n_1}. \tag{6.1}$$

This situation is no longer valid once a conducting 2D material lies at the interface (figure 6.1b). Indeed, a bidimensionnal current density, $\mathbf{J}_{2D} = \sigma_{2D}\mathbf{E}$ with σ_{2D} the 2D conductivity, can occur and is related to a planar component of the polarization density $\mathbf{P}_{2D} = \int \mathbf{J_{2D}} dt$. The higher the 2D conductivity, the closer to the interface the total polarization density direction and the higher the Brewster angle shift. In the limit of an infinite 2D conductivity, the modified Brewster angle θ'_B tends to $\pi/2$.

6.2 Numerical approximation of the shift

To calculate the modified Brewster angle, the generalized reflection Fresnel coefficient in p-polarization should be canceled out once a 2D conducting plane is inserted between two semi-infinite dielectric media of refractive index n_1 and n_2. If one neglects the out-of-plane response, the reflectance is given from eq. 5.63:

$$R_p = \left| \frac{n_1\cos\theta_2 - n_2\cos\theta_1 - \frac{\sigma_S}{\epsilon_0 c}\cos\theta_1\cos\theta_2}{n_1\cos\theta_2 + n_2\cos\theta_1 + \frac{\sigma_S}{\epsilon_0 c}\cos\theta_1\cos\theta_2} \right|^2. \tag{6.2}$$

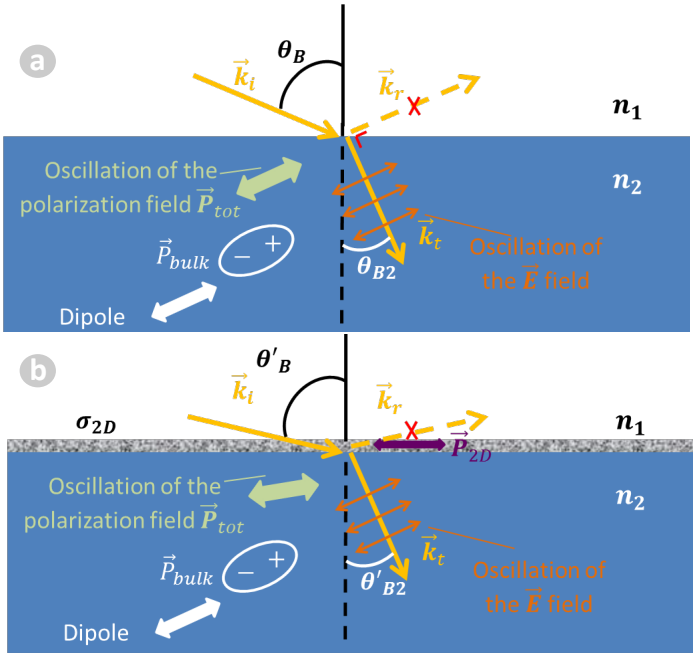

Figure 6.1: Incident p-polarized electromagnetic wave of wavevector $\mathbf{k}_i$ at Brewster angle θ_B impinging on the interface between two dielectric media of refractive indexes n_1 and n_2. The reflected (transmitted) wave has a wave vector $\mathbf{k}_r$ ($\mathbf{k}_t$) and the reflected (refracted) angle θ_B (θ_{B2}) a) Classical Brewster effect, b) Modified Brewster effect due to the presence of a 2D conducting layer at the interface. Reproduced from [B].

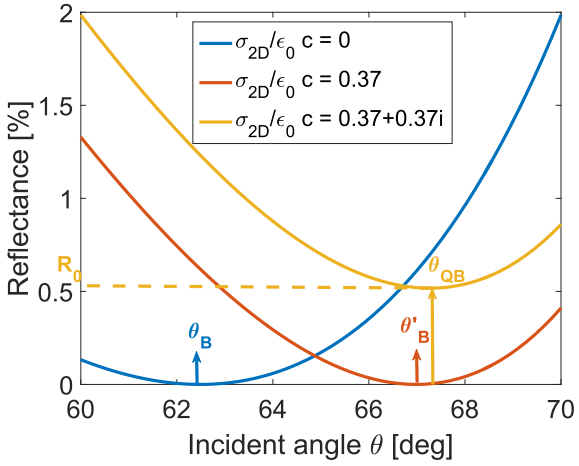

Figure 6.2: Reflectance in p-polarized radiation of a single graphene layer lying over a silicate substrate ($n_2 = 1.92$) at 30 GHz for the bare substrate (blue line), a real conductivity ($\sigma_S = 0.37\,\varepsilon_0 c$, red line) and a conductivity with an artificially high imaginary part ($\sigma_{2D} = 0.37 + 0.37i\,\varepsilon_0 c$, yellow line). The Brewster angle θ_B of bare substrate, the modified Brewster angle θ'_B due to the presence of a 2D conductivity at the interface and the modified quasi-Brewster angle θ_{QB} are indicated on the figure. Reproduced from [B].

To obtain the exact value of this modified Brewster angle θ'_B for real σ_S, one should cancel R_P which leads to the condition:

$$n_1 \cos\theta_2 - n_2 \cos\theta_1 - \frac{\sigma_S}{\epsilon_0 c} \cos\theta_1 \cos\theta_2 = 0. \tag{6.3}$$

This equation corresponds to a quartic equation in $\cos\theta_1$ and can be solved numerically to extract $\theta_1 \equiv \theta'_B$ for a given σ_{2D}. For example, CVD graphene in the microwave range has particularly high surface conductivity $\sigma_S = 0.37\,\varepsilon_0 c$ (at 30 GHz [77]). As shown in figure 6.2a, the subsequent shift of the Brewster angle is $67.0° - 62.4° = 4.6°$ ($n_1 = 1$, $n_2 = 1.92$ for SiO_2 at $30\,GHz$). If the imaginary part of the conductivity is non-zero, the minimum reflectance in p-polarized radiation is never zero and has its minimal value (R_0) at the quasi-Brewster angle θ_{QB}. However, even for an intentionally high imaginary part (for instance $\Re(\sigma) = \Im(\sigma)$), R_0 is very small and $\theta_{QB} \approx \theta'_B$ (figure 6.2a).

Equation (6.3) can be solved approximately for small angular shift $\Delta = \theta'_B - \theta_B$. Here, I propose another approximation than those made in the article [B]. With θ'_{B2} the refracted angle at the shifted Brewster incidence, defining $\alpha = \frac{n_2}{n_1}$, $\beta = \sqrt{1+\alpha^2}$ the following relations can be written:

$$\begin{aligned} \sin\theta_B &= \frac{\alpha}{\beta} & \cos\theta_B &= \frac{1}{\beta} \\ \cos\theta'_B &= \frac{1-\alpha\Delta}{\beta} & \cos\theta'_{B2} &= \frac{1}{\beta}\left(\alpha - \frac{\Delta}{\alpha^2}\right) \end{aligned} \tag{6.4}$$

where I used the first order approximations $\cos\Delta \cong 1$, $\sin\Delta \cong \Delta$ and $\Delta^2 \cong 0$. The

solutions to eq. (6.3) is then:

$$\Delta = \frac{\frac{\sigma_S}{\varepsilon_0 c}}{\alpha\left(\frac{\sigma_S}{\varepsilon_0 c} + n_1\beta\right) + \frac{1}{\alpha^3}\left(\frac{\sigma_S}{\varepsilon_0 c} - n_1\beta\right)}. \tag{6.5}$$

If $n_2 \gg n_1$ [1] and $\frac{\sigma_S}{\varepsilon_0 c} \ll 1$, the approximation for low conductivity presented in the article [B] is retrieved:

$$\Delta = \frac{n_1}{n_2^2}\frac{\sigma_S}{\varepsilon_0 c}. \tag{6.6}$$

This equation is remarkable by its simplicity and shows that the shift in Brewster angle depends linearly on the conductivity for small conductivity. Figure 6.3a shows the Brewster angle as a function of the surface conductivity, for the exact value retrieved numerically from (6.3), and the approximated value. The first approximation (eq. (6.5), in red) is close to the exact solution (in black) while the second approximation (6.6, in blue) is valid only for low conductivity. To better estimate the validity of the approximations, the relative error made on θ'_B, compared with the exact solution for the two approximations is depicted on figure 6.3. The horizontal dashed line indicates a 1% error and defines roughly our domain of validity of the approximations. The second approximation is only valid for surface conductivity verifying

$$\frac{\sigma_S}{\varepsilon_0 c} < 0.2 \tag{6.7}$$

as, for example, graphene in the visible range (see later). It should be emphasized that those approximations were derived considering the a purely real 2D conductivity. However, as demonstrated earlier, θ_{QB} and $\theta_{B'}$ do not significantly differ for a small imaginary part of the 2D conductivity.

The previous analysis is for an infinite substrate. However in order, to better correspond to experimental situations, the finite thickness of the substrate should be accounted for. This finite thickness is responsible of backside reflections at the second interface between the substrate and the surrounding medium. This situation can be handled by adapting the reflection coefficient. The reflection coefficient of eq. (6.2) is now written $R_{12,c}$ where the first subscript stands for the direction of propagation of the wave, from medium 1 (incident) to medium 2 (substrate) here, and the second subscript for the presence of the conducting layer at the interface (c) or not (f, "free"). If the thickness of the substrate is much bigger than the coherence length (in the experiment, a Xenon light is used, with small coherence length), interferences can be neglected and the total reflectance becomes [169]:

$$R_{tot} = R_{12,c} + T_{12,c}R_{21,f}\sum_{i=0}^{\infty}\left(R^i_{21,c}R^i_{21,f}\right)T_{21,c} \tag{6.8}$$

with

$$T_{12,c} = T_{21,c} = \frac{4n_1 n_2\cos\theta_1\cos\theta_2}{\left|n_1\cos\theta_2 + n_2\cos\theta_1 + \frac{\sigma}{\varepsilon_0 c}\cos\theta_1\cos\theta_2\right|^2}, \tag{6.9}$$

[1] This seemingly very strong condition is justified retrospectively by the simplicity and validity of the obtained formula.

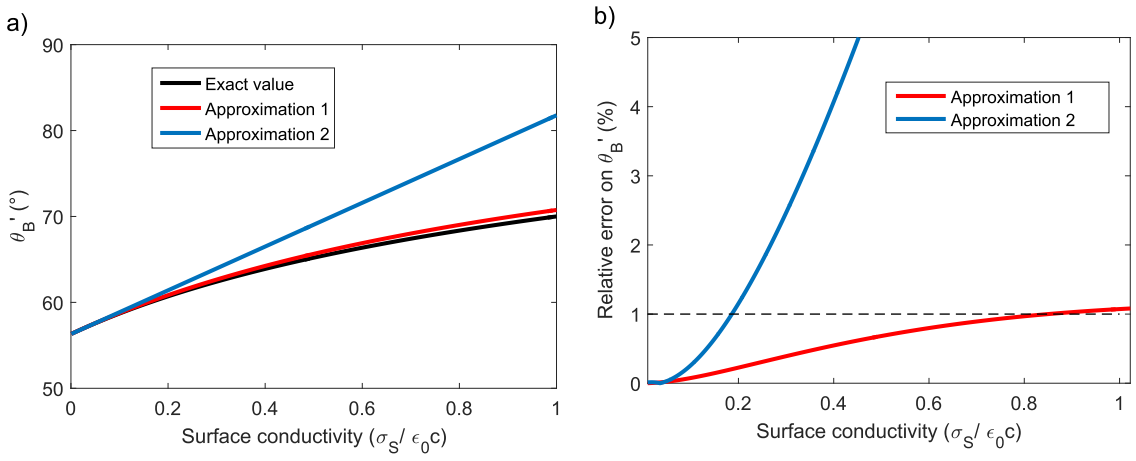

Figure 6.3: a) Shifted Brewster angle for the approximation of equations (6.5) (approximation 1) and (6.6) (approximation 2). b) Relative errors on the approximations with $n_2 = 1.5$.

the transmittance at the first interface, and the sum is done over all the multiple reflections. Calculating analytically the sum in equation (6.8), it gives:

$$R_{tot} = R_{12,c} + \frac{T_{12,c}^2}{1 - R_{12,f} R_{12,c}} R_{12,f} \tag{6.10}$$

As the first term of equation (6.10) vanishes at the modified Brewster angle θ'_B (for a real conductivity), the second vanishes at the usual Brewster angle θ_B due to the factor $R_{12,f}$ (see figure 6.4, in red for $= R_{12,c}$, in blue for $R_{12,f}$). In the vicinity of both Brewster angles (which are separated by a few degrees), reflectance is close to zero and transmittance is close to unity. Therefore, the coefficient in front of $R_{12,f}$ is close to unity near the Brewster angles. Moreover, near these angles, the curve corresponding to the total reflectance can be approximated as the sum of two parabolas, using a series expansion of each term around their zeros. As $R_{12,f}$ and $R_{21,c}$ are very similar functions, corresponding to the same reflection phenomena with a small perturbation for $R_{12,c}$, the quadratic coefficients of both parabolas are the same. With this condition, the minimum of the resulting curve arises exactly at the middle between the two minima ie. the total quasi-Brewster angle (where the reflectance is minimum) θ''_B considering a finite substrate, is half way between the usual Brewster angle θ_B and the modified Brewster angle θ'_B:

$$\theta''_B = \frac{\theta'_B + \theta_B}{2} \tag{6.11}$$

and it consequently gives a angular shift divided by two compared to the value for an infinite substrate:

$$\Delta = \theta''_B - \theta_B = \frac{\theta'_B - \theta_B}{2}. \tag{6.12}$$

Therefore, the approximations (6.5) and (6.6) must be scaled down by a factor $\frac{1}{2}$ when considering a finite substrate.

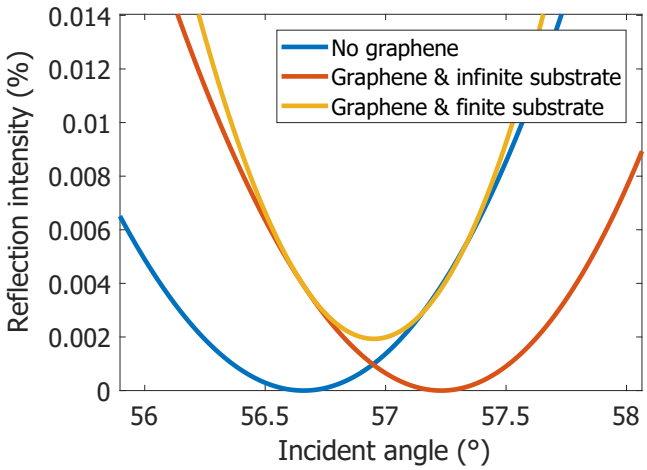

Figure 6.4: Reflectance for a plane wave at the interface between air ($n_1 = 1$) and silica glass ($n_2 = 1.5$) , with or without graphene ($\sigma/\varepsilon_0 c = \pi\alpha$) at the interface and considering finite or infinite substrate. Reproduced from [B].

6.3 Application to graphene and other 2D materials

The Brewster shift can be evaluated in graphene using the Kubo formula described in section 1.3 [2]. The Brewster angle can be tuned by adjusting the Fermi level E_F as depicted in figure 6.5 for different realistic values of the Fermi level and for a single layer of graphene deposited on silica glass with a frequency dependent refractive index reported in the literature [170]. The modification of the Fermi level from 0.3 to 0.5 eV causes a shift as high as $\Delta \approx 1°$ in the C-band (around 1550 nm) of telecommunications. The largest shift in Brewster angle is predicted around 266 nm and is related to the excitonic resonance [74, 171]. Other conducting 2D materials are emerging such as silicene, germanene or stanene. Optical conductivities of those materials are scarcely available [172, 173]. Table 6.1 reports the expected shift in Brewster angle at some particular wavelengths using data from [172]. The substrate is considered as silica glass as before. The shift can also be quite large for those other 2D materials, even in the visible range.

Heterostructures and multilayers of 2D materials can also be considered in order to modify the conductivity. As seen before, the effective 2D conductivity can be defined as the sum of the conductivity of each 2D material layer i.e. $\sigma_{2D,tot} = \sum \sigma_{2D,i}$ [77, 171]. This approximation stands if the different layers are electronically decoupled with respect to each other, e.g. by the insertion of a dielectric layer or by a twisted stacking in the case of graphene.

[2] Temperature here is $T = 300$ K, the relaxation time is $\tau = 75$ fs. The hopping parameter from the tight-biding model is $t = 2.6$ eV and the parameters of the Fano model for the excitonic correction are $q = -1.4$ eV, $E_{res} = 4.85$ eV, $\Gamma = 780$ meV

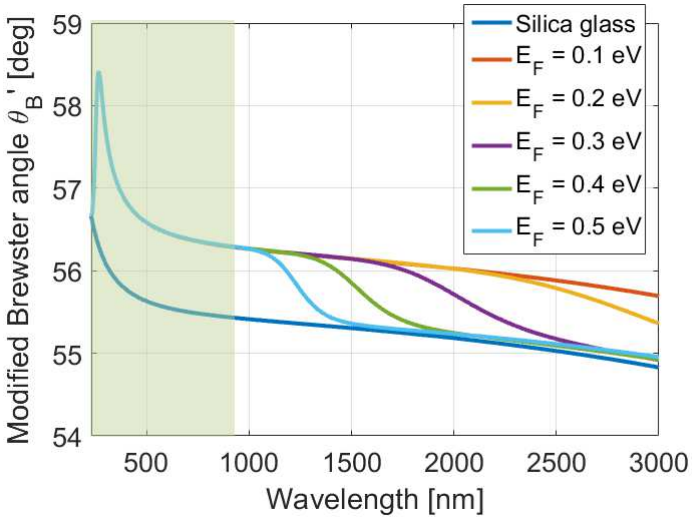

Figure 6.5: Modified Brewster angle for graphene deposited on silica glass for several Fermi level values obtained by solving equation (6.3) numerically. The shaded area corresponds to the region of the experiment, i.e. UV, visible and near-infrared. Reproduced from [B].

2D material	$\sigma/\varepsilon_0 c$	**Wavelength** λ **[nm]**	$\Delta\theta$ **[deg]**
Stanene	0.092	708	2.5
Stanene	0.177	413	4.7
Stanene	0.1898	331	5.0
Silicene	0.093	608	2.5
Silicene	0.328	260	8.3
Germanene	0.092	608	2.5
Germanene	0.188	342	5.0
Germanene	0.171	273	4.4

Table 6.1: Shift in Brewster angle due to a conducting 2D material deposited on silica glass for several wavelengths. The 2D conductivity is taken form reference [172] and the shift is calculated using equation (6.6). Reproduced from [B].

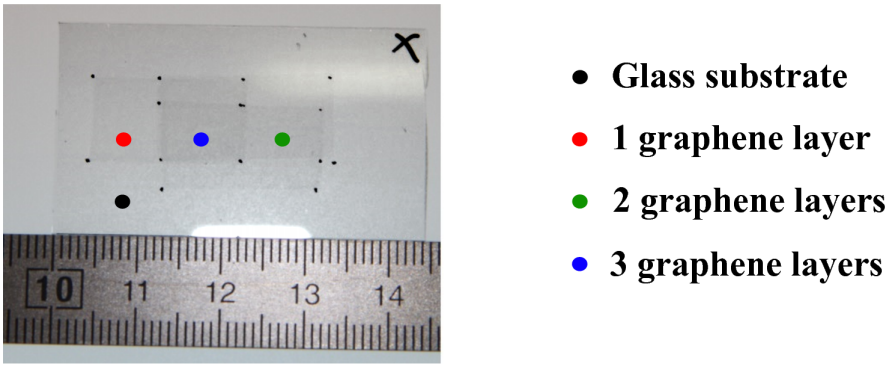

Figure 6.6: Optical image of the multilayer sample. Reproduced from [B].

6.4 Experimental results

Samples with respectively one, two and three graphene layers transferred on silica glass were fabricated (figure 6.6). The samples were then characterized by simultaneous micro-reflection and micro-Raman mapping using a home-made set-up as described in [174] to verify the number of layers on the sample. The three layers sample is of lower quality with much uncertainty in the number of layers over the analyzed surface.

The determination of the modified Brewster angle was done using spectroscopic ellipsometry from the ultraviolet (UV) to the near-infrared (NIR) spectral range, i.e. from 230 to 960 nm. The spectral and angular evolution of one of the two normalized Fourier coefficients of the ellipsometric signal (the β coefficient) was used to determine the Brewster angles. At a given wavelength, the coefficient β was acquired for several incident angles around the Brewster angle of the glass substrate, from $52°$ to $64°$ by step of $0.2°$. Close to the Brewster angle, β depends linearly on the incident angle θ and its value is zero at this particular angle [175]. The Brewster angle is deduced by fitting the data using a linear regression model.

The value of the Brewster angle shift Δ can be evaluated for a single graphene layer in the NIR-visible domain if one uses the universal conductivity ($\sigma_0 = \pi\alpha\,\varepsilon_0 c$) in equation (6.6) divided by two in order to take backside reflections into account. With $n_1 = 1$ and $n_2 = 1.5$, one gets

$$\Delta \approx \frac{1}{2}\frac{n_1}{n_2^2}\pi\alpha \approx 0.29°. \tag{6.13}$$

Figure 6.7a shows the experimental Brewster angle measured on the bare glass substrate, as well as on mono-, bi- and trilayer graphene areas. The mean values of the Brewster angle are plotted with the corresponding confidence interval (confidence level arbitrarily fixed at 99.9 %), resulting from data analysis on 9 different acquisitions on arbitrarily selected zones of each graphene area. An increase of the Brewster angle of about $0.3°$ per graphene layer is observed in the visible range, in very good agreement with the

prediction (eq. 6.13). In the UV spectral range, the peak at 268 nm corresponds to the π-plasmon. These measurements confirm that the deposited graphene is responsible for these modifications of the Brewster angle [176]. The optical conductivities of one, two and three layers are deduced from equation (6.6) (figure 6.7b). In the visible and near infrared range, the conductivity is close to the universal constant value $\sigma_0 = \pi\alpha\,\varepsilon_0 c$ for one layer, and $2\sigma_0$ for two layers, as expected for high quality graphene. The three layer area shows a larger shift than foreseen. This has to be related with the larger uncertainty on the number of layers and the presence of structural imperfections. Indeed, the statistical analysis using Raman spectroscopy following the approach described in [174] has shown that the uncertainty for the three layers area is much larger than for the other areas, see fig. 6.8. Apart from that, our results are in line with the one obtained by Mak *et al* which are based on the optical measurement of the reflectance contrast [171].

At higher energy (UV), the position of the peak at 268 nm (4.6 eV) is in good agreement with Mak *et al.* The intensity of the peak is greatly enhanced, nearly reaching eight times the universal conductivity for a single layer and up to eighteen times for three layers, while the previously cited work gives a maximum value of less than four times the universal conductivity for a single layer and fifteen for three layers. As the approximation of low conductivity is no more valid in this range, quantitative conclusions on the resonant maximal value of the conductivity cannot be drawn.

Conclusion

The Brewster angular shift is explained by the change in the effective polarization of the substrate accounting for the conducting layer at the interface. This shift can be easily determined by an approximated formula for a given material. On the other hand, the conductivity of the 2D material or the number of layers may be determined with a non-invasive method from the measurement of the Brewster angle on a coated substrate. Due to graphene tunability, it can be used to actively control the optical reflection at surfaces by means of a gate voltage. Applications in telecommunications could be imagined. For example, in [16], they proposed an ultra-broadband THz intensity modulator based on the control of the Brewster angle using the tunability of the conductivity of graphene.

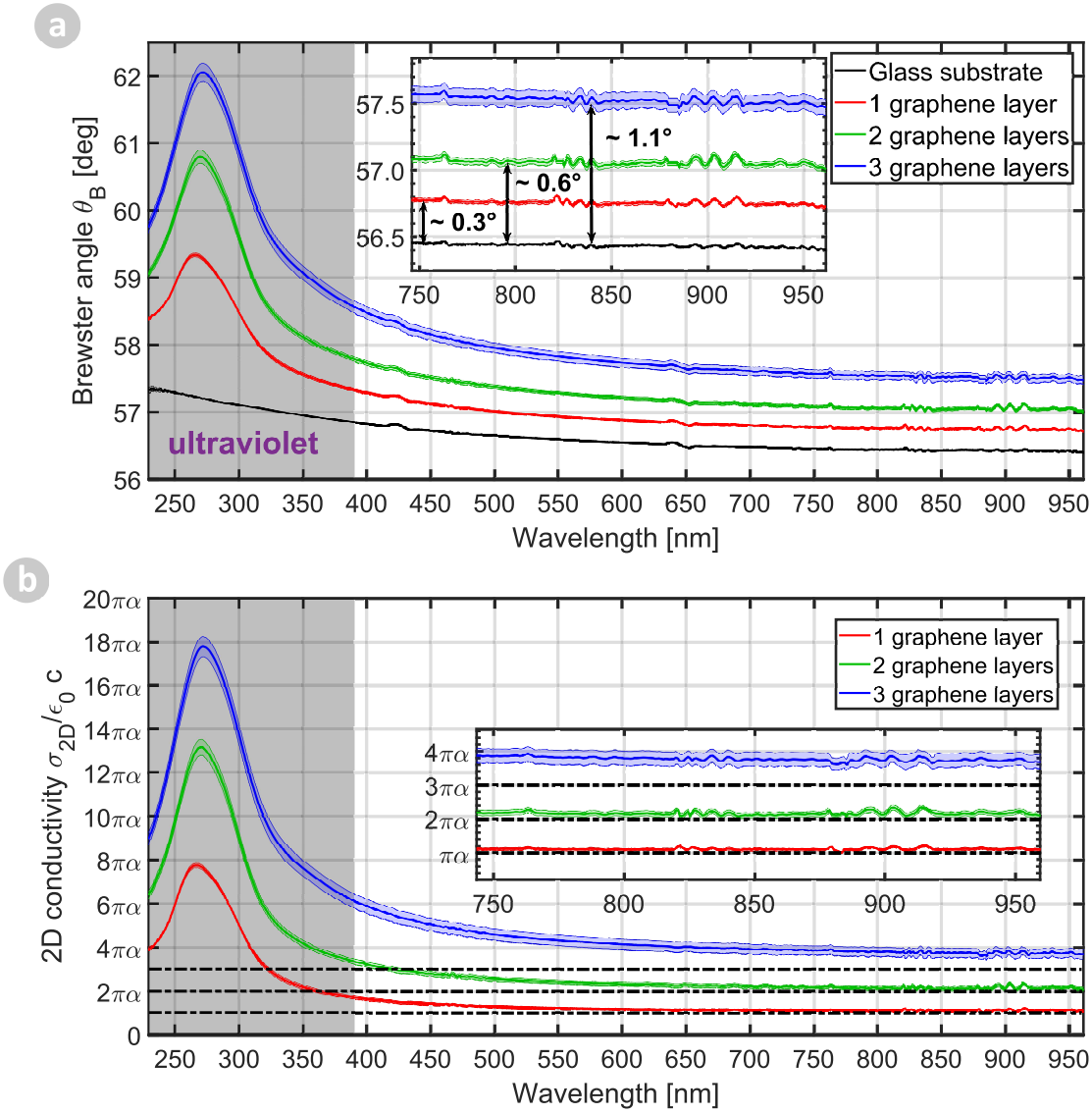

Figure 6.7: a) Brewster angle θ_B for a glass substrate (black), a mono- (red), bi- (green) and trilayer (blue) graphene. Inset: zoom in the $750 - 950$ nm region. b) Retrieved conductivity using the second approximation. Doted lines correspond to multiple integers of σ_0. Reproduced from [B].

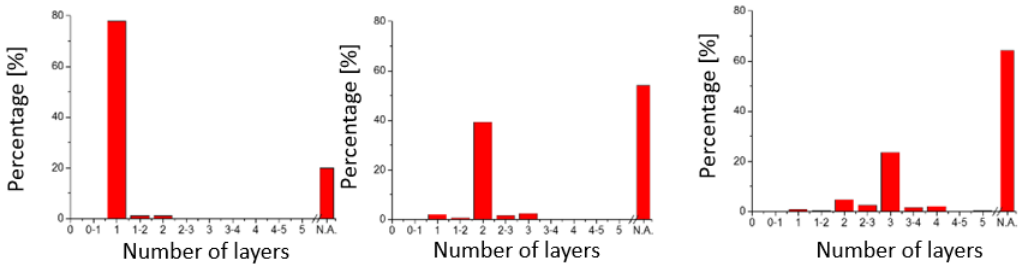

Figure 6.8: Number of layers histograms for the monolayer region (left), the bilayer region (middle) and the trilayer region (right). Reproduced from [B].

Chapter 7

Plasmons in nanostructured 2D materials

Conducting 2D materials sustain propagating and localized plasmons in the same manner than metallic nanoparticles do. In the first section, localized surface plasmon resonances (LSPRs) are investigated in graphene nanosdisks and nanodisk dimers in a classical framework. Second harmonic generation is efficient in such system thanks to the plasmonic resonance. Then, corrugated graphene is shown to exhibit LSPRs in the visible range using TDDFT. These plasmons, localized in the nanometer-sized ripples of graphene, have been experimentally detected using surface enhance Raman spectroscopy. In the last part, 1D polaritons are theoretically investigated. Those plasmons appear in a 1-dimensional conducting channel, arising from atomic restructuration in 2D materials. This phenomenon is investigated for metallic grain boundaries and edges of TMDs.

7.1 Plasmons in graphene nanodisks

In this section, I briefly summarize the results of our article [A], obtained during and after my internship in the laboratory of nanophotonics and metrology of Pr. O. Martin, form the EPFL, Switzerland. One of the research themes of his lab is the study of non-linear phenomena from metasurfaces or plasmonic nanostructures.

Non-linear phenomena such as second-harmonic generation (SHG), sum-frequency generation or four-wave mixing require high field intensity to be efficient [177]. The field enhancement caused by plasmon resonances can efficiently increases the non-linear response. 2D materials have been studied for several years for their potential applications in non-linear optics [178]. A large variety of non-linear phenomena have been investigated in 2D materials and heterostructures in the recent years [179–183].

In the article [A], field enhancement close to graphene nanodisks and nanodisk dimers is investigated. The SHG response of such systems is studied, as a function of relative positions of the disks.

Plasmon in a single graphene disk

The plasmonic resonances of graphene disks of diameters of several tens to several hundreds of nanometers have been largely investigated in the last decade [38, 82, 184–188]. First, these results are reproduced for a single nanodisk of 100 nm using a SIE method coupled with an eigenmode method. The surface integration has been performed with an optimized approach in order to improve the numerical accuracy [189]. This improvement was mandatory due to the very short distance between opposite triangles in the discretization mesh, a direct consequence of the ultra-low thickness (of 0.5 nm) of the material with respect to the average triangle size. The permittivity of graphene is obtained using the Kubo formula (see section 1.3), with typical value for the Fermi energy ($E_F = 0.4$ eV), the relaxation time τ ($\hbar\tau^{-1} = 1.6$ meV) and the temperature of $T = 300$ K [25, 38]. Furthermore, a term has been added to the conductivity to take into account the contribution of the edge electron states, resulting from the finite nature of the nanostructures [190] (the reader may refer to [A] for more details). The nonlinear polarization is computed considering the component χ^2_{nnn} of the surface tensor, where n denotes the normal to the surface mesh triangles. The implementation of all the tensor elements in the SIE formalism, which is straightforward, is not mandatory to assess the multipolar nature of the second harmonic wave. Moreover, the frequency dependence for χ^2_{nnn} which is set to 1 in the present work, is not considered here, allowing to obtain qualitative results. The incident plane wave propagates perpendicularly to the disk. The scattering cross-section from a single graphene nanodisk is plotted in figure 7.1, on the left. The scattering spectrum reveals two peaks, one at 0.153 eV and the other at 0.307 eV. It was demonstrated that, if only the Drude-like conductivity of graphene is considered, the resonance frequency ω_{pl} of the dipolar mode for a single nanodisk of suspended graphene (without substrate), depends on its diameter and the Fermi energy

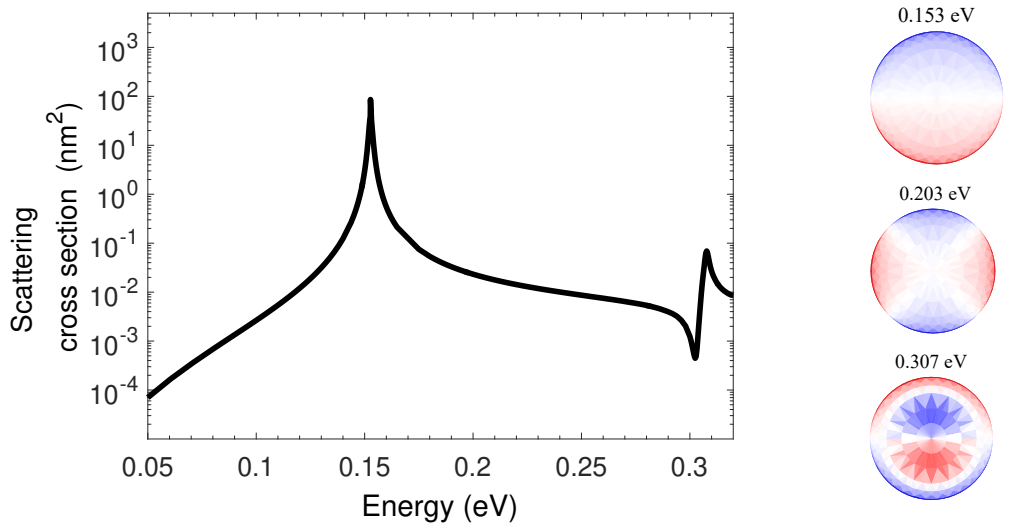

Figure 7.1: On the left: scattering by a 100 nm diameter graphene nanodisk (logarithmic scale) as a function of the incident electromagnetic wave energy ; on the right: eigenmode patterns at 3 different energies. The three eigenmodes found between 0.1 and 0.32 eV corresponding respectively to: a dipolar mode, a quadrupolar mode, and an octupolar mode. Red and blue colors correspond to positive and negative surface charges whereas white represents a zero surface charges. Reproduced from [A].

and is given by (see section 1.3):

$$\hbar\omega_p = \frac{e}{2\pi}\left(\frac{12.5E_F}{\varepsilon_0 d}\right)^{1/2}. \tag{7.1}$$

For the chosen parameters, this equation gives a resonant energy at 0.151 eV. The maximum of the first peak in the scattering cross-section spectrum occurs at 0.153 eV, indicating that this resonance corresponds to the dipolar mode. This observation is confirmed by an eigenmode analysis (figure 7.1, on the right) which is in excellent agreement with eq. (7.1). The small difference in energy is attributed to the modification of the conductivity caused by the electronic edge states, which are not considered in eq. 7.1. A second resonance is observed at 0.307 eV (see eigenmode in figure 7.1 on the right). A multipolar analysis revealed that this mode corresponds to an octupole. The eigenmode analysis revealed a third mode at 0.204 eV, corresponding to a quadrupolar resonance. However, this mode cannot be excited due to its symmetry, hence the absence of a corresponding peak in the scattering spectrum.

Plasmon in a dimer of graphene disks

In this section, dimers composed of graphene nanodisks with different gap sizes g are considered (figure 7.2). The z-axis is defined perpendicular to the graphene plane and the

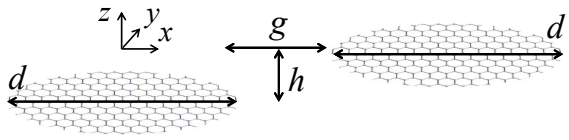

Figure 7.2: Schematic view of the graphene disk dimer with gap size g, diameter d and vertical shift h. Reproduced from [A].

x-axis and y-axis are defined, respectively, parallel and perpendicular to the dimer axis. The incident wave propagates along the z-axis and is polarized along the x-axis. The gap size g (measured along the x-axis) ranges from 2 nm to 640 nm. For extremely small distances, e.g. 2 nm, quantum effects such as quantum tunneling arise [191, 192] but most importantly the kind of edge termination near the gap region influences dramatically the field enhancement [38]. As these effects have not been taken into account here, the results obtained for a gap size of 2 nm should be put into perspective.

Three peaks are observed in the scattering cross-section spectrum (figure 7.3, top panel). The two peaks at low energy blueshift as the gap size increases. On the contrary, the spectral position of the highest energy peak (around 0.3 eV) is only slightly influenced by the gap size. Interestingly, the scattering intensity does not decrease significantly with the increase of the gap size for the dipolar mode (figure 7.3, inset).

It is well known that, due to the coupling between the LSPRs, the near-field intensity is enhanced in the nanogap [193]. In particular, it was shown that this enhancement could be as high as 10^6 for graphene disks [38]. The spectra for the field amplitude enhancement, $\frac{E_t}{E_{app}}$ with E_t the amplitude of the total field and E_{app} the amplitude of the applied field , evaluated at the center of the nanogap for different gap sizes (figure 7.3, bottom panel), clearly indicate that there are other modes excited between 0.2 eV and 0.3 eV, not visible in the far-field response. The charge distributions at all the resonant frequencies are represented in figure 7.4 for a gap size of 2 nm. The dipolar and quadrupolar bonding modes correspond to the two modes at low energies observed in the spectra. Their bonding nature results in the adequate symmetry for these modes being excited by an incident plane-wave at normal incidence. The bonding dipolar mode permits to enhance the intensity in the nanogap by up to seven orders of magnitude, in agreement with previous research [38]. The other modes also have a bonding nature, but it takes place between higher order modes. For all the observed modes, the near-field enhancement increases as the distance between the graphene nanodisks decreases.

It is thus expected that the SHG process would be greatly enhanced at these resonances when the gap size is small, in particular for an incident energy of 0.135 eV. This prediction is investigated in the next section.

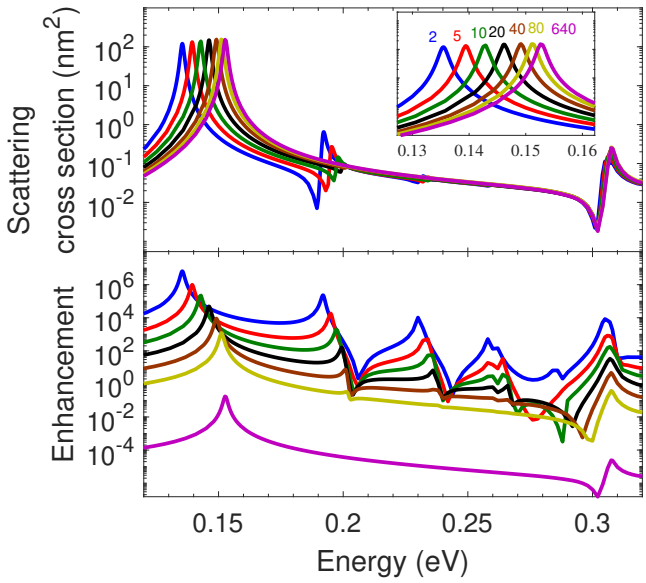

Figure 7.3: Dimers of graphene disks. Top panel: Scattering cross-section shown in logarithmic scale; inset: zoom on the dipolar mode at the resonance; bottom panel: Enhancement of the field intensity between the two disks shown in logarithmic scale; as function of the incident wave energy for a dimer of 100 nm diameter graphene disks with gap sizes ranging from $g = 2$ nm to 640 nm. There is no vertical shift between the two disks ($h = 0$ nm). Reproduced from [A].

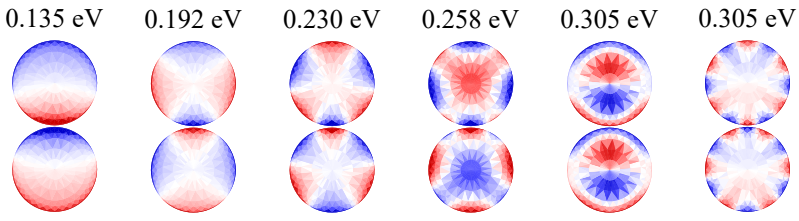

Figure 7.4: Normalized imaginary part (five first column) and real part (last column) of the charge distribution at the graphene nanodimer surface, evaluated at the energy of each peak observed in figure 7.3. Reproduced from [A].

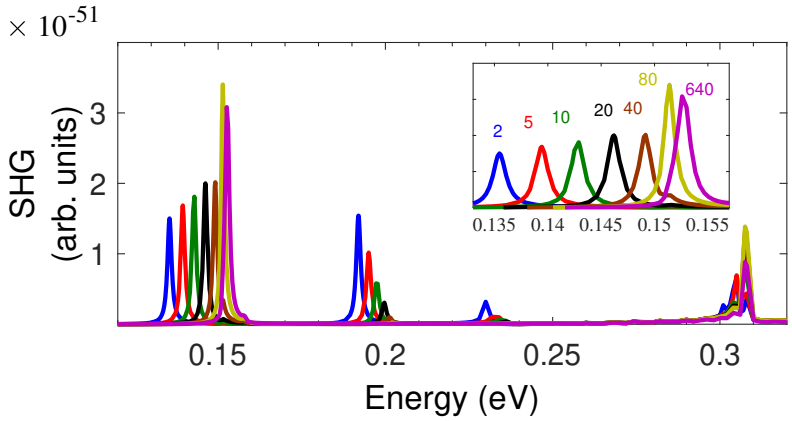

Figure 7.5: Second harmonic intensity shown in linear scale ; inset: zoom on the dipolar mode at the resonance - as function of the incident wave energy for a dimer of 100 nm diameter graphene disks with gap sizes ranging from $g = 2$ nm to 640 nm. Reproduced from [A].

SHG by a dimer of graphene disk

It is well known that SHG is not possible for centrosymmetric materials such as graphene. However this argument is only valid in the electric dipolar approximation and for local dynamical conductivity. At local surface plasmon resonance, high local field and gradient lead to high multipolar response, as predicted for graphene [194]. SHG response is also expected for nanostructured systems for which the symmetry is locally broken at the edge.

Contrary to the expectations, the SHG scattering cross-section is not enhance for the smaller gaps (figure 7.5). It is even the inverse that happens for the dipolar mode. The larger the gap, the higher the SHG response. This behavior is explained by the so called silencing of the SHG emitted from the gap due to the symmetry of the nonlinear sources. The same effect has been reported in the case of dimers composed of gold nanorods [195]. Indeed, the sources of the second harmonic waves standing at each side of the nanogap oscillate out of phase. As a consequence, the SH waves coming from each side of the nanogap tend to annihilate each other in the far-field, suppressing an otherwise high contribution to far-field SH intensity. This silencing effect increases as the distance between the nanodisks, i.e. between the out-of-phase SH sources, decreases. This tends to compensate the fundamental intensity enhancement occurring in the gap, resulting in an attenuation of the SHG.

In order to overcome the limitation in the SHG yield due to the silencing effect, it is necessary to reduce the destructive interference between the SH fields coming from the nonlinear sources at each side of the nanogap. One simple way to achieve this is to vertically shift, i.e. along the propagation direction z of the incident wave (see figure 7.2), one of the nanodisks relatively to the other. The maximum of SH intensity is plotted as a function of the vertical shift in figure 7.6. Although a small vertical shift of 1 or 2 nm already dramatically enhances the SH intensity in the near-field (figure 7.6, left panel,

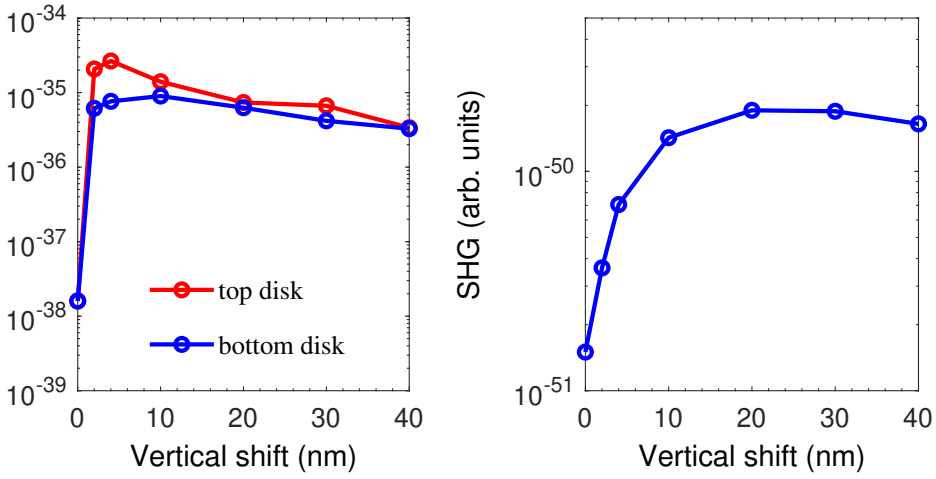

Figure 7.6: SHG from a dimer composed of two 100 nm graphene nanodisks with a gap size $g = 2$ nm as a function of the vertical shift h between the disks. Left panel: near-field intensity in the middle of the gap in the xy plane and next to the top or bottom disk; Right panel: far-field intensity. Reproduced from [A].

the intensity is taken 1 nm away from the edge of a disk), the symmetry breaking is not high enough to stop the destructive interference occurring in the far-field (figure 7.6, right panel). A vertical shift as high as 20 nm is required to maximize the SHG in the far-field. Indeed, the symmetry breaking along with a strong enhancement of the near-field intensity allows an improvement in the yield of the SHG. For a gap size of 2 nm, the vertical shift permits to enhance the SHG up to a factor of 10. This phenomenon can also be used to determine the vertical shift between two adjacent graphene nanodisks, with a resolution close to 1 nm. This high resolution is directly related to the vanishing thickness of the graphene layer.

Conclusions

Surface plasmon resonances in dimers of graphene disks dramatically enhance the electric field intensity. Although the enhancement is larger for closer nanodisks, the silencing effect decreases the SHG coming from the disks. A symmetry breaking enables to greatly enhance the second harmonic response of the system. Here, a vertical shift between the disks is proposed but various methods are also possible such as a difference in the Fermi energy of the graphene disks or different substrates for each disk.

Second harmonic effects in graphene nanostructures have been continuously theoretically studied in the recent years, for example in nanoribbons and nanosquares [120, 196, 197], but experimental investigations are still lacking to confirm the second harmonic generation in graphene nanostructures.

7.2 Plasmons in corrugated graphene

As seen in the previous section, plasmons in nanostructured graphene occurs in the infrared or THz range for particles sizes around hundreds of nanometers. According to eq. (7.1) [34], the plasmon frequency scale as $\omega_{pl} \propto d^{-1/2}$ with d the characteristic length of the nanoparticle. In order to exploit graphene plasmons in the visible range, the size of the nanoparticles must be shrunk to a few nanometers. However, at such a small scale, the losses become prohibitive due to the charge carrier scattering on the edges [35, 39]. In article [D], it is shown that strong nanocorrugation in graphene enables the confinement of plasmonic resonance in nanometer-size structures. The resonance frequency of these plasmons is actually in the visible range which is of great interest for applications in biosensing or wave-guiding. The results of [D] are discussed in this section

Experimental evidences of plasmons in corrugated graphene

When graphene sheets are synthesized, they are not completely flat. Microscopic ripples form in supported graphene as well as in suspended graphene such that it is thermodynamically stable [54]. These defects do not normally have a major impact on the electronic and, a fortiori, optical properties of graphene. However, amplifying these ripples may change the fundamental properties of graphene and paves the way for a various range of new properties. The team of Levente Tapasztó of the Centre for Energy Research in Budapest has synthesized graphene with unprecedentedly strong nanoscale corrugations. They performed cyclic thermal annealing on mechanically exfoliated graphene flakes on SiO_2/Si substrate. The resulting samples have been analysed through topographic STM (figure 7.7) . The root mean square roughness value extracted is estimated to 0.5 nm with an aspect ratio $h_{max}/R = 0.5$, where h_{max} stands for the maximum height of the corrugation and R stands for the in-plane radius of the corrugation.

SERS measurements were performed on the different samples. The most striking result was the observation of a strong Raman signature for an excitation at 633 nm on the corrugated graphene (figure 7.8) compared to the quasi-flat graphene, without exposing it to any chemical solution. The analysis of the spectrum revealed that this strong signature originated from Copper(II) phthalocyanine (CuPC) molecules, one of the most current dye, probably present due to contamination. It was determined by STM that the CuPC molecules were present at a very low density. The observation of a peak due to CuPC that is 20 times higher than the G band of graphene indicates that there is a huge enhancement of the Raman response due to the corrugated graphene. Such high enhancement in SERS is usually due to plasmonic resonance in the substrate at the given excitation frequency. This leads to the hypothesis that corrugated graphene is a good platform to sustain high quality plasmons. In the following, I show that theoretically, plasmons are possible in graphene ripples.

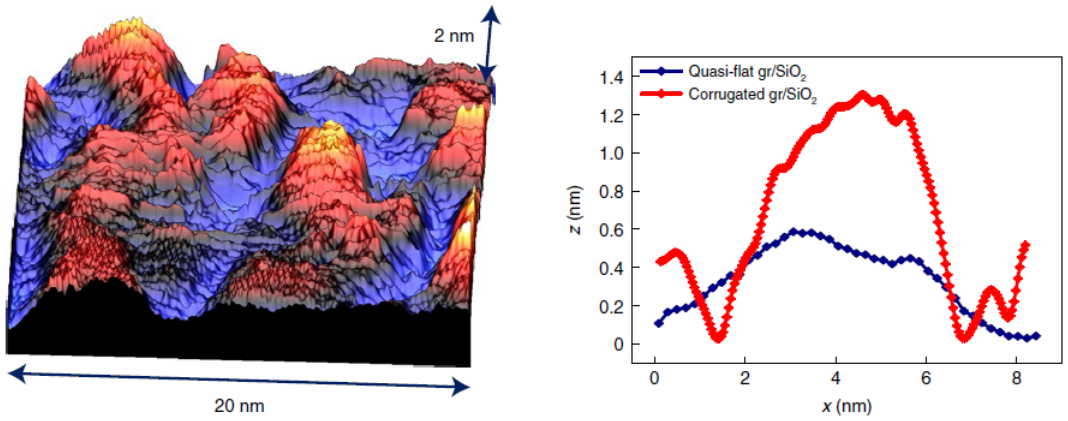

Figure 7.7: On the left: topographic STM images of graphene sheets prepared by cyclic thermal annealing, displaying particularly strong nanoscale corrugations, with lateral size below 10 nm and height of about 1 nm; on the right: typical graphene ripple geometries measured for nanocorrugated ($h_{max}/R \sim 0.5$) and as-exfoliated (quasi-flat) graphene ($hmax/R \sim 0.15$) on SiO_2; x and z are the in-plane and out-of-plane coordinates, respectively. Reproduced from [D].

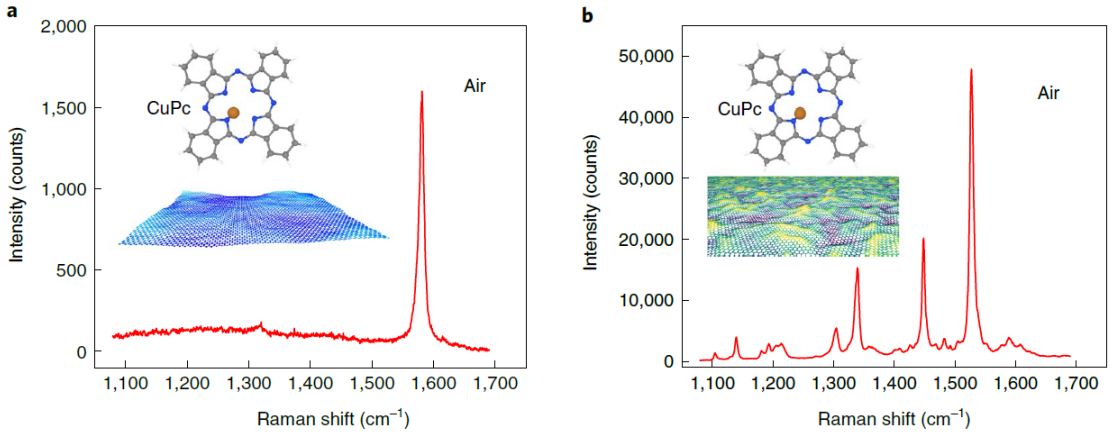

Figure 7.8: Raman spectra (633 nm) of quasi-flat (a) and nanocorrugated (b) graphene sheets subjected to air, the latter detecting high intensity CuPC contamination peaks from nominally clean laboratory air. Reproduced from [D].

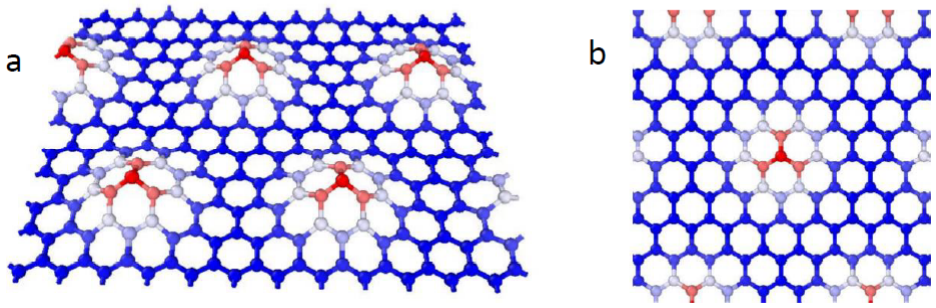

Figure 7.9: Model geometry of the corrugated graphene. (a) 3D image of the geometry (b) 2D top view of the geometry. The C-C bonds around the hill are colored. Reproduced from [D].

Theoretical model of corrugated graphene

The corrugated graphene cannot be directly simulated using the conductivity of graphene in classical electrodynamics because the fundamental electronic properties of graphene are modified. Therefore, DFT calculation must be performed on a simplified system to study the optical properties of such system. Indeed, the corrugations observed experimentally are much larger that what is possible to study in TDDFT. A smaller system, representing a ripple with the same aspect ratio as the graphene corrugations presented in figure 7.7 ($h_{max}/R \sim 0.5$) has been proposed. In the DFT unit cell, 50 atoms are disposed with a hill of 2.5 Å height and a vacuum layer of 25 Å (figure 7.9). In this case, the curvature of the ripple is approximately the same as in the synthesized samples. The main influence of the corrugations on the electronic properties can therefore be reproduced. Obviously, this theoretical model has a periodicity that is not present in the real samples. However, this periodicity was not expected to dramatically change the optical properties.

To investigate the influence of nanoscale deformations on the electronic structure of graphene, tunnelling spectroscopy measurements were performed (figure 7.10a). Tunnelling spectra acquired on nanocorrugations display distinctive features (peaks and shoulders) around ±450 mV compared to spectra measured on quasi-flat areas of the same sample. The density of states averaged over the graphene nanocorrugation calculated using the DFT code SIESTA (figure 7.10b) displays good agreement with the experimental tunnelling spectra. Plotting the spatial distribution of the calculated local density of states (LDOS) at energies near the LDOS peak clearly provides evidence for electronic states localized on the graphene nanoprotrusion (figure 7.10b inset).

Optical response of corrugated graphene

Ellispometry measurements were performed in order to obtain the refractive index and the surface conductivity of the corrugated graphene samples.

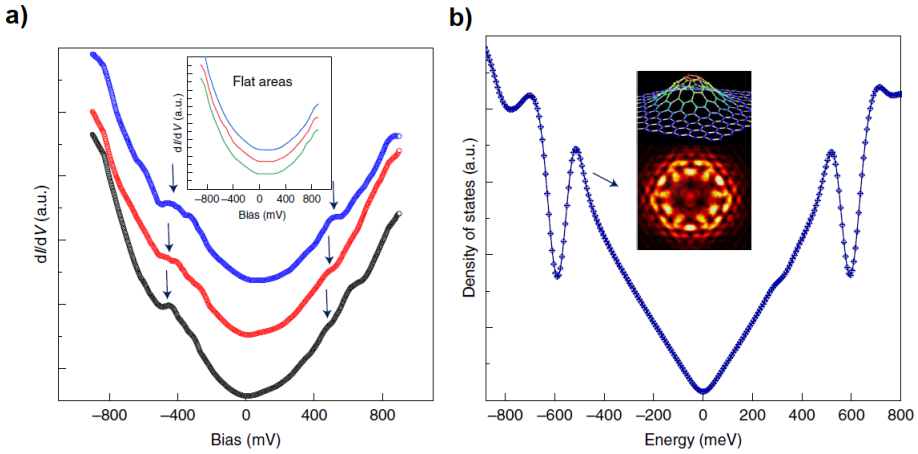

Figure 7.10: Electronic structure of graphene nanocorrugations. a) Tunnelling spectra measured on $D \sim 5$ nm graphene corrugations with aspect ratios $(h_{max}/R) \sim 0.4\check{}0.5$, displaying peak-/shoulder-like features around ± 450 mV. The inset shows tunnelling spectra recorded on quasi-flat areas of the sample. b) DFT-calculated (with SIESTA) electronic density of states averaged over a model graphene nanoprotrusion of similar aspect ratio $(h_{max}/R \sim 0.4)$. The inset shows the spatial distribution of the LDOS, revealing the localization of specific electronic states on the nanocorrugation. Spectra of different colours have been acquired at different spatial locations for both nanocorrugated and flat areas. Reproduced from [D].

In parallel, the surface susceptibilities have been computed in the TDDFT approach using the GPAW code (details can be found in the appendix). The in-plane conductivity of flat and corrugated graphene in reduced unit of the theoretical conductivity of graphene in the visible range ($\sigma_0 = e^2/4\hbar$) is shown in figure 7.11. The computed conductivity of flat graphene is approximately σ_0 in the infrared and visible range and slightly increases in the UV range due to the presence of π-plasmon.

In the visible range (500 - 800 nm), well-defined peaks appear. Some of these peaks can be related to the optical transitions associated with the maxima (peaks) in the DOS (figure 7.12, calculated with GPAW), although no one-to-one correspondence can be established. For example, the peak at 785 nm corresponds approximately to the transition energy indicated on figure 7.12 of 1.59 eV.

The experimental and simulated surface conductivities and refractive indexes are shown in figure 7.13. There is reasonably good agreement between the curves despite the fact that the atomic configuration is simplified compared to the corrugation of the sample. This good agreement shows that the theoretical model catches the main optical features of the corrugated graphene samples.

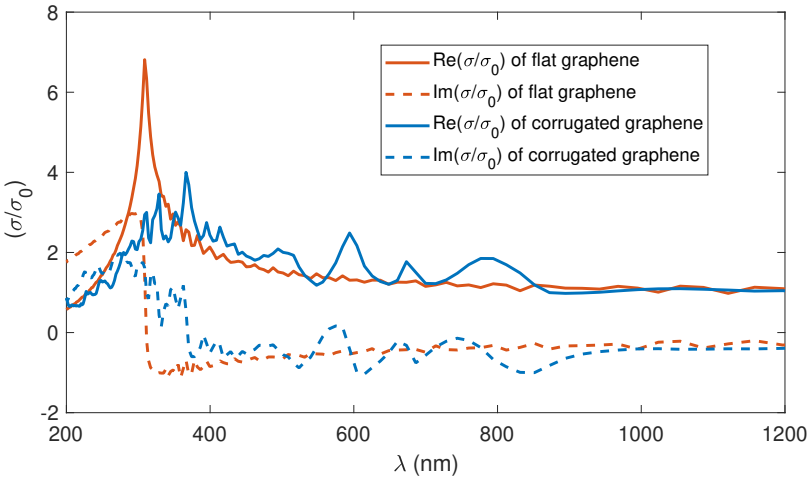

Figure 7.11: Conductivity of flat and corrugated graphene in the visible and infrared ranges. Reproduced from [D].

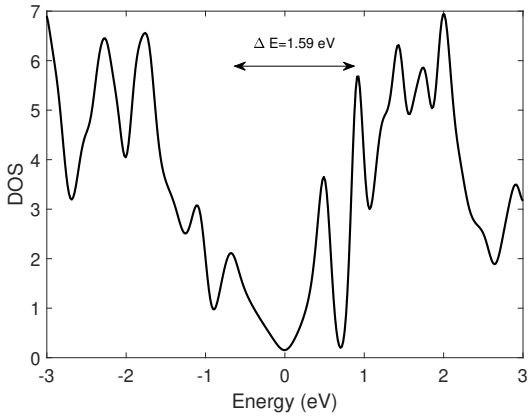

Figure 7.12: Density of states of the graphene corrugation with high aspect ratio, calculated in TDDFT with GPAW. Reproduced from [D].

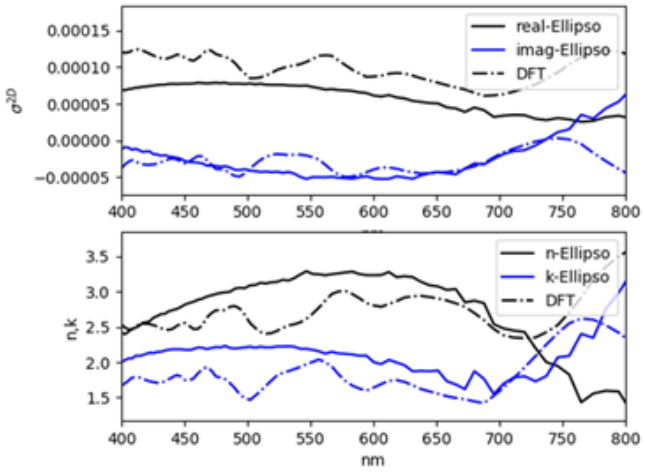

Figure 7.13: Comparison of optical conductivity obtained from DFT calculations and refractive index and extinction obtained from spectroscopic ellipsometry measurements displaying a reasonably good agreement up to 750 nm. Reproduced from [D].

Plasmon eigenmode analysis of corrugated graphene

The eigenmode analysis presented in section 2.1 was performed on the system of figure 7.9 using the GPAW code [198]. Over the 673 eigenmodes, 4 of them display interesting features (figure 7.14). Two of the modes (mode 2 in blue, mode 4 in green) have the real part of the eigenvalue crossing the zero line, at 2.9 eV and 3.1 eV for mode 2 and at 3.9 eV for mode 4. Their respective loss functions have peaks around the corresponding energies. However, two other modes have large loss functions, modes 1 (red) and 3 (purple), in particular where their dielectric function is close to zero. To fix the ideas, for each mode, one frequency is selected, represented by a vertical line in figure 7.14: 1.9 eV for mode 1, 2.9 eV for mode 2, 3.6 eV for mode 3 and 3.9 eV for mode 4.

To determine which modes are crucial for the optical properties, the weight of each mode is calculated (figure 7.16). The two modes which have their dielectric function crossing the zero line (modes 2 and 4) have a vanishing weight, hence they cannot be excited by light and they do not contribute to the macroscopic spectra (figure 7.15). However, the two other modes have approximately a unit (maximum) weight in the frequency range where their loss function is high (below 3.2 eV for mode 1 and above 3.2 eV for mode 3). In consequence, for energy lower than 3.2 eV, the mode 1 determines the optical behavior of the ripple, while at energy larger than 3.2 eV, it is determined by the mode 3.

The spatial charges distribution corresponding to these 4 main eigenmodes are plotted in figure 7.17. The first mode is a dipolar mode localized around the hill, which is coherent with the fact that this resonant mode is visible in the macroscopic spectra. The others modes exhibit more complicated behavior with partially delocalized charges. These charge distributions show that the plasmon are mainly localized around the ripple.

Scanning near-field optical microscopy (SNOM) has also been performed on the

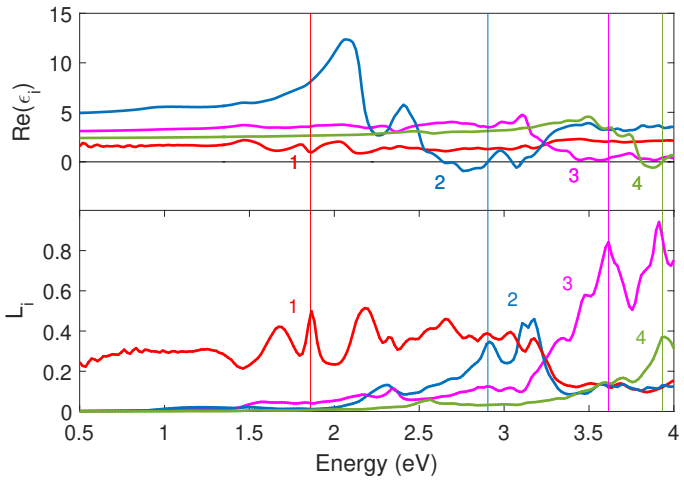

Figure 7.14: Result of the eigenmode analysis. Top: Real part of each eigenvalue ε_i; bottom: Loss function associated to each eigenvalues. Reproduced from [D].

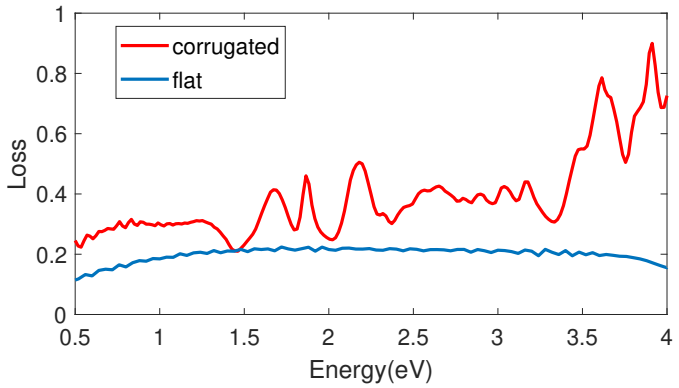

Figure 7.15: Total (macroscopic) loss function of flat and corrugated graphene.

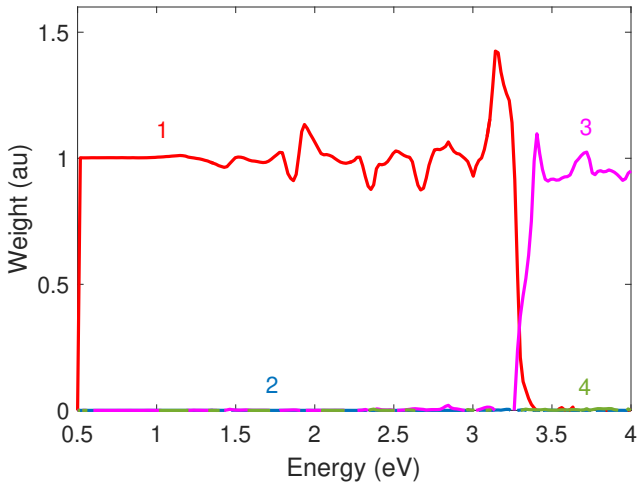

Figure 7.16: Weight of the modes.

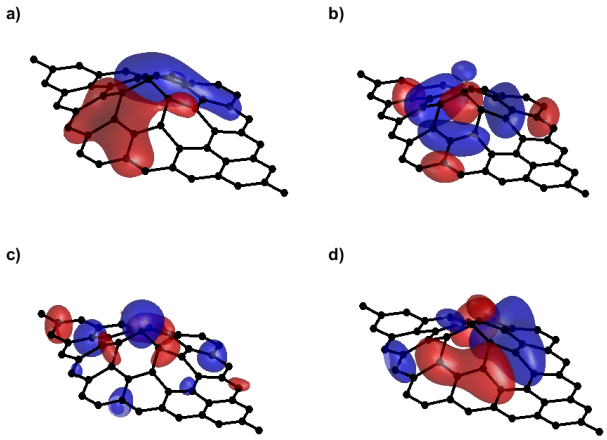

Figure 7.17: 3D charge density distributions of a) mode 1 at 1.9 eV b) mode 2 at 2.9 eV c) mode 3 at 3.6 eV d) mode 4 at 3.9 eV.

samples. Interference patterns have been observed on the SNOM image (figure 7.18), suggesting the presence of propagating plasmons in nanocorrugated graphene. It has been theoretically predicted and experimentally confirmed that when separated nanostructures, hosting localized plasmons, are located in the close vicinity of each other (at a distance smaller than the excitation wavelength), their interaction can give rise to propagating plasmon modes [26, 199]. However, the TDDFT calculation do not corroborate this hypothesis. Indeed, when an excitation with a non-vanishing momentum $\mathbf{k}$ is chosen, the optical spectra does not change and in particular the peak do not shift in energy. Therefore the plasmons evidenced by the eigenmode method have no dispersion. In consequence these propagating plasmons cannot be describe by our simple theoretical model and are not described in details here.

EELS spectroscopy of corrugated graphene

In order to explain how localized electronic phenomena happen in the nanocorrugation, reflection EELS experiments [200] have been performed (figure 7.19). It turned out that the energy provided by the electron irradiation leads to a rapid (order of seconds) structural relaxation (smoothing) of graphene nanocorrugation on SiO_2 substrate. A significant quenching of the π-plasmon is observed the EELS spectra of the corrugated samples. After a few minutes of irradiation, the intensity of this π-plasmon rapidly evolves into full-intensity peak, corresponding to quasi-flat graphene and associated with a smoothing of the graphene (figure 7.19a). In the numerical simulation (figure 7.19b) the quenching and the small red-shift of the π-plasmons of corrugated graphene compared to flat layer is qualitatively reproduced. However we do not observe the extinction of the peak because the density of corrugations is much larger in the experimental samples than in the theoretical system, in which a high number of carbon atoms stands in flat areas.

The quenching of the π-plasmon is explained by a change of hybridization from sp^2

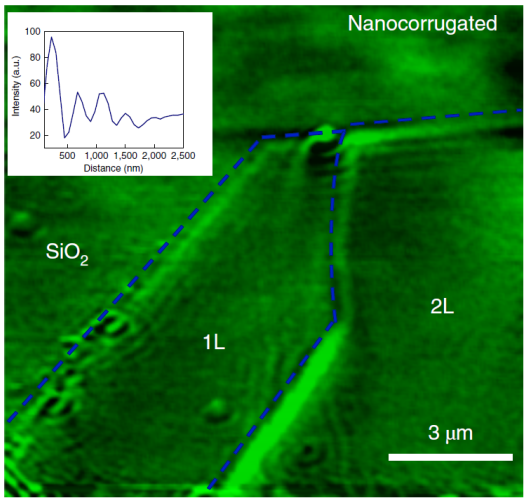

Figure 7.18: SNOM image (wavelength $\lambda = 488$ nm) of nanocorrugated graphene revealing clear interference maxima and oscillations in the proximity of edges (marked by dashed lines) and defects. The inset shows a line cut perpendicular to the graphene edge. 1L represents the single layer and 2L the bilayer graphene areas on the SNOM images. Reproduced from [D].

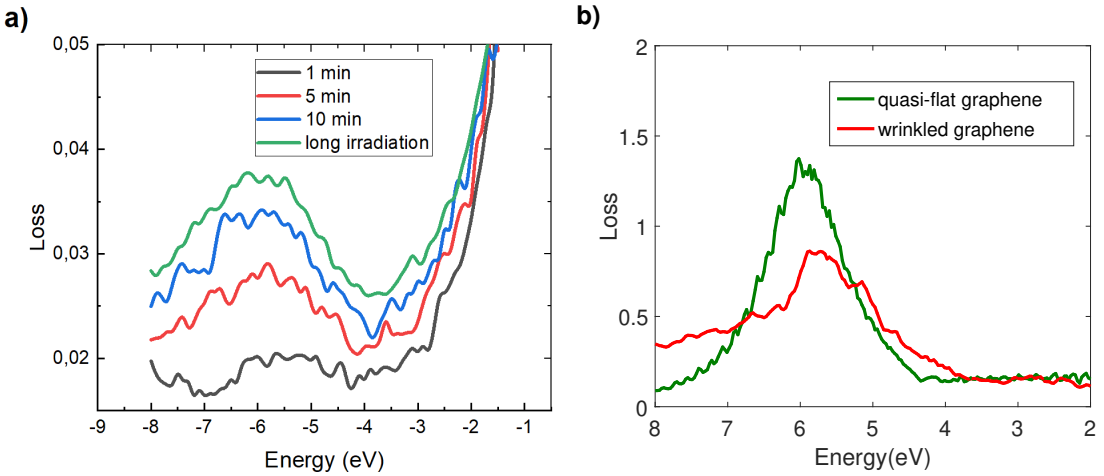

Figure 7.19: a) Reflection electron energy loss spectra of nanocorrugated graphene sheets as a function of electron irradiation time displaying a strong suppression of the graphene Pi plasmon peak near 6 eV in corrugated samples that gradually recovers by smoothing out the corrugation with irradiation dose. b) EELS calculated from TDDFT for flat (green) and corrugated graphene (red). Reproduced from [D].

to sp^3. This change of hybridization due to the curvature of the corrugated graphene is probably at the origin of the localization of the charge in the ripples.

Conclusions

Plasmon resonances have been investigated in nanocorrugated graphene. The extremely small spatial extension of the corrugations allows us to tune the frequency resonance of the plasmon up to the visible range, which was long awaited. These plasmons have been theoretically analyzed using the eigenmode decomposition of the dielectric function. Here, two modes have been shown to contribute to the macroscopic spectra using this method.

The enhancement of the field due to the plasmon allows us to perform surface enhanced Raman spectroscopy which has been shown to be very efficient to detect some molecules in very low concentration. Such SERS substrate are interesting in biosensing. As an example, diabetics would benefit from SERS if their blood glucose level can be determined daily from such non-invasive spectroscopy. The only invasive operation would be the subcutaneous application of a substrate, which must be done only once [40]. However, the bio-compatibility of graphene must be investigated first before considering such application for corrugated graphene.

7.3 Plasmons in grain boundaries of TMDs

It has been shown before that plasmons can occur in nanoparticles and nanocorrugations of 2D materials. Here, other types of nanostructure are considered: grain boundaries and edges. Grain boundaries are line defects present on 2D material with atomic reconstructions that change the local electronic properties (see section 1.2). Atomic reconstructions also arise at the edges of nanostructures (e.g. nanoribbons). For nanostructures of the size of a few nanometers, these atomic reconstructions can dramatically change the electronic properties in such a way that 1D conducting channel can be formed, even in insulating or semi-conductor 2D materials [201–203]. These conducting channels are a good platform to sustain plasmonic resonance confined in 1D. Such extremely confined plasmons have already been evidenced at the edges of MoS_2 nanoribbons [37, 204].

Grain boundaries of 2D materials can also exhibit metallic behavior, such as in graphene [203], h-BN [202] and TMDs [201]. In particular, mirror twin boundaries (MTB) are boundaries (sometimes referred as joined edges defects [205]) in 2D TMDs with a mirror symmetry between the two grains [41, 201, 206–208]. At the boundaries, the atomic reconstructions change the electronic properties and breaks the spatial symmetry but far from the boundaries the properties are the same as those of the pristine 2D materials. Several types of MTB have been identified lately, most of which exhibit metallic behavior associated with localized electronic states at the Fermi level [41, 201]. For example, in [41], the authors calculated the density of state (DOS) of a MTB of $MoSe_2$, which shows a non-zero density of state in the bandgap due to the metallic states (figure 7.20).

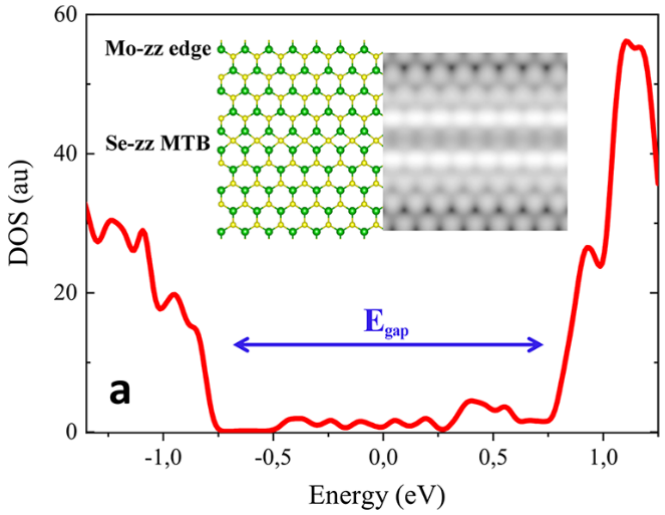

Figure 7.20: Calculated DOS of a $MoSe_2$ MTB. The inset shows the simulated STM images of the corresponding atomic structures. Reproduced from [41].

Some TMDs even exhibit a high density of MTBs, that forms complex quasi-periodic structures of a few nanometers [209]. Optical phenomena like photo-luminescence [210] and bi-exciton emission [211] have also been reported in these grain boundaries.

Here, using the eigenmode method, I study the plasmonic response of some MTBs using the GPAW code. More in-depth investigations could increase the robustness of this research but it is planned to publish these results in the near future.

Atomic structures of MTB

A single MTB cannot be directly included as a periodic feature in a supercell in DFT because of the mirror inversion of the lattice. Two solutions exist to overcome this problem. The first one is to include a second MTB which inverses the lattice again such that periodic boundary conditions are possible. The second one is to include the MTB in the middle of a ribbon. For this second solution, a vacuum interval must be added in the cell in order to avoid interactions between repeated ribbons. Both these solutions have been used in this work.

Two metallic MTBs, experimentally highlighted in [201], have been selected. Similarly to what has been done for the numerical modelling in [41], ribbons of $MoSe_2$ containing these MTBs have been modelled (figure 7.21a,b). The ribbons are periodic along the x-axis, have a width w of 3.5 nm and the unit cells have a vacuum interval of 1.5 nm. The first ribbon (figure 7.21a) has edges of selenium atoms (in green). The second one (figure 7.21b) has edges of molybdenum atoms (in purple). Unrealistically, the edges of these ribbons are not passivated. For completeness, a passivated ribbon, with hydrogen atoms bonded to the selenium atoms forming the edges of the first ribbon, has been considered but the electronic properties of the MTB are not influenced at all by the passivation of the edges. The focus of this work being in the MTBs, these results are

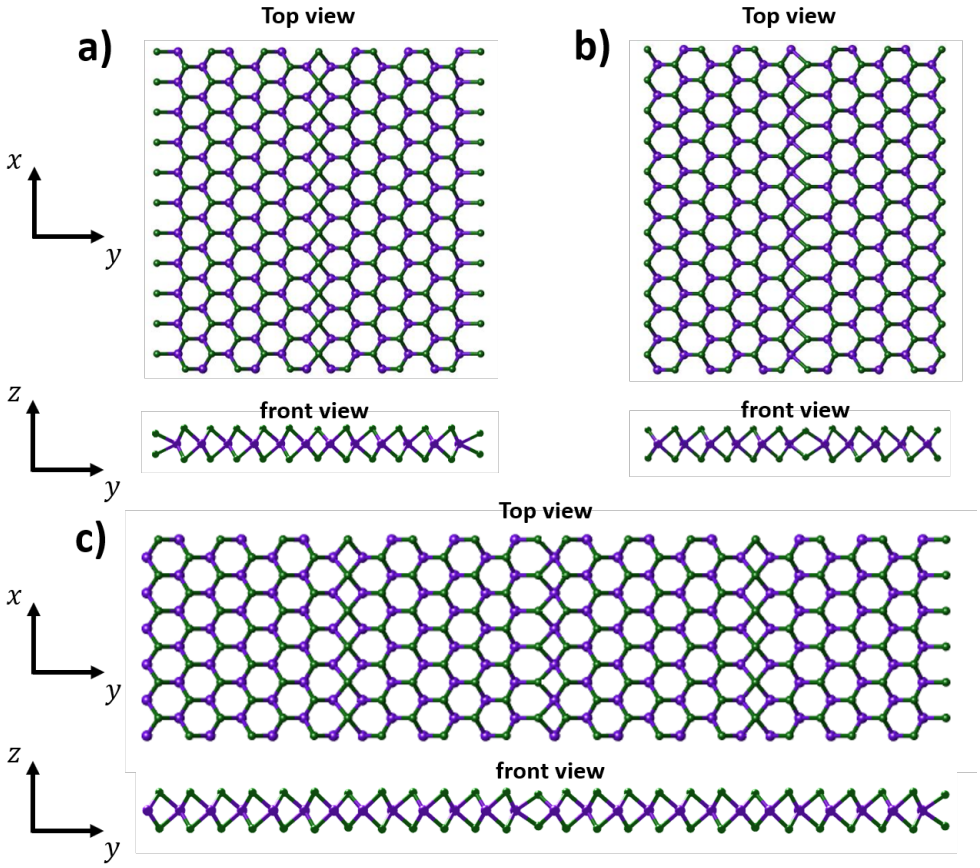

Figure 7.21: Structure of $MoSe_2$ with MTBs. a) Ribbon of width 3.5 nm with selenium boundary in the middle;b) Ribbon of width 3.5 nm with molybdenum boundary in the middle; c) 2D plane with repeating MTBs. Figure created using the Molecule3D MATLAB function [212].

therefore not shown here. The last structure that has been modelled is a 2D plane with periodic alternating repetitions of the two previous MTBs along the y-axis (figure 7.21c).

Band structure of the MTBs

The band structures along the x-axis of the three structures are plotted in figure 7.22. The metallic states of the MTBs and the edges are associated to the bands crossing the Fermi level in the band structure. The metallic bands associated to the MTBs or the edges may be discriminated by analysing the electronic density map for each metallic state. Master student David Antognini Silva has done it in its master thesis [213]. Those bands are labelled with $B1$ for the first boundary (first ribbon, figure 7.22a) and $B2a$, $B2b$ and $B2c$ for the second boundary (second ribbon, figure 7.22b). The other metallic bands are edge states. As the 2D plane of figure 7.21c contains both MTBs, the metallic bands associated to both MTBs are present in its band structure but not the edge bands (figure 7.22c). This confirms the analysis of the metallic states of [213]. These MTB bands are only slightly modified for the planar structure of figure 7.21c compared to those of the

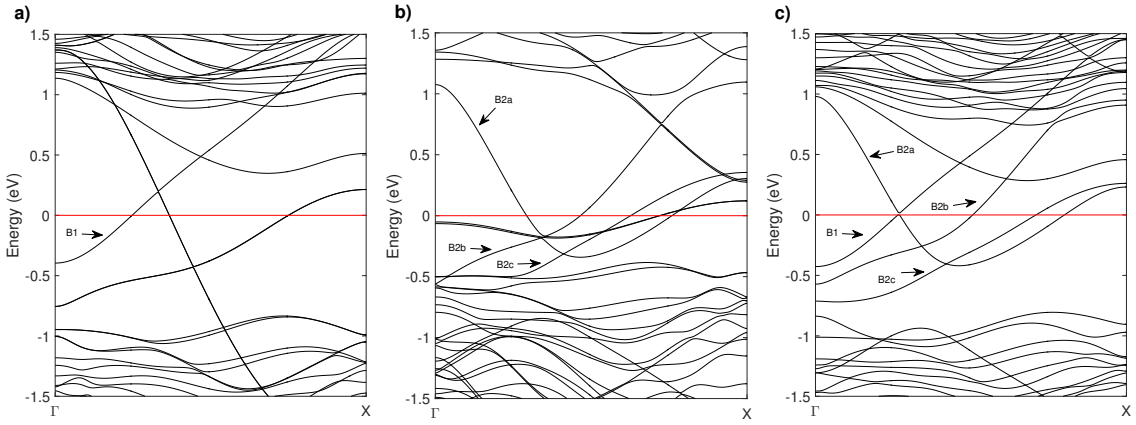

Figure 7.22: Band structure of a) the first ribbon of figure 7.21a; b) the second ribbon of figure 7.21b; c) the 2D plane of figure 7.21c. The Fermi level is depicted has a horizontal red line.

ribbons of figure 7.21a and b. It suggest that the localized states do not disturbs one another.

Eigenmode analysis of the MTBs

At first, only the plasmon in the the first ribbon (figure 7.21a) is investigated. The results of the eigenmode decomposition for an arbitrary value of the momentum $q = 0.15\,\text{Å}^{-1}$ are presented in figure 7.23. Three modes are interesting here. The first two modes (blue and red) are edge modes and have their eigenvalues crossing zero around 0.39 eV, with a peak at the corresponding energy in the loss spectrum. The last one (yellow) is a MTB mode and has its eigenvalue crossing zero and the peak of the loss spectrum at 0.55 eV.

To determine the nature of the plasmonic excitation, the potential and charge density profiles of these modes at the resonance energy are plotted (figure 7.24). On this figure, the position of the ribbon is delimited by the dashed grey lines. The potential of the first two modes (in blue and orange) are maximum near the edges, with an inversion of the sign for the second mode. They are, respectively, the symmetric and anti-symmetric hybridization of the plasmonic modes of the conducting edges. The third mode is the plasmonic mode of the MTB, with a maximum value of the potential in the middle of the ribbon. The charge density profiles are more complicated due to spatial oscillations of the charge but follow the same trends as the potential.

The weights of these three modes are displayed on figure 7.25. The first edge mode (symmetric mode) has a large weight below 0.4 eV. The weight is not maximum ($w \neq 1$) because the mode is localized in a small section of the unit cell. As the weight is the product of the spatial average of the potential and the charge density, (see eq. (2.117)), delocalized modes contribute more efficiently to the total spectra even if they are non-resonant. On the other hand, the anti-symmetric mode has a vanishing weight. This

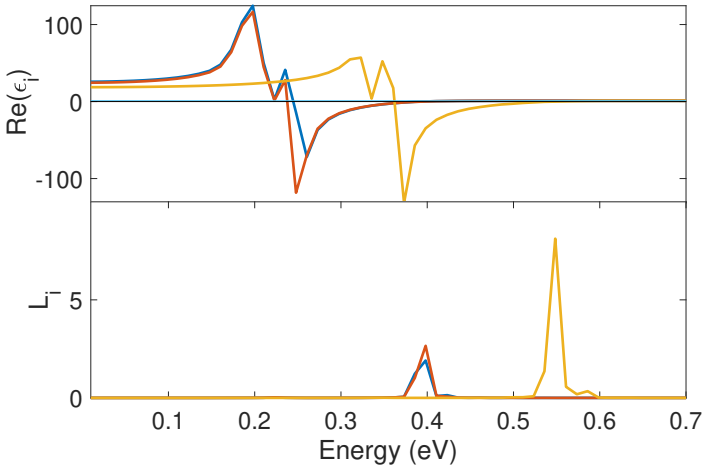

Figure 7.23: Eigenvalues and loss functions associated to two edge modes (red and blue) and the MTB mode (yellow) for the ribbon A (figure 7.21a).

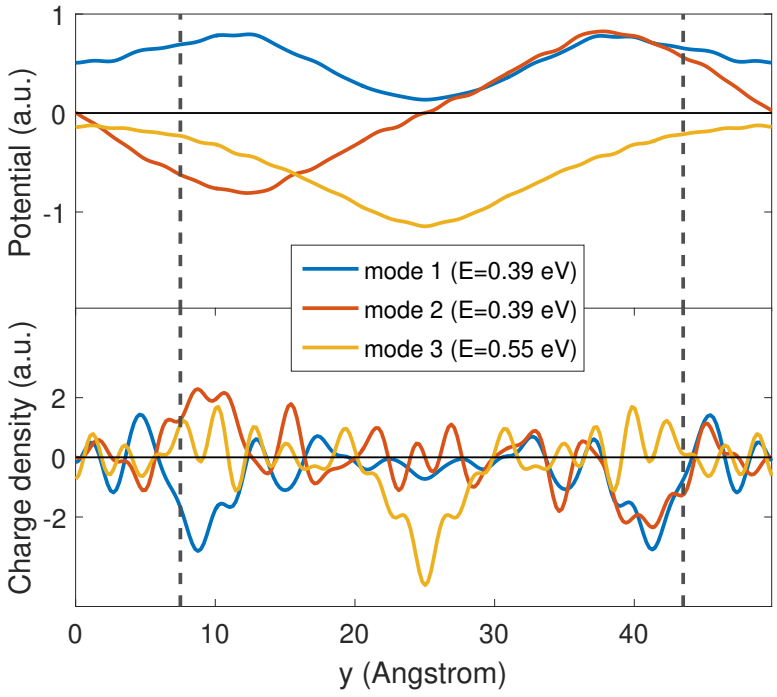

Figure 7.24: Potential (top) and charge density (bottom) across the ribbon for the two edge modes (red and blue) and the MTB mode (yellow). The dashed grey lines correspond to positions of the edges of the ribbon.

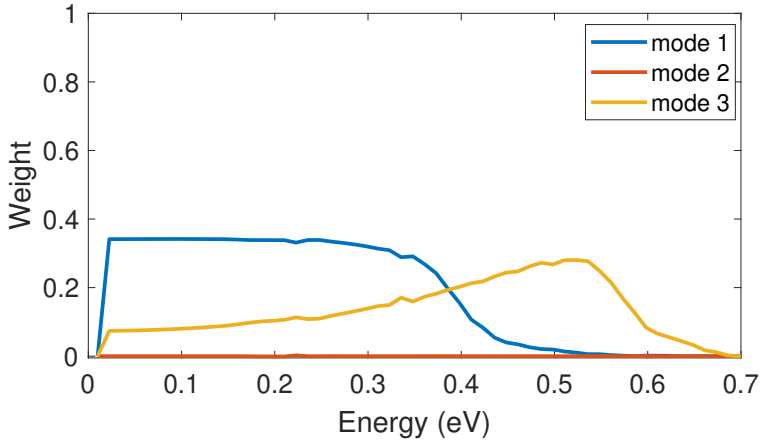

Figure 7.25: Weight of the three modes corresponding to edge modes (1 and 2) and a MTB mode (mode 3).

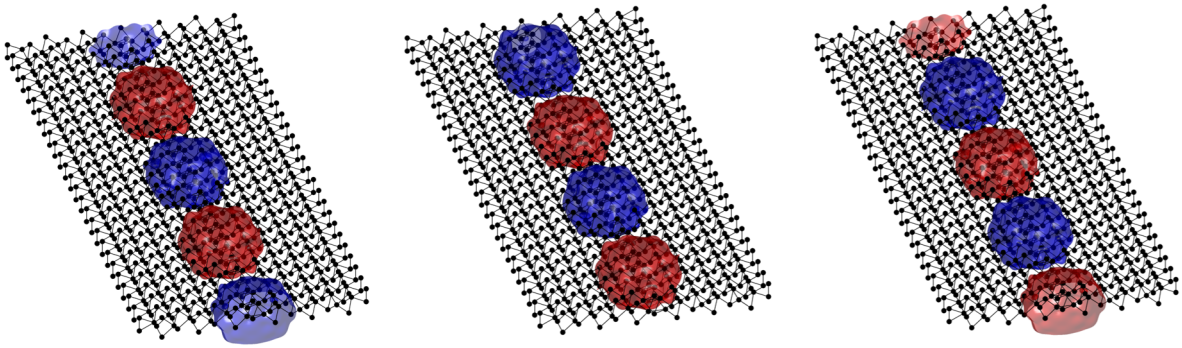

Figure 7.26: Isosurface of the charge density for the MTB mode at the resonance frequency, positive potential is in red, negative potential is in blue. Three different times of the oscillation of period T are considered : $t = 0$ (left), $t = T/4$ (middle), $t = T/2$ (right).

is expected as the average charge and potential of an anti-symmetric mode is null. In consequence, this mode does not contribute to the macroscopic response of the ribbon. The MTB mode (mode 3) has a large weight around $0.5 - 0.6$ eV, near the resonance frequency.

To better understand the nature of the plasmon, 3D visualization (as isosurface) of the potential of the MTB mode is shown in figure 7.26 (positive potential is in red, negative potential is in blue). It is visualized at three different times ($t = 0$, $t = T/4$, $t = T/2$, with T the period), in order to show the propagation of the plasmon. It is now clear that this mode corresponds to a longitudinal wave propagating along the ribbon axis and centered on the MTB. The plasmon is thus a polariton confined in a 1D grain boundary.

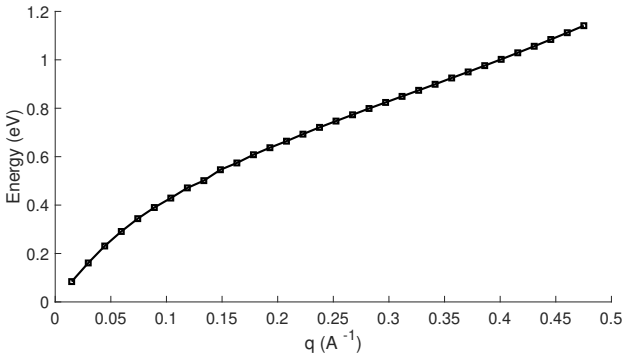

Figure 7.27: Dispersion relation of the MTB mode.

Dispersion relation of the MTB plasmonic mode

The dispersion relation of the 1D plasmon polariton has been calculated (figure 7.27). This dispersion is similar to what is obtained for plasmon at the edges of MoS_2 ribbons [204]. In this article, the authors notice that there is non-negligible contribution of the interband transitions that lower the energy of the plasmon. Here, the slight bend around $q = 0.1\,\text{Å}^{-1}$ may be attributed to interband transition but further investigations are still needed. Due to the momentum mismatch, this kind of plasmon cannot interact with light but can be excited with fast electrons, similarly to polaritons at the surface of metallic materials.

Robustness of the MTB plasmon

It has already been observed that the metallic states of the MTB are hardly affected by the change of the structure (ribbon or 2D plane). Here, the robustness of the plasmon resonance is investigated further. First, the plasmon modes of the two MTBs are compared to the plasmons modes of the same MTB in the periodic 2D plane (figure 7.28). The curves for both MTBs (figure 7.21, MTB 1: yellow and orange, MTB 2: blue) are similar whether they come from the ribbon (solid lines) or the 2D plane (dashed lines). The change in resonance energy is around 10% for the first MTB and only 1% for the second MTB. Nevertheless, the global plasmonic behavior of the MTBs does not depend on the environment of the MTB.

In figure (7.29), the maximum value of the weight of the MTB mode (at 0.45 eV) is plotted in function of the size of the vacuum layer along the y-axis (perpendicular to the ribbon). The maximum weight depends quasi-linearly to the vacuum layer size. It is again explained by the fact that the weight is proportional to the spatial average of both the charge density and potential, which are localized in the center of the MTB. Thus, increasing the vacuum layer size does not change the total charge density and potential associated to the mode but decreases the average. It is expected that the same decrease in weight happens if the width of the ribbon is increased, without changing the vacuum layer. However, this has not yet been verified numerically. On the other

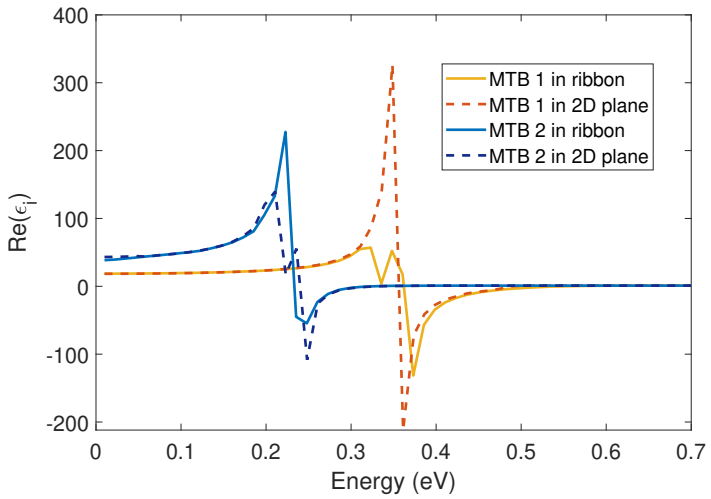

Figure 7.28: Eigenvalues of the dielectric function for two different MTB modes. First MTB in yellow and orange; second MTB in blue. MTB in the ribbon: solid lines; in the 2D plane: dashed lines.

hand, the eigenvalue of the mode does not change with the size of the cell. Therefore, the eigenvalue associated to the MTB can be seen as the intrinsic dielectric function of the MTB.

Modelling large structures

The previous results pave the way to study complex structures composed of MTB like those observed in [209] (figure 7.30). Indeed, the eigenvalue of the mode corresponds to the dielectric function of the MTB, which just needs to be scaled depending on the size of the unit cell. In particular, a structure as in the STM image in figure (7.30) could be modelled using classical electrodynamics approaches, where the MTB is considered as a different material with its own permittivity, embedded in a material with the permittivity of the pristine 2D material. For example in DDA, this particular MTB could be modeled as line of dipoles with polarizability calculated from the dielectric function of the MTB, surrounded by dipoles of polarizability calculated from the dielectric function of the planar $MoSe_2$. A benchmark could be done by comparing the optical spectra of the periodic structure presented above (figure 7.21c) obtained with this effective method and with the TDDFT method.

Conclusions

One-dimensional plasmon polaritons have been investigated in TMDs. These plasmons occur in 1D metallic channel originating from atomic reconstructions. The reconstruction affects the edges of nanoribbons or quantum dots [214, 215] but also grain boundaries

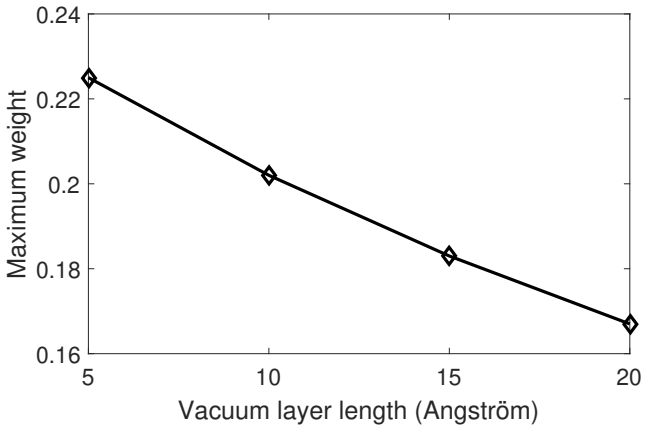

Figure 7.29: Maximum weight of the MTB mode compared to the size of the vacuum layer.

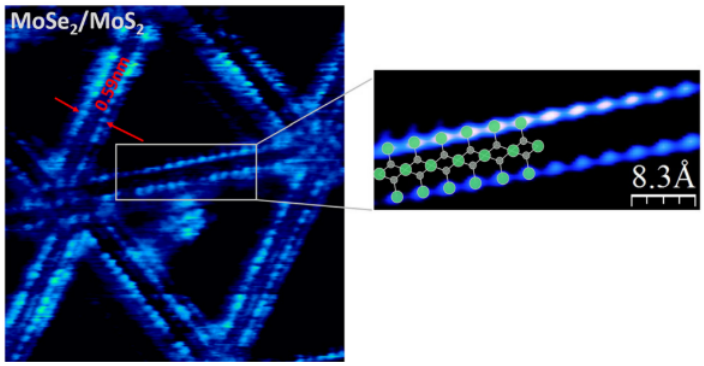

Figure 7.30: STM images of a complex structure with MTBs and an atomic model. Reproduced from [209].

arising naturally as defects on 2D materials. These grain boundaries can form complex structures that are difficult to study using an ab initio approach. Therefore, it is suggested to use an effective model in a classical electrodynamics approach.

Experimentally, the detection of these plasmons can be used to characterize the materials and estimate the density of defects. On the other hand, one may take advantage of these plasmons by using the 2D materials as substrate for SERS measurements as proposed in the previous section with corrugated graphene.

Conclusions and perspectives

2D materials are a playground for nanophotonic researchers due to the broad variety of phenomena distinctive from those in bulk materials. In this thesis, two main subjects were discussed: the modelling of 2D materials and the investigation of plasmons in nanostructured 2D materials. Several original results have been proposed on these topics, and a few other in auxiliary works. Hereafter I summarized these findings.

The modelling of 2D materials for optical calculations has been debated recently. Two models are usually used to describe 2D materials: a 3D model, using an effective permittivity, and a 2D model, using the surface susceptibility. The difference between these two models, and in particular the effect of the anisotropy in these models, have been barely investigated in the literature. On the modelling of 2D materials, I have theoretically shown that

- the surface irreducible susceptibility χ_S is the intrinsic response function of a 2D material only for in-plane polarization. Another response function, the surface external susceptibility ξ_s, must be defined for the out-of-plane polarization;

- for a vertical heterostructure, the accurate effective model is to add the surface irreducible susceptibility of each 2D material for in-plane polarization, and to add the surface external susceptibility of each 2D material for out-of-plane polarization;

- for horizontal heterostructure, the accurate optical effective model is to consider the 2D structure as isotropic in the plane, with a surface irreducible susceptibility in the plane equal to the weighted sum of the surface irreducible susceptibility of each 2D materials, while for the out-of-plane polarization, the effective external susceptibility is the weighted sum of the surface external susceptibility of each 2D material;

- these effective models are not able to describe plasmonic resonances occurring in heterostructures and, in general, the RCWA is more adapted to study such systems. However, for curved system, other complex systems, the effective models could be efficient when the RCWA cannot be applied;

- the 3D thin film model and the 2D surface polarization sheet model are equivalent for small phase shift if the anisotropy is accounted for, but the 3D model is more representative of the reality;

- ideally the isotropic thin film model should not be used, because an artificial plasmonic resonance may take place for out-of-plane polarization;

- the out-of-plane response of the different 2D materials and nanostructures considered in the thesis is negligible below 10 eV and becomes important at higher energies.

In brief, the appropriate quantities to describe a single 2D material layer are the surface susceptibilities. However, the most accurate theoretical model for 2D materials is an anisotropic 3D model due to the non-vanishing thickness of 2D materials.

Further research is needed on some points. First, some approximations have been done in the TDDFT calculations. In order to obtain better quantitative results for the optical anisotropic response of 2D materials, the GW and the BSE approaches should be used. The consequences of the random-phase approximation are also to be discussed in this context. Moreover, the long range Coulomb interaction arising for the out-of-plane polarization between repeated layers in the TDDFT calculations also affects substantially the optical spectra. Some solutions have been proposed in the literature to discard this effect, and they could be implemented to further increase the accuracy of the calculations.

A further analysis of the microscopic dielectric function of 2D materials is also needed to determine its spatial variation near the atomic plane, in both in-plane and out-of-plane polarizations.

Only a few simple systems have been investigated, but a large variety of 2D materials and heterostructures can be studied using these findings. Besides, these results could not only be used for better modelling of 2D materials in numerical simulations but also for a more accurate experimental determination of the optical constants of 2D materials.

A modification of the Brewster angle due to conducting 2D materials deposited on a dielectric surface has been highlighted in the literature. On this modification of the Brewster angle, I have reported that

- the surface irreducible susceptibility of a conducting 2D material may be determined from measurement of the Brewster angle shift induced by the 2D material;
- the Brewster angle can be actively modified by an electric control of the Fermi level of a graphene layer at the interface, with potential applications in optical telecommunications.

However, the anisotropy of the 2D material was not accounted in the study, and further investigations that include the out-of-plane response of the 2D material would permit to determine more accurately the Brewster shift in the UV.

Plasmons in nanowires of noble metals have been studied recently for their potential application as nanophotonics waveguides of reduced size compared to conventional waveguides. About such nanowires, I have reported that

- gold nanowires of high aspect ratio sustain Fabry-Perot plasmonic modes even below $0.1\,eV$;

- the Fabry-Perot modes are robust against laser-induced modification of the wire extremities at low incident energy, but can be tuned by laser irradiation at higher energies.

Further theoretical investigations would be of great interest in order to better understand the effect of nanoparticles at the extremities of the nanowire and their influence on the reflection coefficient of the electromagnetic wave at these extremities.

Plasmons in 2D materials are interesting for their high confinement and their long propagation distance. Graphene plasmon resonances stand in the infrared and it has been long awaited to achieve plasmon resonance in the visible range. On plasmons in nanostructured 2D materials, I have reported that

- dimers of 100 nm-diameter graphene disks enhance the field drastically at plasmonic resonance, when the distance between the two disks is close to the nanometer scale;
- second harmonic generation is silenced in these dimers due to the symmetry of the system, and a slight symmetry breaking greatly increases the second harmonic response;
- an eigenmode method based on the diagonalization of the microscopic dielectric function is efficient to study localized or propagating plasmons in nanostructures of a few nanometers;
- corrugated graphene sustains localized plasmons at resonance frequencies in the visible range;
- corrugated graphene can be used as a substrate for highly sensitive biosensing using surface enhance Raman spectroscopy;
- mirror twin boundaries in TMDs are metallic channels that can sustain 1D plasmon polariton;
- high density of grain boundaries in monolayer 2D materials could be studied using an effective model in classical electrodynamics if the dielectric function associated to the grain boundaries is calculated using the eigenmode method.

As it has already been pointed out above, several improvements can be made in the TDDFT calculations of the corrugated graphene and the grain boundaries of TMDs: calculations performed with the GW and the BSE approaches would give better quantitative results. Calculating the transverse microscopic dielectric function is also interesting in order to investigate accurately the optical response of these larger structures.

An effective approach, as proposed in the last point, would need an adapted method of classical electrodynamics. The DDA method (for example with the homemade code

ddeels) seems to be an appropriate choice but it is not adapted for periodic materials. Moreover, the DDA method does not account for non-local dielectric functions. If one wants to study propagating plasmons, this two features should be implemented.

To conclude, the modelling of 2D materials and their anisotropy is now much clearer thanks to recent articles, this thesis and the submitted paper [F]. It seems that not much remains to do on this topic, and now the models can be used to perform more accurate calculations and experimental determinations of optical constants of 2D materials. For the study of plasmons in nanostructured 2D materials, the eigenmode method has to be proven efficient in the investigation of quantum systems. It paves the way to the study of a large variety of 2D materials structures at the nanoscale.

Appendix

Inputs file

As an example, the input file to calculate the ground state, the optical response functions and the eigenmode decomposition of the microscopic dielectric function of graphite is given below.

```
import numpy as np
import scipy.io
from ase import Atoms
from gpaw import GPAW, PW, FermiDirac
from gpaw.response.df import DielectricFunction

# Creating the unit cell
a=1.406643
c=3.35
pbc=True
graphite = Atoms('C4',
                 scaled_positions=[(1 / 3.0, 1 / 3.0, 0),
                                   (2 / 3.0, 2 / 3.0, 0),
                                   (0, 0, 0.5),
                                   (1 / 3.0, 1 / 3.0, 0.5)],
                 cell=[(np.sqrt(3) * a / 2, 3 / 2.0 * a, 0),
                       (-np.sqrt(3) * a / 2, 3 / 2.0 * a, 0),
                       (0, 0, 2 * c)],
                 pbc=pbc)

# Parameters of the GS calculation
calc=GPAW(mode=PW(400),
          xc='LDA',
          kpts=(60,60,20),
          random=True,
          occupations=FermiDirac(0.025),
          nbands=40,
          convergence={'bands':30})

# Launch GS calculation
graphite.set_calculator(calc)
graphite.get_potential_energy()

calc.write('graphite.gpw','all')

# Parameters for the response functions calculation
df=DielectricFunction(calc='graphite.gpw',
                      domega0=0.01,
                      omegamax=40.0,
                      eta=0.025,
```

```
                      ecut=80,
                      name='graphite',
                      integrationmode='tetrahedron integration')
q=[1.0/10, 0.0, 0.0 ]

# calculation of the EELS spetrum
df.get_eels_spectrum(q_c=q,filename='graphite_EELS')

#calculation of the susceptibility in direction x
df.get_polarizability(q_c=q,direction='x',filename='polarizability_x.
    csv')

# calculation of the eigenmodes
r,w,eigenvalues,omega0,eig0,v_ind,n_ind,weight,v_res,n_res,v_m,n_m=df.
    get_eigenmodes(q_c=q)

# Saving the outputs
scipy.io.savemat('grid.mat',mdict={'r':r})
scipy.io.savemat('freq.mat',mdict={'w':w})
scipy.io.savemat('eigen.mat',mdict={'eigenvalues':eigenvalues})
scipy.io.savemat('omega0.mat',mdict={'omega0':omega0})
scipy.io.savemat('eigen0.mat',mdict={'eig0':eig0})
scipy.io.savemat('v_ind.mat',mdict={'v_ind':v_ind})
scipy.io.savemat('n_ind.mat',mdict={'n_ind':n_ind})
scipy.io.savemat('weight.mat',mdict={'weight':weight})
```

Other examples of input files can be found in the website of the GPAW code [158].

Modified script for the calculation of the eigenmodes

The script that calculates the eigenvalues and eigenvectors of the dielectric function (provided within the code GPAW [158]) has been corrected and modified, in particular to calculate the weight of each eigenmode. The modifications are notified by a comment beginning with *BM*.

```
def get_eigenmodes(self, q_c=[0, 0, 0], w_max=None, name=None,
                       eigenvalue_only=False, direction='x',
                       checkphase=True):

        """Plasmon eigenmodes as eigenvectors of the dielectric matrix
    ."""

        assert self.chi0.world.size == 1

        pd, chi0_wGG, chi0_wxvG, chi0_wvv = self.calculate_chi0(q_c)
        e_wGG = self.get_dielectric_matrix(xc='RPA', q_c=q_c,
                                           direction=direction,
                                           symmetric=False)

```

```
        kd = pd.kd

        # Get real space grid for plasmon modes:
        r = pd.gd.get_grid_point_coordinates()
        w_w = self.omega_w * Hartree
        if w_max:
            w_w = w_w[np.where(w_w < w_max)]
        Nw = len(w_w)
        nG = e_wGG.shape[1]

        eig = np.zeros([Nw, nG], dtype=complex)
        eig_all = np.zeros([Nw, nG], dtype=complex)
        weight = np.zeros([Nw,nG],dtype=complex) #BM
        vm=np.zeros([Nw,nG],dtype=complex) #BM
        nm=np.zeros([Nw,nG],dtype=complex) #BM
        # Find eigenvalues and eigenvectors:
        e_GG = e_wGG[0]
        eig_all[0], vec = np.linalg.eig(e_GG)
        eig[0] = eig_all[0]
        vec_dual = np.linalg.inv(vec)
        omega0 = np.array([])
        eigen0 = np.array([], dtype=complex)
        v_ind = np.zeros([0, r.shape[1], r.shape[2], r.shape[3]],
                         dtype=complex)
        n_ind = np.zeros([0, r.shape[1], r.shape[2], r.shape[3]],
                         dtype=complex)

        # Loop to find the eigenvalues that crosses zero
        # from negative to positive values:
        for i in np.array(range(1, Nw)):
            e_GG = e_wGG[i]  # epsilon_GG'(omega + d-omega)
            eig_all[i], vec_p = np.linalg.eig(e_GG)
            vec_dual_p = np.linalg.inv(vec_p)
            overlap = np.abs(np.dot(vec_dual, vec_p))
            index = list(np.argsort(overlap)[:, -1])
            if len(np.unique(index)) < nG:  # add missing indices
                addlist = []
                removelist = []
                for j in range(nG):
                    if index.count(j) < 1:
                        addlist.append(j)
                    if index.count(j) > 1:
                        for l in range(1, index.count(j)):
                            removelist+= \
                               list( np.argwhere(np.array(index) == j)
[1])
                for j in range(len(addlist)):
                    index[removelist[j]] = addlist[j]

            vec = vec_p[:, index]
            vec_dual = vec_dual_p[index, :]
```

```
64            eig[i] = eig_all[i, index]
65            weight[i]=vec[0,:]*(np.transpose(vec_dual[:,0])) #BM:
    weight of each mode
66            vm[i]=vec[0,:] #BM: Mean value of potential and charges
67            nm[i]=np.transpose(vec_dual[:,0])
68
69
70            for k in [k for k in range(nG)
71                      # Eigenvalue crossing:
72                      if (eig[i - 1, k] < 0 and eig[i, k] > 0)]:
73              a = np.real((eig[i, k] - eig[i - 1, k]) /
74                          (w_w[i] - w_w[i - 1]))
75                # linear interp for crossing point
76                w0 = np.real(-eig[i - 1, k]) / a + w_w[i - 1]
77                eig0 = a * (w0 - w_w[i - 1]) + eig[i - 1, k]
78                print('crossing found at w = %1.2f eV' % w0)
79                omega0 = np.append(omega0, w0)
80                eigen0 = np.append(eigen0, eig0)
81
82                # Fourier Transform:
83                qG = pd.get_reciprocal_vectors(add_q=True)
84                coef_G = np.diagonal(np.inner(qG, qG)) / (4 * pi)
85                qGr_R = np.inner(qG, r.T).T
86                factor = np.exp(1j * qGr_R)
87                v_temp = np.dot(factor, vec[:, k])
88               #BM: I commented this line : n_temp = np.dot(factor,
    vec[:, k] * coef_G)
89                n_temp = np.dot(factor,np.conj(np.transpose(vec_dual[k
    ,:]))) #BM : corrected the calculation of the left eigenvector
90                if checkphase:  # rotate eigenvectors in complex plane
91                    integral = np.zeros([81])
92                    phases = np.linspace(0, 2, 81)
93                    for ip in range(81):
94                        v_int = v_temp * np.exp(1j * pi * phases[ip])
95                        integral[ip] = abs(np.imag(v_int)).sum()
96                    phase = phases[np.argsort(integral)][0]
97                    v_temp *= np.exp(1j * pi * phase)
98                    n_temp *= np.exp(1j * pi * phase)
99                v_ind = np.append(v_ind, v_temp[np.newaxis, :], axis
    =0)
100               n_ind = np.append(n_ind, n_temp[np.newaxis, :], axis
    =0)
101
102       #BM: Adding a field/charge map to save (e.g. frequency n*20
    and mode n*5)
103           if i==20:
104               qG = pd.get_reciprocal_vectors(add_q=True)
105               coef_G = np.diagonal(np.inner(qG, qG)) / (4 * pi)
106               qGr_R = np.inner(qG, r.T).T
107               factor = np.exp(1j * qGr_R)
108               v_res = np.dot(factor, vec[:, 5])
```

```
                n_res = np.dot(factor, np.conj(np.transpose(vec_dual
[1, :])))


        kd = self.chi0.calc.wfs.kd
        if name is None and self.name:
            name = self.name + 'eigenmodes.pckl'
        elif name:
            name = name + 'eigenmodes.pckl'
        else:
            name = '%+d%+d%+d-eigenmodes.pckl' % tuple((q_c * kd.N_c).
round())

        # Returns: real space grid, frequency grid,
        # sorted eigenvalues, zero-crossing frequencies + eigenvalues,
        # induced potential + density in real space.
        if eigenvalue_only:
            pickle.dump((r * Bohr, w_w, eig),
                        open(name, 'wb'), pickle.HIGHEST_PROTOCOL)
            return r * Bohr, w_w, eig
        else:
            pickle.dump((r * Bohr, w_w, eig, omega0, eigen0,
                         v_ind, n_ind, weight,v_res,n_res,vm,nm), open
(name, 'wb'), #BM: added weight,v_res,n_res,vm,nm
                        pickle.HIGHEST_PROTOCOL)
            return r * Bohr, w_w, eig, omega0, eigen0, v_ind, n_ind,
weight,v_res,n_res,vm,nm  #BM: added weight,v_res,n_res,vm,nm
```

Parameters of the TDDFT calculations

Parameters such as the vacuum layer thickness, the k-point grid, and the cut-off energies have been selected to converge the desired results (if numerically possible: for corrugated graphene, the k-point grid is not optimal due to the highly demanding computations). The parameters for all the systems are displayed in the table below.

Material	vacuum layer(s)	k-point grid (x,y,z)	Energy cut-off	Exchange-correlation functional	number of bands	TDDFT cut-off energy
Graphite	-	(60,20,20)	400 eV	LDA	40	80 eV
Graphene	23.5 Å	(256,256,1)	350 eV	PBE	40	150 eV
hBN	23.5 Å	(256,256,1)	350 eV	PBE	40	150 eV
Graphene-hBN	20.1 Å	(256,256,1)	300 eV	PBE	40	150 eV
$MoSe_2$	12 Å	(128,128,1)	400 eV	GLLB-SC	240	100 eV
Corrugated graphene	25 Å	(48,48,1)	400 eV	LDA	140	20 eV
Ribbons of $MoSe_2$	15 Å	(128,1,1)	400 eV	GLLB-SC	240	30 eV
$MoSe_2$ with 2 MTBs	15 Å	(64,64,1)	400 eV	GLLB-SC	240	30 eV

The choices of the exchange-correlation functionals are explained here:

- For graphite it was shown that the optical constant are well reproduced with the LDA [103].
- For graphene and hBN, the PBE functionnal is shown to give better results than LDA [216].
- For corrugated graphene, due to the highly demanding calculations, the LDA was chosen. It is not a serious downside as only qualitative results are expected.
- For $MoSe_2$, the GLLB-SC is chosen because it is known to give a more accurate band-gap in semi-conductors [217]. In the figure below, the band structure of $MoSe_2$ is plotted. The bandgap energy is 1.53 eV which is exactly in the range of value found by experimental works, between 1.52 and 1.58 eV [218].

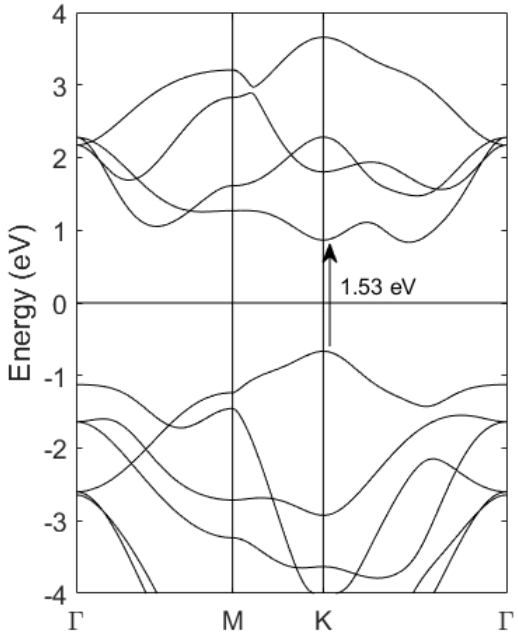

Figure 31: Bandstructure of $MoSe_2$ using the exchange-correlation functional GLLB-SC. The arrow shows the direct bandgap.

Bibliography

1. Avouris, P., Heinz, T. F. & Low, T. *2D materials: Properties and Devices* 201–201 (Cambridge, 2017).
2. Novoselov, K. S. *et al.* Electric Field Effect in Atomically Thin Carbon Films. *Science (80-.).* **306,** 666–669 (2004).
3. Novoselov, K. S. Nobel Lecture: Graphene: Materials in the Flatland. *Rev. Mod. Phys.* **83,** 837–849 (2011).
4. Castro Neto, A. H., Guinea, F., Peres, N. M. R., Novoselov, K. S. & Geim, A. K. The electronic properties of graphene. *Rev. Mod. Phys.* **81,** 109–162 (2009).
5. Radisavljevic, B., Radenovic, A., Brivio, J., Giacometti, V. & Kis, A. Single-layer MoS2 transistors. *Nat. Nanotechnol.* **6,** 147–150 (2011).
6. Lin, Y & Connell, J. W. Advances in 2D boron nitride nanostructures: nanosheets, nanoribbons, nanomeshes, and hybrids with graphene. *Nanoscale* **4,** 6908–6939 (2012).
7. Mak, K. F. *et al.* Measurement of the Optical Conductivity of Graphene. *Phys. Rev. Lett.* **101,** 196405 (2008).
8. Lobet, M., Majerus, B., Henrard, L. & Lambin, P. Perfect electromagnetic absorption using graphene and epsilon-near-zero metamaterials. *Phys. Rev. B* **93,** 235424 (2016).
9. Leyong Jiang, Qingkai Wang, Yuanjiang Xiang, Xiaoyu Dai & Shuangchun Wen. Electrically Tunable Goos–Hänchen Shift of Light Beam Reflected From a Graphene-on-Dielectric Surface. *IEEE Photonics J.* **5,** 6500108–6500108 (2013).
10. Li, X. *et al.* Experimental observation of a giant Goos–Hänchen shift in graphene using a beam splitter scanning method. *Opt. Lett.* **39,** 5574 (2014).
11. You, Q. *et al.* Giant and controllable Goos-Hänchen shifts based on surface plasmon resonance with graphene-MoS2 heterostructure. *Opt. Mater. Express* **8,** 3036–3048 (2018).
12. Hermosa, N. Reflection beamshifts of visible light due to graphene. *J. Opt.* **18,** 025612 (2016).
13. Bludov, Y. V., Peres, N. M. R. & Vasilevskiy, M. I. Unusual reflection of electromagnetic radiation from a stack of graphene layers at oblique incidence. *J. Opt.* **15,** 114004 (2013).
14. Chang, M.-C. & Yang, M.-F. Optical signature of topological insulators. *Phys. Rev. B* **80,** 113304 (2009).
15. Xu, G., Cao, M., Liu, C., Sun, J. & Pan, T. Tunable lateral and angular shifts of a reflected beam from a graphene-based structure. *Opt. - Int. J. Light Electron Opt.* **127,** 2521–2524 (2016).

16. Chen, Z. *et al.* Graphene controlled Brewster angle device for ultra broadband terahertz modulation. *Nat. Commun.* **9,** 1–7 (2018).

17. Romagnoli, P. *et al.* Making graphene visible on transparent dielectric substrates: Brewster angle imaging. *2D Mater.* **2,** 035017 (2015).

18. Malik, N. A. *et al.* Experimental Study of Few-Layer Graphene: Optical Anisotropy and Pseudo-Brewster Angle Shift in Vacuum Ultraviolet Spectral Range. *Adv. Photonics Res.* **2,** 2000207 (2021).

19. Li, Y. & Heinz, T. F. Two-dimensional models for the optical response of thin films. *2D Mater.* **5** (2018).

20. Matthes, L., Pulci, O. & Bechstedt, F. Influence of out-of-plane response on optical properties of two-dimensional materials: First principles approach. *Phys. Rev. B* **94,** 205408 (2016).

21. Jayaswal, G. *et al.* Measurement of the surface susceptibility and the surface conductivity of atomically thin MoS 2 by spectroscopic ellipsometry. *Opt. Lett.* **43,** 703 (2018).

22. Xu, Z. *et al.* Optical detection of the susceptibility tensor in two-dimensional crystals. *Commun. Phys.* **4,** 215 (2021).

23. Dell'Anna, L., He, Y. & Merano, M. Reflection, transmission, and surface susceptibility tensor of two-dimensional materials. *Phys. Rev. A* **105,** 053515 (2022).

24. Valuev, I., Belousov, S., Bogdanova, M., Kotov, O. & Lozovik, Y. FDTD subcell graphene model beyond the thin-film approximation. *Appl. Phys. A Mater. Sci. Process.* **123,** 1–7 (2017).

25. Koppens, F. H. L., Chang, D. E. & García de Abajo, F. J. Graphene Plasmonics: A Platform for Strong Light–Matter Interactions. *Nano Lett.* **11,** 3370–3377 (2011).

26. Maier, S. A. *et al.* Local detection of electromagnetic energy transport below the diffraction limit in metal nanoparticle plasmon waveguides. *Nat. Mater.* **2,** 229–232 (2003).

27. Ditlbacher, H. *et al.* Silver Nanowires as Surface Plasmon Resonators. *Phys. Rev. Lett.* **95,** 257403 (2005).

28. Brongersma, M. L. & Shalaev, V. M. The Case for Plasmonics. *Science (80-.).* **328,** 440–441 (2010).

29. Li, Q. & Qiu, M. Plasmonic wave propagation in silver nanowires: guiding modes or not? *Opt. Express* **21,** 8587 (2013).

30. Rossouw, D. & Botton, G. A. Plasmonic Response of Bent Silver Nanowires for Nanophotonic Subwavelength Waveguiding. *Phys. Rev. Lett.* **110,** 066801 (2013).

31. Martin, J. *et al.* High-Resolution Imaging and Spectroscopy of Multipolar Plasmonic Resonances in Aluminum Nanoantennas. *Nano Lett.* **14,** 5517–5523 (2014).

32. Barnard, E. S., White, J. S., Chandran, A. & Brongersma, M. L. Spectral properties of plasmonic resonator antennas. *Opt. Express* **16,** 16529 (2008).

33. Mkhitaryan, V. *et al.* Can Copper Nanostructures Sustain High-Quality Plasmons? *Nano Lett.* **21,** 2444–2452 (2021).

34. Fang, Z. *et al.* Gated Tunability and Hybridization of Localized Plasmons in Nanostructured Graphene. *ACS Nano* **7,** 2388–2395 (2013).

35. Thongrattanasiri, S., Manjavacas, A. & García De Abajo, F. J. Quantum finite-size effects in graphene plasmons. *ACS Nano* **6,** 1766–1775 (2012).

36. Andersen, K. & Thygesen, K. S. Plasmons in metallic monolayer and bilayer transition metal dichalcogenides. *Phys. Rev. B - Condens. Matter Mater. Phys.* **88,** 1–5 (2013).

37. Rossi, T. P. *et al.* Effect of edge plasmons on the optical properties of MoS2 monolayer flakes. *Phys. Rev. B* **96,** 1–10 (2017).

38. Thongrattanasiri, S. & Garcia de Abajo, F. J. Optical Field Enhancement by Strong Plasmon Interaction in Graphene Nanostructures. *Phys. Rev. Lett.* **110,** 187401 (2013).

39. Yan, H. *et al.* Damping pathways of mid-infrared plasmons in graphene nanostructures. *Nat. Photonics* **7,** 394–399 (2013).

40. Sharma, B., Frontiera, R. R., Henry, A. I., Ringe, E. & Van Duyne, R. P. SERS: Materials, applications, and the future. *Mater. Today* **15,** 16–25 (2012).

41. Koós, A. A. *et al.* Influence of Native Defects on the Electronic and Magnetic Properties of CVD Grown MoSe2 Single Layers. *J. Phys. Chem. C* **123,** 24855–24864 (2019).

42. Jackson, J. D. *Classical Electrodynamics* 3rd Editio, 832 (Wiley, 1998).

43. Maier, S. A. *Plasmonics: Fundamentals and Applications* 1–223 (Springer US, Boston, MA, 2007).

44. Stockman, M. I. Nanoplasmonics: The physics behind the applications. *Phys. Today* **64,** 39–44 (2011).

45. Andersen, K., Jacobsen, K. W. & Thygesen, K. S. Spatially resolved quantum plasmon modes in metallic nano-films from first-principles. *Phys. Rev. B* **86,** 245129 (2012).

46. Grosso, G. & Parravicini, G. *Solid State Physics* (Elsevier, 2000).

47. Shrivastav, A. M., Cvelbar, U. & Abdulhalim, I. A comprehensive review on plasmonic-based biosensors used in viral diagnostics. *Commun. Biol.* **4,** 1–12 (2021).

48. Oulton, R. F., Sorger, V. J., Genov, D. A., Pile, D. F. & Zhang, X. A hybrid plasmonic waveguide for subwavelength confinement and long-range propagation. *Nat. Photonics* **2,** 496–500 (2008).

49. Mubeen, S. *et al.* On the plasmonic photovoltaic. *ACS Nano* **8,** 6066–6073 (2014).

50. Mounet, N. *et al.* Two-dimensional materials from high-throughput computational exfoliation of experimentally known compounds. *Nat. Nanotechnol.* **13,** 246–252 (2018).

51. Geim, A. K. & Novoselov, K. S. The rise of graphene. *Nat. Mater.* **6,** 183–191 (2007).

52. Fasolino, A., Los, J. H. & Katsnelson, M. I. Intrinsic ripples in graphene. *Nat. Mater.* **6,** 858–861 (2007).

53. Meyer, J. C. *et al.* The structure of suspended graphene sheets. *Nature* **446,** 60–63 (2007).

54. Lui, C. H., Liu, L., Mak, K. F., Flynn, G. W. & Heinz, T. F. Ultraflat graphene. *Nature* **462,** 339–341 (2009).

55. *Graphene flagship, https://graphene-flagship.eu*

56. Zheng, J. *et al.* High quality graphene with large flakes exfoliated by oleyl amine. *Chem. Commun.* **46,** 5728–5730 (2010).

57. Nicolosi, V., Chhowalla, M., Kanatzidis, M. G., Strano, M. S. & Coleman, J. N. Liquid exfoliation of layered materials. *Science (80-.).* **340** (2013).

58. Kitaura, R. *et al.* Chemical vapor deposition growth of graphene and related materials. *J. Phys. Soc. Japan* **84,** 1–13 (2015).

59. Thanh Trung, P. *et al.* Direct growth of graphene on Si(111). *J. Appl. Phys.* **115,** 223704 (2014).

60. Pham, T. T. *et al.* Higher-indexed Moiré patterns and surface states of MoTe2/graphene heterostructure grown by molecular beam epitaxy. *npj 2D Mater. Appl.* **6,** 48 (2022).

61. Hus, S. M. & Li, A. P. Spatially-resolved studies on the role of defects and boundaries in electronic behavior of 2D materials. *Prog. Surf. Sci.* **92,** 176–201 (2017).

62. Bolotin, K. I. *et al.* Ultrahigh electron mobility in suspended graphene. *Solid State Commun.* **146,** 351–355 (2008).

63. De Fazio, D. *et al.* High-Mobility, Wet-Transferred Graphene Grown by Chemical Vapor Deposition. *ACS Nano* **13,** 8926–8935 (2019).

64. Roldán, R. *et al.* Electronic properties of single-layer and multilayer transition metal dichalcogenides MX2 (M = Mo, W and X = S, Se). *Ann. Phys.* **526,** 347–357 (2014).

65. Larentis, S., Fallahazad, B. & Tutuc, E. Field-effect transistors and intrinsic mobility in ultra-thin MoSe 2 layers. *Appl. Phys. Lett.* **101** (2012).

66. Sarkar, D. *et al.* MoS 2 Field-Effect Transistor for Next-Generation Label-Free Biosensors. *ACS Nano* **8,** 3992–4003 (2014).

67. Nourbakhsh, A. *et al.* MoS 2 Field-Effect Transistor with Sub-10 nm Channel Length. *Nano Lett.* **16,** 7798–7806 (2016).

68. Geim, A. K. & Grigorieva, I. V. Van der Waals heterostructures. *Nature* **499,** 419–425 (2013).

69. Dean, C. R. *et al.* Boron nitride substrates for high-quality graphene electronics. *Nat. Nanotechnol.* **5,** 722–726 (2010).

70. Mayorov, A. S. *et al.* Micrometer-scale ballistic transport in encapsulated graphene at room temperature. *Nano Lett.* **11,** 2396–2399 (2011).

71. Cao, Y. *et al.* Unconventional superconductivity in magic-angle graphene superlattices. *Nature* **556,** 43–50 (2018).

72. Falkovsky, L. A. & Varlamov, A. A. Space-time dispersion of graphene conductivity. *Eur. Phys. J. B* **56,** 281–284 (2007).

73. Mak, K. F., Ju, L., Wang, F. & Heinz, T. F. Optical spectroscopy of graphene: From the far infrared to the ultraviolet. *Solid State Commun.* **152,** 1341–1349 (2012).

74. Stauber, T., Peres, N. M. R. & Geim, A. K. Optical conductivity of graphene in the visible region of the spectrum. *Phys. Rev. B* **78,** 085432 (2008).

75. Falkovsky, L. A. & Pershoguba, S. S. Optical far-infrared properties of a graphene monolayer and multilayer. *Phys. Rev. B* **76,** 153410 (2007).

76. Rouhi, N. *et al. Broadband Conductivity of Graphene from DC to THz* in *2011 11th IEEE Int. Conf. Nanotechnol.* (2011), 1205–1207.

77. Batrakov, K. *et al.* Flexible transparent graphene/polymer multilayers for efficient electromagnetic field absorption. *Sci. Rep.* **4,** 7191 (2015).

78. Lobet, M., Reckinger, N., Henrard, L. & Lambin, P. Robust electromagnetic absorption by graphene/polymer heterostructures. *Nanotechnology* **26,** 285702 (2015).

79. Grigorenko, A. N., Polini, M. & Novoselov, K. S. Graphene plasmonics. *Nat. Photonics* **6,** 749–758 (2012).

80. García de Abajo, F. J. Graphene Plasmonics: Challenges and Opportunities. *ACS Photonics* **1,** 135–152 (2014).

81. Christensen, J., Manjavacas, A., Thongrattanasiri, S., Koppens, F. H. L. & García De Abajo, F. J. Graphene plasmon waveguiding and hybridization in individual and paired nanoribbons. *ACS Nano* **6,** 431–440 (2012).

82. Fang, Z. *et al.* Active Tunable Absorption Enhancement with Graphene Nanodisk Arrays. *Nano Lett.* **14,** 299–304 (2014).

83. Vacacela Gomez, C., Pisarra, M, Gravina, M, Riccardi, P & Sindona, A. Plasmon properties and hybridization effects in silicene. *Phys. Rev. B* **95,** 085419 (2017).

84. Ando, Y. Topological Insulator Materials. *J. Phys. Soc. Japan* **82,** 102001 (2013).

85. Di Pietro, P. *et al.* Observation of Dirac plasmons in a topological insulator. *Nat. Nanotechnol.* **8,** 556–560 (2013).

86. Yin, J. *et al.* Plasmonics of topological insulators at optical frequencies. *Opt. InfoBase Conf. Pap.* **Part F81-E,** e425–8 (2017).

87. Kandrai, K. *et al.* Signature of Large-Gap Quantum Spin Hall State in the Layered Mineral Jacutingaite. *Nano Lett.* **20,** 5207–5213 (2020).

88. Payne, M. C., Teter, M. P., Allan, D. C., Arias, T. A. & Joannopoulos, J. D. Iterative minimization techniques for ab initio total-energy calculations: molecular dynamics and conjugate gradients. *Rev. Mod. Phys.* **64,** 1045–1097 (1992).

89. Perdew, J. P., Burke, K. & Ernzerhof, M. Generalized Gradient Approximation Made Simple, 3865–3868 (1996).

90. Bernadotte, S., Evers, F. & Jacob, C. R. Plasmons in molecules. *J. Phys. Chem. C* **117,** 1863–1878 (2013).

91. Gross, E. K. U. & Maitra, N. T. in *Fundam. Time-Dependent Density Funct. Theory* 53–99 (Springer Berlin Heidelberg, 2012).

92. Onida, G., Reining, L. & Rubio, A. Electronic excitations: density-functional versus many-body Green's-function approaches. *Rev. Mod. Phys.* **74,** 601–659 (2002).

93. Shishkin, M. & Kresse, G. Implementation and performance of the frequency-dependent GW method within the PAW framework. *Phys. Rev. B* **74,** 035101 (2006).

94. Richard Milton Martin. *Electronic Structure: Basic Theory and Practical Methods* 1st editio, 650 (Cambridge University Press, 2008).

95. Blöchl, P. E., Först, C. J. & Schimpl, J. Projector augmented wave method:ab initio molecular dynamics with full wave functions. *Bull. Mater. Sci.* **26,** 33–41 (2003).

96. Delerue, C. & Lannoo, M. *Nanostructures* (Springer Berlin Heidelberg, Berlin, Heidelberg, 2004).

97. Hybertsen, M. S. & Louie, S. G. Ab initio static dielectric matrices from the density-functional approach. I. Formulation and application to semiconductors and insulators. *Phys. Rev. B* **35,** 5585–5601 (1987).

98. Keldysh, L., Maradudin, A. A. & Kirzhnitz, D. A. *The dielectric function of Condensed systems* (eds Keldysh, L., Maradudin, A. A. & Kirzhnitz, D. A.) (Elsevier, 1989).

99. Ehrenreich, H. & Cohen, M. H. Self-consistent field approach to the many-electron problem. *Phys. Rev.* **115,** 786–790 (1959).

100. Adler, S. L. Quantum Theory of the Dielectric Constant in Real Solids. *Phys. Rev.* **126,** 413–420 (1962).

101. Wiser, N. Dielectric Constant with Local Field Effects Included. *Phys. Rev.* **129,** 62–69 (1963).

102. Marinopoulos, A. G. *et al.* Anisotropy and Interplane Interactions in the Dielectric Response of Graphite. *Phys. Rev. Lett.* **89,** 076402 (2002).

103. Marinopoulos, A. G., Reining, L., Rubio, A. & Olevano, V. Ab initio study of the optical absorption and wave-vector-dependent dielectric response of graphite. *Phys. Rev. B* **69,** 245419 (2004).

104. Bechstedt, F. & Enderlein, R. Inverse dielectric function of a superlattice including local field effects and spatial dispersion. *Superlattices Microstruct.* **2,** 543–549 (1986).

105. Moharam, M. G. & Gaylord, T. K. Rigorous coupled-wave analysis of planar-grating diffraction. *J. Opt. Soc. Am.* **71,** 811 (1981).

106. Vigneron, J. P. *et al.* Theory of electromagnetic energy transfer in three-dimensional structures. *Ultramicroscopy* **61,** 21–27 (1995).

107. Sarrazin, M., Herman, A. & Deparis, O. First-principle calculation of solar cell efficiency under incoherent illumination. *Opt. Express* **21,** A616 (2013).

108. Zhao, B. & Zhang, Z. M. Perfect mid-infrared absorption by hybrid phonon-plasmon polaritons in hBN/metal-grating anisotropic structures. *Int. J. Heat Mass Transf.* **106,** 1025–1034 (2017).

109. Xiong, J. & Wu, S.-T. Rigorous coupled-wave analysis of liquid crystal polarization gratings. *Opt. Express* **28,** 35960 (2020).

110. Emerick, G. *Modélisation des propriétés optiques des multicouches anisotropes latéralement structurées* MA thesis (University of Namur, 2019).

111. Deparis, O. *Cours de photonique théorique et numérique* University of Namur, 2021.

112. Purcell, E. M. & Pennypacker, C. R. Scattering and absorption of light by nonspherical dielectric grains. *Astrophys. J.* **186,** 705–714 (1973).

113. Draine, B. T. & Flatau, P. J. Discrete-Dipole Approximation For Scattering Calculations. *J. Opt. Soc. Am. A* **11,** 1491 (1994).

114. Geuquet, N. & Henrard, L. EELS and optical response of a noble metal nanoparticle in the frame of a discrete dipole approximation. *Ultramicroscopy* **110,** 1075–1080 (2010).

115. Rao, S, Wilton, D & Glisson, A. Electromagnetic scattering by surfaces of arbitrary shape. *IEEE Trans. Antennas Propag.* **30,** 409–418 (1982).

116. Butet, J., Gallinet, B., Thyagarajan, K. & Martin, O. J. F. Second-harmonic generation from periodic arrays of arbitrary shape plasmonic nanostructures: a surface integral approach. *J. Opt. Soc. Am. B* **30,** 2970 (2013).

117. Alber, I. *et al.* Visualization of Multipolar Longitudinal and Transversal Surface Plasmon Modes in Nanowire Dimers. *ACS Nano* **5,** 9845–9853 (2011).

118. Rossouw, D., Couillard, M., Vickery, J., Kumacheva, E. & Botton, G. A. Multipolar Plasmonic Resonances in Silver Nanowire Antennas Imaged with a Subnanometer Electron Probe. *Nano Lett.* **11,** 1499–1504 (2011).

119. Makarov, S. V. *et al.* Light-Induced Tuning and Reconfiguration of Nanophotonic Structures. *Laser Photon. Rev.* **11,** 1700108 (2017).

120. Zhou, R., Yang, S., Liu, D. & Cao, G. Confined surface plasmon of fundamental wave and second harmonic waves in graphene nanoribbon arrays. *Opt. Express* **25,** 31478 (2017).

121. Olmon, R. L. *et al.* Optical dielectric function of gold. *Phys. Rev. B* **86,** 235147 (2012).

122. Jeanguillaume, C. & Colliex, C. Spectrum-image: The next step in EELS digital acquisition and processing. *Ultramicroscopy* **28,** 252–257 (1989).

123. Arenal, R. *et al.* Extending the analysis of EELS spectrum-imaging data, from elemental to bond mapping in complex nanostructures. *Ultramicroscopy* **109,** 32–38 (2008).

124. Ashley, J. & Emerson, L. Dispersion relations for non-radiative surface plasmons on cylinders. *Surf. Sci.* **41,** 615–618 (1974).

125. Zhang, S. *et al.* Chiral Surface Plasmon Polaritons on Metallic Nanowires. *Phys. Rev. Lett.* **107,** 096801 (2011).

126. Tancogne-Dejean, N., Giorgetti, C. & Véniard, V. Optical properties of surfaces with supercell ab initio calculations: Local-field effects. *Phys. Rev. B - Condens. Matter Mater. Phys.* **92,** 1–10 (2015).

127. Merano, M. Fresnel coefficients of a two-dimensional atomic crystal. *Phys. Rev. A* **93,** 013832 (2016).

128. Majérus, B., Dremetsika, E., Lobet, M., Henrard, L. & Kockaert, P. Electrodynamics of two-dimensional materials: Role of anisotropy. *Phys. Rev. B* **98,** 125419 (2018).

129. Guilhon, I. *et al.* Out-of-plane excitons in two-dimensional crystals. *Phys. Rev. B* **99,** 161201 (2019).

130. Huidobro, P. A., Kraft, M, Kun, R, Maier, S. A. & Pendry, J. B. Graphene, plasmons and transformation optics. *J. Opt.* **18,** 044024 (2016).

131. Li, X. B. *et al.* Edge mode graphene plasmons based all-optical logic gates. *Photonics Nanostructures - Fundam. Appl.* **33,** 66–69 (2018).

132. Smirnova, D. A., Noskov, R. E., Smirnov, L. A. & Kivshar, Y. S. Dissipative plasmon solitons in graphene nanodisk arrays. *Phys. Rev. B - Condens. Matter Mater. Phys.* **91,** 3–8 (2015).

133. Yeung, K. Y. M. *et al.* Far-infrared graphene plasmonic crystals for plasmonic band engineering. *Nano Lett.* **14,** 2479–2484 (2014).

134. Meera, V. & Setlur, G. S. Ellipsometry of graphene on a substrate. *J. Appl. Phys.* **107,** 033525 (2010).

135. Hashemi, M., Farzad, M. H., Asger Mortensen, N & Xiao, S. Enhanced absorption of graphene in the visible region by use of plasmonic nanostructures. *J. Opt.* **15,** 055003 (2013).

136. Zhan, T., Shi, X., Dai, Y., Liu, X. & Zi, J. Transfer matrix method for optics in graphene layers. *J. Phys. Condens. Matter* **25,** 215301 (2013).

137. Dong, B. *et al.* Large tunable optical absorption of CVD graphene under total internal reflection by strain engineering. *Nanotechnology* **25,** 455707 (2014).

138. Majérus, B. *et al.* Modified Brewster angle on conducting 2D materials. *2D Mater.* **5,** 025007 (2018).

139. Poddubny, A., Iorsh, I., Belov, P. & Kivshar, Y. Hyperbolic metamaterials. *Nat. Photonics* **7,** 948–957 (2013).

140. Novoselov, K. S., Mishchenko, A., Carvalho, A. & Castro Neto, A. H. 2D materials and van der Waals heterostructures. *Science (80-.).* **353** (2016).

141. Li, F., Wei, W., Zhao, P., Huang, B. & Dai, Y. Electronic and Optical Properties of Pristine and Vertical and Lateral Heterostructures of Janus MoSSe and WSSe. *J. Phys. Chem. Lett.* **8,** 5959–5965 (2017).

142. Wang, J., Ma, F., Liang, W., Wang, R. & Sun, M. Optical, photonic and optoelectronic properties of graphene, h-NB and their hybrid materials. *Nanophotonics* **6,** 943–976 (2017).

143. Farmani, A., Yavarian, M., Alighanbari, A., Miri, M. & Sheikhi, M. H. Tunable graphene plasmonic Y-branch switch in the terahertz region using hexagonal boron nitride with electric and magnetic biasing. *Appl. Opt.* **56,** 8931 (2017).

144. Ren, K. *et al.* Electronic and optical properties of van der Waals vertical heterostructures based on two-dimensional transition metal dichalcogenides: First-principles calculations. *Phys. Lett. Sect. A Gen. At. Solid State Phys.* **383,** 1487–1492 (2019).

145. Li, P. *et al.* Collective near-field coupling and nonlocal phenomena in infrared-phononic metasurfaces for nano-light canalization. *Nat. Commun.* **11,** 3663 (2020).

146. Zhang, Q. *et al.* Interface nano-optics with van der Waals polaritons. *Nature* **597,** 187–195 (2021).

147. Das, T., Chakrabarty, S., Kawazoe, Y. & Das, G. P. Tuning the electronic and magnetic properties of graphene/ h -BN hetero nanoribbon: A first-principles investigation. *AIP Adv.* **8** (2018).

148. Hüser, F., Olsen, T. & Thygesen, K. S. How dielectric screening in two-dimensional crystals affects the convergence of excited-state calculations: Monolayer MoS2. *Phys. Rev. B - Condens. Matter Mater. Phys.* **88,** 1–9 (2013).

149. Liu, Y., Bartal, G. & Zhang, X. All-angle negative refraction and imaging in a bulk medium made of metallic nanowires in the visible region. *Opt. Express* **16,** 15439 (2008).

150. Correas-Serrano, D., Gomez-Diaz, J. S., Tymchenko, M. & Alù, A. Nonlocal response of hyperbolic metasurfaces. *Opt. Express* **23,** 29434 (2015).

151. Rahmanzadeh, M., Rejaei, B., Memarian, M. & Khavasi, A. Analytical and rigorous method for analysis of an array of magnetically-biased graphene ribbons. *Opt. Express* **27,** 28395 (2019).

152. Qi, H. J., Zhang, D. P., Shao, J. D. & Fan, Z. X. Matrix analysis of an anisotropic optical thin film. *Europhys. Lett.* **70,** 257–263 (2005).

153. Idemen, M. Universal Boundary Relations of the Electromagnetic Field. *J. Phys. Soc. Japan* **59,** 71–80 (1990).

154. Felderhof, B. U. & Marowsky, G. Electromagnetic radiation from a polarization sheet located at an interface between two media. *Appl. Phys. B Photophysics Laser Chem.* **44,** 11–17 (1987).

155. Felderhof, B. U. & Marowsky, G. Linear optics of polarization sheets. *Appl. Phys. B Photophysics Laser Chem.* **43,** 161–166 (1987).

156. Polyanskiy Mikhail. *Refractive Index Database*

157. Enkovaara, J. *et al.* Electronic structure calculations with GPAW: a real-space implementation of the projector augmented-wave method. *J. Phys. Condens. Matter* **22,** 253202 (2010).

158. *https://wiki.fysik.dtu.dk/gpaw/*

159. Sevilla, J. R. M. & Putungan, D. B. Graphene-hexagonal boron nitride van der Waals heterostructures: an examination of the effects of different van der Waals corrections. *Mater. Res. Express* **8,** 085601 (2021).

160. Trevisanutto, P. E., Giorgetti, C., Reining, L., Ladisa, M. & Olevano, V. Ab Initio GW many-body effects in graphene. *Phys. Rev. Lett.* **101,** 1–4 (2008).

161. Chen, Z. & Wang, X.-Q. Stacking-dependent optical spectra and many-electron effects in bilayer graphene. *Phys. Rev. B* **83,** 081405 (2011).

162. Mak, K. F. *et al.* Tuning Many-Body Interactions in Graphene: The Effects of Doping on Excitons and Carrier Lifetimes. *Phys. Rev. Lett.* **112,** 207401 (2014).

163. Park, H. G. *et al.* Temperature Dependence of the Dielectric Function of Monolayer MoSe2. *Sci. Rep.* **8,** 1–10 (2018).

164. Caramella, L., Onida, G., Finocchi, F., Reining, L. & Sottile, F. Optical properties of real surfaces: Local-field effects at oxidized Si (100) (2×2) computed with an efficient numerical scheme. *Phys. Rev. B - Condens. Matter Mater. Phys.* **75,** 1–9 (2007).

165. Dean, C. *et al.* Graphene based heterostructures. *Solid State Commun.* **152,** 1275–1282 (2012).

166. Wang, L. *et al.* New Generation of Moiré Superlattices in Doubly Aligned hBN/-Graphene/hBN Heterostructures. *Nano Lett.* **19,** 2371–2376 (2019).

167. De Angelis, C., Locatelli, A., Mutti, A. & Aceves, A. Coupling dynamics of 1D surface plasmon polaritons in hybrid graphene systems. *Opt. Lett.* **41,** 480 (2016).

168. Stenzel, O. *The Physics of Thin Film Optical Spectra* (Springer International Publishing, Cham, 2016).

169. Stenzel, O. *The Physics of Thin Film Optical Spectra* 85–93 (Springer International Publishing, Cham, 2016).

170. Kitamura, R., Pilon, L. & Jonasz, M. Optical constants of silica glass from extreme ultraviolet to far infrared at near room temperature. *Appl. Opt.* **46,** 8118 (2007).

171. Mak, K. F., Shan, J. & Heinz, T. F. Seeing Many-Body Effects in Single- and Few-Layer Graphene: Observation of Two-Dimensional Saddle-Point Excitons. *Phys. Rev. Lett.* **106,** 046401 (2011).

172. Matthes, L., Pulci, O. & Bechstedt, F. Optical properties of two-dimensional honeycomb crystals graphene, silicene, germanene, and tinene from first principles. *New J. Phys.* **16** (2014).

173. John, R. & Merlin, B. Optical properties of graphene, silicene, germanene, and stanene from IR to far UV ? A first principles study. *J. Phys. Chem. Solids* **110,** 307–315 (2017).

174. Bayle, M. *et al.* Determining the number of layers in few-layer graphene by combining Raman spectroscopy and optical contrast. *J. Raman Spectrosc.* **49,** 36–45 (2018).

175. Hiroyuki, F. *Spectroscopic Ellipsometry: Principles and Applications* 392 (Wiley, 2007).

176. Kravets, V. G. *et al.* Spectroscopic ellipsometry of graphene and an exciton-shifted van Hove peak in absorption. *Phys. Rev. B* **81,** 155413 (2010).

177. Boyd, R. W. *Nonlinear optics* 613 (Academic Press, 2008).

178. Mikhailov, S. A. & Ziegler, K. Nonlinear electromagnetic response of graphene: frequency multiplication and the self-consistent-field effects. *J. Phys. Condens. Matter* **20,** 384204 (2008).

179. Lobet, M. *et al.* Probing Graphene χ (2) Using a Gold Photon Sieve. *Nano Lett.* **16,** 48–54 (2016).

180. Dremetsika, E. & Kockaert, P. Enhanced optical Kerr effect method for a detailed characterization of the third-order nonlinearity of two-dimensional materials applied to graphene. *Phys. Rev. B* **96,** 235422 (2017).

181. Zhou, R., Guo, T., Huang, L. & Ullah, K. Engineering the harmonic generation in graphene. *Mater. Today Phys.* **23,** 100649 (2022).

182. Autere, A. *et al.* Nonlinear Optics with 2D Layered Materials. *Adv. Mater.* **30** (2018).

183. Ullah, K., Meng, Y., Shi, Y. & Wang, F. Harmonic Generation in Low-Dimensional Materials. *Adv. Opt. Mater.* **10,** 1–24 (2022).

184. Yan, H., Xia, F., Li, Z. & Avouris, P. Plasmonics of coupled graphene microstructures. *New J. Phys.* **14,** 125001 (2012).

185. Yan, H. *et al.* Tunable infrared plasmonic devices using graphene/insulator stacks. *Nat. Nanotechnol.* **7,** 330–334 (2012).

186. Thongrattanasiri, S., Koppens, F. H. L. & García de Abajo, F. J. Complete Optical Absorption in Periodically Patterned Graphene. *Phys. Rev. Lett.* **108,** 047401 (2012).

187. Ramirez, F., Liu, B. & Shen, S. Extreme blueshift of surface plasmon resonance frequency in graphene nanodisk stacks. *J. Quant. Spectrosc. Radiat. Transf.* **158,** 27–35 (2015).

188. Rosolen, G. & Maes, B. Asymmetric and connected graphene dimers for a tunable plasmonic response. *Phys. Rev. B - Condens. Matter Mater. Phys.* **92,** 1–7 (2015).

189. Raziman, T. V., Somerville, W. R. C., Martin, O. J. F. & Le Ru, E. C. Accuracy of surface integral equation matrix elements in plasmonic calculations. *J. Opt. Soc. Am. B* **32,** 485 (2015).

190. Christensen, T., Wang, W., Jauho, A. P., Wubs, M. & Mortensen, N. A. Classical and quantum plasmonics in graphene nanodisks: Role of edge states. *Phys. Rev. B - Condens. Matter Mater. Phys.* **90,** 1–16 (2014).

191. Zuloaga, J., Prodan, E. & Nordlander, P. Quantum Description of the Plasmon Resonances of a Nanoparticle Dimer. *Nano Lett.* **9,** 887–891 (2009).

192. Scholl, J. A., García-Etxarri, A., Koh, A. L. & Dionne, J. A. Observation of Quantum Tunneling between Two Plasmonic Nanoparticles. *Nano Lett.* **13,** 564–569 (2013).

193. Romero, I., Aizpurua, J., Bryant, G. W. & García De Abajo, F. J. Plasmons in nearly touching metallic nanoparticles: singular response in the limit of touching dimers. *Opt. Express* **14,** 9988–9999 (2006).

194. Cox, J. D., Marini, A. & de Abajo, F. J. G. Plasmon-assisted high-harmonic generation in graphene. *Nat. Commun.* **8,** 14380 (2017).

195. Berthelot, J. *et al.* Silencing and enhancement of second-harmonic generation in optical gap antennas. *Opt. Express* **20,** 10498 (2012).

196. Ren, Q., You, J. W. & Panoiu, N. C. Large enhancement of the effective second-order nonlinearity in graphene metasurfaces. *Phys. Rev. B* **99,** 1–10 (2019).

197. You, J. W. & Panoiu, N. C. Tunable and dual-broadband giant enhancement of second-harmonic and third-harmonic generation in an optimized graphene-insulator-graphene metasurface. *Phys. Rev. B* **102,** 121403 (2020).

198. Yan, J., Mortensen, J. J., Jacobsen, K. W. & Thygesen, K. S. Linear density response function in the projector augmented wave method: Applications to solids, surfaces, and interfaces. *Phys. Rev. B* **83,** 245122 (2011).

199. Rüting, F. Plasmons in disordered nanoparticle chains: Localization and transport. *Phys. Rev. B - Condens. Matter Mater. Phys.* **83,** 1–5 (2011).

200. Wang, Z. L. & Cowley, J. M. Reflection electron energy loss spectroscopy (reels): A technique for the study of surfaces. *Surf. Sci.* **193,** 501–512 (1988).

201. Lehtinen, O. *et al.* Atomic Scale Microstructure and Properties of Se-Deficient Two-Dimensional MoSe 2. *ACS Nano* **9,** 3274–3283 (2015).

202. Park, H. J. *et al.* One-dimensional hexagonal boron nitride conducting channel. *Sci. Adv.* **6** (2020).

203. Lahiri, J., Lin, Y., Bozkurt, P., Oleynik, I. I. & Batzill, M. An extended defect in graphene as a metallic wire. *Nat. Nanotechnol.* **5,** 326–329 (2010).

204. Andersen, K., Jacobsen, K. W. & Thygesen, K. S. Plasmons on the edge of MoS2 nanostructures. *Phys. Rev. B - Condens. Matter Mater. Phys.* **90,** 1–5 (2014).

205. Le, D. & Rahman, T. S. Joined edges in MoS2: Metallic and half-metallic wires. *J. Phys. Condens. Matter* **25,** 4–9 (2013).

206. Barja, S. *et al.* Charge density wave order in 1D mirror twin boundaries of single-layer MoSe 2. *Nat. Phys.* **12,** 751–756 (2016).

207. Batzill, M. Mirror twin grain boundaries in molybdenum dichalcogenides. *J. Phys. Condens. Matter* **30,** 493001 (2018).

208. Jolie, W. *et al.* Tomonaga-Luttinger Liquid in a Box: Electrons Confined within MoS2 Mirror-Twin Boundaries. *Phys. Rev. X* **9,** 11055 (2019).

209. Diaz, H. C., Ma, Y., Chaghi, R. & Batzill, M. High density of (pseudo) periodic twin-grain boundaries in molecular beam epitaxy-grown van der Waals heterostructure: MoTe2/MoS2. *Appl. Phys. Lett.* **108** (2016).

210. Nan, H. *et al.* Strong photoluminescence enhancement of MoS2 through defect engineering and oxygen bonding. *ACS Nano* **8,** 5738–5745 (2014).

211. Kim, M. S. *et al.* Biexciton Emission from Edges and Grain Boundaries of Triangular WS2 Monolayers. *ACS Nano* **10,** 2399–2405 (2016).

212. André. *Molecule3D, https://nl.mathworks.com/matlabcentral/fileexchange/55231-molecule3d* 2022.

213. Antognini Silva, D. *Étude numérique par DFT de joints de grains (MTBs) et de leur influence sur les propriétés électroniques d'hétérostructures latérales de TMDCs 2D* MA thesis (University of Namur, 2019).

214. Bertel, R., Mora-Ramos, M. E. & Correa, J. D. Electronic properties and optical response of triangular and hexagonal MoS 2 quantum dots. A DFT approach. *Phys. E Low-Dimensional Syst. Nanostructures* **109,** 201–208 (2019).

215. Gutiérrez, H. R. *et al.* Extraordinary room-temperature photoluminescence in triangular WS 2 monolayers. *Nano Lett.* **13,** 3447–3454 (2013).

216. Wirtz, L. & Rubio, A. The phonon dispersion of graphite revisited. *Solid State Commun.* **131,** 141–152 (2004).

217. Kuisma, M., Ojanen, J., Enkovaara, J. & Rantala, T. T. Kohn-Sham potential with discontinuity for band gap materials. *Phys. Rev. B - Condens. Matter Mater. Phys.* **82,** 1–7 (2010).

218. Gusakova, J. *et al.* Electronic Properties of Bulk and Monolayer TMDs : Theoretical Study Within DFT Framework (GVJ-2e Method). **1700218,** 1–7 (2017).